Stellar activity in exoplanet hosts

Enrique Herrero Casas

Stellar activity in exoplanet hosts

Memòria presentada per
Enrique Herrero Casas

per optar al grau de
Doctor per la Universitat de Barcelona

Barcelona, juliol de 2014

.

Programa de doctorat en Física

Stellar activity in exoplanet hosts

Memòria presentada per
Enrique Herrero Casas
per optar al grau de
Doctor per la Universitat de Barcelona

Directors:

Dr. Ignasi Ribas
Dra. Carme Jordi

Tutora:

Dra. Carme Jordi

June 22, 2014

Agraïments

Abans d'entrar en matèria, voldria expressar el meu més sincer agraïment a totes les persones que han contribuït, de manera directa o indirecta, al treball que aquí es presenta. Primer de tot vull destacar els meus directors de tesi, l'Ignasi i la Carme. He tingut la sort de poder treballar acompanyat per la seva motivació i els seus coneixements i experiència en el camp dels exoplanetes i la física estel·lar. Sense tot això aquest treball no hagués estat possible.

També vull agrair el bon ambient i hospitalitat que m'han acompanyat durant els anys de doctorat per part dels companys, tant durant les temporades al Departament d'Astronomia i Meteorologia (UB) com a l'Institut de Ciències de l'Espai (CSIC-IEEC). He gaudit sempre de bona companyia i de suport en els meus projectes. Guardo especial bon record de la meva estada a l'Osservatorio Astrofisico di Catania (INAF) pels consells i el bon fer de Nuccio Lanza, amb qui vaig poder aprofundir en les tècniques de modelització d'estrelles i obtenir alguns dels resultats importants d'aquest treball.

Un agraïment molt especial ha de ser per a la meva família, per al meu germà, per a l'Elena i per a tots els meus amics propers, ja que sense saber-ne gaire o gens de física estel·lar, han escrit bona part d'aquest treball quan han suportat els meus bons i mals moments, la meva presència o absència. Estic molt content pels resultats assolits i perquè tots ells n'hagin estat coautors.

Per últim, no em vull oblidar d'enviar un agraïment també als meus enemics. N'hi ha pocs, potser es compten amb els dits d'una mà, però sovint s'han esforçat per posar-me els pals a la rodes que després han estat el meu incentiu per fer les coses ben fetes.

Aquest treball ha comptat amb el suport econòmic d'una beca JAE Pre-Doc (CSIC). També ha estat parcialment finançat pels *Plan Nacional de Astronomía y Astrofísica* (AYA2009-06934, AYA2012-39612-C03-01, AYA2012-39551-C02-01 i AYA2013-48318-C2-1-R) del *Ministerio de Economía y Competitividad*.

Resum

Actualment, la major part dels esforços en la cerca i caracterització d'exoplanetes de tipus terrestre es centren en aquells que orbiten estrelles de baixa massa. Aquestes constitueixen la gran majoria de la població de la nostra galàxia (aproximadament un 75% de les estrelles són de massa inferior a la solar) i a més el seu interès rau en el fet que el senyal fotomètric i espectroscòpic dels planetes de tipus terra que hi orbiten és major degut a la menor diferència amb la mida i la massa de l'estrella. D'altra banda, algunes característiques importants de l'estructura i processos d'aquest tipus d'estrelles són encara poc coneguts, i per tant és essencial una bona caracterització prèvia d'aquestes, en especial de les estrelles de tipus M, com un dels propers passos en el camp de l'exoplanetologia. En concret, els fenòmens d'activitat estel·lar, degut a la presència de taques i fàcules on el perfil espectral i el comportament convectiu és diferent al de la fotosfera, introdueixen variacions en les mesures fotomètriques i espectroscòpiques amb una periodicitat modulada per la rotació de l'estrella. La seva caracterització és essencial per a l'estudi d'exoplanetes.

L'abast dels grans avenços en les tècniques observacionals està facilitant que l'astronomia amateur faci una important aportació a l'observació fotomètrica de trànsits d'exoplanetes. En aquest treball, la col·laboració amb l'astrònom amateur Ramon Naves (Observatori Montcabrer) ha conduit al descobriment i l'anàlisi de variabilitat fotomètrica a l'estrella WASP-33 (Herrero et al. 2011), hostatgera de tipus A5 d'un planeta gegant amb trànsits amb un període d'1,21986 dies, esdevenint la primera estrella coneguda de tipus δ Scuti amb un planeta. L'anàlisi realitzada a partir de periodogrames Lomb-Scargle i diversos mètodes de pesat de les dades va desvetllar la possible commensurabilitat de les oscil·lacions fotomètriques amb el període orbital del planeta, suggerint algun tipus d'interacció d'aquest amb l'estrella hostatgera. Es tracta d'oscil·lacions d'una escala d'amplitud i periodicitat similars a aquelles relacionades amb l'activitat estel·lar, però vinculades a un fenomen de pulsacions, en aquest cas, en una estrella massiva.

L'estudi dels fenòmens d'activitat a la fotosfera d'estrelles de baixa massa s'ha realitzat a través de diverses tècniques que ens han permès modelitzar o bé simular relacions entre les propietats estel·lars i les dades observables. L'activitat estel·lar a la fotosfera està relacionada amb la intensitat del camp magnètic, i aquest amb la velocitat de rotació de l'estrella en termes de l'efecte dinamo. Diverses relacions empíriques per a estrelles de tipus G, K i M, on existeix un embolcall convectiu, permeten establir correlacions entre determinats indicadors d'activitat, com $\log(R'_{HK})$, i el període de rotació. Aquestes correlacions ens han permès generar mostres estadístiques d'estrelles amb distribucions estocàstiques pel que fa a les seves propietats i a la seva disposició geomètrica, poblant així el diagrama activitat - $v \sin i$ i perme-

tent realitzar estimacions de l'angle de l'eix de rotació de l'estrella, i, quan existeixen mesures de $\log(R'_{HK})$ i de la velocitat de rotació projectada, $v \sin i$. Assumint sempre una alineació entre els eixos de l'òrbita i de la rotació, les estrelles amb inclinacions properes a 90° representarien les millors candidates per a una cerca de planetes per trànsit. Aquest estudi estadístic s'ha aplicat a una mostra real de 1200 estrelles de baixa massa provinents de diversos catàlegs amb mesures de $\log(R'_{HK})$ i $v \sin i$, obtenint-ne un subconjunt d'un 10% per al qual l'eficiència d'una cerca de planetes per trànsits es podria veure incrementada entre un factor 2 i 3 respecte a una cerca sobre el conjunt total (Herrero et al. 2012).

La fotometria de gran precisió de les recents missions espacials Kepler i CoRoT ha permès, a banda del descobriment d'alguns centenars de sistemes planetaris, l'estudi de la variabilitat estel·lar a gairebé totes les escales de temps on els fenòmens d'activitat hi tenen alguna influència. Les tècniques de modelització de taques, tant per mètodes analítics com per mètodes d'integració de superfície, permeten obtenir informació física de la superfície de l'estrella a partir de sèries temporals fotomètriques i espectroscòpiques. Durant aquest treball hi ha hagut una estreta col·laboració amb el Grup d'Estrelles Actives i Sistemes de l'OACT (INAF), en concret amb A. F. Lanza, per a l'anàlisi de fotometria d'estrelles actives de tipus M observades per Kepler a través de tècniques d'integració de superfície i un model de màxima entropia per al mapejat de la distribució de regions actives. Ens hem centrat en l'objecte LHS 6343 A, un dels components d'una parella òptica de dues estrelles M que mostra eclipsis produïts per una companya nana marró cada 12,718 dies. A més, també hi apareix una oscil·lació fotomètrica d'aquest mateix periode desfassada $\sim 100°$ en relació als eclipsis i persistent al llarg dels més de 500 dies d'observació. La modelització acurada de les dades ha permès explicar aquestes oscil·lacions amb la presència de regions actives que apareixen preferentment a una longitud fixa en relació a la posició de la companya nana marró, assenyalant una possible connexió magnètica entre els dos components (Herrero et al. 2013). Les regions actives mostrarien una deriva sistemàtica, indicant un periode de rotació de la primària de $13,14 \pm 0,02$ dies. D'altra banda, s'ha estudiat també una explicació alternativa per les oscil·lacions fotomètriques a LHS 6343 A en termes de l'efecte "Doppler-beaming". Hem utilitzat una aproximació Bayesiana a través de mètodes de Monte Carlo per tal d'ajustar l'efecte de modulació el·lipsoidal i de "Doppler-beaming", mostrant que aquest darrer és el major causant de les oscil·lacions persistents observades a la fotometria. Als residus de l'ajust s'hi ha realitzat una cerca de freqüències, trobant-hi un període principal de $42,5 \pm 3,2$ dies, possiblement relacionat amb la rotació de l'estrella (Herrero et al. 2014a).

L'activitat estel·lar és la responsable del soroll que s'observa a diferents escales d'amplitud i de temps en les sèries temporals de dades fotomètriques, astromètriques i espectroscòpiques. Aquest soroll representa una de les principals limitacions en les ciències planetàries. Per tal de caracteritzar-lo, hem dissenyat una metodologia per simular la fotosfera d'una estrella activa en rotació mitjançant la integració de petits elements de superfície a partir de models d'atmosfera Phoenix (Allard et al. 2011). La metodologia s'ha implementat en el simulador `StarSim`, desenvolupat expressament per aquest treball, que permet obtenir sèries temporals d'espectres sintètics d'estrelles de baixa massa incloent tots els efectes que tenen una influència significativa en la signatura espectral dels elements de la superfície estel·lar, permetent caracteritzar

així el senyal produït per l'activitat i estudiar-ne la relació amb els paràmetres físics de l'estrella, així com els efectes introduïts en les mesures d'exoplanetes en estrelles actives. El programa permet obtenir el senyal de l'activitat donada la resposta d'un determinat filtre o instrument d'observació i per a qualsevol distribució de regions actives especificada o generada estadísticament, donant com a resultat la corba fotomètrica, la corba de velocitats radials i els desplaçaments astromètrics produïts per la presència de regions actives. La metodologia ens ha permès proposar algunes estratègies per tal de corregir les observacions de trànsits de l'efecte de taques a l'estrella, que poden introduir variacions significatives en la mesura del radi del planeta. Hem mostrat que es poden utilitzar observacions simultànies en bandes visibles per tal de mitigar els efectes de l'activitat en l'infrarroig mitjà en un factor entre 20 i 100, podent arribar a precisions de l'ordre de 10^{-5} (en unitats de flux relatiu) fins i tot per a estrelles relativament actives (Herrero et al. 2014b). Els efectes astromètrics de l'activitat s'han estudiat per una mostra sintètica de 10000 estrelles de tipus solar amb distribucions estocàstiques de regions actives seguint el patró del Sol. S'ha comprovat que els desplaçaments astromètrics observats en el 33% serien detectables donada la resolució teòrica de la missió espacial Gaia si les estrelles es trobessin a menys de $26,7$ parsecs.

Ens hem centrat en detall en el cas de l'estrella HD 189733, hostatgera d'un planeta gegant, la qual ha estat àmpliament estudiada i per la qual hi ha disponibles dades fotomètriques (MOST) i espectroscòpiques (SOPHIE) simultànies, podent-ne relacionar el senyal de l'activitat en els dos tipus d'observables. A partir de la modelització realitzada per Lanza et al. (2011a) i realitzant successius ajustos amb el simulador `StarSim`, s'ha obtingut un mapa de la superfície que permet reproduir acuradament la corba de llum i les velocitats radials. Aquesta distribució de taques s'ha utilitzat per estudiar-ne els efectes produïts sobre els trànsits al llarg dels 30 dies d'observacions. Hem mostrat que els efectes dels events d'ocultació de taques són significatius fins i tot a l'infraroig mitjà. A més, els efectes cromàtics de la presència de taques no ocultades sobre la mesura del radi del planeta mostren un senyal amb una signatura i amplitud molt similar al de l'atmosfera d'un planeta dominada per pols. Aquesta amplitud es modula linealment amb la cobertura projectada de taques, que té variacions temporals significatives en el cas de HD 189733. Per tant cal una modelització simultània del mapa de la superfície quan es fa un estudi de l'atmosfera de l'exoplaneta HD 189733 b a través d'espectroscopia de transmissió. El model de velocitats radials permet explicar la major part de les observacions fins a la precissió típica dels errors sistemàtics de SOPHIE. Alguns dels residuals es podrien explicar per la presència de fàcules o variacions temporals ràpides en la mida d'algunes regions actives. El soroll produït per l'activitat en una sèrie típica de ~ 30 observacions espectroscòpiques introdueix una incertesa de ~ 0.011 M_{Jup} en la massa del planeta.

Els resultats d'aquest treball conclouen que és essencial una correcta modelització del senyal de l'activitat estel·lar en el camp de les ciències exoplanetàries, i es proporcionen algunes eines i estratègies per tal de caracteritzar i corregir aquests efectes i obtenir-ne informació astrofísica. En un futur proper s'optimitzarà la implementació al simulador `StarSim` per tal de poder modelitzar dades reals de manera més eficient, a més d'estudiar estratègies per minimitzar els efectes de l'activitat en les mesures de velocitats radials.

Abstract

Most of the efforts on the search and characterization of Earth-like exoplanets are currently focused on low mass stars. These represent the vast majority of the population in our galaxy (about 75% of the stars have a lower mass than the Sun) and their interest lies in the fact that the photometric and spectroscopic signal of orbiting Earth-like planets is higher due to lower star-planet size and mass ratios. However, several important properties related to the structure and processes in this type of stars are still unknown, so a careful characterization is essential, especially for M-type stars, as one of the next steps in exoplanet sciences. Specifically, stellar activity effects, due to the presence of spots and faculae which have a different spectral and convective behavior than the quiet photosphere, introduce variations on photometric and spectroscopic measurements with a periodicity modulated by the stellar rotation. Their characterization is essential for exoplanet sciences.

The availability of the most recent advances in observational equipment and techniques is allowing the amateur astronomy community to make significant contributions on the photometric follow up of exoplanet transits. In this work, a collaboration with the amateur astronomer Ramon Naves (Montcabrer Observatory) led to the discovery and analysis of the photometric variability of WASP-33 (Herrero et al. 2011), an A5-type star hosting a giant transiting planet with a period of 1.21986 days, then becoming the first exoplanet host with δ Scuti oscillations. The photometry was analysed with Lomb-Scargle periodograms and several methods of data weighting, revealing the possible commensurability of the photometric pulsations with the orbital period of the planet, thus suggesting some type of star-planet interactions. The oscillations show an amplitude and timescale that are of the same order that those typically produced by stellar activity, but in this case related to a phenomenon of pulsations in a relatively massive star.

The characterization of stellar activity in low mass stars was carried out through several techniques that allowed us both to model and to simulate the relationships between the observational data and the stellar properties. Stellar activity in the photosphere is related to the magnetic field intensity, which is in turn modulated by the stellar rotation rate in terms of the dynamo action. Several empirical relations for G-, K- and M-type stars, where a convective envelope is present, allow to find correlations between certain activity indicators, such as the chromospheric $\log(R'_{HK})$, and the rotation period of the star. These correlations allowed us to generate synthetic samples of stars with stochastic distributions of stellar and geometric properties, thus populating the activity - $v \sin i$ diagram and allowing to estimate the inclination of the rotation axis, i, when accurate measurements of $\log(R'_{HK})$ and the projected rotation rate, $v \sin i$, are available. Assuming a spin-orbit alignment,

the subset of stars with inclinations close to 90° would presumably contain the best candidates for a targeted planet search with the transit technique. The statistical distribution of stellar inclinations in the activity - $v \sin i$ diagram was studied and applied to a sample of 1200 real low mass stars coming from different catalogs with $\log(R'_{HK})$ and $v \sin i$ measurements available. A subset with the 10% most suitable stars for a targeted transit search was presented. A search within this subset would have an expected rate of findings increased in a factor of 2 o 3 with respect to a search on the initial sample (Herrero et al. 2012).

The high precision photometry provided by the space missions Kepler and CoRoT has allowed not only to discover several hundreds of exoplanetary systems, but also to study stellar variability at most of the timescales where the phenomena related to activity have some significant effect. Spot modelling techniques, either analytic or surface integration methods, allow to obtain some physical information about the stellar surface from time series photometric and spectroscopic data. In this work there has been a close collaboration with the Group of Active Stars and Systems of the OACT (INAF), especially with A. F. Lanza, for the analysis of the photometry of active M-type stars observed by Kepler through surface integration techniques and a maximum entropy model for the obtention of the distribution and evolution of active regions. We focused on the target LHS 6343 A, one of the two M-dwarf components of an optical binary showing eclipses produced by a brown dwarf companion with a period of 12.718 days, apart from photometric oscillations with the same periodicity and a phase lag of $\sim 100°$ from the eclipses, persisting for more than 500 days. The accurate modelling of the Kepler data allowed to explain these oscillations with the presence of active regions appearing at a specific longitude from the sub-companion point, thus suggesting a possible magnetic connection between both components (Herrero et al. 2013). The active regions show a systematic drift, indicating a rotation period of the primary of 13.14 ± 0.02 days. On the other hand, we also studied an alternative explanation for the photometric oscillations in LHS 6343 A in terms of the Doppler-beaming effect. We used a Bayesian approach implemented through a Monte Carlo Markov chain method to model the ellipsoidal and Doppler-beaming effects, showing that the last is the main cause of the observed oscillations. The residuals of the fit were analysed, finding a main period of 42.5 ± 3.2 days, which could be related to the rotation rate of the star (Herrero et al. 2014a).

Stellar activity effects are responsible for the noise observed at different amplitude and timescales on time series photometric, astrometric and spectroscopic data. Such noise represents one of the main limitations for exoplanetary sciences nowadays. In order to characterize it, we designed a methodology to simulate the photosphere of an active rotating star through the integration of small surface elements from Phoenix atmosphere models (Allard et al. 2011). The methodology is implemented in the simulator `StarSim`, especially developed during this work, that allows to obtain time series synthetic spectra of low mass stars accounting for all the effects that have some significant influence on the spectral signature of the elements of the stellar surface. This allows to characterize the signal produced by activity and to further study its relationship with the stellar properties, as well as the possible effects produced on exoplanet measurements in active stars. The simulator provides the activity signal for a given instrumental response or filter passband and for any specified or stochastically generated distribution of active regions, giving as result the photometric light curve,

the radial velocity curve and the astrometric shifts produced by the presence of active regions. The methodology allowed us to present several strategies in order to correct or reduce the effects of spots on the photometry of exoplanet transits, as these may induce significant variations on the measurement of the planetary radius. We showed that simultaneous observations in a visible band can be used in order to reduce the effects of spots in infrared observations by a factor of 20 to 100, providing precisions up to 10^{-5} (in relative flux units) even for relatively active stars (Herrero et al. 2014b). The astrometric effects of activity were studied for a synthetic sample of 10000 Sun-like stars with stochastic distributions of active regions following a solar pattern. We showed that the astrometric shifts observed in 33% of the sample would be detectable given the theoretical resolution of the Gaia space mission if the stars were located at 26.7 parsecs or closer.

We used the simulator `StarSim` to carry out a comprehensive analysis of HD 189733, a K5 star hosting a giant planet, which has simultaneous photometric (MOST) and spectroscopic (SOPHIE) data available, thus allowing to study activity signals on both type of data. The results from the spot modelling by Lanza et al. (2011a) were used as initial parameters in order to fit the distribution of spots using the program `StarSim`, accurately reproducing the light curve and radial velocity observations. Such distribution of spots was used in order to study the effects of activity on the exoplanet transits during the 30 days of the observations. We showed that the effects of spot-crossing events are significant even for mid-infrared wavelengths. Moreover, the chromatic effects of spots not occulted by the planet show a signal with a wavelength dependence and amplitude that are very similar to the signature of the atmosphere of a planet dominated by dust. Such amplitude is linearly scaled with the projected filling factor of spots, which presents significant variations in the case of HD 189733, so a simultaneous modelling of the distribution of spots is needed when studying the atmosphere of HD 189733 b through transmission spectroscopy. The radial velocity theoretical curve is in agreement with the observations up to the typical instrumental systematics of SOPHIE. Some of the residuals could be explained by the presence of faculae or fast evolution of spots not reproduced by our model. The noise produced by activity in a typical series of ~ 30 spectroscopic observations introduces an uncertainty of ~ 0.011 M_{Jup} in the planetary mass.

The results from this work conclude that it is essential to correctly model the stellar activity signals for exoplanetary sciences, and we provide some tools and strategies to characterize such effects and extract astrophysical information. In the near future, the methodology implemented in the simulator `StarSim` will be further developed in order to be able to model real photometric and spectroscopic data in a more efficient way, as well as to present strategies for the minimization of stellar activity effects on radial velocity measurements.

Contents

Chapter 1

Introduction

1.1 Activity in low mass stars

Low mass stars represent the vast majority of the stellar population of the Milky Way. In particular, main sequence M-type stars are essential to complete the knowledge of the structure and dynamics of the Galaxy, as well as for the understanding of the stellar interior structure and energy transport processes in convection and magnetic field frameworks. However, their detailed physics are rather unkwown due to their intrinsic faintness ($M_V \sim 9$ for M0, $M_V \sim 15$ for M5). The better understanding of M-type dwarfs would also allow optimizing the current techniques for planetary searches and characterization.

Low mass stars are known to have strong magnetic fields responsible for part of the heating of the stellar atmosphere through non-radiative processes, powering their steady-state emission from X-ray to radio wavelengths (Walkowicz et al. 2008; Berger 2006) and inducing the appearance of flares. The atmospheres of M dwarfs represent a laboratory to analyse these manifestations of activity for a better understanding of the dynamo action and its correlation with mass, rotation and age.

The fraction of stars presenting magnetic activity is a function of spectral type and age. Early M-dwarfs are rarely observed to be active as traced by the Hα emission, whereas 70% of M7 stars manifest activity (Joy & Abt 1974; Gizis et al. 2000; West et al. 2004). This is thought to be an age effect, as early M dwarfs have shorter active lifetimes than late M dwarfs (West et al. 2008). The intensity of the activity has been measured in terms of indicators such as $L_{\mathrm{H}\alpha}/L_{\mathrm{bol}}$ (i.e., the ratio of luminosity emitted in Hα to the bolometric lominosity). The large scatter cannot be explained from a relation with age (West & Basri 2009). Other activity indices are related to the Ca II H & K lines emission and to the X-ray emission. Multi-epoch spectroscopic observations would be needed in order to study how activity variations in individual stars change as a function of age.

The origin of the magnetic fields in low mass stars (later than mid-F) is in the outer convective envelope, where the magnetic diffusivity is strongly enhanced by fluid motions (Rüdiger et al. 2011). The dynamo effect consists on the generation of magnetic fields from the motion of an electrically conducting fluid (i.e., converting kinetic energy into magnetic energy) and is thought to operate in many astrophysical objects like planets, stars and galaxies. Low mass stars produce large scale dynamos, which generate magnetic fields on spatial scales larger than that of the convection. The presence of activity cycles of the same periodicity of the field decay

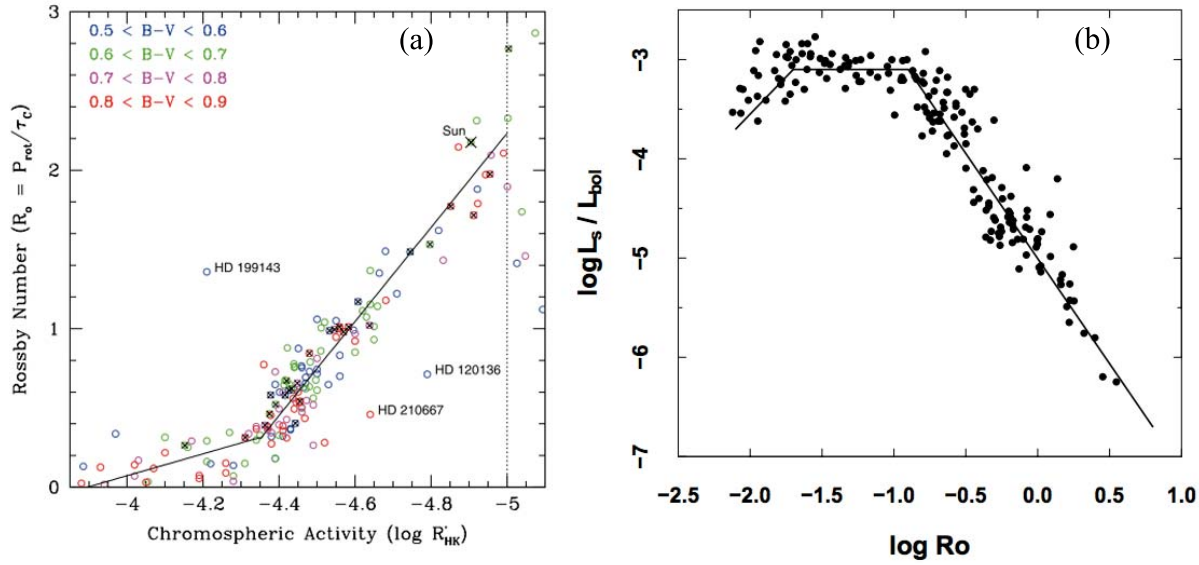

Figure 1.1: Measurements of rotation-activity relations in main sequence stars for a range of spectral types. (a) The Rosby number R_o as a function of the chromospheric activity index $\log(R'_{\rm HK})$ including linear fits for the very active and active regimes (from Mamajek & Hillenbrand 2008). (b) The X-ray emission vs. the Rosby number, showing linear, saturation and super-saturation regimes (from Feigelson et al. 2003). A more detailed description can be found in Chapter 3 and references therein.

times of these processes points out that their origin is the dynamo action. This also explains the observed correlation between activity and rotation (Kraft 1967; Noyes et al. 1984), and in combination with empirical rotation-age relations (due to the loss of angular momentum as stars leave the pre-main sequence and arrive to the main sequence), the well known rotation-age-activity relations are obtained (see Skumanich 1972). For a broad range of spectral types, when a convective envelope is present, both chromospheric and coronal activity indices indicate an increase in intensity with increasing rotation velocity (see Fig. 1.1), until it is saturated at a threshold velocity that depends upon stellar mass (Pizzolato et al. 2003). The measurement of rotation rates in the unsaturated part of the rotation-activity relations is difficult because rotational velocities in this range correspond to different $v \sin i$, that in the case of M dwarfs, are not currently detectable by Doppler broadening measurements. Chapter 3 will focus on these relations for the generation of simulated samples of activity and rotation data of low mass stars.

The situation is more complicated among the lower-mass M dwarfs (i.e., below $\sim 0.35 M_{\odot}$, Chabrier & Baraffe 1997), as their interior is fully convective and they do not possess a tachocline that originates the dynamo action as in Sun-like stars. In these cases, the magnetic field generation is modelled by a small-scale dynamo without the Ω-effect that is present in partially convective stars (Durney et al. 1993). However, there is evidence that some rotation-activity correlation still persists in the regime of fully convective M dwarfs (Delfosse et al. 1998; Mohanty & Basri 2003; Reiners & Basri 2007). In fact, no strong breaks in the measurements of magnetic fields through Bf values are observed for the range of spectral types where stars become fully convective (M3 - M4), similarly to what is observed for activity indices like X-ray and Hα emission (Reiners & Basri 2009; Reiners et al. 2009).

The presence of large flare events in low mass dwarfs has also been related to the emergence of internal magnetic fields at the stellar surface. There are a few statistical studies of the occurrence of flares in M dwarfs (Audard et al. 2000; Welsh et al. 2007), but very little is known about the dependence of their frequency and intensity with spectral type and age. Kowalski et al. (2009) analysed a sample of M dwarfs observed with the SDSS, finding that the most luminous flares occur on the earlier-type stars and that the phenomena of flaring is strongly correlated with the appearance of Hα emission in the quiet spectrum.

The recent advancements in observational techniques, such as spectropolarimetric Doppler imaging of the magnetic field distribution or the different photometric spot modelling techniques, are providing new insights into the comprehension of the effects of magnetic activity on the surface of low mass stars. A description and example of the implementation of spot modelling technique can be found in Chapter 4. At the same time, the advent of recent space missions like CoRoT and Kepler has provided large-scale time series data that is allowing the characterization of activity on all timescales. The long time baseline of these photometric missions may cover most of the frequencies of the effects produced by activity on low mass stars (i.e., rotational modulation of spots, evolution of spots and activity cycles). Also, the improvement of the statistics of flare rates provided by these space missions, when short cadence data are available, is of particular interest for M dwarfs.

Being the most abundant population, the interest on low mass stars has also increased since the discovery of the first extrasolar planet (Mayor & Queloz 1995), because of their advantages as targets for exoplanet searches, both through photometric and spectroscopic techniques, as they present a higher planet-to-star signal ratio than in the case of stars with the luminosity of the Sun or higher. Therefore, an additional issue is the impact of magnetic fields and the subsequent stellar activity on the detection of planets and on their formation, evolution and habitability. Atmospheres and habitability conditions of close-orbiting planets may be significantly affected by long duration exposure to high energy radiation from (UV and X-ray), and in this way it is especially important to understand the conditions that give rise to high energy emission in M dwarfs. Stellar flares are also a concern for the habitability of planets orbiting cool stars, as their habitable zones may be ~ 0.2 AU or less from the star, making those planets especially vulnerable to the effects of stellar activity (Lammer et al. 2007). Therefore, a better evaluation of the effects of flaring, considering their frequency and intensity, is essential to estimate the potential habitability of planets around M dwarfs.

1.2 The search for Earth-like planets

Exoplanet research has experienced an exponential growth over the past few years, thus becoming a revolutionary field in astrophysics. This is both because of the impressive discoveries made recently and also because of the inherent appeal of the topic. The identification of potentially terrestrial exoplanets (with masses below 10 $M_\oplus$) and the observation of molecular species in the atmosphere of hot Jupiters are among the major advancements of the past five years in this area (e.g., Mayor et al. 2009; Swain et al. 2009). More than 1800 planets have been discovered up to now using both photometric and spectroscopic techniques, and orbiting around all type of stars, from A to M. On average, one or more planets orbit every star in our Galaxy, according to the current statistical estimates (Cassan et al. 2012). The variety of planets includes some with very short periods (< 1 day), eccentricities higher than 0.9 and circumbinary systems. Planetary temperatures span over two orders of magnitude, and a continuum of sizes and masses are found

from super-Jupiters down to sub-Earth objects (Fressin et al. 2013).

The detection of methane in the atmosphere of HD 189733b by Swain et al. (2008) opened a new branch in the characterization of exoplanets. Additional carbon-bearing species, such as carbon-monoxide and dioxide, have been observed in recent years (Tinetti et al. 2010; Snellen et al. 2010). Water vapour seems to be common in hot Jupiters with temperatures ranging from 800 to 2200 K, while very hot Jupiters, where temperatures can be around 3000 K, harbor exotic species that are also found in the atmospheres of brown dwarfs, metal oxides or metal hydrides (Swain et al. 2013). These species may significantly influence the vertical thermal profile of the planetary atmosphere, as well as its albedo. In the visible, the spectrum of hot Jupiters seems to be dominated by Rayleigh scattering, indicating the presence of hazes or dust (Knutson et al. 2007; Pont et al. 2013).

While the current techniques for the detection of exoplanets have allowed the discovery of "extreme cases" compared to the Solar System scennario, strong biases still exist in the parameter space of the characteristics of the known exoplanets (see Fig 1.2). In the near future, the Gaia space mission (from the European Space Agency) is expected to find several thousands of new planets through astrometry, which will presumably be at intermediate separations from their host stars (Perryman 2002). Transit and radial velocity techniques are biased towards close-in planets, while instruments for direct imaging (e.g., ESO-VLT SPHERE and SUBARU SCExAO) are built to detect massive planets at large separations from the host star.

Transiting planets (of which more than 1100 are known to date) allow to obtain the planetary radius from the measurement of the transit depth, and the mass when combined with radial velocity observations. This in turn provides an estimation of the planetary bulk density, and thus allow to make a comparison between different interior structures and compositions. Fortney et al. (2007) obtain theoretical models for planetary interiors of different compositions and a first classification of a sample of transiting planets. It is thought that different bulk densities are related to different scenarios of the formation mechanism. An intriguing point is the diversity of densities found for planets of less than 10 $M_{\oplus}$, some of them thought to be rocky planets (so called super-Earths, such as CoRoT-7 b, Kepler-10 b, Kepler-62 e, f) and typically orbiting with short periods, while others present much lower densities, typically orbiting cool stars or having long periods (GJ 1214b, Kepler-11d, e, f).

Exoplanet search programs are currently focused on the goal of finding Earth-like planets in the habitable zone of their host stars, that is to say, orbiting within the limiting planet-star distances where the equilibrium temperature in a planet with sufficient atmospheric pressure is adequate for the presence of liquid water (Kasting 2010; Kopparapu et al. 2013). Up to now, about 15 super-Earths are known to orbit in the habitable zone, and statistical estimates indicate that about one half of low mass stars could harbor Earth-size planets (0.5 - 2 $R_{\oplus}$) within the habitable zone boundaries (Kopparapu 2013). One possible "shortcut" to find a potentially habitable planets is to carry out the searches around low mass stars (M dwarfs). In this case, observations are most suited in the near infrared because of the spectral energy distribution of the target stars. M-type exoplanet hosts have two major advantages: 1) because of the lower stellar mass and luminosity, habitable planets are closer in, have shorter orbital periods and hence induce higher amplitude reflex motions on the star; and 2) because of the smaller radius, a transit of a terrestrial planet has a depth of a few per cent and therefore it is suitable for discovery and follow up even from the ground.

The search for exoplanets around M-type stars is blooming with new experiments (like the MEarth transit search; Irwin et al. 2008) and projects for the near future (e.g., the CARMENES

radial velocity search). A critical element to the success of these initiatives is to attain a detailed characterization of the targets. This is chiefly because of the inherent stellar activity that affects M-type stars causing both photometric and radial velocity jitter (e.g., Wright 2005). Such jitter is related to the overall light modulation induced by starspots but also because of the time variability of their position and properties.

1.3 Aims of this work

The aim of this work is to characterize the effects of stellar activity at the different timescales that produce jitter in photometric and spectroscopic observations of exoplanetary sciences. Then, we propose strategies in order to improve the current methodologies for planet search and characterization. This is done both through the modelling of observational data and through simulations that allow us to perform statistical studies to correlate activity jitters with stellar properties.

The work is divided into the following main topics:

- The first is centered on the analysis of the variability in the relatively massive host star of the exoplanet WASP-33 b. The oscillations were reported by Herrero et al. (2011) as a result of a collaboration with the amateur astronomy community, and represent the discovery of the first δ Scuti exoplanet host star. WASP-33 is a very particular system with a hot Jupiter planet in a close-in retrograde orbit. The intriguing point of the δ Scuti oscillations is that their periodicity seems to be commensurable with the orbital motion of the planet. Despite not being an active star, the study is included in the first part of the work as it introduces several computing methodologies commonly used for the analysis of the photometric and spectroscopic variability produced by activity. This part is presented in Chapter 2, including a discussion on the possible star-planet interactions that might be inducing the observed variability.

- The current knowledge on the rotation - activity correlations for low mass stars are reviewed in the second topic of the work. Stars with different stellar axis inclinations are located in specific areas of the activity - $v \sin i$ diagram. Using the chromospheric activity tracer $\log(R'_{HK})$ and based on empirical relations, we simulate catalogs with large sample of stars of different spectral types to study their statistical distribution on the activity - $v \sin i$ diagram. The results are applied to real observed stars in order to identify those that have a higher probability to be oriented nearly equator-on (inclination close to 90°). Assuming spin-orbit alignment, this should significantly increase the efficiency of a targeted transit search with the transit technique. The description and results of this methodology are presented in Chapter 3.

- The third topic is centered on a review of the current spot modelling techniques for the study of the distribution of active regions in the surface of low mass stars and its connection with the structure of their magnetic fields. In particular, we use a surface integration technique based on regularized maximum entropy algorithms of minimization from Lanza et al. (2003) in order to model the Kepler photometric data of LHS 6343 A, an M4V star with a brown dwarf companion that eclipses the primary every 12.7138 days. The data present a constant modulation which is synchronized with the eclipses and can be explained by persistent groups of spots in one of the faces of the M dwarf, which would

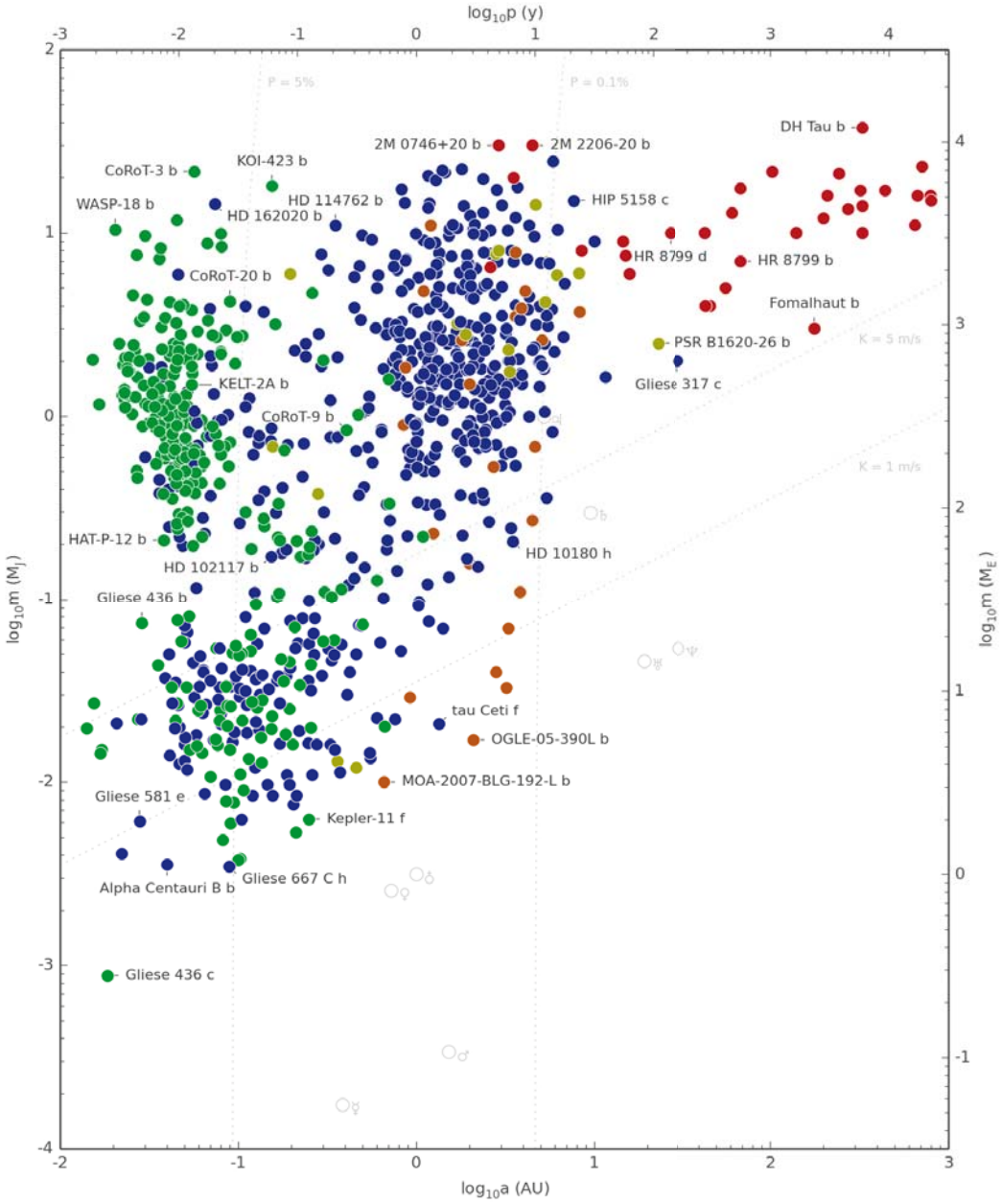

Figure 1.2: The planetary mass m vs. the semi-major axis a for the exoplanets known until 2nd January 2014. Distinct colours indicate the discovery technique: radial velocity (dark blue), transit (dark green), timing (dark purple), direct imaging (dark red) and microlensing (dark orange). Solar System planets are plotted for reference with their corresponding symbols. Reference lines indicate a rough measurement of the difficulty of detecting planets through radial velocity and transit techniques. Dashed lines trace the combinations of m and a values that produce the indicated radial velocity semi-amplitude K for a planet orbiting a solar-mass star (assuming $m_{\rm p} << M_*$). Dashed lines trace the m (for Jupiter-density) and a values where the geometric probability, P, of transit for a solar-radius star (assuming a circular orbit, so that e and ω can be ignored) is the indicated value (less than the indicated proportion of all planets to the right of a given line will have transiting orbits). Image: Wikipedia, Open Exoplanet Catalogue.

be tidally coupled with the companion. A second analysis reveals that the photometry is significantly affected by Doppler-beaming, being the main explanation for the observed oscillations. This is described in Chapter 4.

- Finally, we present the sophisticated stellar surface simulator `StarSim` methodology to generate synthetic time series of photometric and spectroscopic observations of active rotating stars. This is based on the simulation of the stellar photosphere with surface integration techniques and the use of the most recent available models for low mass stars, including all significant effects affecting the flux intensities and the wavelength of spectral features. The capability to reproduce the signature of active regions and transiting planets on a wide range of spectral types may help us to investigate the effects of activity, both systematic and random, on planet measurements, as well as to design strategies in order to correct data for activity jitter. The methodology of the simulations and several applications are presented in Chapter 5. In particular, the K0V-type star HD 189733 hosting a hot Jupiter with a period of 2.2 days and with a modulation in its light curve due to the presence of starspots has been studied and modelled with `StarSim`. This study is also included in Chapter 5.

The exploitation of the methodology that we present in Chapter 5 is still in progress. Further work is being done for the optimization of the implementation of the program routines in order to be able to perform the inverse problem and model photometric and spectroscopic data of active stars to obtain detailed surface maps and accurate properties. Simulations of individual cases and large statistical samples are being carried out in order to better understand the effects of activity on exoplanet transit observations and remove or minimize the activity jitter from radial velocity measurements. A short description of the future prospects as well as the conclusions of the work are included in Chapter 6.

Chapter 2

WASP-33: The first δ Scuti exoplanet host star

This chapter is based on the paper Herrero et al. (2011). We report the discovery of photometric oscillations in the host star of the exoplanet WASP-33 b (HD 15082). The data were obtained in the R band in both transit and out-of-transit phases using the 0.3-m telescope at the Montcabrer Observatory and the 0.8-m telescope at the Montsec Astronomical Observatory. Observations from the Exoplanet Transit Database were also used. Proper fitting and subsequent removal of the transit signal reveals stellar photometric variations with a semi-amplitude of about 1 mmag. The detailed analysis of the periodogram yields a structure of significant signals around a frequency of 21 cyc per day, which is typical of delta Scuti type variable stars. An accurate study of the power spectrum reveals a possible commensurability with the planet orbital motion with a factor of 26, but this remains to be confirmed with additional time-series data that will permit the identification of the significant frequencies. These findings make WASP-33 the first transiting exoplanet host star with delta Scuti variability and a very interesting candidate to search for star-planet interactions.

2.1 Introduction

Most of the $\sim$ 1100 transiting exoplanets that have been discovered up to date are orbiting solar-type or late-type stars. WASP-33 b, a gas giant planet showing transits on a fast-rotating main-sequence A5 star, represents a singular case that offers the possibility of studying an intermediate-mass planet host. WASP-33 b was first reported as a transiting planet candidate by Christian et al. (2006), but it was not officially announced as an exoplanet until the study of Collier Cameron et al. (2010). The relatively long time lapse may be explained because the host star (HD 15082, $V = 8.3$) is a fast rotator ($v \sin i = 86$ km s^{-1}) and this hampers precise radial velocity work. Collier Cameron et al. (2010) carried out a detailed study considering both photometry and spectral line profile variations during transits and established an upper mass limit of 4.1 M_J for the planet. In addition, the authors showed evidence of non-radial pulsations in the star and suggested γ Dor-type variability. Furthermore, they also found that WASP-33 b

orbits the star in retrograde motion and that the orbit is inclined relative to the stellar equator.

Here we use observations taken at the amateur Montcabrer Observatory and the professional fully robotic Montsec Astronomical Observatory – OAdM (Colomé et al. 2008), as well as additional observations from the Exoplanet Transit Database (hereafter ETD[1]). These allow us to provide the first evidence for photometric oscillations on the star WASP-33, and to analyze their amplitude and periodicity. The presence of a large planet close to a star may cause tidal effects responsible of multiperiodic non-radial pulsations, and in special cases radial pulsations, on its host star (Schuh 2010). However, there is only one known exoplanet orbiting a pulsating star, V391 Pegasi (sdB type), which was discovered using the timing method (Silvotti et al. 2007). Bazot et al. (2005) performed the first asteroseismic analysis for a solar-like planet host star, μ Arae, modelling 43 p-modes which were previously identified by Bouchy et al. (2005a). Recently, Kepler data were used to characterize the exoplanet host HAT-P-7 through an analysis of its simultaneously discovered solar-like oscillations (Christensen-Dalsgaard et al. 2010). WASP-33 is the first case where δ Scuti pulsations have been observed on a known transiting exoplanet host star.

2.2 Observations and photometry

The first observations in our dataset were obtained from Montcabrer Observatory on dates August 26, September 7 & 14 and October 20, 2010, using a 0.3-m Schmidt-Cassegrain telescope and a SBIG ST8-XME camera with an AO-8 adaptive optics system, working at a 1.03" per pixel scale. This is an amateur private observatory having Minor Planet Center code 213 located in the suburbs of Barcelona, Spain. Photometry in two additional nights with very good photometric conditions (September 21 & 28, 2010) was obtained from OAdM using a fully robotic 80-cm Ritchey-Chrétien telescope and a FLI PL4240 2k×2k camera with a plate scale of 0.36" per pixel. All the photometry described above was carried out in the Johnson R band and by defocusing the images to increase the photometric precision. Aperture photometry was performed to the images, using three or four comparison stars as available. The first transit was observed with the aim of improving the definition of the existing light curves, most of them incomplete so far (Collier Cameron et al. 2010), whereas the follow-up photometry was obtained at several orbital phases in order to further study the oscillations that the first photometric dataset seemed to suggest.

Additional recent transit photometry of WASP-33 is available at the ETD, including some diagrams and a parameter analysis of each transit. WASP-33 b transit R band photometric data from K. Hose (August 23, 2010), F. Hormuth (August 26, 2010) and C. Lopresti (September 11, 2010) were used in our analysis. All the photometry datasets used in this study are listed in Table 2.1. The root mean square (rms) residuals given in the third column, in spite of being affected by the pulsations, give an idea of the precision of the photometry from each observatory.

2.3 Data analysis and discussion

The transit photometry datasets were analyzed using `JKTEBOP` code (Southworth et al. 2004a,b), which is based on the EBOP code written by Paul B. Etzel (Popper & Etzel 1981). Each transit

[1] http://var2.astro.cz/ETD

Table 2.1: Photometric datasets used in this work. Montcabrer Observatory and OAdM data were specially acquired during the course of this work. The rest of the photometry is public at the ETD. In transit observations, the photometric root mean square (rms) residual per measurement and the transit time deviation (TTD) with respect to the mid-transit ephemeris given in Collier Cameron et al. (2010) (see text) are calculated from the fits represented in Fig. 2.2.

Author/ Observatory	Date	Transit / Out of tr.	rms (mmag)	TTD (min)
K. Hose	23 Aug	T	3.7	4.10 ± 1.31
Montcabrer	26 Aug(a)	T	2.8	9.76 ± 1.01
F. Hormuth	26 Aug(b)	T	2.7	3.18 ± 0.86
Montcabrer	7 Sept	OOT	3.1	
C. Lopresti	11 Sept	T	3.9	-1.66 ± 1.62
Montcabrer	14 Sept	OOT	2.3	
OAdM	21 Sept	OOT	1.6	
OAdM	28 Sept	T	2.1	2.83 ± 0.50
Montcabrer	20 Oct	T	1.8	7.55 ± 0.86

Table 2.2: Transit parameters fitted using `JKTEBOP`. The transit depth was computed from the fit. The error bars are 1-σ uncertainties.

Parameter	Value
$r_1 + r_2$	0.309 ± 0.007
r_2/r_1	0.1066 ± 0.0008
i (°)	85.8 ± 2.0
$T_0 - 2450000$	5431.8879 ± 0.0003
rms (mmag)	3.44
Depth (mmag)	14.3 ± 0.2

light curve was corrected for a slight trend using low-order polynomials. Preliminary fits were run using `JKTEBOP` by solving for the sum of the radii relative to the orbital semi-major axis (star + planet; $r_1 + r_2$), ratio of radii (r_2/r_1), inclination, and time of transit. This was done prior to combining all the transits by including a shift to normalize their out-of-transit level so that consistent parameters were obtained for all the transits. The period was fixed to that given in Collier Cameron et al. (2010), $P_{\rm orb} = 1.2198669$ d. To properly weigh the observations from different authors, we performed a running average of the residuals from a preliminary fit in bins of 20 minutes, selecting as individual error for each point the standard deviation of its bin. The best fit to the overall transit photometry is shown in Fig. 2.1 and the associated parameters are given in Table 2.2. All parameters are consistent within the uncertainties with those in Collier Cameron et al. (2010). A pulsation trend is clearly present on the residuals of this fit, and as Fig. 2.2 illustrates, it is already apparent to the eye that all the curves (some of them separated by more than 50 d) show "bumps" that always appear at the similar orbital phases (note, e.g., the phases just after the egress).

To better determine the characteristic period of the observed pulsations, we carried out individual fits to each transit by leaving the inclination and transit time as free parameters and fixing the relative radii of the star and the planet according to the global result. This was done to minimize the possible effects of transit time variations caused by unknown third bodies in

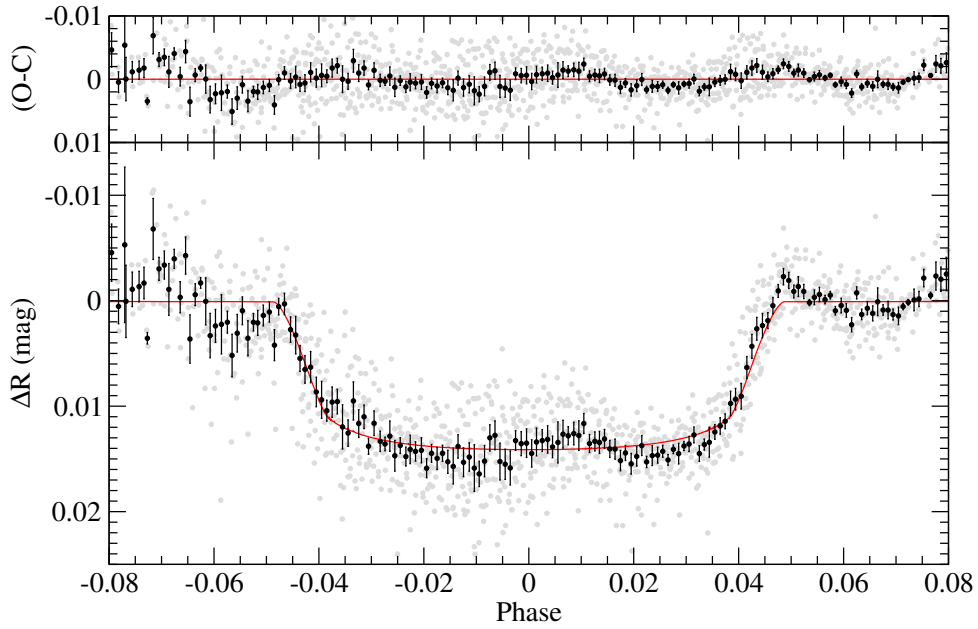

Figure 2.1: Best fit to the overall R band transit photometry phase-folded (grey symbols) and binned in steps of 0.001 in phase (black symbols) for better visualization. The top panel shows the residuals of this fit. Error bars are computed as the mean value error of each bin.

the system on the residuals and the effect of trend corrections on the transit depth. We find that the inclination of each individual fit is well within the uncertainty of that determined for the combination of the transits. In Table 2.2 the transit time deviations of each transit are also listed, however, their scarcity and possible systematics caused by the pulsation precludes us of drawing any conclusions about the presence of additional planets in the system.

As already shown, the residuals of the transit fits show a clear oscillation pattern that is also present in the out-of-transit photometry obtained for WASP-33. The presence of oscillations during the entire orbital period, including out-of-transit phases as shown in Fig. 2.3, rules out the possibility of the "bumps" seen in transit as being caused by the effect of the gravity darkening in a rapidly rotating star such as WASP-33 (Barnes 2009). Thus, we combined the residuals from the transit fits and the out-of-transit light curves in a single curve to better determine the period of the oscillations. Figure 2.4 shows the results of running a periodogram on these data with the PERIOD04 code[2] (Lenz & Breger 2005) that is based on the discrete Fourier transform algorithm. A main peak around a frequency of 21 d^{-1} is clearly present in this figure, corresponding to a period of about 68 min. However, a close inspection of this peak reveals that it is composed of several other peaks that are an imprint of the window function associated to our data. The second structure around 6 d^{-1}, which is similar to the typical length of the individual photometric series, is probably spurious and may be related to the detrending and the flux-shift of the different light curves.

To better analyse the structure of this peak, we fitted the theoretical transit light curve to the original data by adding a sinusoidal modulation of the light of the system, thus performing a phase dispersion minimization algorithm (Stellingwerf 1978). The minimization of this

[2]http://www.univie.ac.at/tops/period04/

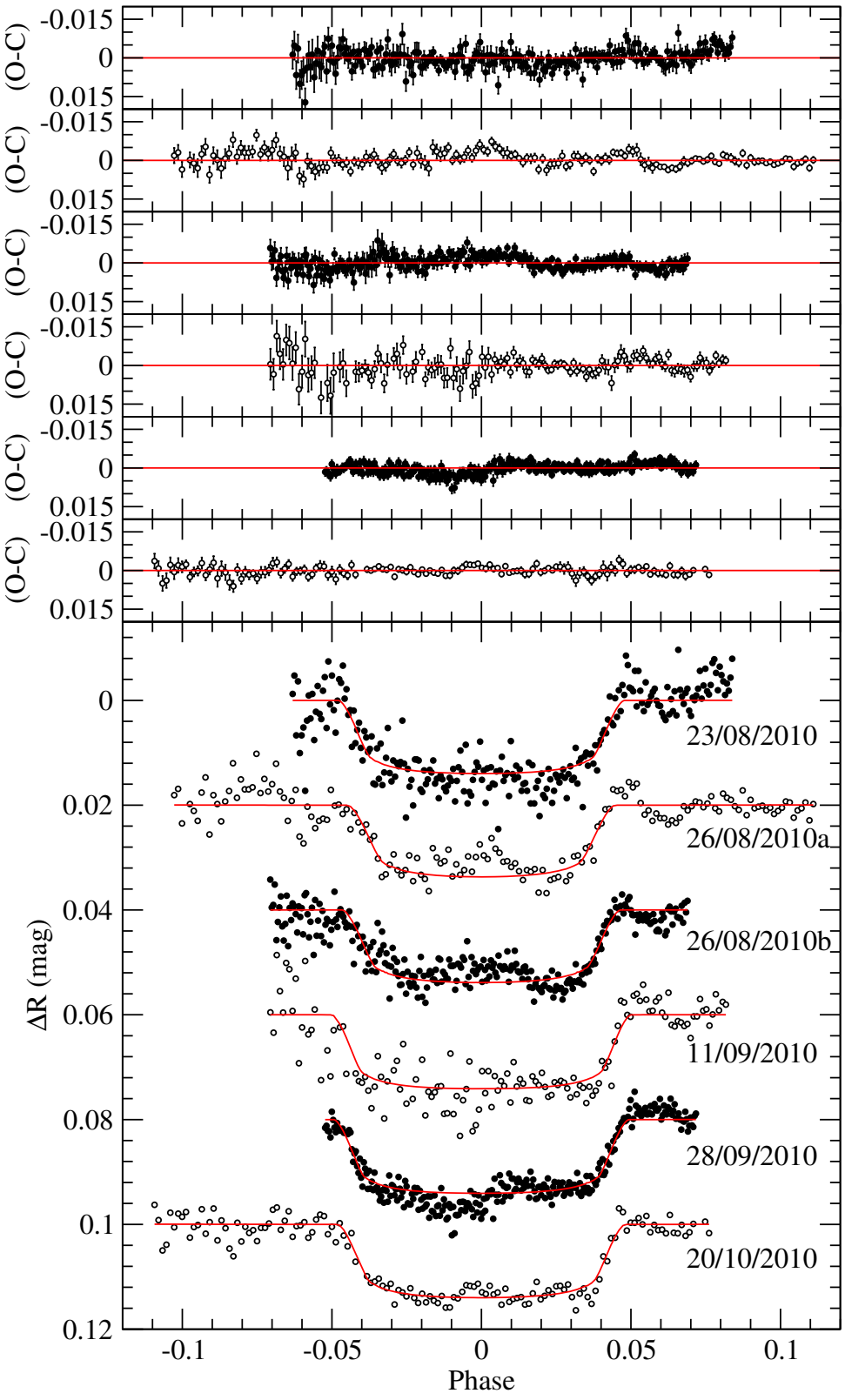

Figure 2.2: R band transit photometry of WASP-33. The solid line is the best fit to each curve with the relative radii of the star and the planet fixed to those found in the global fit using the `JKTEBOP` code. The residuals are shown in the upper panels in the same order as transits are displayed. See Table 2.1 for reference.

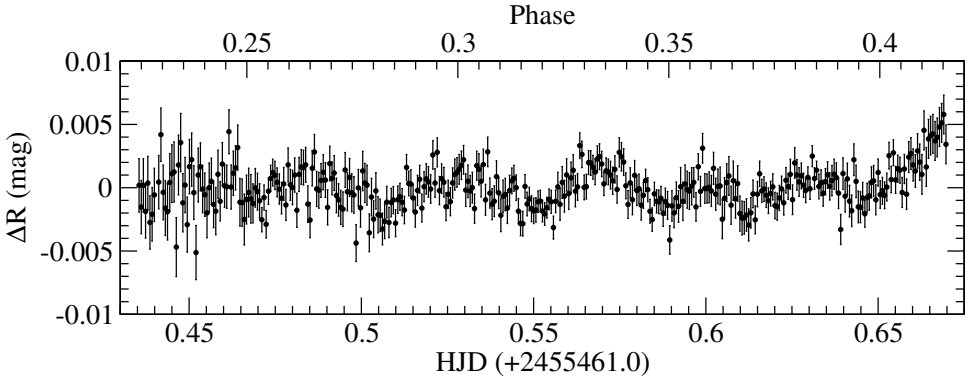

Figure 2.3: Out-of-transit photometry of WASP-33 obtained from OAdM on 21 September, 2010.

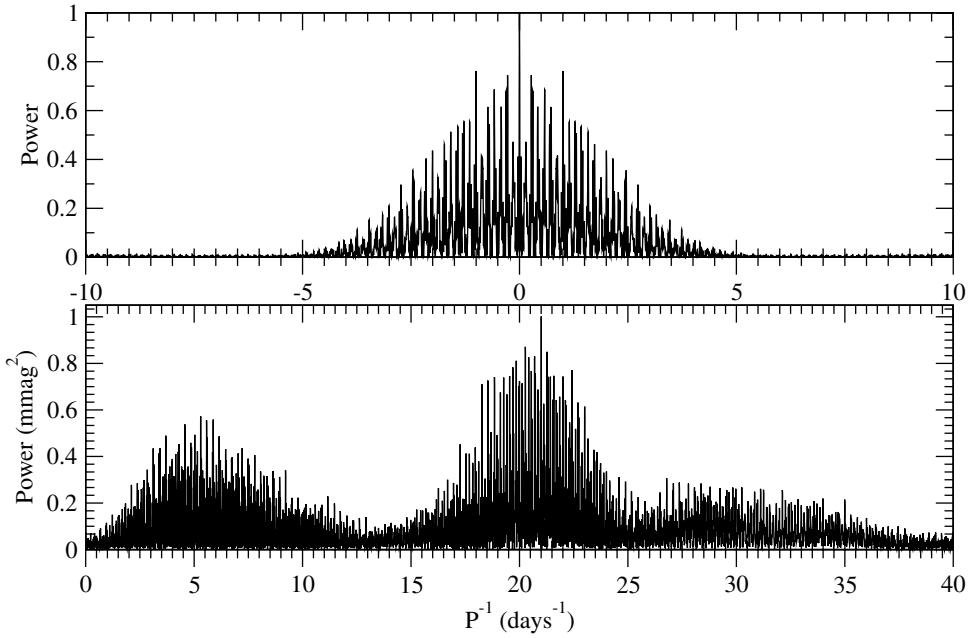

Figure 2.4: Periodogram of the transit residuals and out-of-eclipse phases of WASP-33 using PERIOD04 code. Top panel displays the window function.

parametric fit was performed by means of a Levenberg-Marquardt algorithm (Press et al. 1992). Because of the degeneracy on the solutions, we fitted the amplitude of the modulation and tested a grid of frequency and phase difference values. A key element to consider is the weighing of each data point. At the high precision of our photometry, photon noise is not a good measure of the uncertainty of the measurement because systematic effects in the form of correlated noise dominate (e.g., Pont et al. (2006)). Therefore, we applied a two-step process in which we performed the analysis assuming an initial constant arbitrary value of the standard deviation σ=1 for each data point. The best-fitting solution was then used to calculate a new value for σ as the local value of the rms residual (computed as the running average of the residuals in bins of 20 minutes), and a final fit was run with weights set accordingly. As can be seen in Fig. 2.5, the lowest χ^2 is found for a pulsation with a semi-amplitude of 0.98±0.05 mmag and a frequency of 21.004±0.004 d^{-1} at a phase difference with the mid-transit time of 264±12° (at reference epoch from Table 2.2). This corresponds to a period of $P = 68.56 \pm 0.02$ min. Figure 2.6 shows the overall residuals and the out-of-eclipse photometry phase-folded according to this best-fitting period. As a result of the separation between observing nights, the main feature in Fig. 2.5 is composed of many equidistant peaks with similar χ^2. Interestingly, the periodogram peak with lower resulting rms differs from the one above as it occurs for a pulsation of about 0.86 mmag in semi-amplitude with frequency of 21.311±0.004 d^{-1} corresponding to a pulsation period of 67.57 ± 0.02 min. This illustrates the relatively strong impact of the weighing scheme because the signal is weak and our time series is relatively short. The latter frequency is especially interesting as is happens to be commensurable with the planet's orbital motion with a factor of 25.997±0.005.

Line-profile tomography in Collier Cameron et al. (2010) provided strong evidence for non-radial pulsations in WASP-33 with a period around one day, similar to those usually found in γ Dor stars. Moreover, the authors point out the possibility that the retrograde orbiting planet could be tidally inducing them. Both the period of the photometric oscillations presented here and the stellar properties from Collier Cameron et al. (2010) ($T_{\mathrm{eff}} = 7400 \pm 200$ K, $\log g = 4.3 \pm 0.2$) locate WASP-33 well within the δ Scuti instability strip. Handler & Shobbrook (2002) present a discussion on the different properties of δ Scuti and γ Dor pulsators. Using the formalism there it can be shown that the pulsation constant of WASP-33 ($\log Q_{\mathrm{WASP-33}} = -1.45$) perfectly corresponds to the δ Scuti domain. The power spectrum of δ Scuti pulsators is usually very rich, as illustrated by the 75+ frequencies identified for FG Vir (Breger et al. 2005), but asteroseismic modelling is especially difficult for fast rotators as WASP-33. Given this evidence, a different scenario considering that WASP-33 belongs to the relatively rare class of hybrid pulsators, showing simultaneous δ Scuti and γ Dor oscillations (Handler et al. 2002; Handler 2009), may be possible.

One scenario that should be explored in spite of all the evidence is the possibility that the photometric variations are ellipsoidal in nature and are not caused by pulsations. Indeed, the tidal bulge travels particularly fast over the stellar surface, because the orbital motion of the planet is retrograde with respect to the stellar rotation. Note that there is an indeterminacy in the stellar rotation velocity because it is not a given assumption that the inclination of the stellar spin axis corresponds to the planet's orbital inclination. But a simple calculation, equalling the pulsation frequency found here to that of the relative orbital motion of WASP-33 b above the star surface, renders the ellipsoidal variation scenario as physically not valid since the star would have to rotate at a largely super-critical speed in terms of gravitational break-up. It is more likely that the tidal bulge rotates over the stellar surface with a frequency of about 2 d^{-1}, which

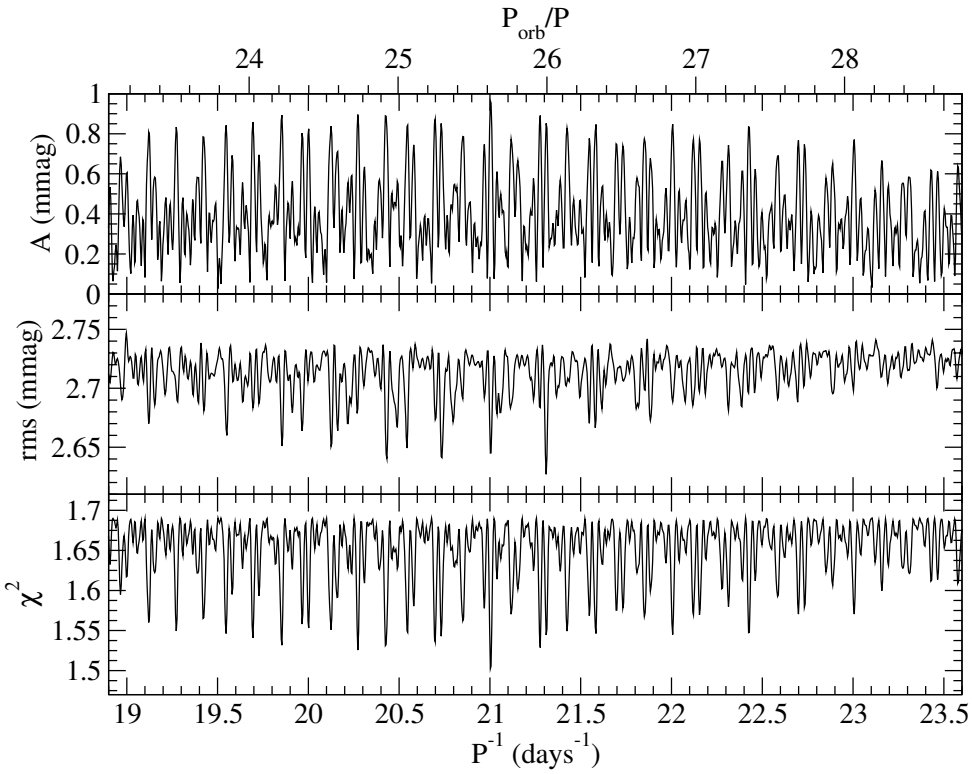

Figure 2.5: Results from the Levenberg-Marquardt algorithm method displaying the structure of the main periodogram peak. Both amplitude and χ^2 give best fits for 21.00 d^{-1}, while the rms is minimized for a pulsation of frequency 21.31 d^{-1}, which is commensurable with the planet's orbital period (see text).

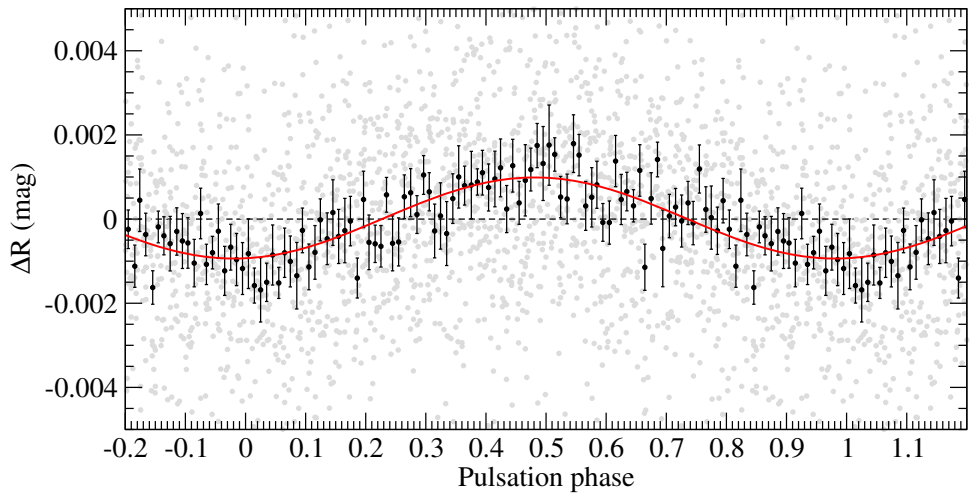

Figure 2.6: Residuals of the transit fits and out-of-eclipse photometry of WASP-33 phase-folded according to the period of the pulsation found in this work, i.e., 68.56±0.02 min, (grey symbols) and 0.01 phase binning (black symbols). The solid curve is the best fit sinusoidal modulation with an amplitude of 0.98 mmag.

is the net combination of the orbital and rotation frequencies, and is far from the frequencies we find relevant in the periodogram.

As seen above, the periodogram is still not defined sufficiently well to assess the true pulsation spectrum of WASP-33. However, given the potential interest, we find it appropriate to briefly address here the possibility of the coupling between the pulsation and the orbit. If the pulsation frequency of 21.311 ± 0.004 d^{-1} turned out to be real, this could suggest the existence of some kind of star-planet interactions that lead to a high-order commensurability of 26 between the pulsation and orbital periods. Very few cases are known to date of a δ Scuti variable belonging to a close binary system (Willems & Claret 2005). The best described candidate for tidally-induced oscillations is HD 209295, which simultaneously presents γ Dor and δ Scuti type pulsations, and which was photometrically found to show several p-modes directly related to the orbital motion of its companion (Handler et al. 2002). This poses the tantalizing possibility of a similar situation occurring in WASP-33, which will certainly be much clearer when additional photometry is acquired and puts constraints on the δ Scuti frequency spectrum.

2.4 Conclusions

High-precision R band photometry has allowed us to present the discovery of photometric oscillations in WASP-33, thus becoming the first transiting planet host with δ Sct pulsations. These oscillations have a period of about 68 minutes and a semi-amplitude of 1 mmag. The frequency spectrum of WASP-33 is still not well defined because the size and significance of the peaks depends on the scheme used to weigh the data. In a particular weighing criterion, the most significant period comes out to be commensurable with the orbital period at a factor of 26. If this association is assumed to be physically relevant, the multiplicity hints at the existence of planet-star interactions. In any case, gaining insight into the nature of WASP-33 will necessarily require the collection of additional data (possibly multi-colour) with longer time baseline and to carry out pulsation and dynamical modelling. The WASP-33 system now represents a new benchmark in the world of exoplanets that can provide valuable information on stellar pulsations (through, e.g., transit surface mapping), on the tidal interactions between planets and stars, and on the dynamical evolution of planetary systems.

Chapter 3

Optimizing exoplanet searches

This chapter is based on the work presented in Herrero et al. (2012). We investigate the activity-rotational velocity relations for low mass stars with a convective envelope to develop a method aiming to increase the efficiency of a targeted exoplanet search with transit technique. We build a catalog of main sequence GKM-type stars using isochrones, an isotropic distribution of inclinations and empirical relations to obtain their rotation periods and activity indexes. The position of the stars in the activity - $v \sin i$ diagram allows to statistically trace the areas containing higher ratio of stars with inclinations ¿ 80°, assuming spin-orbit alignment. A similar statistics is applied to stars from real catalogs with $\log(R'_{HK})$ and $v \sin i$ data to find their probability of being oriented equator-on. We present our method to generate the simulated star catalog and the subsequent statistics to find the highly inclined stars from real catalogs using the activity - $v \sin i$ diagram. Several catalogs from the literature are analyzed and a subsample of stars with the highest probability of being equator-on is presented. Assuming spin-orbit alignment, the efficiency of an exoplanet transit search in the resulting subsample of probably highly inclined stars is estimated to be two to three times higher than with a general search without preselection.

3.1 Transiting planets around low mass stars with inclination constraints

In the past years, the great development in the exoplanet detection techniques and the new space missions and ground-based instrumentation is yielding a high rate of new discoveries. Transiting planets represent a treasure in exoplanet research because they give us the possibility to determine both their size and mass (the latter with a radial velocity follow-up), and also to study in detail the properties of their atmospheres (López-Morales 2011). The stellar light filtered through the planet's atmosphere during a transit allows us to obtain the transmission spectrum (Charbonneau et al. 2002; Tinetti et al. 2007), while the planet's dayside emission spectrum can be obtained during secondary eclipses, yielding measurements of the composition and thermal structure of the planet's atmosphere among other properties (Burrows et al. 2005, 2006; Grillmair et al. 2008). Exoplanet searches using the transit technique are nowadays pro-

viding a great number of new findings. Since the first observation of a transit for the planet HD 209458 b (Charbonneau et al. 2000; Henry et al. 2000), 185 transiting exoplanets[1] have been detected and confirmed to date, more than 1200 candidates from the Kepler mission are awaiting confirmation (Borucki et al. 2011a,b) and more discoveries are expected from several ongoing surveys. Detecting an Earth-like planet transiting a Sun-like bright star is one of the main objectives of exoplanet research today.

Most exoplanet transit detection programs that are currently underway are focused on large catalogs of stars with no pre-selection, basically performing photometry of every possible target up to a certain limiting magnitude. This necessarily makes such surveys quite inefficient, because huge amounts of data are processed for a relatively low transiting planet yield. However, some stellar properties could be used to select those stars that may stand the best chances for finding transiting planets. This can be especially important for some space missions, such as CoRot and Kepler (and future missions like PLATO and TESS), which must preselect the targets and only downlink the data from the specific pixels containing the stars of interest. One possible way to perform a preselection is a metallicity-biased survey. In the case of solar-type stars it is known that planet existence is strongly correlated with the presence of heavy elements in the host star (Marcy et al. 2005, e.g.,). Stellar spectral type and age could also be considered for searches of terrestrial planets in the so-called 'habitable zone' (HZ; Kaltenegger et al. (2010)), which is defined as the region around a star where one would expect conditions for the existence of liquid water on a planet's surface. This depends on the stellar luminosity, and so does the period of the planets orbiting in the HZ. An example of a targeted survey with a preselection of low mass stars is the MEarth project (Charbonneau et al. 2008). While the preselection increases the probability of detecting transits, limiting the target list to given stellar properties can result in the introduction of selection effects on the properties of the exoplanets to be discovered that need to be properly accounted for.

Considering a general targeted search of transiting planets, little effort has been made in the past to put constraints on the input star catalogs with the goal of increasing the transit detection rate. Relevant ideas were presented by Beatty & Seager (2010): transit probabilities can be enhanced if we are able to constrain the inclination of the stellar axes, and this can significantly lower the number of targets to be observed in a transit survey. A targeted transit search would imply to observe only a specific sample of bright stars, which would be spread over the entire sky. This would require several observatories at different latitudes and, in principle, a significant amount of telescope time, because the stars would be observed one at a time. The detection of transits or even the discovery of a habitable Earth-analog with this approach is unrealistic. However, if stellar inclination can be estimated for a substantial sample of bright stars and expecting planets to orbit close to the stellar equator plane, we could select and observe only those stars that have a higher probability to be equator-on, and therefore lower the number of targets and increase the transit detection probability. In an isotropic distribution of the stellar rotation axes, only about 17% of the stars would have spin axis inclinations above 80°.

Beatty & Seager (2010) calculated how constraining stellar inclination affects the transit probabilities and the reduction of the number of targets that need to be observed for a certain number of findings. They also discussed several ways to measure stellar inclination, but this seems to be the limiting point for the application of this approach. Perhaps the most plausible possibility is to obtain stellar inclinations from spectroscopic $v \sin i$ measurements. For this, the true rotational period of the star could be determined from photometric modulations caused by

[1] http://exoplanet.eu/

spots (Messina & Guinan 2003; Lane et al. 2007) or a modulation of the Ca II H and K emission fluxes (Noyes et al. 1984), and the stellar radius could be obtained from stellar models. The major shortcoming of this method arises from the uncertainties in all the ingredients: $v \sin i$, stellar rotational period and stellar radius. Moreover, the behavior of the sine function itself becomes a drawback because it is weighed toward $\sin i = 1$, thus changing very slowly near $i = 90°$. All this makes it necessary to know the observed quantities to better than 1% accuracy if one aims to select the stars with $i > 82°$ (Soderblom 1985). With the currently available techniques, it is not feasible to measure $\sin i$ to better than 10%. This approach would also be very time-intensive, requiring high-resolution spectroscopy and long time-series photometry. Therefore, it is impractical to obtain a relatively large catalog of stellar inclination data.

Another approach is discussed in this paper, where we constrain the inclination through the relation between the activity and the projected rotational velocity of the star. Section 3.2 presents the principles of the approach. In Sect. 3.3 we describe the simulation of extensive samples of stars used to better understand this relation and to determine the probability for an observed star to have its spin axis inclination above a specific angle. This allows us to select the best candidates for a targeted exoplanet transit search. Measurements of an activity indicator, such as $\log(R'_{HK})$, and of $v \sin i$ are necessary to constrain stellar inclinations with this method. A catalog selection is described in Sect. 3.4 together with the implementation of the selection method and the compilation of a subset of stars that are expected to have inclinations close to 90°. In Sect. 3.6 we discuss the applicability of this preselection method and the complementarity of the subsequent targeted transit search with the currently ongoing exoplanet searching methods.

3.2 Stellar inclination from activity and rotation

A feasible approach to estimate stellar axis inclinations with the currently available data is to exploit the relation between stellar activity and rotation for main-sequence late-type stars (Soderblom 1985; Pizzolato et al. 2003; Kiraga & Stepien 2007). In these objects, the regime of differential rotation at the convective envelope plays a key role in generating the magnetic fields through the dynamo effect. These magnetic fields are essentially responsible for the entire phenomena that are generally known as stellar activity, and are also thought to be the main rotation-braking mechanism caused by angular momentum loss through interaction with the stellar wind. Essentially, the stellar mass (or spectral type), which is related to the depth of the convective layer, and the rotational period determine the amount of stellar activity (Kitchatinov & Rüdiger 1999). This can be measured through several indicators (Soderblom 1985; Mallik 1998; Hempelmann et al. 1995). Strong evidence exists for an activity-rotation relation extending from solar-type stars to less massive dwarfs (Pizzolato et al. 2003; Kiraga & Stepien 2007).

If an activity indicator like $\log(R'_{HK})$ can be compared to the projected rotational velocity for a huge sample of stars (Jenkins et al. 2011), then those stars with $i \approx 90^{\circ}$ ($\sin i \approx 1$) will have the highest $v \sin i$ values for a certain activity, covering a specific area on the activity-$v \sin i$ diagram for each spectral type. By studying the relationship between chromospheric activity and projected rotational velocity through such a diagram, statistics can be performed to find the area containing preferentially stars with $i \approx 90^{\circ}$, even without exactly knowing the correlation between activity, rotation and spectral type. A significant sample of stars is needed preliminary to perform a study of the activity-$v \sin i$ relations for the different spectral types. However, some complications arise when one attempts to compile $\log(R'_{HK})$ and $v \sin i$ data, since the current

measurements are too scarce and imprecise. A solution to this is the simulation of a large sample of stars (Sect. 3.3).

The basic assumption in a selection of highly inclined stars for a targeted transit search lies in the alignment between the stellar rotation and the planet's orbital spin axis. Although from conservation of angular momentum we would expect the planet to orbit close to the stellar equator plane, recent spectroscopic observations during exoplanet transits have revealed significant spin-orbit missalignments for 10 of 26 hot Jupiters (Triaud et al. 2010) through the Rossiter-McLaughlin effect (Rossiter 1924; McLaughlin 1924). These planets are thought to have formed far out from the star and to have migrated inward. In this process, planet-planet scattering and Kozai oscillations caused by additional companions could significantly affect the obliquity of the orbit (Wu & Murray 2003; Rasio & Ford 1996). In spite of scarce statistics, spin-orbit missalignments have only been observed in hot Jupiters, and assuming that a planet has formed and migrated in a disc, the majority is expected to be in aligned orbits. Several multiple transiting systems have recently been found by Kepler (Lissauer et al. 2011a,b), giving more weight to the existence of planets with spin-orbit aligment.

It is also worthwhile to note that Sabha et al. (2010) reported evidence that hot Jupiters orbiting close to their stars can affect their angular momentum evolution by interaction with their coronal fields (Lanza 2009). This would complicate our approach, because slightly different rotation rates would be expected for stars with giant planets, which would prevent us from predicting the stellar axis inclination from the same activity-$v \sin i$ distribution as for general stars. However, this effect has only been observed for hot giant planets orbiting very close to early-type stars, and the possible induced rotation rate bias is lower than the typical $v \sin i$ precisions. Therefore, no actual complexities are added.

3.3 Stellar sample simulation

3.3.1 Aims and assumptions

The simulation of a significant sample of stars containing the basic data for the subsequent analysis is needed if we desire to study accurately the correlation between chromospheric activity and projected rotational velocity. The resulting sample should follow the available activity and $v \sin i$ data from different existing catalogs, including the effects of observational errors and cosmic dispersions for the different parameters. A simulation of this kind can be achieved using evolutionary models and several empirical relations.

Among the output data of the simulation will be the stellar projected inclination determined from an isotropic distribution of the rotation axes. Different inclinations cover different areas in the activity-$v \sin i$ diagram, and while the current available observed data are too scarce to properly study their distribution and trends, the simulation presented here will allow us to accurately study how they are distributed in the diagram and perform a selection of observed stars from real data using the method described in Sect. 3.3.3. The possible bias resulting from our selected sample will be discussed in Sect. 3.6. The main idea of the method is not to determine stellar inclinations of real stars, but to estimate the probability for each star to have an inclination higher than a certain value. This means, under the assumption of spin-axis alignment, defining a subset of stars for which a transit search would be most efficient.

Our study is limited to G, K, and M dwarfs ($0.6 < (B - V) < 1.6$). This is mainly because

we require a convective envelope to assume the connection between the rotation rate and the level of stellar activity. Therefore, we are constraining $B-V$ so that the spectral range covered by our selection strategy contains all stars whose activity has been observed to be scaled by the rotation period. This includes up to late M-type stars, so the same analysis can be performed there (Mohanty & Basri 2003; West & Basri 2009; Irwin et al. 2011). However, our method finds some limitations when applied to M-type stars because the magnetic activity is known to rapidly saturate at a given level as the rotation rate increases. A more extensive discussion on this is given in Sect. 3.6.

3.3.2 Generation of the sample

The masses of the simulated stars are generated so that they follow the distribution of the present-day mass function for the solar neighborhood by Miller & Scalo (1979) and so that they are limited to within 0.15 $M_\odot$ and 1.05 $M_\odot$. These limits account for the spectral range we are interested in covering. The upper limit is set at stars of spectral type G0. For higher mass stars the depth of the convection is increasingly low and hence stellar activity may be significantly less intense (Gray 1982). On the other hand, we exclude stars later than ∼M4 where, as will be shown in Sects. 3.3.3 and 3.4, the activity-rotation pattern leaves little chance for our selection method because of the precision of the current $v \sin i$ data.

Our sample is restricted to main-sequence stars because the magnetic activity behavior in evolved stars is still only poorly understood. Therefore, the stellar ages were generated considering the main sequence lifetime, which depends on the stellar mass and was calculated by fitting the terminal age main-sequence points from the evolutionary tracks of Pietrinferni et al. (2004), generated using the BaSTI web tool[2]. We obtained the following expression for the main-sequence lifetime τ_{ms}:

$$\begin{aligned}\log \tau_{ms} = 9.92 - 3.85 \log M/M_\odot + 2.50(\log M/M_\odot)^2 - \\ -1.67(\log M/M_\odot)^3.\end{aligned} \tag{3.1}$$

The upper limit on age only affects G-type stars, because the ages of lower mass stars are limited by the range covered by the evolutionary models used later to compute the stellar radius and color index (Marigo et al. 2008). As a result, the age distribution for most of the spectral range is flat, ranging from 0.1 to 12.6 Gyr. The oldest low mass stars are expected to be inactive and very slow rotators (Barnes 2007), and hence they would show very low values of $v \sin i$. As will be seen later in Sects. 3.3.3 and 3.4, such $v \sin i$ values are likely to be far from the measurement possibilities of current spectrographs if we want to distinguish and select different ranges of stellar inclinations. Therefore, the exclusion of old K- and M-type stars does not introduce any limit to the optimization method that we are designing.

The $(B-V)$ color indices are derived from mass and age values using stellar models (Marigo et al. 2008). Because we are simulating samples of stars in the solar neighborhood, interstellar absorption is negligible and no reddening was considered. The simulated sample is limited to a specific range in $(B-V)$ between 0.6 and 1.6. This is important because one of our goals is to study the variations in the activity-rotation behavior with spectral type and how this can affect the possibility of resolving different ranges of inclination. The statistics described in Sect. 3.3.3

[2]http://albione.oa-teramo.inaf.it/

Table 3.1: Coefficients for the age-rotation relations (expression 3.2) used in the simulation.

Sp. Type	Parameter	Value	Std. error
G	P_0	2.361	2.722
	a	6.579	3.609
	b	0.763	0.253
K	P_0	2.158	2.092
	a	10.224	2.922
	b	0.663	0.131
M	P_0	-6.624	13.107
	a	25.797	15.333
	b	0.711	0.268

will help to set some criteria concerning the validity of our selection method at different $(B-V)$ ranges.

Once $(B-V)$ and age are known for a given star, the rotation period can be obtained using known empirical relations. Around the age of most of open clusters, many observations converge to follow a $t^{1/2}$ spin-down law. In Barnes (2003) and Barnes (2007), observations from several open clusters were used to obtain the rotation rate as a function of spectral type for F, G and K stars and calibrating the age dependence using the Sun. The age-rotation relations by Engle & Guinan (2011) were obtained from stars in the spectral range covered by the simulation, which have age determinations through different indirect methods, and therefore represent a more suitable approach for our purposes. They follow an empirical expression of the form

$$P_{rot}(\text{days}) = \mathrm{P_0} + \mathrm{a} \cdot [\text{Age(Gyr)}]^{\mathrm{b}} \tag{3.2}$$

for a specific $(B-V)$. However, as we will discuss in Sect. 3.4, very similar results are obtained if the expression of Barnes (2007) is used instead.

Three independent empirical relations of the form of expression 3.2 were obtained for G-, K- and M-type dwarfs. The coefficients of the best fit are presented in Table 3.1. The mean $(B-V)$ was calculated for each of the three samples. Knowing the $(B-V)$ of our simulated stars, their period was obtained by interpolating the results given by the three relations. A Gaussian error was added to the rotational periods obtained to consider a cosmic dispersion around the age-rotation relations. The standard deviation for this Gaussian distribution was estimated from the standard deviation of the rotational period data provided by Engle & Guinan (2011), which is close to 1 day and slightly depends on age.

The stellar radius was obtained from linear interpolation of the evolutionary models of Marigo et al. (2008), and the equatorial rotation velocity can be calculated from the rotational period. An isotropic distribution of rotation axis orientations was assumed to generate the inclination of each simulated star, which yielded about 9% of the sample with $i > 85°$ and 17% with $i > 80°$ (see Fig. 3.1). An additional Gaussian dispersion component was added to the resulting $v \sin i$ values to include the measurement uncertainty. High-resolution spectroscopy and cross-correlation techniques are currently yielding $v \sin i$ measurements with errors lower than ~ 0.5 km s^{-1} (de Medeiros & Mayor 1999; Głębocki & Gnaciński 2003).

Several empirical relations exist that correlate Ca II H and K emission with rotational period

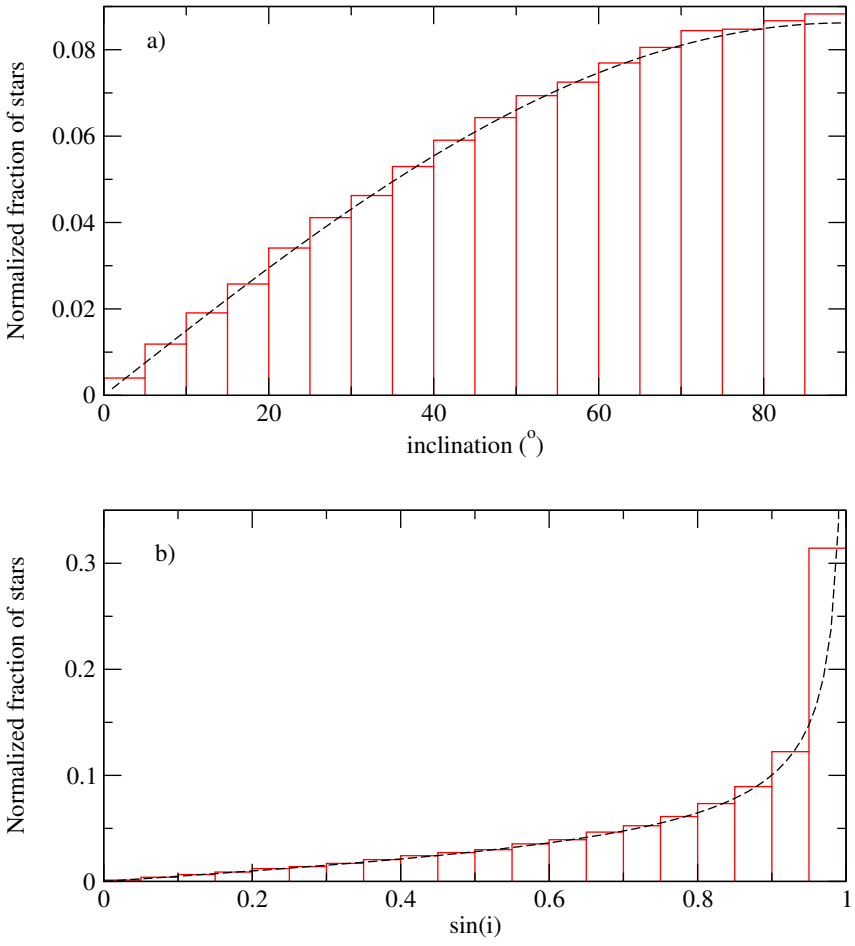

Figure 3.1: a) Frequency of stars in the simulated sample depending on the inclination of their rotation axis toward our line of sight, considering an isotropic distribution resulting from the simulation. b) Frequency of $\sin i$ values in the same distribution. The behavior of the sine function, weighed toward $\sin i = 1$, impedes a selection of highly inclined stars. The analytic functions that describe the distributions are also plotted in both graphs (dashed lines).

and spectral type. Because we lack sufficient data for an accurate study, the description of the stellar chromospheric activity in terms of the stellar dynamo has been difficult (Donahue et al. 1996; Montesinos et al. 2001). Noyes et al. (1984) reported rotation periods for a sample of main-sequence stars and demonstrated that chromospheric flux scales with the Rossby number, $Ro = P_{\rm rot}/\tau_c$, where $P_{\rm rot}$ is the rotation period and τ_c is the convective overturn time near the bottom of the convection zone, which is an empirical function of the spectral type. This gives a much better correlation than the activity-period, but obtaining Ro is complex owing to the difficulties in measuring the stellar rotation rate and the estimate of the turnover time based on stellar interior models (Kim & Demarque 1996). Noyes et al. (1984) give an empirical calibration for the turnover time in terms of $(B-V)$, considering an intermediate value for the ratio of mixing length to scale height, $\alpha = 1.9$. The fit is given by the polynomial expression:

$$\log \tau_c = \begin{cases} 1.362 - 0.166x + 0.025x^2 - 5.323x^3, & \text{x}>0 \\ 1.362 - 0.14x, & \text{x}<0 \end{cases} \tag{3.3}$$

where $x = 1-(B-V)$ and τ_c is the turnover time in days. This was used in our simulation to compute the convective turnover times and the Rossby numbers for each star. However, as Gilman (1980) and Noyes et al. (1984) show, different values of α make stars deviate from Eq. (3.3), although the best correlation is found for $\alpha = 1.9$ considering mixing-length theory models. In our calculated convective turnover times, a Gaussian dispersion with $\sigma_{\log \tau_c} = 0.03$ dex was added to the $\log \tau_c$ values to take this dispersion into account. Mamajek & Hillenbrand (2008) give a relation between the chromospheric index $\log(R'_{HK})$ and the Rossby number from a larger sample, which we used to obtain the activity for each of our simulated stars. The calculation of the final $\log(R'_{HK})$ also accounts for a Gaussian dispersion, as the data in Mamajek & Hillenbrand (2008) show. The amplitude of this Gaussian dispersion, $\sigma_{\log(R'_{HK})}$, is scaled with Ro being always near 0.04 dex.

3.3.3 Statistics on the simulated samples

All parameters from the simulated stars were generated from empirical relations, so the resulting sample should properly account for the trends that real observed stars show in the activity-$v \sin i$ diagram. The large error bars in many of the available $v \sin i$ measurements (some of them which only upper limits) and the selection biases in the observed catalogs make it difficult to compare our simulated sample with observations. Therefore, a careful selection of observational catalogs will be necessary to correctly check the agreement with the simulated data. The Gaussian dispersions introduced in the different empirical relations at several steps of the simulation and the observational uncertainty added to the obtained $v \sin i$ values, as described in Sect. 3.3.1, are critical to obtain a simulated sample that properly fits real data.

As expected, our simulations show a clear increase in the mean projected rotation velocity for higher chromospheric activity for all spectral ranges (see Fig. 3.2). Also, stars with inclinations close to 90° are placed at the right hand side of the distribution, thus defining the envelope region of interest, clearly distinguishable from stars with other orientations. The contamination comes from the cosmic dispersions and observational uncertainties. Fig. 3.2 clearly shows that the distribution in activity-$v \sin i$ becomes more densely concentrated for later spectral types, because inactive stars tend to be very slow rotators, which in turn requires very precise $v \sin i$ measurements to apply our selection method. The discontinuity in the expression used to compute $\log(R'_{HK})$ from the Rossby numbers (Mamajek & Hillenbrand 2008) for the simulated

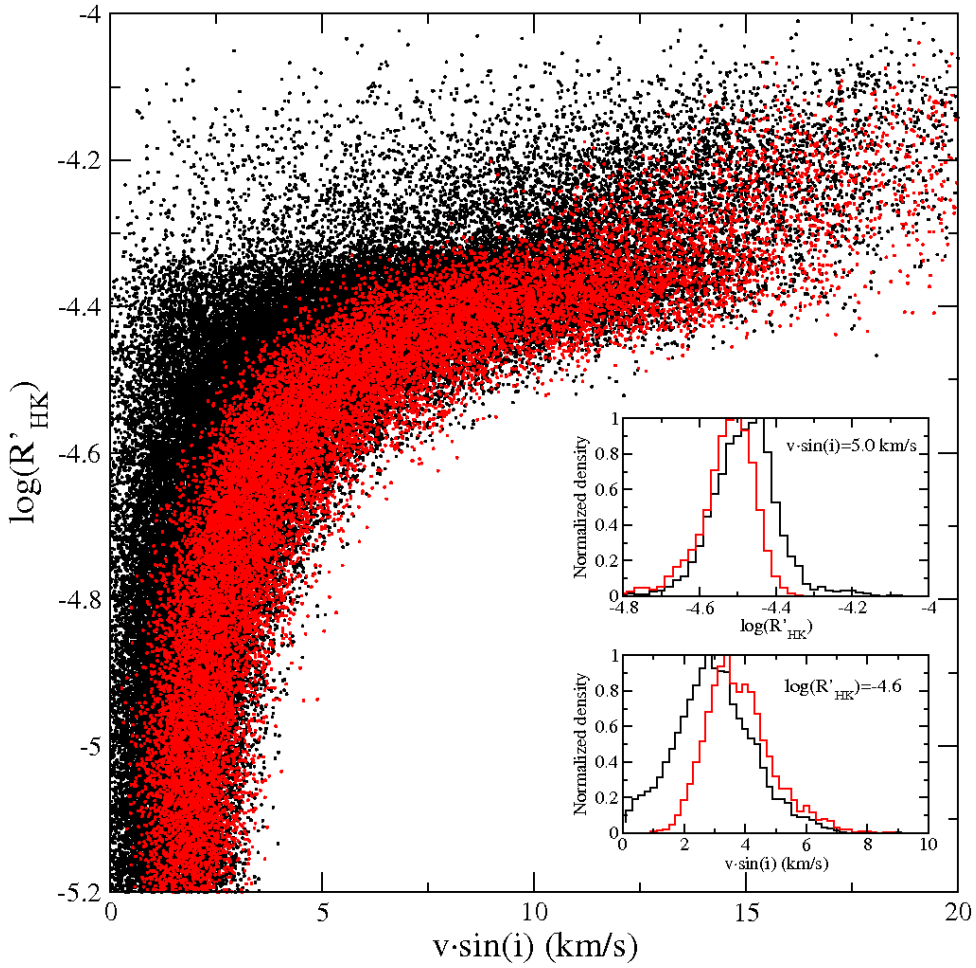

Figure 3.2: Sample of 100,000 solar-type stars ($0.6 < (B-V) < 0.7$) simulated with the procedure described in Sect. 3.3.1. Random errors with a Gaussian distribution ($\sigma = 0.5$ km s^{-1}) were added to the $v \sin i$ values. Stars with projected axis inclinations above 80° are represented in red and trace the envelope region at the right hand of the distribution. For a constant $\log(R'_{HK})$, stars are expected to have a very similar equatorial velocity in terms of the rotation and activity evolution assumptions, and so different $v \sin i$ are mainly caused by different axis projections. The histograms in the two overlayed plots show the density distribution of the simulated samples at two cuts made at constant $\log(R'_{HK}) = -4.8$ and $v \sin i = 7.5$km/s, respectively.

stars causes a small bump in the activity-$v \sin i$ distribution near $\log(R'_{HK}) = -4.35$, which is more evident for later spectral types (see Figs. 3.2 and 3.3). Although this could be avoided by using a single expression for the calculation, like the one obtained by Noyes et al. (1984), it would be at the expense of losing precision in the general shape of the distribution.

With a sufficient amount of stars in the activity-$v \sin i$ diagram and the possibility of generating a sample for any spectral type, we can define an efficiency parameter for each location in the diagram. This is defined as the probability for a star in that location to have an inclination angle above a certain angle, and can be calculated by defining a small region in the diagram around the star and then computing the ratio

$$\epsilon_\alpha = \frac{N_{i>\alpha}}{N_T}, \tag{3.4}$$

where $N_{i>\alpha}$ is the number of simulated stars in the region with axis inclinations above a given α angle and N_T is the total number of stars in the same region. For a specific $(B-V)$-limited sample, and given fixed cosmic dispersions and Gaussian errors for the observables, the efficiency ϵ is a property of each location in the activity-$v \sin i$ diagram, and therefore regions of interest for transit searches can be studied. To quantify the increase effectiveness of the present methodology, we assumed $\alpha = 80^\circ$ because most of the known transiting planets are found above this inclination angle. In a general sample with an isotropic distribution of rotation axes, we would expect 17.3% of the stars to have $i > 80^\circ$, so that $\epsilon_T = 0.173$. We may define the normalized efficiency as

$$P = \frac{\epsilon_{80^o}}{\epsilon_T} = \frac{1}{\epsilon_T}\frac{N_{i>80^o}}{N_T}, \tag{3.5}$$

so that $P = 1$ for a non-selected sample and $P > 1$ for selected subsamples with an increased high-inclination probability.

While the efficiency for a non-selected sample of stars would be $\epsilon \approx 0.173$, this increases as we move to regions at the right hand side of the distribution in the activity-$v \sin i$ diagram, so increasing P. For simulated samples limited in spectral type, an envelope polynomial function of the form $y = a_1 + a_2/x$ was calculated by fitting the subset of stars with $i > 85^\circ$, splitting the function into two to account for the inactive and the active part of the distribution. Successive shifts were aplied to the envelope function, while the efficiency was calculated considering all the stars lying in the region below it (see Fig. 3.3). One can study the efficiency changes and test the applicability of the selection method for different specral types by scanning the activity-$v \sin i$ diagram with the envelope function that traces equal-inclination regions and performing these statistics.

Four samples of different spectral types are represented in Fig. 3.3. In all cases, highly inclined stars trace the envelope region of the distribution, but considering the observational and cosmic dispersions, very inactive or active stars (at the saturation zone) for later spectral types become indistinguishable in the activity-$v \sin i$ diagram in terms of stellar inclination. The empirical errors of the activity calculation (see Sect. 3.3.1) and a $\sigma = 0.5$ km s^{-1} for $v \sin i$ were considered in all cases. The range of $(B-V)$ is also critical, because the rotation rate can change significantly with stellar mass in the main-sequence. Figure 3.3 highlights this and also shows how the efficiency decays as the width of the envelope region increases towards the upper-left part of the distribution and more stars are included in the statistics.

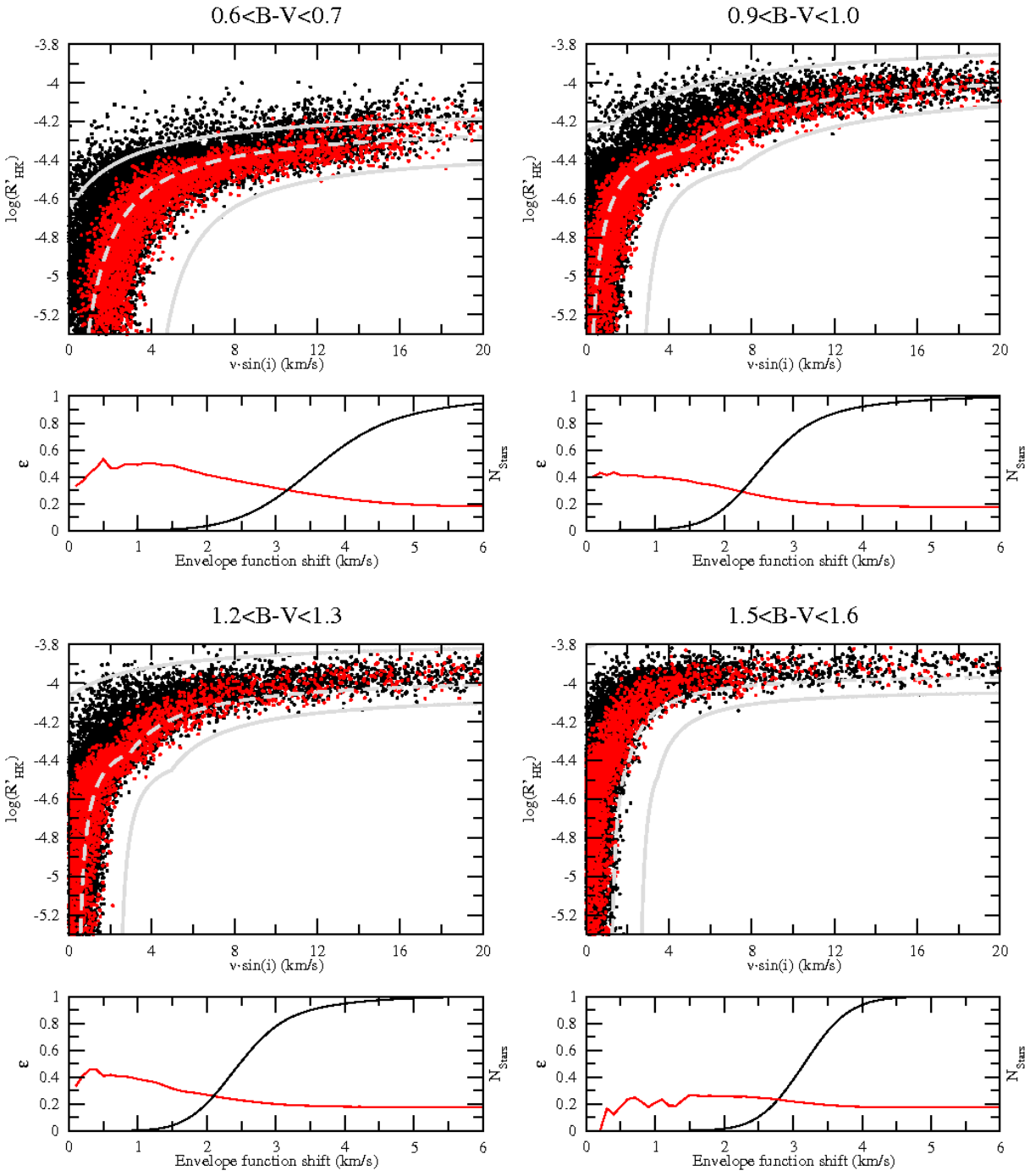

Figure 3.3: Four simulated samples limited in color index as indicated. Stars with $i > 80°$ are plotted in red. The gray envelope function, calculated as described in Sect. 3.3.3, is shifted from the right hand side of the distribution to the left considering a slope so that it scans the high-inclination region (see text). At each step the efficiency (Eq. 3.4, with $\alpha = 80°$) is calculated for the subsample below the envelope function. The red line in the bottom diagrams shows the evolution of ϵ as the region limited by the function is expanded to the left, and the black line indicates the total fraction of stars in the region ($N_{Stars} \sim 1$). As expected, ϵ tends to ~ 0.17 for $N_{Stars} \sim 1$. The dotted gray line in the upper diagrams indicates the region where $\epsilon = 0.26$, therefore the efficiency is increased by 50% with respect to a non-preselected sample.

The envelope function previously obtained is first shifted by a certain amount to increasing $v \sin i$ until all active stars lie at lower $v \sin i$. Then, it is shifted back to decreasing $v \sin i$ at very small steps, considering a slope so that it scans regions of equal inclination. The two lines define the boundaries of the region of interest where the statistics is calculated. As expected, the efficiency decreases as more stars from the part of the distribution with lower $v \sin i$ are included in the region. For the earlier spectral types, a region containing the 15% of the entire sample yields $P \approx 2.0$, which represents doubling the probability of $i > 80°$ with respect to a non-preselected sample. M-dwarfs show a less discriminating distribution in the diagram and thus the efficiency only reaches ~ 1.5 (50% increase than a non-preselected sample) for a small region containing 1.5% of the total simulated sample.

A similar approach to the previous statistics permits the calculation of the efficiency at a specific location in the diagram. For a real observed star that is to say the probability for this star to have an inclination angle above 80°, and thus evaluate its suitability as a candidate for a transit search. Instead of performing the calculation of the efficiency ratio (Eq. 3.4) in a wide region as before, a small region around the point of interest can be defined. For real data, we determined this region from the observational uncertainties in $v \sin i$ and $\log(R'_{HK})$. Also, observational errors in $(B-V)$ for the star were taken into account to limit the spectral range of the simulated sample used to calculate P. In this case, the Gaussian errors for the observables are not introduced when generating the simulated data points, because they are already taken into account when defining the box where the efficiency is calculated.

3.4 Data selection and analysis

The main goal of the generation of a simulated sample of stars is to provide the basis for performing the statistics described in Sect. 3.3.3 to real data. Currently, several catalogs exist that compile high-resolution spectroscopy measurements of both Ca II H and K fluxes and projected rotation velocities. However, special care has to be taken when selecting the data and cross-matching catalogs, because different authors use different spectral resolutions and reduction techniques, and this results in a diversity of precisions, detection limits and possible selection biases.

A first test for the high-inclination selection method is to perform the efficiency statistics on the stars that already have known transiting planets. Although several of them have been observed to be spin-orbit missaligned (Triaud et al. 2010), the majority of the stars with transiting planets are expected to have inclinations close to 90°, and therefore we should obtain a high efficiency rate when calculating the statistics with the properly generated star sample for each object. It is important to notice that while the Rossiter-McLaughlin effect provides a measurement of the spin-orbit angle on the plane of the sky, there is still a component to be determined, and this is related to the stellar inclination and the planet orbit angle toward the line of sight. Therefore, the information given by the Rossiter-McLaughlin measurements is complementary to the one our statistical method can provide, since both angles are independent.

Also relevant are the results from Canto Martins et al. (2011), showing that no significant correlations exist between chromospheric activity indicator $\log(R'_{HK})$ and planet presence or parameters. This is important if we aim to apply the described activity-$v \sin i$ statistics to these stars, using the same empirical approach as in Sect. 3.3 for the observed stars.

Lists of $v \sin i$ measurements for stars with planets can be found in Schlaufman (2010) and

Gonzalez et al. (2010), while Knutson et al. (2010) compiled $\log(R'_{HK})$ and $v \sin i$ data from several authors. The best-quality measurements of the subset of G, K and M-type stars were selected and are presented in Table 3.2. When available, the error bars of the listed parameters were used to constrain the generated sample and the box where the statistics is calculated. Otherwise, a typical box size of 0.1 dex in $\log(R'_{HK})$ and 0.5 km s^{-1} in $v \sin i$ was adopted. For each star, a simulated sample of 10^6 stars was generated, covering a range around its $(B-V)$ value (0.04 magnitudes when no errors are available for photometry), and the efficiency was calculated with the simulated stars inside the defined box in the activity-$v \sin i$ diagram.

The efficiency values presented in Table 3.2 were calculated using Eq. (3.4) with $\alpha = 80°$, and then normalizing by the factor 0.173 as explained in Sect. 3.3. The normalized efficiency (P) is the factor by which the probability of having $i > 80°$ is increased (compared with a non-preselected sample of stars). Because of the uncertainties considered for the box size where the statistics was calculated, very few transiting host stars show a normalized probability $P > 2$. However, the mean probability of $i > 80°$ for this sample is 1.41, about 40% higher than for a general sample (expected to give $\overline{P} \approx 1.00$). Of the 21 stars in sample where the statistics was performed, 13 show $P > 1.00$ and 9 show $P > 1.50$. Our strategy would have selected these objects, and hence a number of the transiting planets in the list could have been found in the subsequent targeted search.

As can be seen in Fig. 3.4, where two subsets of different spectral types are shown, most of the stars lie close to the right side region of the simulated samples. Four of them are even located to the right hand of the entire distribution, and consequently no statistics could be performed around them. These cases should be investigated in more detail and are probably due to underestimated $v \sin i$ error bars. Alternatively, they could be explained by anomalously low values of $\log(R'_{HK})$, corresponding to a deep minimum of the activity cycle, but we deemed this to be quite improbable.

The next step is the application of the formalism to catalogs of $\log(R'_{HK})$ and $v \sin i$ measurements with the aim of selecting a sample with a higher probability of high spin-axis inclinations. In this case, a result of $P = 2.00$ or even $P = 1.50$ can be considered interesting. For example, the preselection of a sample of stars with $P_{mean} = 1.50$ would represent a 50% increase on the ratio of highly inclined stars, which would be a 50% increase on the efficiency of a planet transit search assuming a spin-orbit alignment.

Fig. 3.3 shows that the performance of the selection method that we are developing is more efficient for stars between certain activity thresholds. It is difficult to constrain the inclination angle for fast rotators at the saturated activity regime, because a wide range of $v \sin i$ values show very similar activity levels at this early stage of the stellar evolution. On the other hand, inactive stars for most spectral types present rotation rates that are too low to resolve different stellar inclinations given the dispersion of the empirical relationships and the uncertainties of observational quantities. The activity-$v \sin i$ relation makes the statistics for these stars difficult or unreliable for higher $(B-V)$ indices (see Sect. 3.3.3), and they should be excluded from the selection process to avoid false positives. A $\log(R'_{HK})$ threshold depending on $(B-V)$ was calculated by considering a $v \sin i \geq 1$ km s^{-1} limit and applying the envelope functions previously used for studying the distribution (see Sect. 3.3). These functions trace the right hand side edge of the distribution for each $(B-V)$ interval, and therefore their cut at $v \sin i = 1$ km s^{-1} can be used to define the inactive limit. This was made for each 0.1 mag interval ($0.6 < (B-V) < 1.6$) and finally a simple polynomial function was fitted, obtaining $\log(R'_{HK})_{\rm lim} = -3.45 - 1.36/(B-V)$. Stars below this inactive limit are not considered for the analysis and

Table 3.2: List of G-, K- and M-type exoplanet parent stars with available data. Activity-$v \sin i$ distributions of simulated samples where used to calculate the normalized efficiency parameter P (see text). This gives the probability of each star to have a rotation axis inclination above 80°, divided by the same probability considering a sample with an isotropic distribution of rotation axes.

Star	$(B-V)$	$\log(R'_{HK})$	$v \sin i$ (km/s)	P	Ref.
HD 17156	0.64	-5.022	5.0±0.8	-	1,3
HD 80606*	0.77	-5.10±0.04	2.0±0.4	-	3,4
HD 149026	0.61	-5.030	6.0±0.5	-	1,5
HD 189733	0.93	-4.50±0.05	4.5±0.5	2.38	3,4
GJ 436	1.52	-5.23±0.02	1.0±0.9	1.68	4,6
TrES-1*	0.78	-4.738	1.1±0.3	0.80	1,7
TrES-2	0.62	-4.949	2.0±1.0	0.97	1,2
TrES-3	0.71	-4.549	1.5±1.0	0.09	1,8
CoRoT-2	0.69	-4.331	11.8±0.5	2.09	1,9
CoRoT-7	0.80	-4.802	1.3±0.4	1.04	1,10
Kepler-4	0.62	-4.936	2.2±1.0	1.06	1,11
Kepler-6	0.68	-5.005	3.0±1.0	3.06	1,12
WASP-2*	0.84	-4.84±0.10	1.6±0.7	1.61	13
WASP-4	0.74	-4.50±0.06	2.0±1.0	0.37	1,14
WASP-5	0.66	-4.72±0.07	3.5±1.0	1.70	13
WASP-13	0.60	-5.263	2.5±2.5	1.00	1,15
WASP-19	0.70	-4.660	4.0±2.0	1.56	1,16
XO-1	0.69	-4.958	1.11±0.67	0.80	1,17
XO-2	0.82	-4.988	1.3±0.3	2.78	1,18
HAT-P-3	0.87	-4.904	0.5±0.5	0.67	1,19
HAT-P-10	1.01	-4.823	0.5±0.2	0.02	1,20
HAT-P-11	1.02	-4.584	1.5±1.5	0.99	21
HAT-P-12	1.13	-5.104	0.5±0.4	1.02	1,22
HAT-P-13	0.73	-5.138	2.9±1.0	-	1,23
HAT-P-15	0.71	-4.977	2.0±0.5	2.55	1,24

* Spin-orbit misalignment detected through Rossiter-McLaughlin effect.

References: (1) Knutson et al. (2010); (2) Schlaufman (2010); (3) Gonzalez et al. (2010); (4) Wright et al. (2004); (5) Sato et al. (2005); (6) Głębocki & Gnaciński (2003); (7) Narita et al. (2007); (8) Sozzetti et al. (2009); (9) Bouchy et al. (2008); (10) Bruntt et al. (2010); (11) Borucki et al. (2010b); (12) Dunham et al. (2010); (13) Triaud et al. (2010); (14) Gillon et al. (2009); (15) Sabha et al. (2010); (16) Hebb et al. (2010); (17) McCullough et al. (2006); (18) Burke et al. (2007); (19) Torres et al. (2007); (20) Bakos et al. (2009b); (21) Bakos et al. (2010); (22) Hartman et al. (2009); (23) Bakos et al. (2009a); (24) Kovács et al. (2010).

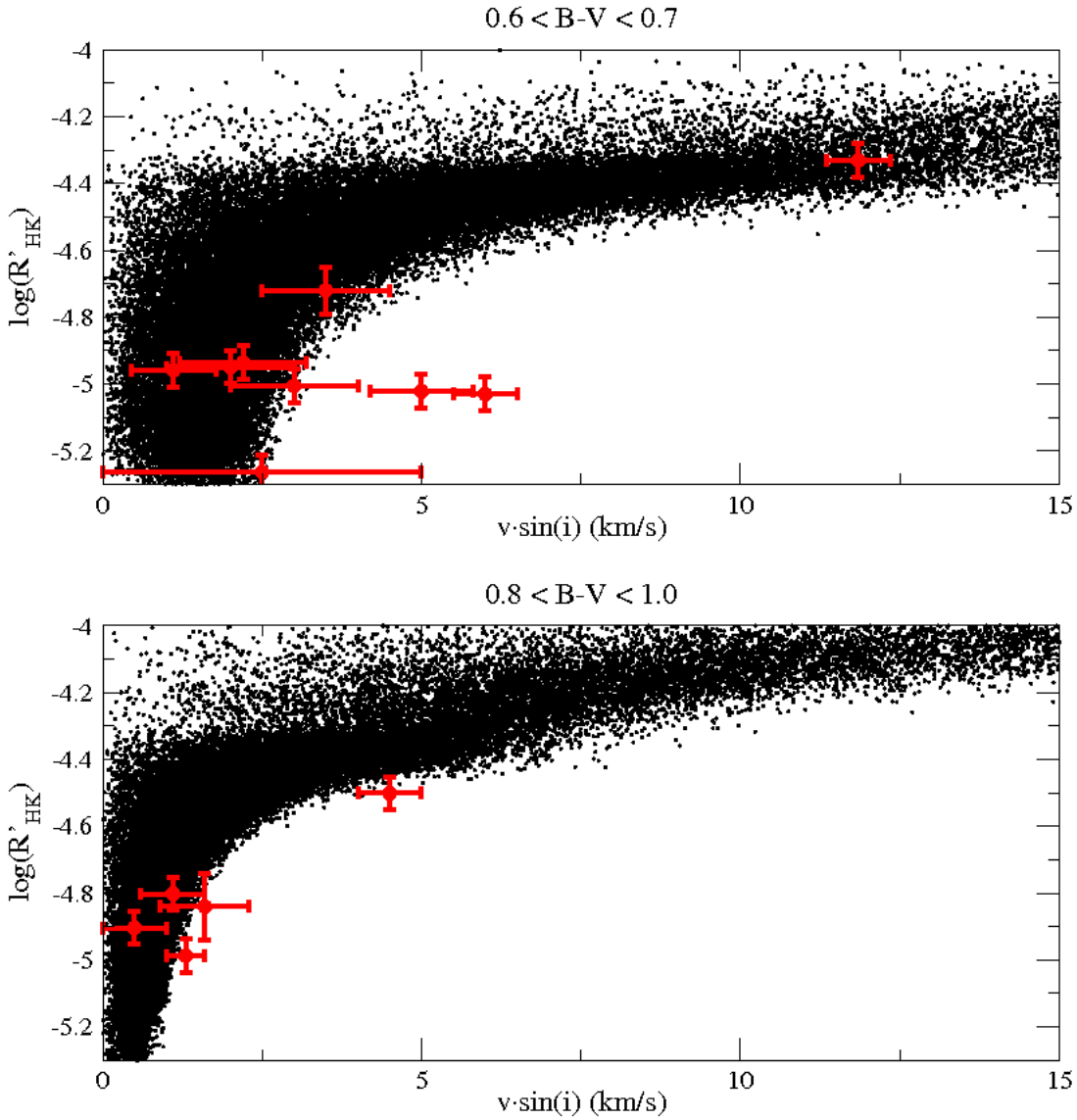

Figure 3.4: Two subsets of transiting planet host stars (red symbols): solar type (top diagram) and early K-type (bottom diagram). Individual color indices and errors are used to constrain the $(B-V)$ range of the simulated sample for each star and error bars were used to define the box to calculate the statistics (see text). Note that real data points are shown for simulated samples of a wider spectral range for convenience.

Table 3.3: List of analyzed samples of stars with $\log(R'_{HK})$, $v \sin i$ and (B-V) data. Only G-, K- and M-type stars in the main sequence are included.

Data source	N. of stars	Number of stars with $P > 1.5$	$P > 2.0$	$P > 2.5$
Dc91, Gb03 & Kh09	189	37	29	16
Jk10 & Kh09	509	209	124	66
Gy06, Gb03 & Kh09	113	34	24	13
Wr04, Gb03 & Kh09	239	64	44	32
Hr96, Gb03 & Kh09	99	24	15	9
Lp10 & Kh09	49	8	4	2
Total	1198	376	240	138

References: Dc91 (Duncan et al. 1991), Gb03 (Głębocki & Gnaciński 2003), Gy06 (Gray et al. 2006), Hr96 (Henry et al. 1996), Jk10 (Jenkins et al. 2011), Kh09 (Kharchenko & Roeser 2009), Lp10 (López-Santiago et al. 2010), Wr04 (Wright et al. 2004).

selection process.

3.5 A catalog for transit surveys

Ca II H and K flux measurements of 1296 stars made at Mount Wilson Observatory were published by Duncan et al. (1991). We converted the S fluxes, together with their uncertainties, to the more standard activity index $\log(R'_{HK})$ with the method described by Noyes et al. (1984). The catalog was cross-matched with the list of about 39000 $v \sin i$ measurements compiled by Głębocki & Gnaciński (2003), rejecting those that are upper limits or have large uncertainties. We furthermore cross-matched the resulting catalog with the photometry from the 2.5-ASCC (Kharchenko & Roeser 2009) to obtain color indices. Finally, main-sequence G-, K- and M-type stars were selected, resulting in 189 objects. Additionally, Jenkins et al. (2011) present chromospheric activity and rotational velocities for more than 850 solar-type and subgiant stars. Hipparcos distances from van Leeuwen (2007) were used to reject evolved or subgiant objects, as described by Jenkins et al. (2011), and color indices were obtained from Kharchenko & Roeser (2009), resulting in 509 main-sequence stars in the spectral range of the analysis. The catalogs with chromospheric activity data of Henry et al. (1996), Wright et al. (2004) and Gray et al. (2006) were also cross-matched with the rotational velocities by Głębocki & Gnaciński (2003) and the color indices from the 2.5-ASCC. Finally, López-Santiago et al. (2010) presented spectroscopic data, including rotational velocities and Ca II H and K flux for 57 main-sequence stars in the $0.6 < (B - V) < 1.6$ range.

The complete list of catalogs of G-, K- and M-type ($0.6 < (B - V) < 1.6$) main-sequence stars compiled here is presented in Table 3.3, together with the total number of stars and the number of those found to have a high inclination normalized efficiency over 1.5, 2.0 and 2.5. All results, including the efficiency calculated for each individual star from the input catalogs, are shown in Table 3 (available online).

From the 1198 stars analyzed, a subsample of 376 have a high inclination probability increased by 50% ($P > 1.5$) or more. This subsample contains the stars where a planet transit

search would be most efficient. The fact that different source catalogs result in a different ratio of stars with $P > 1.5$ is caused by biases toward more active or inactive stars in the different catalogs and because our selection method is more sensitive to the mid and active regime of the activity-$v \sin i$ diagram (see Sect. 3.3.3). Tighter sample selections would produce a higher rate of transit findings while observing fewer stars. This is a trade-off worth considering. For example, 240 (20%) of the input stars show $P > 2.0$ and 138 (11%) give $P > 2.5$, which means a probability higher than 0.43 of being equator-on ($i > 80°$). Therefore, assuming spin-orbit alignment, at least 43% of the stars that harbor planets in this subset are expected to show transits. In general, for stars with spin-orbit aligned planets with $R_{star}/a < \cos(80^o)$ and selected with $P > P'$, we can predict that at least $P' \cos(80^o)$ of them will show transits.

3.6 Limits and application of the methodology

As shown in Sect. 3.5, our strategy for targeted transiting planet searches results in a reduction of the initial stellar sample and an increase in the probability of finding transits. It is important to stress that we are not measuring stellar inclinations directly, but merely setting constraints via the estimation of the statistical parameter ϵ (or P). This gives the probability for each star to have a rotation axis inclination above 80°, and consequently to be oriented nearly equator-on. The probability can be calculated for every star with $\log(R'_{HK})$ and $v \sin i$ measurements. A preselection of stars with a high value of P is expected to provide a considerably higher rate of transiting planets than a non-preselected sample. Obviously, some stars with transiting planets may not be selected during the process and some targets with $i < 80°$ will inevitably be included in the selection, but the ratio of stars with $i > 80°$ will always be higher (and even more so as we increase the value of P) in the selected sample than in the unselected one, which is the main aim of our approach.

Several aspects should be taken into account in discussing the credibility of the resulting probabilities and the validity of the subsequent selected sample to serve as the input catalog for high-efficiency transit searches.

Firstly, the method for selecting high-inclination stars is based on performing statistics on simulated samples, and accordingly depends on the accuracy of the empirical relations, distributions and dispersions used in the simulation. As we describe in detail in Sect. 3.3, these relations were obtained from observed data of stars in the solar neighborhood that show certain correlations and dispersions. The expressions that describe these correlations and the Gaussian dispersions that best reproduce the observed data were implemented in the simulation of the stellar sample, and hence the results are simulated samples of stars that correctly reproduce the parameters observed in the solar neighborhood. On the other hand, a better description of both the chromospheric activity and the rotation rate dependence on mass and age, based on more accurate data, could help to better correlate the simulated samples with the observations in the activity-$v \sin i$ diagrams.

Secondly, the precision of the measurements of Ca II H and K flux and $v \sin i$ for each analyzed sample of real stars is important and should be considered, because very large error bars would make the statistics uncertain and useless. Some of the currently published measurements of $\log(R'_{HK})$ and $v \sin i$ are quite imprecise or do not have error determinations. Ca II H and K flux usually present variability for active stars, so several measurements taken at different epochs are needed to determine the average chromospheric activity and its uncertainty. We considered

all objects with available $\log(R'_{HK})$ measurements, applying an error box of a mean size of 0.1 dex for the data without published uncertainties. For future studies and more accurate results, stars showing chromospheric activity variations or having a single $\log(R'_{HK})$ measurement may not be considered or should be analyzed separately. The $v \sin i$ measurements require high-resolution spectroscopy and a very thorough analysis. Many of the published values are only upper limits, have large error bars or no associated uncertainties. Since the rotation velocities are critical at the selection process, only data with the best precision were used in the analysis and results.

Finally, the introduction of some biases and selection effects is evident in our approach, and we here analyze whether this could influence the planet detection and characteristics. As described in detail in Sect. 3.3.3, the statistics provide a better discriminating power for different values of stellar inclinations at the top part of the activity-$v \sin i$ diagram, and this prompted us to disregard the most inactive stars to avoid a high level of contamination (see Sect. 3.4). Therefore, our method is much more sensitive for active stars and the resulting selection will be biased toward this part of the sample. This means that we are rejecting part of the slow rotators of the sample, and hence the older stars. This bias will only have some noticeable effect on late-type stars ($(B-V) > 1.0$). For example, M-type stars older than ~ 1 Gyr are expected to have $\log(R'_{HK}) < -4.5$, and the activity-$v \sin i$ distribution for M stars precludes us from constraining inclinations in the range below this limit.

It is important to note that the active/young range of late-type stars is the most unexplored in exoplanet searches. Radial velocity surveys are forced to reject active stars that tend to show high rotational velocities and radial velocity jitter. Also, transit photometric surveys (especially ground-based) are likely to be inefficient for this kind of stars owing to the time-varying photometric modulations caused by starspots. On the other hand, selected equator-on stars resulting from our method will have estimated rotation periods, which makes them suitable stars for targeted searches where both the signal of the spot modulation and the possible transits could be detected and analysed. Therefore, a targeted search based on selected bright active stars expected to have $i \sim 90^\circ$ would be complementary to most exoplanet searches currently ongoing. The observables required for our method, mainly resulting from high-resolution spectroscopy, require specific equipments and can be time-intensive when considering huge amounts of stars. On the other hand, a single measurement is needed for each star, while a photometric monitoring or radial velocity search requires long time-series for each of the objects. Moreover, the same data from spectroscopic surveys that are required by our methodology can be useful for many other purposes.

Although there is a considerable amount of $\log(R'_{HK})$ and $v \sin i$ data available nowadays (see Sect. 3.4), future high-resolution spectroscopic observations with better precision may help to obtain even more selective samples for possible targeted transit searches. This strategy, besides being complementary to the currently ongoing radial velocity and transit surveys, can be more efficient than a general photometric search without preselection, which requires multiple photometric measurements of a huge amount of stars to result in a relatively low rate of transit detections. In addition, targeted observations carrying out time-series photometry of multiple objects are possible today with the increasing number of small robotic observatories. Moreover, many amateur astronomers are achieving high-precision photometry and have suitable equipment to take part in a project involving observations of multiple stars for a transit search. The availability and capabilities of amateur or small telescopes may represent the most appropriate strategy for a targeted transit search on bright stars.

3.7 Conclusions

The main idea of our work was to design and carry out a method to select the best stellar candidates for a transit search from constraints on their rotation axis inclination. One feasible way to do so with the currently available data is to make a statistical estimation of the inclinations by studying the distribution of the stars from different spectral types in the activity-$v \sin i$ diagram. The need to perform a simulation of stellar properties arose from the lack of a large database of $\log(R'_{HK})$ and $v \sin i$ measurements with sufficient quality, and allowed us to accurately study the distribution of stars with different inclinations in the activity-$v \sin i$ diagram using the statistics described in Sect. 3.3.3. Moreover, the successive steps made to design the simulation chain use the set of empirical relations that best describe the properties of the stellar sample in the solar neighborhood. This can also be useful to other fields.

With the possibility to obtain large simulated samples of stars constrained in $(B - V)$, we designed a relatively simple statistics that can be performed for every object with $(B - V)$, $\log(R'_{HK})$ and $v \sin i$ data. As a result of calculating the normalized efficiency P (see Sects. 3.3 and 3.4) of the stars in the currently available catalogs, we proved that a preselection of about 10% of the initial samples can be made, achieving a mean efficiency that is 2 to 3 times better. Assuming the existence of spin-orbit aligned planets around all stars, this means that an exoplanet transit search with a success rate 3 times higher can be designed. The application of our approach on the 1200 stars with currently available data has resulted in a catalog containing the most suitable sample for a transit search.

In the future, even more extensive catalogs with more precise measurements of chromospheric activity and $v \sin i$ will help in deriving more accurate relations for the simulation of the stellar samples, and also in obtaining more reliable results for the selection of highly inclined stars. On the other hand, an observing strategy considering a targeted exoplanet transit search should be designed taking advantage of the increasing availability of small robotic observatories and also photometric monitoring nano-satellites that may be launched in the near future and that could profit from the pre-selected samples of stars resulting from the presented method.

Chapter 4

Modelling the light curve of LHS 6343 A

This chapter presents current techniques to map the surface of rotating spotted stars and the work published in Herrero et al. (2013) on the study of the Kepler target LHS 6343 A, one of the members of a M4V+M5V visual binary system presenting transits by a brown dwarf every 12.71 days. The particular interest of this transiting system lies in the synchronicity between the transits of the brown dwarf C component and the main modulation observed in the light curve, which is in a first approach assumed to be caused by rotating starspots on the A component. We model the activity of this star by deriving maps of the active regions that allow us to study stellar rotation and the possible interaction with the brown dwarf companion. An average transit profile was derived, and the photometric perturbations due to spots occulted during transits are removed to derive more precise transit parameters. We applied a maximum entropy spot model to fit the out-of-transit optical modulation as observed by Kepler during an uninterrupted interval of ~ 500 days. It assumes that stellar active regions consist of cool spots and bright faculae whose visibility is modulated by stellar rotation. Thanks to the extended photometric time series, we refine the determination of the transit parameters and find evidence of spots that are occulted by the brown dwarf during its transits. The modelling of the out-of-transit light curve of LHS 6343 A reveals several starspots rotating with a slightly longer period than the orbital period of the brown dwarf, i.e., 13.14 ± 0.02 days. No signature attributable to differential rotation is observed. We find evidence of a persistent active longitude on the M dwarf preceding the sub-companion point by $\sim 100^\circ$ and lasting for at least ~ 500 days. This can be relevant for understanding how magnetic interaction works in low mass binary and star-planet systems.

A complementary approach to explain the photometric modulation in LHS 6343 A is exposed in Sect. 4.5, as presented in Herrero et al. (2014a). We prove that most of the out-of-eclipse light modulation is caused by the Doppler-beaming induced by the orbital motion of the primary star. We introduce a model of the Doppler-beaming for an eccentric orbit and also consider

the ellipsoidal effect. The data are fitted using a Bayesian approach implemented through a Monte Carlo Markov chain method. Model residuals are analysed by searching for periodicities using a Lomb-Scargle periodogram. For the first seven quarters of Kepler observations and the orbit previously derived from the radial velocity measurements, we show that the light modulation of the system outside eclipses is dominated by the Doppler-beaming effect. A period search performed on the residuals shows a significant periodicity of 42.5 ± 3.2 days with a false-alarm probability of 5×10^{-4}, probably associated with the rotational modulation of the primary component.

4.1 Spot modelling techniques up to now

Starspots are the most visible manifestation of activity in the photosphere of stars. Their observations on other stars than the Sun (see the review by Strassmeier 2009), both through photometric and through sophisticated spectroscopic techniques such as Doppler imaging, has lead to the measurement of rotation periods on a wide range of rates, as well as to characterize the strength and geometry of magnetic fields through detailed mappings of stellar photospheres. The high precision photometry recently acquired by space missions like MOST (*Microvariability and Oscillations of STars*, Walker et al. 2003), CoRoT (*Convection, Rotation and planetary Transits*, Auvergne et al. 2009) and Kepler (Koch et al. 2010) are providing new insights for the understanding of starspots through long term monitoring of magnetic activity.

Fourier analysis techniques are typically used in order to determine stellar rotation periods from time series photometry. This is made by measuring the main frequency produced by the light modulation due to one or several spots that move into and out of view. However, there are some important limitations for this method. First, the spots need to persist for several rotations, thus their typical time of evolving, growing and vanishing must be significantly longer than the rotation period. Also, this is limited to stars placed preferrably equator-on towards the observer, as the signal of the modulation produced by a spot will decay with $\sin i$, where i is the inclination of the stellar axis. Finally, most stars are known to present differential rotation, so that a range of rates will be observed depending on the latitude of the spots producing the signal. The most commonly used method is to compute Lomb-Scargle periodogram from long time series photometry, as has been made for a sample of CoRoT field stars by Affer et al. (2012) and for Kepler targets by Nielsen et al. (2013).

In recent years, several techniques have been developed in order to reproduce and study the distribution of features in the solar and stellar surfaces that successfully accounts for the variability in the integrated light. The most commonly used models can be divided into two categories: analytical models and surface integration techniques. The first ones use equations that compute the flux variations produced by spots as they cross the stellar disk (see Walkowicz et al. 2013; Croll et al. 2006; Amado & Zboril 2002; Kővári et al. 2006; Mosser et al. 2009), while the second are based on computing the contribution of a grid of small surface elements in the stellar photosphere, and they are usually implemented using a maximum entropy technique such as the methodology presented by Lanza et al. (2003) for the case of the Sun, Lanza et al. (2010) for CoRoT-7 or Herrero et al. (2013) studying the photospheric activity in the Kepler target LHS 6343 (see also Sect. 4.2). Some programs for analytical spot modelling as `SpotModeL` by Ribárik et al. (2003) can treat two-colour light curves simultaneously, and thereby derive the spots temperature contrasts and sizes. This is based on the standard formulae from Budding

(1977) and Dorren (1987), and the lower number of free parameters that typically have analytical models in comparison to the more complex surface integration ones make them less sensitive to the inherent degeneracies and uncertainties. On the other hand, surface integration techniques allow to tune the resolution of the stellar surface map, and hence an accurate distribution of the active regions with no a priori assumptions on the shape of the spots can be obtained, considering also the presence of faculae or 'hot spots'. This is usually suitable to time series photometry with a high signal-to-noise ratio where a detailed modelling is needed, but an individual exploration of the effects of each parameter must be performed in some cases.

Spectroscopic techniques such as Doppler Imaging provide complementary information to photometric spot models. The basic concept of Doppler Imaging is to derive maps of the stellar surfaces by studying the Doppler effects produced by stellar rotation on the observed line profiles. The technique was first proposed by Deutsch (1958), and the inverse problem is implemented in a code by Rice et al. (1989) through maximum entropy image reconstruction techniques. This methodology has the additional capability to provide constraints on the stellar inclination through the measurement of $v \sin i$, and to obtain a better estimation of spots latitudes than with photometric data, where a strong degeneracy exists especially for $\sin i \sim 1$. This technique gives smooth and simple maps of the distribution of active regions in the stellar surfaces. On the other hand, Doppler Imaging is limited to stars where stellar rotation is the dominating effect on the broadening of spectral lines ($v \sin i > 10$ km s^{-1}) to get enough spatial resolution, and also where the inclination is preferably in the range 20 - 70° (see Vogt et al. 1987). Moreover, the dataset must consist on a number of high-resolution, high signal-to-noise ratio spectra obtained at different rotation phases. Therefore, this technique has only been performed in relatively few cases (Strassmeier 2002) compared to photometric spot modelling techniques.

4.2 LHS 6343 A

As said in Sect. 1.1, M-type stars are particularly interesting targets in exoplanet searches since Earth-like planets in their habitable zones are expected to lie within the detection capabilities of some of the currently working instruments. However, the effects of magnetic activity in these stars may sometimes mask or even mimic the signal of a transiting exoplanet (e.g., Bonomo & Lanza 2008; Barnes et al. 2011). High-precision photometry from space offers the opportunity to study the signature of spots and faculae during large uninterrupted intervals of time, so it represents the best way to improve our knowledge of activity patterns in low mass stars in order to further optimize exoplanet searches.

Kepler is a photometric space mission devoted to searching for planets by the method of transits and asteroseismology. The recently released public data contain a large amount of information useful for characterizing stellar pulsations and modulations caused by starspots in solar-like and low mass stars.

Among the M-type stars observed by Kepler, a particularly interesting object is LHS 6343 AB, a visual binary system consisting of an M4V and an M5V star at a projected distance of ~ 40.2 AU. Johnson et al. (2011) report the discovery of a brown dwarf companion (hereafter LHS 6343 C) with a mass of $62.7 \pm 2.4 M_{\rm Jup}$ transiting component A of the system every 12.7138 days. The primary star, LHS 6343 A, shows almost no evidence of chromospheric activity and presents a modulation of very low amplitude in the Kepler optical light curve (see Sects. 4.3 and 4.4.2). The modulation remains stable for more than 500 days and has a period of 12.71±0.28

days, which is synchronized with the orbital motion of the companion. The large separation between the A and C components makes tidal interaction particularly weak in this system. Some other known synchronous systems are CoRoT-3 (Deleuil et al. 2008; Triaud et al. 2009), CoRoT-4 (Lanza et al. 2009a), and τ Bootis (Catala et al. 2007; Walker et al. 2008; Donati et al. 2008), although in the last two cases the star is orbited by a massive planet, not by a brown dwarf (hereafter BD). Since they are F-type dwarf stars, it has been suggested that the close-in brown dwarf or the planets may have synchronized their thin outer convective envelopes during the main-sequence lifetimes of the systems (Donati et al. 2008).

4.3 Observations

About 156,000 targets are being continuously monitored by the Kepler space telescope in a $10^\circ \times 10^\circ$ field near the constellations of Lyra and Cygnus (Koch et al. 2010; Borucki et al. 2010a). Photometry is continuously acquired for time intervals up to $\sim$ 90 days, called "quarters" in Kepler jargon, after which a re-orientation of the spacecraft is required to keep the solar arrays pointed toward the Sun. This maneuver implies a rotation of the field of view on the focal plane making the image of a given star to fall on a different CCD. As a consequence, a jump appears in the raw time series at the end of each quarter. Kepler acquires photometry with a so-called long-term cadence of $\sim$ 30 minutes, except for a subset of selected targets for which the exposure is reduced to about one minute. Long-cadence data have been made publicly available as part of the first quarters data release (Q0-Q6) and their reduction is described in Jenkins et al. (2010a,b).

LHS 6343 (KIC 010002261) has been observed by Kepler during all the first six quarters. The time series contains a total of 22976 data points with $\sim$30 minute cadence and a mean relative precision of 7×10^{-5}, ranging from May 2009 to September 2010. Both A and B components of the system, separated by 0."55 (Johnson et al. 2011), are contained inside the Kepler photometric mask used to measure the flux from the target. Its aperture is optimized by the Kepler pipeline for each individual target. Note that since the image scale is 3."98 per pixel it is not possible to measure separately the fluxes coming from the A and B components even redefining the photometric mask.

Cotrending basis vectors were applied to the raw data using PyKE pipeline reduction software[1] to correct systematic trends, which are mainly related to the pointing jitter of the satellite, detector instabilities and environment variations (Murphy 2012). These are optimized tasks to reduce Kepler Simple Aperture Photometry (hereafter SAP) data[2] as they account for the position of the specific target on the detector plane to correct for systematics. From two to four vectors were used for each quarter to remove the main trends from the raw data (see Fig. 4.1). A low-order (≤ 4) polynomial filtering was then applied to the resulting data for each quarter because some residual trends still remained followed by discontinuities between quarters. These are due to the change of the target position on the focal plane following each re-orientation of the spacecraft at the end of each quarter. Raw SAP data and detrended light curves are shown in Fig. 4.1. As a consequence of this data reduction process, the general trends disappeared, as well as jumps of the photometry between quarters. On the other hand, any possible intrinsic long-term variability of the object ($\geq$ 50 days) has also been removed. The use of low-order

[1] http://keplergo.arc.nasa.gov/PyKE.shtml

[2] The SAP light curve is a pixel summation time-series of all calibrated flux falling within the optimal aperture.

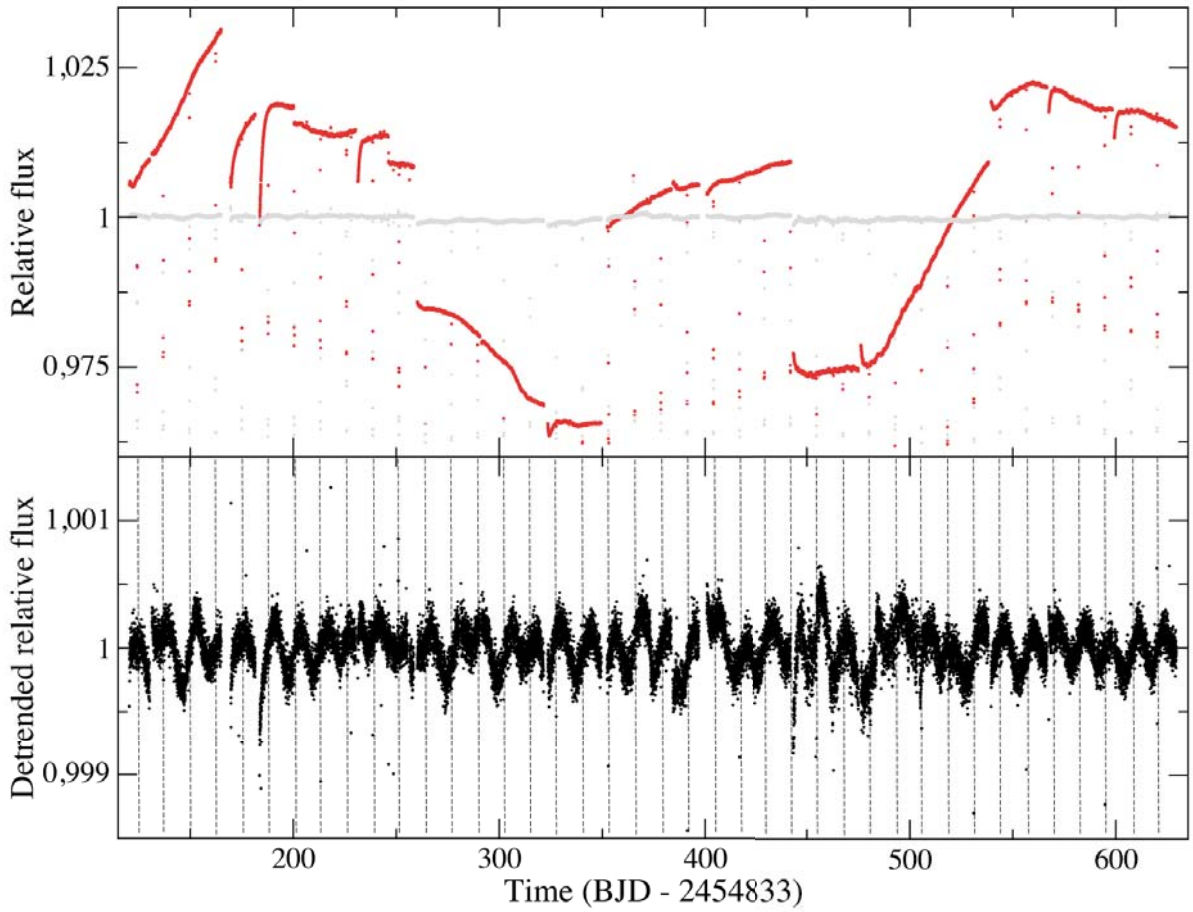

Figure 4.1: *Upper panel:* Kepler SAP light curve of LHS 6343, covering the first six quarters (red dots), and after correction from main trends using cotrending basis vectors (grey dots). *Lower panel:* LHS 6343 light curve after low-order polynomial filtering, as adopted for subsequent analysis. The times of mid-transits of LHS 6343 C are marked by vertical dashed lines.

polynomials to detrend each quarter series of data ensures that the frequency and amplitude of any variability with a timescale comparable with the companion orbital period is preserved. The presence of a number of gaps in the data prevents us from using other detrending methods such as Fourier filtering.

The out-of-transit light curve was cleaned by applying a moving box-car median 3σ-clipping filter to identify and remove outliers. Then it was rebinned with a regular 120 min sampling to reduce the computation load for the spot modelling. This is allowed because variations related to spot activity have timescales of the order of one day or longer. The average standard error of the binned observations is $\sim 5.0 \times 10^{-5}$ in relative flux units. Transits were removed assuming the ephemeris of Johnson et al. (2011). The resulting light curve consists of 5716 data points ranging from BJD 2454953.569 to BJD 2455462.163, i.e., with a duration of 508.593 days.

Studying the photometric variability of LHS 6343, we note that the light curve exhibits a periodic modulation with a low amplitude ($\sim 10^{-3}$ in relative flux units, resulting in a signal-to-noise ratio around $15 - 20$) that remains stable throughout all the time series. The minima

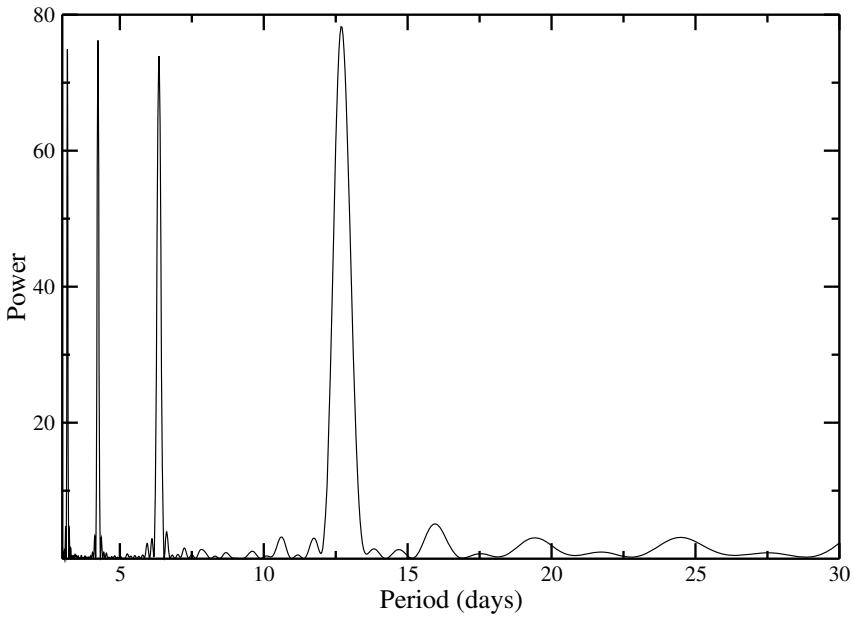

Figure 4.2: Lomb-Scargle periodogram of the out-of-transit light modulation of LHS 6343. A Gaussian fit was applied to the highest peak to obtain the period of the main modulation and its uncertainty (12.71 ± 0.28 days). Peaks corresponding to the harmonics of the main periodicity also appear at higher frequences.

of the modulation are separated by a nearly constant phase interval from the transits of the BD companion, as can be seen in the lower panel of Fig. 4.1, which also shows the long-term coherence of the modulation. This suggests that component A is responsible for the observed variability. A first analysis of the out-of-transit light curve was performed through a Lomb-Scargle periodogram, finding only one significant period of 12.71 ± 0.28 days, thus confirming the synchronicity with the LHS 6343 C orbital period (see Fig. 4.2). The other peaks seen in the periodogram correspond to the harmonics of the main periodicity and have heights similar to that of the main peak because the signal is quasi-periodic, but not exactly sinusoidal in shape. A sinusoidal fit to the light curve with the above period was performed to estimate the phase lag, showing that the light minima precede the mid-transits by 98° in phase. The phased light curve obtained with all the Q0 - Q6 data is presented in Fig.4.3 with overplotted a sinusoidal best fit, showing the difference in phase between the minima of the photometric modulation and the transits.

For further analysis and spot modelling, we assume that all the observed variability is caused by LHS 6343 A. This is also supported by the fact that the system is estimated to be older than 1-2 Gyr from the very low observed chromospheric activity, and most likely near 5 Gyr from brown dwarf mass and radius relations (Johnson et al. 2011; Baraffe et al. 1998). Therefore, the rotation period of the isolated component LHS 6343 B is expected to be longer than that of the observed modulation (Barnes 2003, 2007).

Since both A and B components of the system fall within the Kepler photometric aperture, it is necessary to correct for the flux contribution from star B before performing any modelling on the light curve. Johnson et al. (2011) use the measured $B - V$ colours and V magnitudes to estimate the relative magnitudes of the stars in the Kepler bandpass, obtaining $\Delta K_P =$

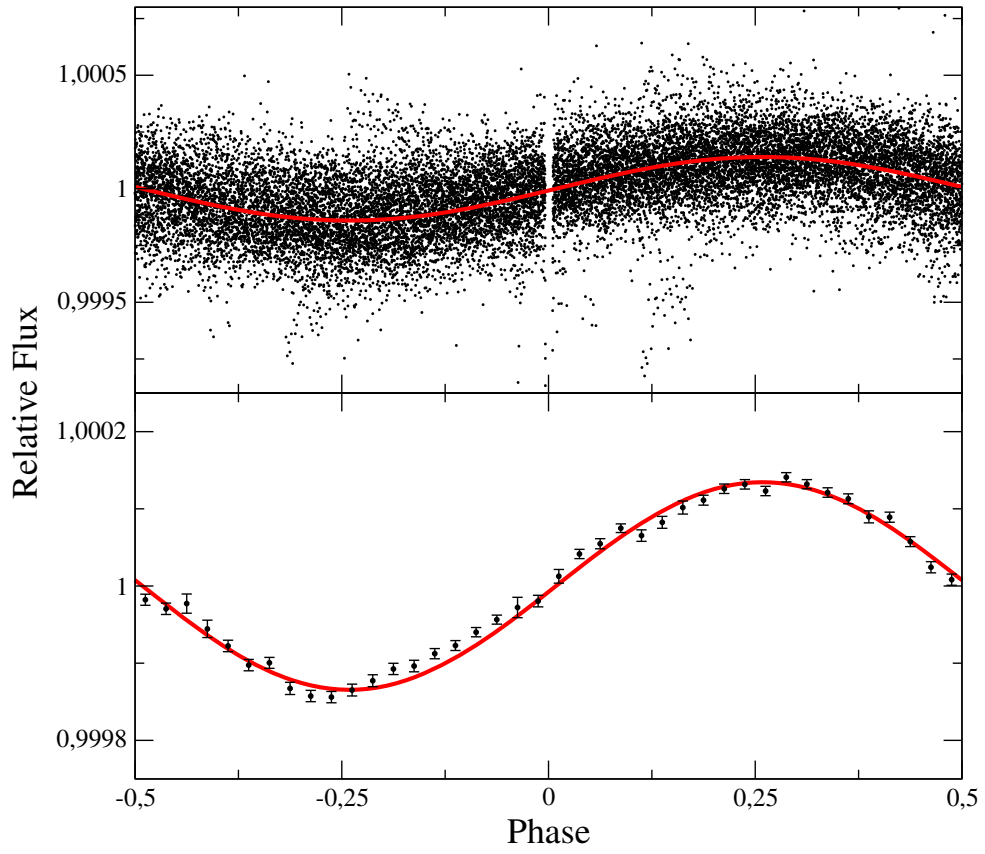

Figure 4.3: *Upper panel:* Kepler light curve of LHS 6343 phased with a period of 12.71 days (black dots). The transits have been removed leaving a gap centered on phase 0. The sinusoidal best fit applied to calculate the phase lead ($\sim 98°$) is plotted as a red solid line. *Lower panel:* The vertical scale is zoomed in and the Kepler data are plotted in 0.025 phase bins to highlight the deviations from a sinusoidal shape which cause the appearance of harmonics of the main frequency in the periodogram of Fig. 4.2. Error bars are 1-σ deviations of the binned flux values.

0.74 ± 0.10. This yields a flux ratio of 1.97 ± 0.19 between star A and B. By assuming that all the modulation comes from star A, we use this value to correct for the dilution of the flux produced by the component B. This hypothesis is valid if the amplitude $\Delta F_{\rm B}$ of the variability of component B satisfies the relationship:

$$\frac{\Delta F_{\rm B}}{F_{\rm A}+F_{\rm B}} \ll \frac{\Delta F_{\rm A}}{F_{\rm A}+F_{\rm B}}, \tag{4.1}$$

where $\Delta F_{\rm A}$ is the variability of component A and $F_{\rm A}+F_{\rm B}$ the total flux of the system. Given the above flux ratio, this implies:

$$\frac{\Delta F_{\rm B}}{F_{\rm B}} \ll (1.97 \pm 0.19)\frac{\Delta F_{\rm A}}{F_{\rm A}} \tag{4.2}$$

In other words, the relative amplitude of the variability of LHS 6343 B must be much lower than twice that of the A component to ensure that our analysis is consistent. This seems to be reasonable in view of the motivations given above.

4.4 Photospheric activity

4.4.1 Introduction

In this Section we study the photospheric activity of LHS 6343 A by applying the spot modelling approach already used for other objects, such as CoRoT-4 (Lanza et al. 2009a) or CoRoT-6 (Lanza et al. 2011b). This allows us to map the longitudinal distribution and evolution of spots in a reference frame co-rotating with the companion orbital period. As we discuss in Sect. 4.4.4, we find an overall migration of the spot pattern, indicating a rotation period of 13.137 ± 0.011 days for LHS 6343 A, and a persistently active longitude, locked at a phase difference of $\sim 100^\circ$ from the sub-companion point. Starspots are systematically enhanced when they approach and cross that longitude during their migration. This leads us to discuss possible magnetic interactions between LHS 6343 A and its brown dwarf companion (cf. Sect. 4.4.5).

4.4.2 Light curve modelling

Transit modelling

Although Johnson et al. (2011) present a transit light curve analysis, recomputing the system parameters considering the currently available dataset is justified, since the more extended Q0-Q6 transit photometry reveals several features related to spot occultations that would cause a bias in the computation of the transit depth if not properly accounted for. Specifically, when the transiting BD occults a dark feature on the disc of the A component, a relative flux increase appears along the light curve leading to a reduced relative depth of the transit (cf., e.g., Ballerini et al. 2012).

For modelling the transits, we retained the original Kepler time cadence of ~ 29.4 minutes without applying the 3σ-clipping filter to the time series. Our fitting procedure for the phased transit photometry is based on the Mandel & Agol (2002) analytic model and is performed by using the `Transit Analysis Package` (Gazak et al. 2012), a graphic user-interface `IDL` tool. This combines a Markov chain Monte Carlo (MCMC) technique to fit light curves and a

wavelet-based likelihood function (Carter & Winn 2009), which is used to compute parameter uncertainties. The model light curve is resampled and rebinned according to the Kepler long-cadence ($\sim$ 29.4 minutes) data sampling to avoid systematic deviations, in particular during the ingress and egress phases (Kipping 2010). The orbital period is fixed to 12.71382 days (Johnson et al. 2011), and the adjusted parameters are the inclination i, the ratio of the companion and primary radii $R_{\rm C}/R_{\rm A}$, the scaled semimajor axis ($a/R_{\rm A}$), and the time of mid-transit T_0. Limb darkening is treated by adopting a quadratic approximation, and the coefficients are interpolated for the specific LHS 6343 A stellar parameters from the tabulated values of Claret & Bloemen (2011). An attempt to derive the limb-darkening coefficients from the data fitting while fixing the rest of the parameters has resulted in unphysical values, probably due to a complex brightness profile and the presence of active regions. Both u_1 and u_2 have therefore been fixed to the values obtained from the tables. In most cases, the low impact of the limb darkening on the shape of the transit – note its almost flat-bottomed profile – and the existing degeneracy with other parameters, such as the inclination, makes this a better approach than obtaining the coefficients from transit modelling.

The eccentricity and argument of periastron are given by Johnson et al. (2011). A low value of the eccentricity ($e \simeq 0.05$) may still affect the transit modelling by increasing its duration by $\sim 5\%$ when the argument of periastron is changed from $\omega = 0^\circ$ to $\omega = 180^\circ$ (cf. Perryman 2011). Indeed, there is a certain probability that the eccentricity is zero because the value is within two standard deviations from zero (assuming a Gaussian distribution of the parameter). Moreover, the eccentricity is a definite positive quantity so any orbital fit to a radial velocity time series with some degree of noise tends to give a non-zero value for this parameter even if the orbit is perfectly circular (cf., e.g., Husnoo et al. 2012). The eccentricity is expected to be zero in our system, which is close to synchronization, but a possible excitation by perturbations caused by the distant B companion cannot be excluded in the absence of a specific study. However, a transit analysis with the assumption of a circular orbit was also performed and obtained no significant change in the parameter values.

A first modelling of the transit was performed by using a Levenberg-Marquardt algorithm, and a three-sigma clipping filter was applied to the positive residuals of this fit to identify and remove the data points affected by occulted spots. Then, an MCMC fitting algorithm was applied and the resulting posterior parameter probability distribution was obtained from the combination of ten chains. Several extra runs were performed by fixing each of the parameters in turn to check the consistency of the results and find possible systematic errors that were added to the final uncertainties. The error on the stellar flux ratio (see Sect. 4.3) was also accounted for in the presented uncertainties. The presence of surface brightness inhomogeneities, associated with stellar activity, makes it especially difficult to accurately model the transit with our long-cadence data because the induced perturbations are often unresolved. This produces an increase in the in-transit residuals. The results are presented in Table 4.1 and the fit displayed in Fig. 4.4. The posterior probability density functions of the parameters obtained by the MCMC modelling are shown in Fig. 4.5 assuming uniform priors.

Our mean transit profile, derived from 41 observed transits of LHS 6343 C after removing the spot perturbations, has a better sampling of the ingress and egress intervals allowing us to reduce the uncertainties on the parameters in comparison with the previous determination by Johnson et al. (2011). Specifically, we find a slightly lower value for the relative radius and a higher value for the inclination, although both are within two standard deviations of their previous values, respectively. That we find a very similar result for R_C/R_A essentially means

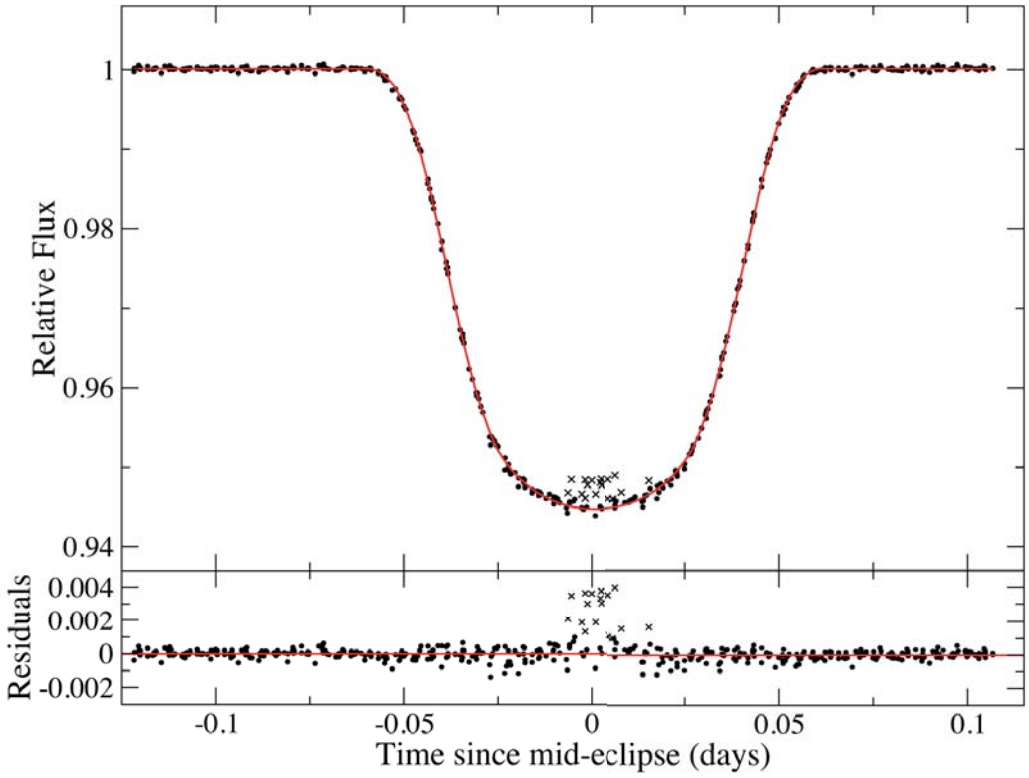

Figure 4.4: *Upper panel:* Kepler LHS 6343 transit photometry from Q0-Q6 (black dots) and the best fit model obtained as described in Sect. 4.4.2 (red line); crosses indicate data corresponding to spot occultations during the transits. They are not used for modelling the transit. *Lower panel:* The residuals of the transit best fit (black dots) and the points corresponding to spot occultations (crosses) vs. the time elapsed from mid-transit.

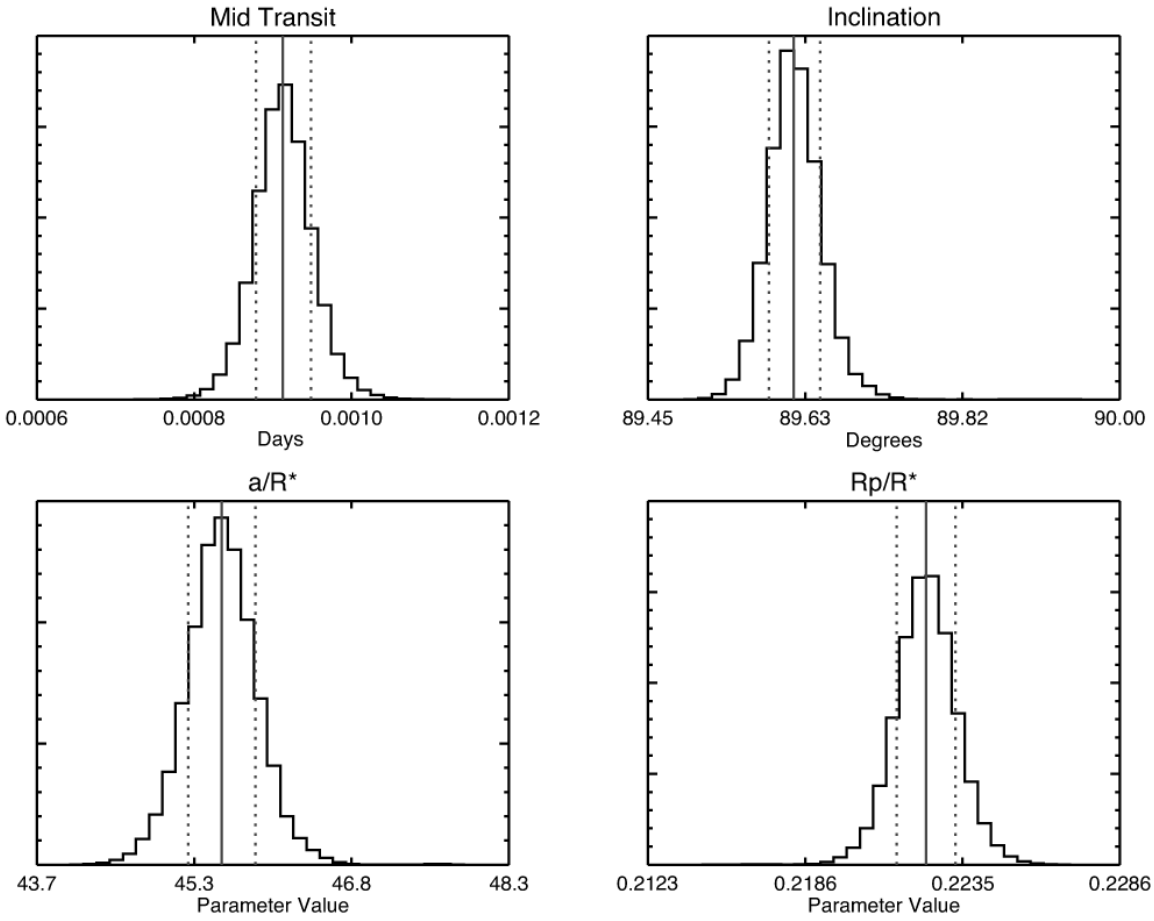

Figure 4.5: Probability density functions for the transit parameters obtained with the MCMC algorithm. The dotted vertical lines correspond to $2-\sigma$ confidence levels.

Table 4.1: Parameters obtained from the transit light curve modelling of LHS 6343 A.

Parameter	Value[a]
Radius ratio (R_C/R_A)	0.221 ± 0.002
Semimajor axis ($a_R = a/R_A$)	45.5 ± 0.4
Orbit inclination (i)	89.60 ± 0.04
Impact parameter (b)	0.30 ± 0.03
Mid transit (BJD-2454957.0)	0.2174 ± 0.0001
Linear limb darkening ($u_{1,A}$)	0.457[b]
Quadratic limb darkening ($u_{2,A}$)	0.374[b]
Eccentricity	0.056 ± 0.032[c]
Argument of periastron, ω (deg)	-23 ± 56[c]
Mean stellar density, ρ_A ($\rho_\odot$)	6.8 ± 0.4

[a] Uncertainties correspond to 85.1% confidence interval from MCMC fitting plus the contribution of systematic errors.
[b] Fixed values obtained from Claret & Bloemen (2011).
[c] Fixed values obtained from Johnson et al. (2011).

that spot occultations did not occur or at least were not significant for the five transit events present in the data analysed by Johnson et al. (2011). On the other hand, the results for the relative orbital semimajor axis a/R_A are in close agreement. Also the mean stellar density as computed from the transit parameters (e.g., Seager & Mallén-Ornelas 2003) is consistent with the mass and radius parameters in Table 4.2, adopted from Johnson et al. (2011).

Some systematic trends are observed in the residuals, almost symmetrically placed around the second and third contacts. They could be due to a complex brightness profile along the occulted chord on the stellar disc. In other words, a quadratic limb-darkening law could not be a good approximation for this very late-type star. Short-cadence data should be used to investigate these systematic deviations further along individual transits.

The occultation of the stellar disc by the BD companion during the transits can be used to resolve the fine structure of the spot pattern and study its evolution (e.g., Silva-Valio et al. 2010; Silva-Valio & Lanza 2011). From the phase-folded data shown in Fig. 4.4, we find evidence of occulted spots that seem to primarily appear close to mid-transit. This could mean that some active regions are associated with the sub-companion point. Therefore, short-cadence data for LHS 6343 would be particularly interesting for further study. This would also help for constraining the projected obliquity and confirm the quasi-synchronicity of the system (cf., e.g., Sanchis-Ojeda & Winn 2011; Sanchis-Ojeda et al. 2011).

Transit residuals are analysed to look for variability in the transit depth. One of the effects producing such a variability could be a change in the third light contributed by the component B. We find that transit residuals are dominated by noise and do not show any modulation or trend, thus confirming that star B is not active enough to produce a detectable variability and is probably rotating with a much longer period than star A. However, since some scatter in the transit depth may be caused also by active regions in star A that are not occulted during transit, it is difficult to use this result to put a strong constraint on the variability of LHS 6343 B.

Spot modelling

The reconstruction of the surface brightness distribution from the rotational modulation of the stellar flux is an ill-posed problem, because the variation in the flux vs. rotational phase contains information only on the distribution of the brightness inhomogeneities vs. longitude. The integration over the stellar disc effectively cancels any latitudinal information, particularly when the inclination of the rotation axis along the line of sight is close to 90°, as is assumed in the present case (see Sect. 4.4.3 and Lanza et al. 2009b). Therefore, we need to include a priori information in the light curve inversion process to obtain a unique and stable map. This is done by computing a maximum entropy (hereafter ME) map, which has been proven to successfully reproduce active region distributions and area variations in the case of the Sun (cf. Lanza et al. 2007).

Our approach has been compared with other spot modelling methods by Mosser et al. (2009) and Huber et al. (2010) and with the maps obtained by spot occultations during the planetary transits in the CoRoT-2 system by Silva-Valio & Lanza (2011). To model the high-precision space-borne photometry of ϵ Eri and k^1 Ceti obtained by MOST (the Microvariability and Oscillation of STar satellite), Croll (2006), Croll et al. (2006), and Walker et al. (2007) have developed a sophisticated approach based on a few circular spots. They use simulated annealing and tempering techniques to explore the multi-dimensional model parameter space and Markov chain Monte Carlo methods to assess the parameter uncertainties. The main limitation of these models is that the reduced χ^2 values of their best fits are significantly greater than the unity. This indicates that the model assumptions, in particular the consideration of only two or three fixed spots, are too simplified to reproduce the true stellar variability down to the level of precision of space-borne photometry.

A similar approach has been applied in the case of the Kepler light curves by Frasca et al. (2011) and Fröhlich et al. (2012) by considering several spots whose areas evolve with time. Although these models allow a convincing determination of the model parameters and their uncertainties, they require a huge amount of computation and their best fits often show systematic deviations suggesting that the spot pattern is more complex than can be described with several circular, non-overlapping starspots. Therefore, we prefer to use a continuous distribution for the spotted area and a regularization approach to find a unique and stable solution.

An important advantage of the ME regularization is that the multi-dimensional parameter space of the objective function to be minimized (cf. Eq. 4.6) has a smoother landscape than the χ^2 landscape of a multi-spot model, thanks to the addition of the configurational entropy term (the function S defined below; cf. the analogous problem of image restoration in Bryan & Skilling 1980). This effectively reduces the problems associated with the presence of several χ^2 relative minima falling in widely separated regions of the parameter space (cf. Croll et al. 2006; Walker et al. 2007). Moreover, we effectively average over many degrees of freedom by only considering the distribution of the spotted area vs. the stellar longitude, which is the only information that can be directly extracted from our unidimensional time series. Therefore, the basic role of our regularization is that of smoothing the distribution of the spot filling factor versus longitude, thus reducing the impact of the noise on the light curve inversion process.

In our model, the star is subdivided into 200 surface elements, namely 200 squares of side 18°, with each element containing unperturbed photosphere, dark spots, and facular areas. The fraction of an element covered by dark spots is indicated by the filling factor f, the fractional area of the faculae is Qf, and the fractional area of the unperturbed photosphere is $1-(Q+1)f$.

The contribution to the stellar flux coming from the k-th surface element at the time t_j, where $j = 1, ..., N$ is an index numbering the N points along the light curve, is given by

$$\begin{aligned} \Delta F_{kj} &= I_0(\mu_{kj}) \{1 - (Q+1) f_k + c_{\rm s} f_k + \\ &\quad Q f_k [1 + c_{\rm f}(1 - \mu_{kj})]\} A_k \mu_{kj} w(\mu_{kj}), \end{aligned} \tag{4.3}$$

where I_0 is the specific intensity in the continuum of the unperturbed photosphere at the isophotal wavelength of the observations; $c_{\rm s}$ and $c_{\rm f}$ are the spot and facular contrasts, respectively (cf. Lanza et al. 2004); A_k is the area of the k-th surface element,

$$w(\mu_{kj}) = \begin{cases} 1 & \text{if } \mu_{kj} \geq 0 \\ 0 & \text{if } \mu_{kj} < 0 \end{cases} \tag{4.4}$$

is its visibility; and

$$\mu_{kj} \equiv \cos\psi_{kj} = \sin i \sin\theta_k \cos[\ell_k + \Omega(t_j - t_0)] + \cos i \cos\theta_k, \tag{4.5}$$

is the cosine of the angle ψ_{kj} between the normal to the surface element and the direction of the observer, with i being the inclination of the stellar rotation axis along the line of sight; θ_k the colatitude and ℓ_k the longitude of the k-th surface element; Ω denotes the angular velocity of rotation of the star ($\Omega \equiv 2\pi/P_{\rm rot}$, with $P_{\rm rot}$ the stellar rotation period), and t_0 the initial time. The specific intensity in the continuum varies according to a quadratic limb-darkening law, as adopted by Lanza et al. (2003) for the case of the Sun, viz. $I_0 \propto a_{\rm p} + b_{\rm p}\mu + c_{\rm p}\mu^2$. The stellar flux computed at the time t_j is then $F(t_j) = \sum_k \Delta F_{kj}$. To warrant a relative precision of the order of 10^{-5} in the computation of the flux F, each surface element is further subdivided into $1^\circ \times 1^\circ$-elements, and their contributions, calculated according to Eq. (4.3), are summed up at each given time to compute the contribution of the $18^\circ \times 18^\circ$ surface element to which they belong.

We fit the light curve by varying the value of f over the surface of the star, while Q is held constant. Even fixing the rotation period, the inclination, and the spot and facular contrasts (see Lanza et al. 2007, for details), the model has 200 free parameters and suffers from non-uniqueness and instability. To find a unique and stable spot map, we apply ME regularization by minimizing a functional Z, which is a linear combination of the χ^2 and the entropy functional S; i.e.,

$$Z = \chi^2(\vec{f}) - \lambda S(\vec{f}), \tag{4.6}$$

where $\vec{f}$ is the vector of the filling factors of the surface elements, $\lambda > 0$ a Lagrangian multiplier determining the trade-off between light curve fitting and regularization. The expression for S is given in Lanza et al. (1998). The entropy functional S attains its maximum value when the star is free of spots. Therefore, by increasing the Lagrangian multiplier λ, we increase the weight of S in the model, and the area of the spots is progressively reduced. This gives rise to systematically negative residuals between the observations and the best-fit model when $\lambda > 0$. The optimal value of λ depends on the information content of the light curve, which in turn depends on the ratio of the amplitude of its rotational modulation to the average error of its points. In the case of LHS 6343 A, the amplitude of the rotational modulation is ~ 0.001, while the average

error of the points is $\sim 5 \times 10^{-5}$ in relative flux units, giving a signal-to-noise ratio of ~ 20. The significant impact of the noise on the light curve makes the regularization a critical process, and a different criterion than that applied for CoRoT-2 (see Lanza et al. 2009b) or CoRoT-6 (see Lanza et al. 2011b) must be adopted, because in those cases the signal-to-noise ratio was > 100. For the present case, we increase the regularization until we obtain $|\mu_{\rm reg}| = \beta\epsilon_0$, where $\mu_{\rm reg}$ is the mean of the residuals of the regularized light curve, and $\epsilon_0 \equiv \sigma_0/\sqrt{N}$ is the standard error of the residuals of the unregularized light curve (i.e., obtained with $\lambda = 0$), defined as the ratio of their standard deviation σ_0 to the square root of the number of data points N in each individual segment of duration $\Delta t_{\rm f}$ fitted by our model (see below). The parameter $\beta \geq 1$ depends on the information content of the light curve and is unity when the signal-to-noise ratio is of the order of 100 or greater. In our case, we determine the optimal value of β a posteriori, by increasing λ until the small random spots associated with the noise are strongly smoothed, while the deviation of the regularized model from the data points is still acceptable (see Sect. 4.4.4 and Appendix A for the effects of varying β on the solution).

In the case of the Sun, by assuming a fixed distribution of the filling factor, it is possible to obtain a good fit of the irradiance changes only for a limited time interval $\Delta t_{\rm f}$, not exceeding 14 days, which is the lifetime of the largest sunspot groups dominating the irradiance variation. In the case of other active stars, the value of $\Delta t_{\rm f}$ must be determined from the observations themselves, looking for the longest time interval that allows a good fit with the applied model (see Sect. 4.4.3).

The optimal values of the spot and facular contrasts and of the facular-to-spotted area ratio Q in stellar active regions are unknown a priori. In our model the facular contrast $c_{\rm f}$ and the parameter Q enter as the product $c_{\rm f}Q$, so we can fix $c_{\rm f}$ and vary Q, estimating its best value by minimizing the χ^2 of the model, as shown in Sect. 4.4.3. Since there are many free parameters in the ME model is large, for this specific application we make use of the model of Lanza et al. (2003), which fits the light curve by assuming only three active regions to model the rotational modulation of the flux plus a uniformly distributed background to account for the variations in the mean light level. This procedure is the same as used to fix the value of Q in the cases of CoRoT-2, CoRoT-4, CoRoT-7, and CoRoT-6 (cf. Lanza et al. 2009a,b, 2010, 2011).

We assume an inclination of the rotation axis of LHS 6343 A of $i \simeq 90^\circ$ in most of our models (see Sect. 4.4.3), coming from the results of the transit modelling (see Sect. 4.4.2). Such a high inclination implies that negligible information on the spot latitude can be extracted from the rotational modulation of the flux, so that the ME regularization virtually puts all the spots around the subobserver latitude (i.e., $\approx 0^\circ$) to minimize their area and maximize the entropy. Therefore, we are limited to mapping only the distribution of the active regions vs. longitude, which can be done with a resolution better than $\sim 50^\circ$ (cf. Lanza et al. 2007, 2009b). Our ignorance of the true facular contribution may lead to systematic errors in the active region longitudes derived by our model because faculae produce an increase in the flux when they are close to the limb, leading to a systematic shift of the longitudes of the active regions used to reproduce the observed flux modulation, as discussed by Lanza et al. (2007) for the case of the Sun and illustrated by Lanza et al. (2009b, cf. Figs. 4 and 5) for CoRoT-2.

Given the dependence of our modelling approach on several parameters, we present a detailed discussion of their impact on our results in Appendix A.

Table 4.2: Parameters adopted for the light curve modelling of LHS 6343 A.

Parameter		Ref.[a]
Star mass ($M_\odot$)	0.370	J11
Star radius ($R_\odot$)	0.378	J11
$T_{\rm eff}$ (K)	3130	J11
$\log g$ (cm s^{-2})	4.85	J11
$a_{\rm p}$	0.1695	CB11
$b_{\rm p}$	1.2041	CB11
$c_{\rm p}$	-0.3736	CB11
$P_{\rm rot}$ (days)	12.7138	J11
ϵ	6.09×10^{-6}	He12
Inclination (deg)	89.60	He12
$c_{\rm s}$	0.536	He12
$c_{\rm f}$	0.115	L04
Q	0.0, 8.0	He12
$\Delta t_{\rm f}$ (days)	8.769	He12

[a] References: CB11: Claret & Bloemen (2011); He12: present work; J11: Johnson et al. (2011); L04: Lanza et al. (2004).

4.4.3 Model parameters

The fundamental stellar parameters are taken from Johnson et al. (2011) and are listed in Table 4.2. A quadratic limb-darkening law is adopted for the stellar photosphere, viz., $I(\mu) \propto a_{\rm p} + b_{\rm p}\mu + c_{\rm p}\mu^2$, where the coefficients $a_{\rm p}$, $b_{\rm p}$, and $c_{\rm p}$ have been obtained for $T_{\rm eff} = 3130$ K, $\log g = 4.85$ [cgs], and solar abundances from the theoretical values computed by Claret & Bloemen (2011) from Phoenix model atmospheres.

The rotation period for modelling the spotted photosphere was fixed to the companion orbital period. This assumption comes from the periodogram analysis giving $P_{\rm rot} = 12.71 \pm 0.28$ days (see Fig. 4.2), which indicates that the system is close to synchronization. As we see in Sect. 4.4.4, any deviation of stellar rotation from synchronization will appear on the ME map as a longitude drift of the active regions versus time.

The rotation period of 12.71 days is used to compute the polar flattening of the star due to the centrifugal potential in the Roche approximation, yielding a relative difference between the equatorial and the polar radii ϵ of 6.09×10^{-6}. The effect of this flattening on the modulation caused by spots is negligible. The relative difference in flux for a $\sim 2\%$ spot coverage would be less than 10^{-6} as a consequence of the gravity darkening in the equatorial regions of the star.

Owing to the lack of a measurement of the Rossiter-McLaughlin effect or precise $v \sin i$ data, the inclination of the stellar axis of LHS 6343 A cannot be constrained. The limit on $v \sin i < 2$ km s^{-1} given by Johnson et al. (2011) does not help because the above rotation period and the radius yield an equatorial rotation velocity of ~ 1.5 km s^{-1}. Nevertheless, we assume that the system is spin-orbit aligned; that is, its inclination is assumed to be equal to that of the orbit of the BD companion, i.e. $89.^\circ60 \pm 0.^\circ04$. The inclination of the stellar spin axis along the line

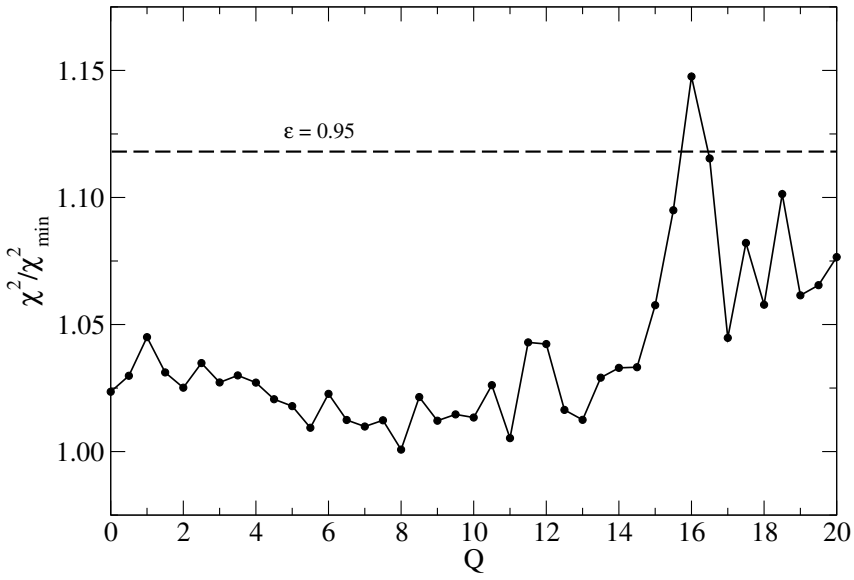

Figure 4.6: The ratio of the χ^2 of the composite best fit of the entire time series to its minimum value vs. the parameter Q, i.e., the ratio of the facular area to the cool spot area in active regions. The horizontal dashed line indicates the 95% confidence level for $\chi^2/\chi^2_{\rm min}$. This does not put any significant constraint on the interval of acceptable Q values owing to the low signal-to-noise ratio of the data.

of sight is the only parameter required to characterize the geometry of the stellar rotation for modelling the out-of-transit light modulation. If we had been interested in also modelling the occultations of starspots during transits, the sky-projected angle between the stellar spin and the orbital angular momentum would have been required, too (e.g., Sanchis-Ojeda et al. 2012).

The maximum time interval $\Delta t_{\rm f}$ that our model can accurately fit with a fixed distribution of active regions has been determined by means of a series of tests dividing the total interval, $T = 508.5936$ days, into N_f equal segments, i.e., $\Delta t_{\rm f} = T/N_{\rm f}$. The simple three-spot model of Lanza et al. (2003) has been applied to fit the individual intervals to reduce the number of free parameters. The optimal $N_{\rm f}$ is given by the minimum value that allows us a good fit to the light curve as measured by the χ^2 statistics. For $N_{\rm f} < 58$, the quality of the fit starts to degrade significantly, so we adopt this as the optimal number of segments, giving $\Delta t_{\rm f} = 8.769$ days (cf. Appendix A). In any case, $\Delta t_{\rm f} > P_{\rm rot}/2$ is required to adequately sample the light modulation produced by a rotating active region, providing us with information on its longitude and area. On the other hand, a too long $\Delta t_{\rm f}$ would result in a low time resolution of our model, so that starspot evolution and migration would be more difficult to trace.

The spot temperature contrast is estimated by the correlation found in Fig. 7 of Berdyugina (2005) that shows that the contrast decreases with decreasing stellar effective temperature. Thus, we adopt a spot temperature deficit of $\Delta T_{\rm s} = -250$ K for LHS 6343 A and compute the spot's intensity contrast considering blackbody emission for the spots and the photosphere in the Kepler passband, yielding $c_{\rm s} = 0.536$. This is not a critical parameter because a variation in $c_{\rm s}$ will only cause a change in the overall spot filling factor, but will not affect either spot longitudes or their time evolution, as discussed in detail by Lanza et al. (2009b). The facular contrast is assumed to be solar-like with $c_f = 0.115$ (Lanza et al. 2004).

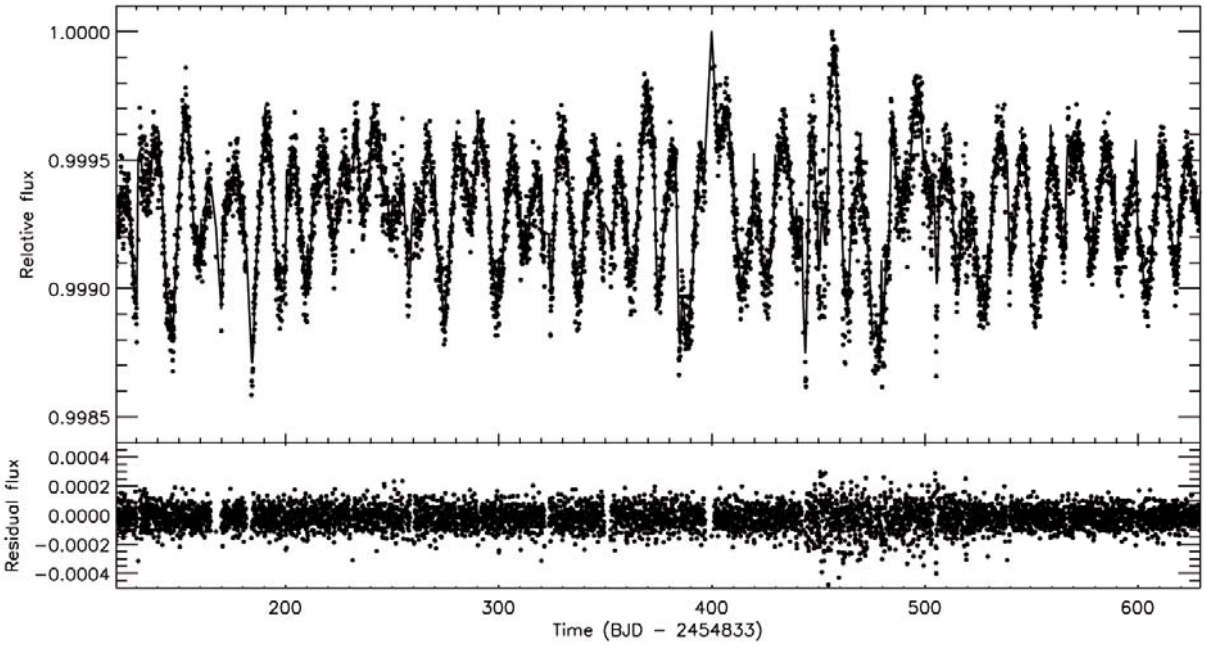

Figure 4.7: *Upper panel:* The out-of-transit light curve of LHS 6343 A (dots) and its ME-regularized best fit for a facular-to-spotted area ratio $Q = 8.0$ (solid line) during the time interval between BJD 2454953.569 and BJD 2455462.163. The flux is normalized to the maximum observed flux along the time series. *Lower panel:* The corresponding residuals.

The ratio Q between the facular and the spotted areas in active regions is estimated by means of the three-spot model introduced by Lanza et al. (2003) simultaneously with the optimal value of $\Delta t_{\rm f}$. Both the flux increase due to the facular component when an active region is close to the limb and the flux decrease due to its spots when that region transits across the central meridian of the disc are modelled by this approach, allowing us to derive the optimal value of Q, if the signal-to-noise ratio of the data is high enough.

In Fig. 4.6 we plot the ratio $\chi^2/\chi^2_{\rm min}$ of the total χ^2 of the composite best fit of the entire time series to its minimum value $\chi^2_{\rm min}$, versus Q. Given the low signal-to-noise ratio of the photometry in our case, we find that there is no clear χ^2-minimum vs. Q so its value is poorly constrained with the best solutions falling in the range between ~ 5 and ~ 11. Therefore, we adopt $Q = 8.0$ for further analysis. This facular-to-spotted area ratio is similar to the one found in the case of the Sun ($Q = 9$, cf. Lanza et al. 2007).

4.4.4 Results

Light curve model

The composite best fit obtained with the ME regularization and $Q = 8.0$ is shown in Fig. 4.7 (upper panel) together with the residuals (lower panel). From a best fit without regularization ($\lambda = 0$) applied to the whole time series (Q0−Q6), we obtain a mean $\mu_{\rm res} = 8.308 \times 10^{-8}$ and a standard deviation of the residuals $\sigma_0 = 6.778 \times 10^{-5}$ in relative flux units, which is slightly higher than the standard error of the mean points. This can be due to short time scale

fluctuations that cannot be fitted with our approach that reproduces variations on a timescale comparable to $\Delta t_{\rm f}$ or longer. On average, we have $N \sim 98$ data points per fitted subset $\Delta t_{\rm f}$.

The Lagrangian multipliers λ for the regularized ME models are iteratively adjusted until the mean of the residuals $\mu_{\rm reg} = -1.365 \times 10^{-5} \simeq -\beta(\sigma_0/\sqrt{N})$, where $\beta = 2$ is established as the optimal value that still leads to an acceptable fit while reducing the information content of the spot maps as much as possible, i.e., maximizing the entropy. A lower value of β improves the fit slightly over small sections of the light curve, but introduces several small spots that change from one time interval to the next without any clear regularity. On the other hand, by selecting $\beta = 2$, we obtain smoother maps with concentrated groups of spots that evolve regularly from one $\Delta t_{\rm f}$ interval to the next, which indicates that we are properly modelling the overall distribution of the active regions on the star. A higher level of regularization ($\beta > 2$) gives unacceptably larger, systematically negative residuals because the maximum entropy criterion reduces the spotted area too much. At the same time, it concentrates the spots into isolated groups, and a pattern with three active regions equally spaced in longitude (i.e, with $\approx 120^\circ$ gaps) begins to appear. This pattern still shows the general migration of the multiple spots appearing in the maps with the optimal regularization (see Sect. 4.4.4), but it is clearly an artefact of the over-regularization, due to the limited signal-to-noise level of our data that favours a reproduction of the light variations by a decreasing number of spots when the regularization is increased (cf. Appendix A).

In either case, the low signal-to-noise ratio of our data requires a relatively strong regularization, and as a consequence, misfits sometimes appear at the matching points between time intervals. Therefore, by decreasing $\Delta t_{\rm f}$, the overall quality of the best fit is not increased in our case. Nevertheless, looking at the residuals of our regularized composite best fit, we see a generally good reproduction of the light variations without systematics that could be attributed to sizable active regions evolving on timescales significantly shorter than $\Delta t_{\rm f}$. We notice that the noise level increases after BJD 2455276 (corresponding to BJD$-2454833 = 443$ in Fig. 4.7), which coincides with the beginning of quarter Q5 and returns to the previous level after BJD 2455371 (BJD$-2454833 = 538$), i.e., at the beginning of quarter Q6. This is a consequence of the rotation of the focal plane of the Kepler telescope between successive quarters, which makes the target be measured on a different CCD.

Distribution of active regions and stellar rotation

The distribution of the spot filling factor f versus longitude and time is plotted in Fig. 4.8 for our ME model with $Q = 8.0$ adopting a reference frame rotating with the orbital period of the BD companion, i.e., 12.7138 days. The origin of the longitude frame corresponds to the subobserver point at the beginning of the Kepler time series (i.e. BJD 2454953.569) and the longitude increases in the same direction as the stellar rotation and the orbital motion of the companion. The subcompanion longitude is fixed at $\sim 257^\circ$ in this reference frame.

Several individual active regions can be identified from the map in Fig. 4.8 showing lifetimes around $15 - 20$ days. Three dotted lines have been drawn connecting the longitudes with higher filling factors to trace the overall migration of the spots. They identify three long-lived active longitudes that migrate backwards at the same constant rate. This indicates that the rotation of the star is somewhat slower than that of our reference frame following the orbital motion of the BD companion. The similarity of the migration rates among the three active longitudes suggests that either the spot latitudes are confined to a thin belt or the star has no detectable

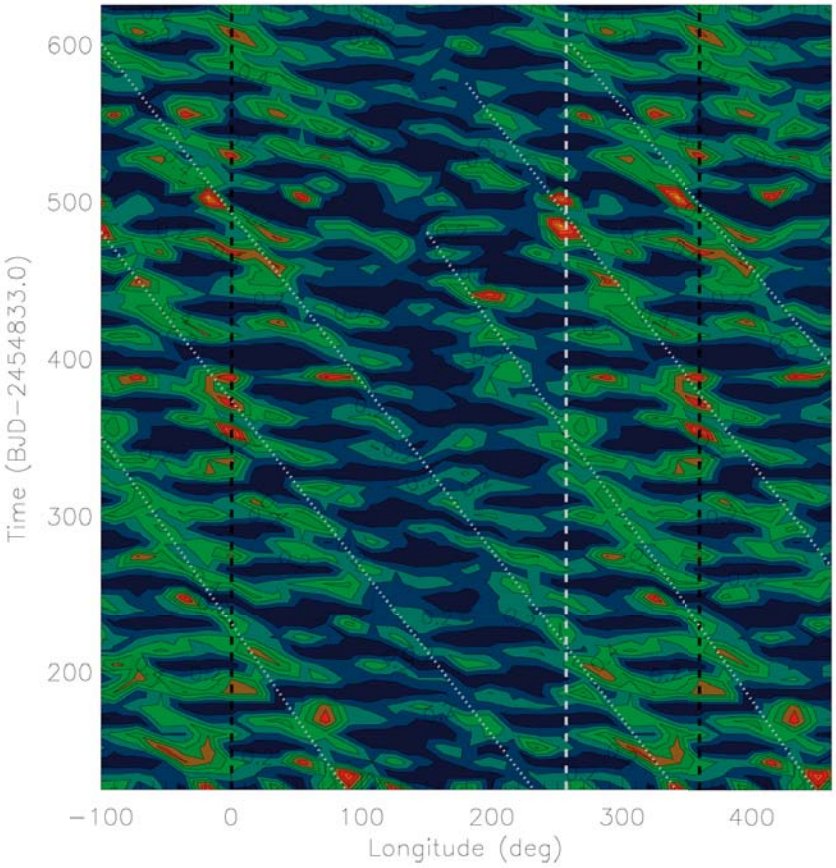

Figure 4.8: Isocontours of the ratio $f/f_{\max}$, where f is the spot covering factor and $f_{\max} = 0.00059$ its maximum value, versus time and longitude for the ME models with $Q = 8.0$. The two dashed black lines mark longitudes 0° and 360° beyond which the distributions are repeated to easily follow spot migration. The dashed white line marks the longitude of the subcompanion point, which is fixed in this reference frame at $\sim 257°$. The contour levels are separated by $\Delta f = 0.1 f_{\max}$ with yellow and orange indicating the maximum covering factor and dark blue the minimum. The dotted white lines trace the migration of the active regions associated with each active longitude (see the text).

Table 4.3: Relative migration rates $\Delta\Omega/\Omega$ obtained from linear fits to the migration of the main active longitudes in Fig. 4.8, and the corresponding mean rotation period $P_{\rm rot}$.

Q	AL_1 (10^{-2} deg/d)	AL_2 (10^{-2} deg/d)	AL_3 (10^{-2} deg/d)	$P_{\rm rot}$ (d)
0.0	-3.20 ± 0.20	-3.34 ± 0.11	-3.24 ± 0.17	13.129 ± 0.015
8.0	-3.34 ± 0.15	-3.34 ± 0.14	-3.30 ± 0.20	13.137 ± 0.011

differential rotation.

By considering the longitudes of the relative maxima of the spot covering factor in Fig. 4.8, a linear fit is performed to find the relative rotation rates associated with the steady migration of the three main starspots. The results are listed in Table 4.3 for two models having a different facular-to-spotted area ratio Q. By assuming a significant facular contribution ($Q = 8.0$), a mean rotation period of 13.137 ± 0.011 days is obtained. This is a significantly slower rotation than the companion orbital motion, showing that the system is slightly out of synchronism. The stellar rotation, as traced by starspots, appears to be rigid since there is no significant difference between the highest and the lowest migration rates. The migration rates for a spot model assuming only dark spots ($Q = 0$) are also reported in Table 4.3, because the longitudes of the spots derived from the maximum entropy modelling may depend on the value of Q (Lanza et al. 2007, 2009b). Nevertheless, very similar results are obtained, thus confirming that the presence of faculae is not actually required to adequately fit the low signal-to-noise photometry of LHS 6343 A (cf. Sect. 4.4.3). In the case of no faculae, a virtually identical mean rotation period of 13.129 ± 0.015 days is obtained from the migration of the spots.

An intriguing phenomenon seen in Fig. 4.8 is that the spot filling factor shows a persistent relative minimum in the longitude range between $\approx 100^\circ$ and $\approx 250^\circ$, while it has a relative maximum between $\approx 250^\circ$ and $\approx 450^\circ$. In other words, the filling factor appears to be systematically enhanced when the migrating starspots approach and cross a longitude leading the subcompanion longitude by $\sim 100^\circ$ in our reference frame. Since the passage of that longitude across the centre of the stellar disc precedes that of the BD companion, this agrees with the light curve that shows a relative light minimum ~ 3.5 days before each transit. This modulation has persisted for more than 500 days, as far as the Kepler data currently cover.

This enhancement of the spot filling factor is highlighted in Fig. 4.9, where the spot coverage factor integrated over the time is plotted vs. longitude in bins of 72°. A wide maximum is evident around $\sim 350^\circ$, meaning that activity tends to be concentrated in a region preceding the subcompanion longitude. This agrees closely with what can be seen in Fig. 4.1, and especially in the phase-folded light curve (Fig. 4.3). Moreover, this explains the results obtained by the Lomb-Scargle periodogram (Fig. 4.2) because only the frequency of the main modulation associated with this activity enhancement, phased to the companion C, is detected by that method. On the other hand, ME modelling allows us to map individual starspots and follow their migration across the longitude where they show an enhancement. Unfortunately, no information on the spot latitudes can be derived with our models, so we cannot establish whether the enhancement of activity at this longitude is produced in a single latitude or if it covers a range of latitudes. As discussed in Sect. 4.4.5, these results strongly suggest some magnetic interaction between

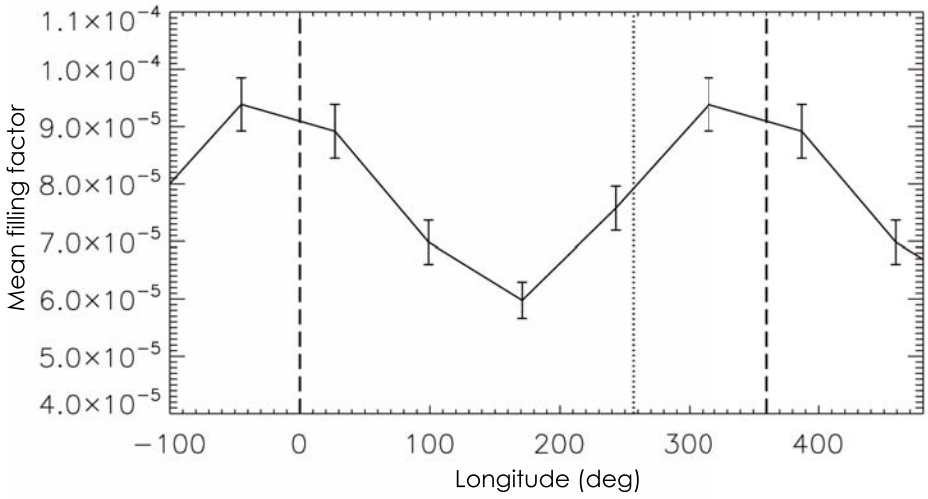

Figure 4.9: The spotted area in 72° longitude bins averaged versus time as derived from the ME regularized models with $Q = 8.0$. The error bars indicate the standard error of the spotted area in the corresponding bin. The dotted line marks the subcompanion point longitude, while the dashed lines indicate the longitudes 0° and 360° beyond which the distribution is repeated for clarity.

LHS 6343 A and its BD companion LHS 6343 C, thus causing spots to mainly appear at a fixed longitude in the reference frame of the companion orbital motion.

The variation in the total spotted area vs. the time is shown in Fig. 4.10. Only slight variations can be seen with a typical timescale of 20-30 days, which can be associated with the typical spot lifetime. Short-term oscillations are most likely related to the noise present in our time series, especially during quarter Q5, residual trends, or gaps in the data (e.g., the one near day ~ 400, see Fig. 4.1). Long-term trends have been removed when detrending the time series from Kepler instrumental effects (see Sect. 4.3), so the mean value of the total spotted area stays approximately constant. The absolute value of the area depends on the adopted spot contrast c_s and the value of Q (for instance, a lower spot temperature would imply a stronger contrast and thus a smaller area), but the relative variations in the area are largely independent of c_s and Q (cf. Lanza et al. 2009b).

4.4.5 Discussion

We find that the rotation of LHS 6343 A is not perfectly synchronized with the orbital motion of the BD companion. Spot modelling is superior to the Lomb-Scargle periodogram for determining the rotation period because a much smaller phase difference is required to distinguish between close periods for a given time baseline. The regular and steady migration of the active longitudes in Fig. 4.8 makes our result quite robust. Unfortunately, the fast evolution of the individual spots together with the low signal-to-noise ratio of the photometry does not allow us to detect any possible differential rotation.

The intriguing point concerning the quasi-synchronous rotation of LHS 6343 A is that the

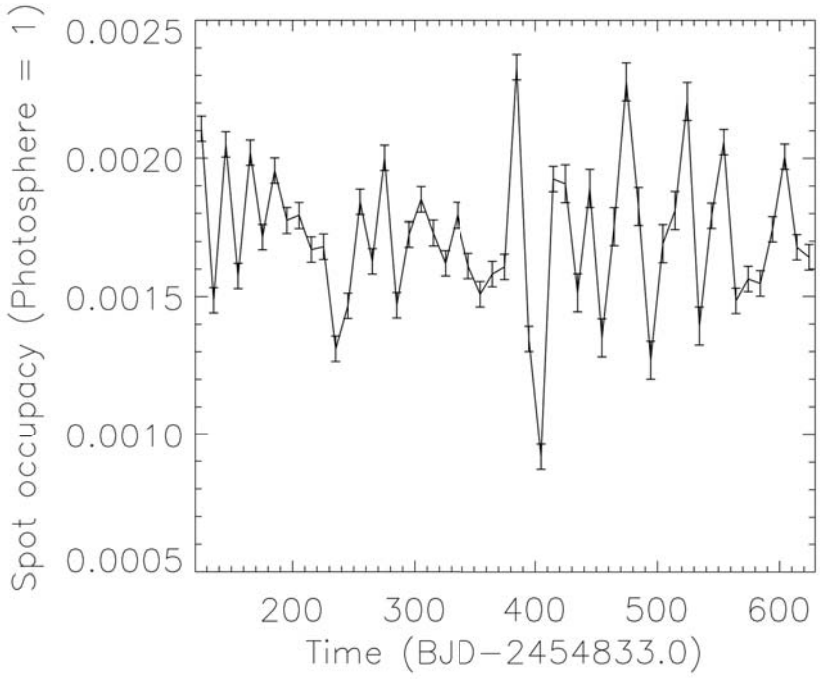

Figure 4.10: The total spotted area versus time as derived from the regularized ME analysis for $Q = 8.0$. The error bars correspond to three standard deviations.

tidal interaction between the star and its BD companion is presently very weak. Using the formalism of Leconte et al. (2010), we estimate a current timescale for the tidal angular momentum exchange between the spin and the orbit of ≈ 7.5 Gyr, if a modified tidal quality factor $Q' = 10^6$ is adopted for the A component. Assuming that the stellar radius was larger by a factor of $3 - 4$ during the pre-main-sequence evolution of the system, the synchronization timescale was shorter by a factor of $\approx 10^3$ at that time, i.e., significantly shorter than the pre-main-sequence lifetime of the A component. Therefore, the system should have reached the ZAMS close to synchronization and with the stellar spin aligned with the orbital angular momentum. Then it evolved to the present state with a likely modest angular momentum loss from the A component. Indeed, a reduced angular momentum loss rate in comparison with earlier main-sequence stars seems to be a characteristic of mid-M dwarfs (cf., e.g., Reiners et al. 2012). Alternatively, the presence of a close-in companion may have reduced the efficiency of the magnetic braking by the stellar wind, as conjectured by Lanza et al. (2010) in the case of stars accompanied by hot Jupiters (cf. also Cohen et al. 2010).

The possibility that magnetic interactions in star-planet systems lead to an enhancement of stellar activity was initially suggested by Cuntz et al. (2000) and Cuntz & Shkolnik (2002). Some evidence has been found in several star-planet systems from the modulation of chromospheric activity indexes in phase with the orbit of the planet rather than with the rotation period of the star (Shkolnik et al. 2005). For HD 179949, HD 189733, and τ Boo, an enhancement of the flux variability has been observed preceding the subplanetary point by $\sim 70^\circ$ during several observing campaigns (Shkolnik et al. 2008).

In the case of LHS 6343 A, where the companion is a low mass BD object, the available

data are photometric, so the activity modulation is observed in the photosphere. Here, a phase lead of 98° between the transits and the photometric minima is observed (see Sects. 4.3 and 4.4.4). The effect peaks once per orbit, thus suggesting a magnetic interaction because two relative maxima per orbit are expected in the case of a tidal interaction due to the symmetry of the tidal bulge. Moreover, the relative amplitude of the flux modulation due to the ellipsoidal deformation of LHS 6343 A does not exceed $\sim 5 \times 10^{-5}$ owing to the large separation of the A and C components (Pfahl et al. 2008). Even considering an orbit with an eccentricity of 0.1, the difference in the ellipsoidal light variation between the periastron and the apoastron does not exceed $\sim 3 \times 10^{-5}$ in relative flux units. Therefore, the observed flux modulation with a relative amplitude of $\sim 10^{-3}$, phased to the orbital motion of the BD, cannot be attributed to the tidal distortion of the primary star.

Similar cases of photospheric active regions rotating in phase with a close-in massive planet have been reported for τ Boo (Walker et al. 2008) and CoRoT-4 (Lanza et al. 2009a). In the former case, a photospheric active region producing a signature of the order of one millimag was observed in different seasons with the MOST satellite. The feature was sometimes dark, sometimes bright and was associated in phase with the persistent chromospheric hot spot discussed above. In the case of CoRoT-4, a preferential longitude for spot appearance was found within $\approx 40° - 50°$ from the subcompanion point. The rotation of both stars is close to synchronization as in the case of LHS 6343 A. Although τ Boo and CoRoT-4 are F-type stars, the same mechanism could be at work in all three cases.

Several models have been proposed to account for the features of the magnetic interaction between stars and close-in planets. They can be extended to the case of a close BD companion as in LHS 6343 AC. The models by McIvor et al. (2006), Preusse et al. (2006), and Lanza (2008) have focussed on interpreting of the phase lag between the planet and the maximum visibility of the chromospheric hot spot by adopting different hypotheses, e.g., a tilted potential stellar magnetic field, a finite propagation time of the magnetic perturbation along the field lines from the planet to the star, or a non-potential twisted field in the stellar corona. They are generally capable of accounting for the phase lag observed in the case of a chromospheric hot spot, but cannot account for an enhancement of the photospheric activity. As shown by the numerical MHD simulations of (Cohen et al. 2009, 2011a,b), when the planetary magnetosphere is inside or in touch with the stellar Alfven surface, a remarkable interaction between the stellar and the planetary fields occurs, and the energy released in the magnetic reconnection can be transferred down to the stellar chromosphere and photosphere. This can account for a localized enhancement of the flux, i.e., a local brightening as in large solar flares that have a white-light photospheric counterpart to their chromospheric and coronal emission. However, the appearance of dark spots associated with a close-by companion requires a different mechanism.

Lanza (2008, 2011) have conjectured that the perturbation of the coronal field and the triggering of flaring activity in the corona may increase the loss rate of magnetic helicity through coronal mass ejections (cf. also Lanza 2012) leading to a perturbation of the stellar dynamo. As reviewed by, e.g., Brandenburg et al. (2012), the operation of the dynamo in late-type stars implies a mechanism that can get rid of the magnetic helicity that is continuously pumped into the small field scales, otherwise the dynamo is rapidly quenched by magnetohydrodynamic effects. In the Sun, coronal mass ejections associated with large flares are regarded as a viable mechanism for accomplishing this goal, therefore an enhancement of flaring activity in stars with close-in companions may help the operation of the dynamo. Since the perturbation moves in phase with the planet, the associated loss of magnetic helicity is non-axisymmetric and may

lead to a modulation of the α effect of the stellar dynamo in phase with the motion of the companion (see Lanza 2008, 2011, for details). In systems that are close to synchronization, the modulation can be particularly effective thanks to the slow relative motion of the companion in the reference frame rotating with the star that increases the duration of the interaction between a stellar coronal structure and the magnetic field of the orbiting body. The phase lag between the starspots and the companion may be explained by adopting a twisted magnetic field interconnecting the spots with the orbiting BD as discussed in Lanza (2008).

An alternative explanation taking into account the destabilizing effects of the tidal perturbation on the magnetic flux tubes inside the red dwarf star cannot of course be excluded. In this scenario, the persistent active longitude would correspond to the periastron passage of the BD companion with the phase lag of $\sim 98^\circ$ being the angular distance of that point from the mid-transit. Recent works suggesting a possible gravitational perturbation of the planets on the solar dynamo may give support to this conjecture (cf., e.g., Abreu et al. 2012, and references therein).

4.4.6 Conclusions

Considering 508 days of Kepler photometry of the visual system LHS 6343, we have computed a new best fit to the mean photometric transit profile of the C brown dwarf component across the disc of the A component. We essentially confirm the transit parameters found by Johnson et al. (2011) and reduce their uncertainties.

A maximum entropy spot model was applied to the Kepler light curve of LHS 6343 to derive maps of the longitudinal distribution of the active regions on the A component, assumed to be responsible for the out-of-transit modulation of the flux. While including faculae is not found to be critical for obtaining an acceptable fit to the light modulation, an optimal fit of the light curve is found for a facular-to-spotted area ratio around $Q = 8.0$.

Our maps show several active regions with a slower rotation rate ($P_{\rm rot} = 13.14 \pm 0.02$ days) than the BD orbital period ($P_{\rm orb} = 12.71$ days), implying that the AC system is quasi-synchronized. Owing to the limited signal-to-noise ratio of the data and the fast evolution of the active regions that have lifetimes of 1520 days, it is not possible to detect any differential rotation signature. On the other hand, the starspot covering factor is observed to be systematically enhanced when the spots cross a longitude leading the substellar point by $\sim 100^\circ$. This effect is also detected in the photometric time series as a modulation with the orbital period of the BD showing minima ~ 3.5 days before each transit. That this active longitude persists for more than ~ 500 days provides evidence that the BD companion does affect the photospheric activity of its host somewhat. We conjecture that a magnetic interaction between the coronal field of the M dwarf and the BD may produce a modulation of the stellar dynamo leading to an increase in activity modulated in phase with the orbital motion (see Sect. 4.4.5).

A monitoring of the system through measurements of the modulation of the chromospheric lines (e.g., Hα or Ca II H&K) and coronal X-ray emission would be very helpful, because a detection of a hot spot in the upper stellar atmosphere with the same phase lag as the detected photospheric active longitude would indicate interactions through magnetic field reconnection, thus supporting the conjectured mechanism.

4.5 Doppler-beaming

4.5.1 Introduction

In addition to the detection of Earth-like exoplanets, the highly accurate photometry provided by the Kepler mission has allowed the community to discover a number of eclipsing binaries and study stellar variability at very low amplitudes. Several detections of flux modulations in binary stars have been associated with relativistic beaming caused by the radial motion of their components (van Kerkwijk et al. 2010; Bloemen et al. 2011). The effect is proportional to the orbital velocity of the component stars and allows one to estimate their radial velocity amplitudes in selected compact binaries. This photometric method to measure radial velocities was first introduced by Shakura & Postnov (1987) and applied by Maxted et al. (2000). In the context of a possible application to CoRoT and Kepler light curves, it was first discussed by Loeb & Gaudi (2003) and Zucker et al. (2007).

In this section, we present a different interpretation than in Sect. 4.2 for the out-of-eclipse light modulation in the Kepler photometry of LHS 6343 A in terms of a Doppler-beaming effect. The Doppler-beaming modelling that we present here shows that the main modulation signal can instead be explained by this effect, and that the radial velocity amplitude as derived from the light curve is compatible with the spectroscopically determined value (Johnson et al. 2011). Doppler-beaming has been previously detected in Kepler light curves of KOI-74 and KOI-81 by van Kerkwijk et al. (2010), KPD 1946+4340 by Bloemen et al. (2011), KIC 10657664 by Carter et al. (2011) and KOI 1224 by Breton et al. (2012). A proper modelling of the effects observed in the light curves of these objects is important because it may give us the opportunity to derive radial velocities from a number of binaries observed by Kepler and to remove the Doppler-beaming modulation to investigate other causes of light-curve variation.

4.5.2 Models of the Doppler-beaming and ellipticity effect

A first-order approximation in $v_{\rm R}/c$ for the flux variation at frequency ν due to Doppler-beaming is (cf. Rybicki & Lightman 1979; Zucker et al. 2007)

$$\left.\frac{\Delta F}{F}\right|_{\rm DB} = -(3-\alpha)\frac{v_{\rm R}(t)}{c}, \tag{4.7}$$

where $v_{\rm R}(t)$ is the radial velocity of the star at time t, c the speed of light, and the spectral index $\alpha \equiv d\ln F_\nu / d\ln\nu$ depends on the spectrum of the star F_ν. Doppler-beaming produces an increase of the bolometric flux for a source that is approaching the observer, that is, when $v_{\rm R} < 0$. In the case of LHS 6343 A, the Doppler shift of the radiation towards the blue when the star is approaching the observer causes the flux in the Kepler passband to increase because we observe photons with a longer wavelength in the rest frame of the source, which corresponds to a higher flux, given the low effective temperature of the star ($T_{\rm eff} \sim 3000$ K). In other words, $\alpha < 0$ for a star as cool as LHS 6343 A.

We computed a mean spectral index by integrating BT-Settl model spectra (Allard et al. 2011) over the photon-weighted Kepler passband,

$$\langle\alpha\rangle = \frac{\int h_\nu \nu F_\nu \alpha d\nu}{\int h_\nu \nu F_\nu d\nu}, \tag{4.8}$$

where h_ν is the response function of the Kepler passband. For the stellar model F_ν we assumed solar metallicity, $T_{\rm eff} = 3130$ K, $\log g = 4.851$ (cm s^{-2}) and an α-element enhancement $[\alpha/{\rm H}] = 0$. The resulting mean spectral index to be used in Eq. (4.7) is $\langle\alpha\rangle = -3.14 \pm 0.08$. The uncertainty comes from the dependence of the spectral index on the model spectrum and the uncertainties of the respective parameters and is evaluated by calculating the integral in Eq. (4.8) by varying the temperature in the range $T_{\rm eff} = 3130 \pm 20$ K and the surface gravity in $\log g = 4.851 \pm 0.008$ (cm s^{-2}) (Johnson et al. 2011). If we compute the spectral index considering the black-body approximation (Zucker et al. 2007), the result is $\langle\alpha_{\rm BB}\rangle \simeq -4.22$ for the Kepler passband. The difference is due to the many absorption features in the spectrum of this type of stars that fall within the Kepler passband.

Assuming a reference frame with the origin at the barycentre of the binary system and the $z-$ axis pointing away from the observer, we can express the radial velocity of the primary component as a trigonometric series in the mean anomaly M by applying the elliptic expansions reported in Murray & Dermott (1999):

$$\begin{aligned} v_{\rm R} &= A\left[\left(1-\frac{9e^2}{8}\right)\cos M + \left(e-\frac{4e^3}{3}\right)\cos 2M \right. \\ &\quad \left. + \frac{9e^2}{8}\cos 3M + \frac{4e^3}{3}\cos 4M\right] \\ &+ B\left[\left(1-\frac{7e^2}{8}\right)\sin M + \left(e-\frac{7e^3}{6}\right)\sin 2M \right. \\ &\quad \left. + \frac{9e^2}{8}\sin 3M + \frac{4e^3}{3}\sin 4M\right] + O(e^4), \end{aligned} \tag{4.9}$$

where $A \equiv K\cos\omega$ and $B \equiv -K\sin\omega$, with K the radial velocity semi-amplitude, ω the argument of periastron, and e the eccentricity of the orbit of the primary component (see, e.g., Wright & Howard 2009). At the epoch of mid-eclipse of the primary by the brown dwarf, the true anomaly is (cf., e.g., Winn 2011): $f_{\rm e} = \frac{\pi}{2} - \omega$. From the true anomaly at mid-eclipse, we find the eccentric anomaly and the mean anomaly:

$$\tan\frac{E_{\rm e}}{2} = \sqrt{\frac{1-e}{1+e}}\tan\frac{f_{\rm e}}{2}, \tag{4.10}$$

and

$$M_{\rm e} = E_{\rm e} - e\sin E_{\rm e}. \tag{4.11}$$

If we measure the time since the mid-eclipse epoch T_0, the mean anomaly appearing in Eq. (4.9) is

$$M = n(t - T_0) + M_{\rm e}, \tag{4.12}$$

because M is zero at the epoch of periastron.

In addition to the Doppler-beaming effect, the ellipsoidal effect can be important in the case of LHS 6343 A, while the reflection effect is negligible because of a relative separation of ~ 45.3 stellar radii in the system and the low luminosity of the C secondary component. Morris (1985) provided formulae to evaluate the effect. In our case, only the coefficient proportional to $\cos 2\phi$, where $\phi = M - M_{\rm e}$ is the orbital angular phase, is relevant because the other terms are at least one order of magnitude smaller due to the large relative separation. In terms of the mean

anomaly, the relative flux modulation due to the ellipsoidal effect is

$$\begin{aligned}\left.\frac{\Delta F}{F}\right|_{\rm E} &= C_1(2)\cos(2M-2M_{\rm e}) = \\ &= [C_1(2)\sin(2M_{\rm e})]\sin 2M + [C_1(2)\cos(2M_{\rm e})]\cos 2M,\end{aligned} \tag{4.13}$$

where

$$C_1(2) = -Z_1(2)\left(\frac{m}{M_*}\right)\left(\frac{R}{a}\right)^3 \sin^2 i, \tag{4.14}$$

m is the mass of the brown dwarf secondary, M_* the mass of the distorted primary star, R its radius, and i the inclination of the orbital plane, which are fixed to those derived by Johnson et al. (2011). Finally, $Z_1(2)$ is a coefficient given by

$$Z_1(2) \simeq \frac{45+3u}{20(3-u)}\left(\tau_{\rm g}+1\right), \tag{4.15}$$

where $u = 1.2$ is the linear limb-darkening coefficient in the Kepler passband, $\tau_{\rm g} \sim 0.32$ the gravity-darkening coefficient estimated for the primary LHS 6343 A, and we neglected the effects related to the precession constant and the (small) eccentricity of the orbit (cf., Morris 1985). Note that at mid-eclipse, $M = M_{\rm e}$, and the ellipsoidal variation is at a minimum, while for $M = M_{\rm e} \pm \pi/2$, that is, in quadrature, it reaches a maximum.

In conclusion, the total relative light variation due to both Doppler-beaming and ellipsoidal effect is

$$\frac{\Delta F}{F} = \left.\frac{\Delta F}{F}\right|_{\rm DB} + \left.\frac{\Delta F}{F}\right|_{\rm E}. \tag{4.16}$$

4.5.3 Results

To fit the proposed model to the data, we applied a Monte Carlo Markov chain (MCMC) approach that allowed us to find, in addition to the best-fit solution, the posterior distribution of the parameters that provides us with their uncertainties and correlations. We followed the method outlined in Appendix A of Sajina et al. (2006) (see also Press et al. 2002; Ford 2006). If $\vec{a} \equiv \{e, \omega, K\}$ is the vector of the parameter values, and $\vec{d}$ the vector of the data points, according to the Bayes theorem we have

$$p(\vec{a}|\vec{d}) \propto p(\vec{d}|\vec{a})p(\vec{a}), \tag{4.17}$$

where $p(\vec{a}|\vec{d})$ is the a posteriori probability distribution of the parameters, $p(\vec{d}|\vec{a})$ the likelihood of the data for the given model, and $p(\vec{a})$ the prior. In our case, the parameters have been derived by Johnson et al. (2011) by fitting the radial velocity and transit light-curves. Therefore, we can use their values and uncertainties to define the prior as

$$\begin{aligned}p(\vec{a}) &= \exp\left\{-\left[\frac{(e-0.056)}{0.032}\right]^2 - \left[\frac{(\omega+23)}{56}\right]^2\right. \\ &\quad \left. - \left[\frac{(K-9.6)}{0.3}\right]^2\right\},\end{aligned} \tag{4.18}$$

where ω is measured in degrees and K in km s^{-1}. The likelihood of the data for given model parameters is

$$p(\vec{d}|\vec{a}) \propto \exp(-\chi^2_{\rm r}), \tag{4.19}$$

where $\chi^2_{\rm r}$ is the reduced chi-square of the fit to the data obtained with our model. The standard deviation of the data used to compute $\chi^2_{\rm r}$ is the mean of the standard deviations evaluated in 40 equal bins of the mean anomaly and is $\sigma_{\rm m} = 2.057 \times 10^{-4}$ in relative flux units. Note that in addition to estimating the standard deviation of the data, we always fitted the unbinned time-series shown in Fig. 4.1. Substituting Eqs. (4.19) and (4.18) into Eq. (4.17), we obtain the posterior probability distribution of the parameters. We sampled from this distribution by means of the Metropolis-Hasting algorithm (cf., e.g., Press et al. 2002), thus avoiding the complicated problem of normalizing $p(\vec{a}|\vec{d})$ over a multi-dimensional parameter space. A Monte Carlo Markov chain is built by performing a conditioned random walk within the parameter space. Specifically, starting from a given point $\vec{a}_i$, a proposal is made to move to a successive point $\vec{a}_{i+1}$ whose coordinates are found by incrementing those of the initial point by random deviates taken from a multi-dimensional Gaussian distribution with standard deviations σ_j, where $j = 1, 2$ or 3 indicate the parameter. With this choice for the proposed increments of the parameters, the step is accepted if $p(\vec{a}_{i+1}|\vec{d})/p(\vec{a}_i|\vec{d}) > u$, where u is a random number between 0 and 1 drawn from a uniform distribution, otherwise we return to the previous point, that is, $\vec{a}_{i+1} = \vec{a}_i$.

We computed a chain of 200 000 points adjusting σ_j to have an average acceptance probability of 23 percent that guarantees a proper sampling and minimises the internal correlation of the chain itself. The mixing and convergence of the chain to the posterior parameter distribution were tested with the method of Gelman and Rubin as implemented by Verde et al. (2003). First we discarded the first 25 000 points that correspond to the initial phase during which the Metropolis-Hasting algorithm converges on the stationary final distribution (the so-called burn-in phase), then we cut the remaining chain into four subchains that were used to compute the test parameter R. It must be lower than 1.1 when the chain has converged on the distribution to be sampled. In our case we found $(R - 1) \leq 4.4 \times 10^{-4}$ for all the three parameters, which indicates convergence and good sampling of the parameter space.

The best-fit model corresponding to the minimum $\chi^2_{\rm r} = 1.0033$ has the parameters $e = 0.0448$, $\omega = -90.^\circ704$, and $K = 9.583$ km s^{-1}. For comparison, the reduced chi-square corresponding to the best-fit parameters of Johnson et al. (2011) is 1.0098.

Our best fit to the data is plotted in Fig. 4.11 where the points are binned for clarity into 40 equal intervals of mean anomaly M. The semi-amplitude of the errorbar of each binned point is the standard error of the flux in the given bin. The posterior distributions of the parameters are plotted in Fig. 4.12. The intervals enclosing between 15.9 and 84.1 percents of the distributions are $0.035 \leq e \leq 0.097$; $-77.^\circ14 \leq \omega \leq 33.^\circ0$; and $9.290 \leq K \leq 9.897$ km s^{-1}. The correlations among the parameters are not particularly significant, as shown by the two-dimensional posterior distributions plotted in Fig. 4.13. The best-fit parameters of Johnson et al. (2011) fall within the 68.2 percent confidence regions of our two-dimensional distributions.

The good agreement between the data and the model demonstrates that most of the light modulation of LHS 6343 A can be accounted for by a Doppler-beaming effect with a fitted semi-amplitude of 1.963×10^{-4} in relative flux units. The contribution of the ellipsoidal effect is very small, with a relative semi-amplitude of only 3.05×10^{-6} as derived by Eqs. (4.13), (4.14), and (4.15).

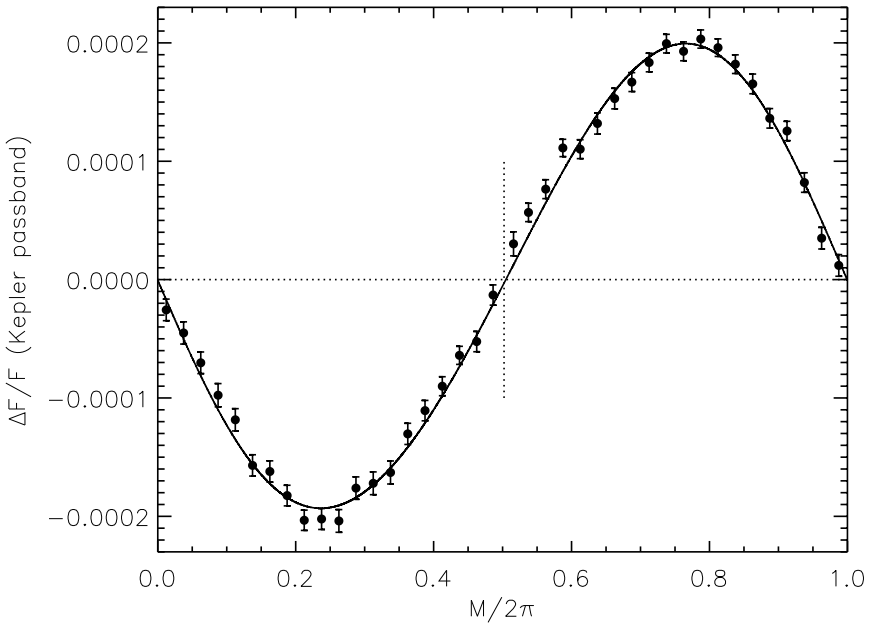

Figure 4.11: Relative flux variation of LHS 6343 A vs. the mean anomaly M of the orbit, binned in 40 equal intervals. The Doppler-beaming plus ellipsoidal effect model for our best-fitting parameters is plotted with a solid line (cf. the text). The value of $M/2\pi$ corresponding to mid-eclipse is marked with a dotted vertical segment, while a horizontal dotted line is plotted to indicate the zero-flux level.

The distribution of the residuals to our best fit is plotted in Fig. 4.14. It can be fitted by a Gaussian of standard deviation 1.929×10^{-4} in relative flux units, although there is an excess of residuals larger than $\sim 4 \times 10^{-4}$ in absolute value. The amplitude of the Doppler-beaming plus ellipsoidal modulation is comparable with the standard deviation of the residuals. This accounts for the quite extended confidence intervals found in the parameter distributions. In other words, the parameters derived by fitting the Doppler-beaming are of lower accuracy than those derived by fitting the spectroscopic orbit because the radial velocity measurements are more accurate. The a posteriori distributions of the fitted parameters in Fig. 4.12 are dominated by their priors, confirming that Doppler-beaming data do not add much information on the model parameters. As a consequence, the best-fit value of ω deviates by more than one standard deviation from the mean of its posterior distribution.

Finally, we plot in Fig. 4.15 the Lomb-Scargle periodogram of the residuals computed with the algorithm of Press & Rybicki (1989). We found a significant periodicity of 42.49 ± 3.22 days with a false-alarm probability (FAP) of 4.8×10^{-4} as derived by analysing 10^5 random permutations of the flux values with the same time-sampling. The second peak in the periodogram is not a harmonic of the main peak and has an FAP of 20.4 percent, thus it is not considered to be reliable. The vertical dotted lines indicate the frequencies corresponding to the orbital period and its harmonics. Note that the signal at these frequencies has been almost completely removed by subtracting our model.

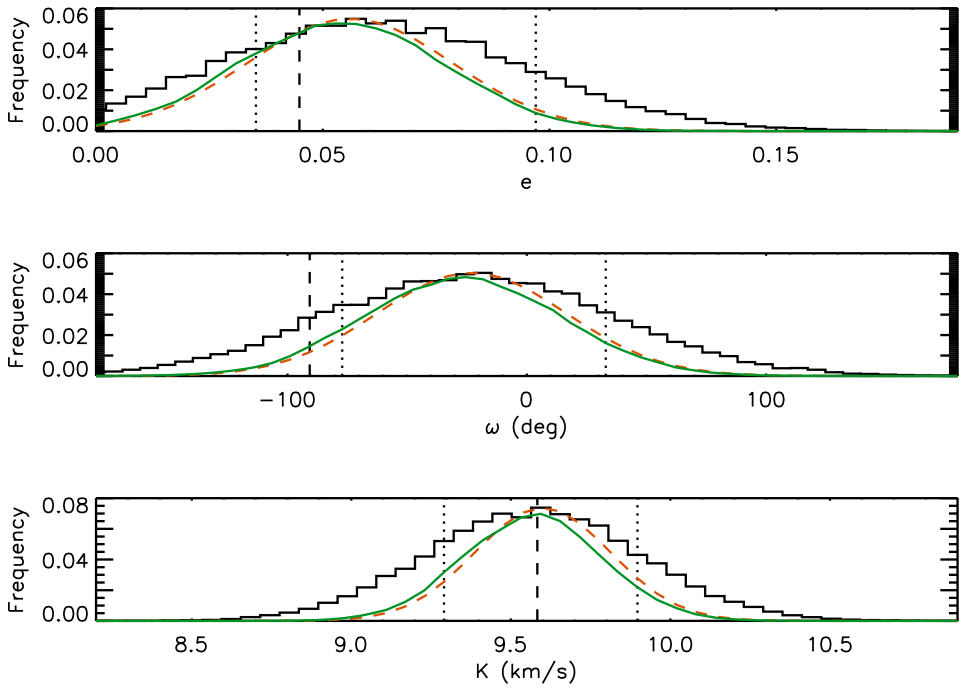

Figure 4.12: Top panel: The histogram shows the a posteriori distribution of eccentricity e as obtained with our MCMC approach. The vertical dashed line indicates the value corresponding to the best fit plotted in Fig. 4.11, while the two vertical dotted lines enclose an interval between 15.9 and 84.1 percents of the distribution. The solid green line is the mean likelihood as computed by means of Eq. (A4) of Sajina et al. (2006), while the orange dashed line is the prior assumed for the parameter. These two distributions have been normalized to the maximum of the a posteriori distribution of the eccentricity. Note that the two distributions are very similar, indicating that fitting Doppler-beaming does not add much constraint to the eccentricity. Middle panel: as upper panel, but for the argument of periastron ω. Lower panel: as upper panel, but for the semi-amplitude of the radial velocity modulation K.

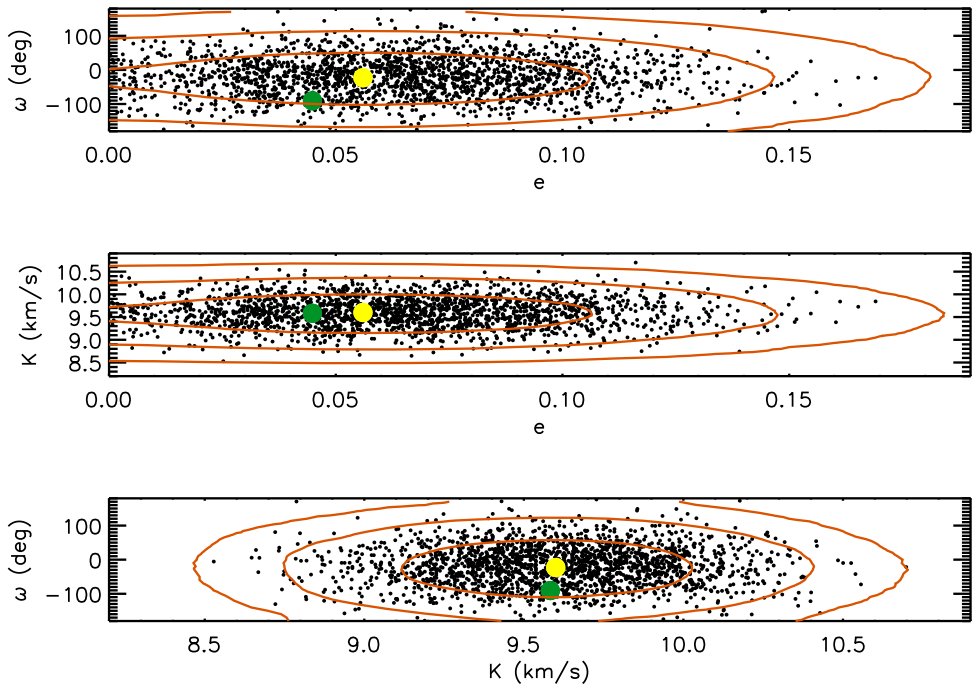

Figure 4.13: Upper panel: two-dimensional a posteriori distribution of the argument of periastron ω vs. the eccentricity e as obtained with the MCMC method. The yellow filled circle corresponds to the best-fit orbital solution of Johnson et al. (2011), while the green circle indicates our best-fit values of the parameters. The orange level lines enclose 68.2, 95, and 99.7 percents of the distribution, respectively. Individual points of the MCMC have been plotted after applying a thinning factor of 100 to the chain for clarity. Middle panel: as upper panel, but for the radial velocity semi-amplitude K and the eccentricity e. Lower panel: as upper panel, but for the argument of periastron ω and the radial velocity semi-amplitude K.

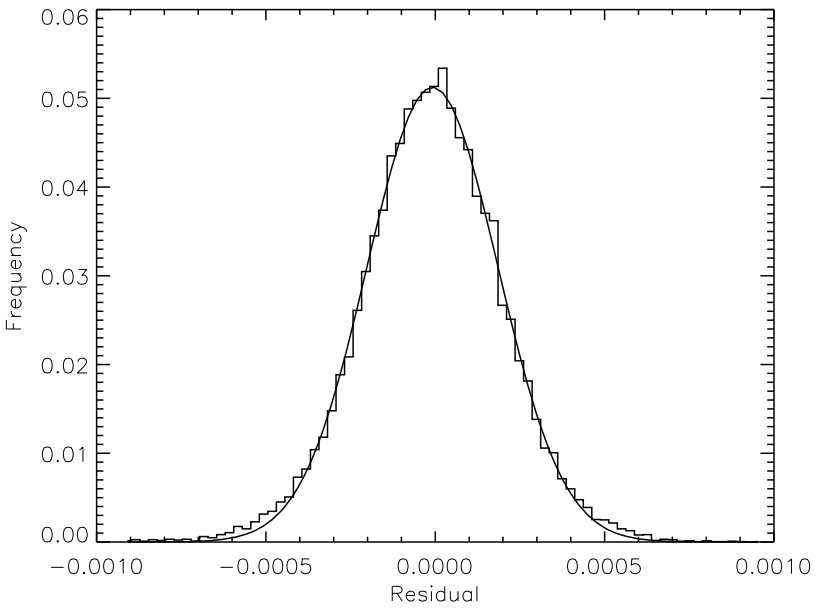

Figure 4.14: Distribution of the residuals resulting from the Doppler-beaming plus ellipsoidal effect model of the photometric data of LHS 6343 A The solid line is a Gaussian fit to the distribution.

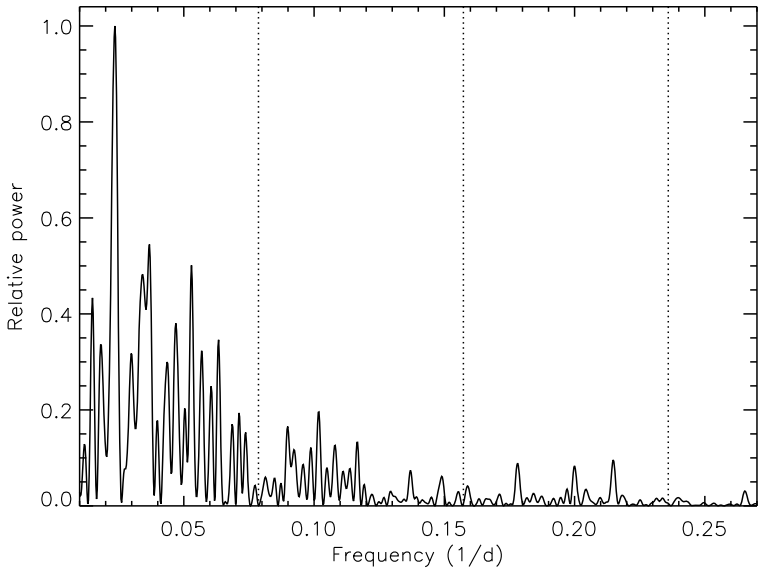

Figure 4.15: Lomb-Scargle periodogram of the residuals resulting from the Doppler-beaming plus ellipsoidal effect model of the photometric data of LHS 6343 A. Dotted lines correspond to the frequency of the orbital period and its harmonics.

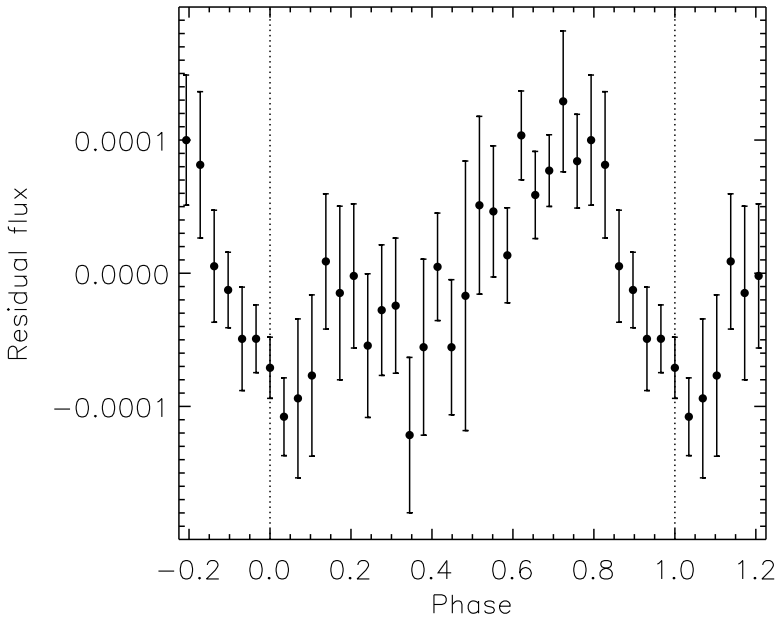

Figure 4.16: Residuals of the Doppler-beaming plus ellipsoidal effect model of LHS 6343 A folded at a periodicity of 42.49 days.

The residuals folded at the periodicity of 42.49 days are displayed in Fig. 4.16, showing the mean residual flux vs. phase in 40 equal bins. A modulation is clearly apparent, suggesting that the primary star's rotation combined with the presence of persistent starspots might be producing this signal. The possibility that the modulation is due to pulsations seems unlikely given the long period, but cannot be completely ruled out (see, e.g., Toma 1972; Palla & Baraffe 2005, and references therein). Given the non-sinusoidal shape of the modulation, we have also considered a phasing of the residuals with half the main period (i.e., 21.102 days), but the dispersion of the points around the mean modulation is remarkably higher.

The non-synchronous rotation of the primary and the eccentricity of the orbit are consistent with time scales of tidal synchronisation and circularisation at least of the order of the main-sequence lifetime of the system as discussed in Sect. 4.4.5.

4.5.4 Conclusions

We have demonstrated that the amplitude and lag of the flux modulation can be accounted for by a Doppler-beaming model instead of being caused by rotational modulation oh photospheric active regions (Sect. 4.2, Herrero et al. 2013). The Doppler-beaming model agrees with the orbital parameters derived by Johnson et al. (2011) by fitting the transits and the radial velocity observations. The ellipsoidal effect was found to be virtually negligible and the reflection effect was not considered given the distance and the luminosity ratio of the two components in the system.

The periodogram of the residuals reveals a significant periodicity at $\sim 42.5 \pm 3.2$ days (FAP of 4.8×10^{-4}), probably related to the rotation period of LHS 6343 A. A more accurate data-

detrending procedure, as is expected to be applied to the final Kepler data release, might be useful to confirm this point and extract more results from the residual analysis.

Chapter 5

Simulations of the photosphere of active stars

Stellar activity patterns are responsible for jitter effects that are observed at different timescales and amplitudes in the measurements obtained from photometric and spectroscopic time series observations. These effects are usually considered just noise, and the lack of a characterization and correction strategy represents one of the main limitations for exoplanet sciences. Accurate simulations of the stellar photosphere based on the most recent available models for main sequence stars can provide synthetic time series data. These may help to investigate the relationship between activity jitters and stellar parameters when considering different active region patterns. Moreover, jitters can be analysed at different wavelength scales (defined by the passbands of given instruments or space missions) in order to design strategies to remove or minimize them. In this Section we present a model for a spotted rotating photosphere built from the integration of the spectral contribution of a fine grid of surface elements, including all significant effects affecting the flux intensities and the wavelength of spectral features. The methodology is implemented in the program `StarSim`, and several cases of synthetic data series for Sun-like stars are presented to illustrate its capabilities. The resulting synthetic time series data generated with this simulator are used in order to characterize the effects of activity jitter in extrasolar planet measurements from photometric and spectroscopic observations and evaluate their astrometric effects. Also, we propose several strategies to correct exoplanet transit observations for the effects of spots when simultaneous observations are available in the visible and near-infrared bands. A particular application for the characterization and modelling of the spectral signature of active regions is considered, showing that the chromatic effects of faculae are dominant for low temperature contrasts of spots. Synthetic multi-band photometry and radial velocity time series are obtained for HD 189733 adopting the known system parameters and stellar surface map. The effects of spot crossing events and non-occulted spots are studied for a set of simulated transits. The results show that the effects of occulted spots are still significant in the mid-infrared, while non-occulted spots can introduce variations in R_p/R_* measurements with a signature and

amplitude which are very similar to the signal of the atmosphere of a transiting planet dominated by dust. Radial velocity jitter limits the measurement of the semiamplitude K to an error of ~ 1.9 m s^{-1} when only ~ 30 measurements are obtained. The work described in this Chapter is also presented in Herrero et al. (2014b) and Herrero et al. (in prep.).

5.1 Introduction

Stellar activity in late-type main sequence stars induces photometric modulations and apparent radial velocity variations that may hamper the detection of Earth-like planets (Lagrange et al. 2010; Meunier et al. 2010a) and the measurement of their transit parameters (Barros et al. 2013), mass and atmospheric properties. A tacit assumption when modelling light and radial velocity curves is that any temporal variation in the calibrated signal from the (unresolved) host star/exoplanet can be attributed to changes in the (small) signal from the exoplanet, and is not a result of variation in either the stellar signal or instrument response.

Late-type stars (i.e., late-F, G, K and M spectral types) are known to be variable to some extent. The effect of stellar activity in the photosphere is seen in the form of spots and faculae, whose relationship with stellar parameters such as mass and age is still not well understood. The signal of these activity patterns is modulated by the stellar rotation period, usually producing a clear peak in the flux power spectrum of the star. The evolution of active regions, characterized by their lifetime and typical size or filling factor, has also been the subject of study of several recent works involving different methods for modelling data from spotted stars (Lanza et al. 2003; Kipping 2012). Also other phenomena exist which may induce periodic signals in photometric and radial velocity data. Pulsations, granulation, long term evolution of active regions and magnetic cycles may limit the capabilities of some planet searches. Such effects need to be subtracted or accounted for the design of searching strategies (Dumusque et al. 2011b,a; Moulds et al. 2013).

Significant improvement in our knowledge of activity effects on starlight will be crucial to make the most of present and future planet search instruments (HARPS-N, CARMENES, ESPRESSO) and space missions. The most up-to-date and comprehensive information on stellar variability comes from the studies with Kepler (stability of 200/40 ppm in a 6.5 hr period on a 11/7 mag (V) star) that are based on the observation and analysis of 150,000 stars taken from the first Kepler data release. Ciardi et al. (2011) have found that 80% of M dwarfs have light dispersion less than 500 ppm over a period of 12 hours, while G dwarfs are the most stable group down to 40 ppm. Kepler operates in the visible (430 to 890 nm) where stellar photometric variability is a factor of 2 or more higher than in the near and thermal IR (the "sweet spot" for the characterization of exoplanet atmospheres) due to increasing contrast between spots and the stellar photosphere with decreasing wavelength. Timescales for stellar activity are very different from those associated with single transit observations (a few hours) and so removal of this spectral variability is possible. As a case in point, photometric modulations in the host of CoRoT-7 b are of the order of 2% (Lanza et al. 2010) and yet a transit with a depth of 0.03% was identified (Léger et al. 2009). Analyses of observations from Kepler have yielded comparable results.

The effects of stellar activity in near IR observations are very different in the case of primary (transit) and occultation observations. Alterations in the spot distribution across the stellar

surface can modify the transit depth, because of the changing ratio of photosphere and spotted areas on the face of the star. This can give rise to spurious planetary radius variations when multiple transit observations are considered. Correction of this effect requires the use of very quiet stars or precise modelling of the stellar surface using external constraints. The situation is much simpler for occultations, where the planetary emission follows directly from the depth measurement. In this case, only activity-induced variations on the timescale of the duration of the occultation need to be corrected to ensure that the proper stellar flux baseline is used. In the particular case of exoplanet characterization space missions, photometric monitoring in the visible will aid in the correction of activity effects in the near and thermal IR, where the planet signal is higher.

In this work we present a methodology to simulate spectra from the spotted photosphere of a rotating star. We use atmosphere models for low mass stars to generate synthetic spectra for the stellar surface, spots and faculae. The spectrum of the entire visible face of the star is obtained by summing the contribution of a grid of small surface elements and by considering their individual signal. Using such simulator, time series spectra can be obtained covering the rotation period of the star or longer. By convolving these with the known passband for a specific instrument, they can be used to study the chromatic effects of spots and faculae on photometric modulation and radial velocity jitter. The results are being used to investigate methodologies to correct or mitigate the effects of activity on spectrophotometric time series data. Our results will allow us to investigate the effects of activity patterns on the measurable stellar flux and hence define the best strategies to optimize exoplanet searches and measurement experiments.

5.2 StarSim: synthetic data of active stars

5.2.1 The models

Phoenix synthetic spectra

Among the most recent model atmosphere grids, we use spectra from the BT-Settl database (Allard et al. 2013) generated with the Phoenix code in order to reproduce the spectral signal for the different elements in the photosphere: quiet photosphere, spots and faculae. These models include revised solar oxygen abundances (Caffau et al. 2011) and cloud model, which allow to reproduce the photometric and spectroscopic properties also in very low mass stars. In our simulations, LTE models are used both for the quiet photosphere and the active regions (spots and faculae). Non-LTE models from Fontenla et al. (2009) are to be considered in order to model faculae in future versions of the code, as they have shown to better reproduce the spectral irradiance of active features over all the magnetic cycle in the case of the Sun (Fontenla et al. 2011). Synthetic spectra from BT-Settl models are available for 2600 K $< T_{\rm eff} <$ 70000 K, $+3.5 \leq \log g \leq +5.0$ and several values of alpha enhancement and metallicity. An example for a solar-type star is shown in Fig. 5.1.

These models include the effects of convection as described by the mixing length theory of turbulent transport (Vitense 1953) characterized by the mixing length parameter α as discussed by Ludwig et al. (1999) using 3D radiative models. Convection has a significant impact on line profiles, which are modified when active regions cross the stellar surface, and hence it is responsible for a significant part of the jitter observed in radial velocity measurements (Meunier et al. 2010a).

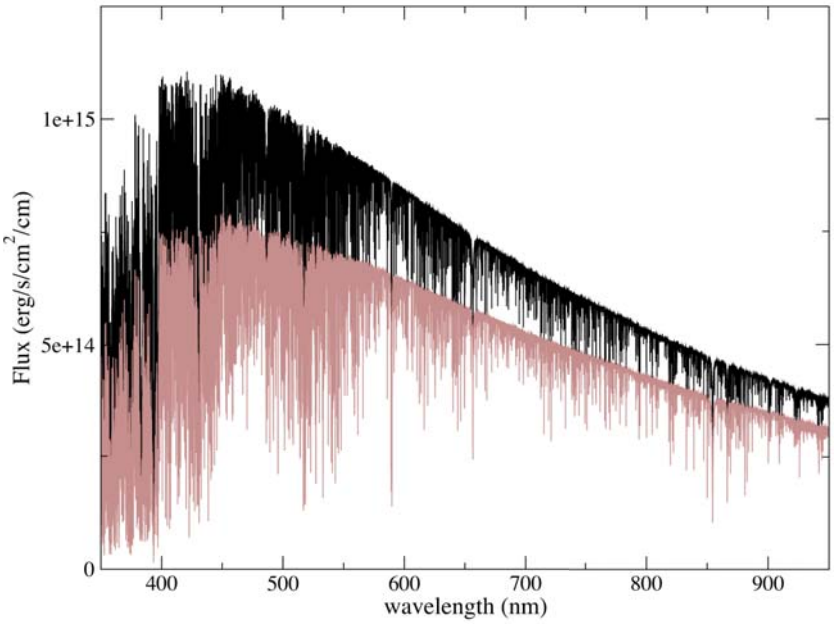

Figure 5.1: Solar-like star spectrum for $T_{\rm eff}$ =5770 K and $\log g$ = 4.5 (black) generated with BT-Settl models, compared to a spectrum of a spot for the same star, assuming $\Delta T_{\rm spot}$ = 350 K (brown).

A BT-Settl database of spectra is currently available for resolutions defined by a sampling $\geq$0.05Å, which is not enough to study line profiles and obtain accurate radial velocity measurements. In order to perform simulations for radial velocity jitter studies and line profiles, high resolution spectra computed by Husser et al. (2013) are used instead. The library is also based on the Phoenix code, and the synthetic spectra cover the wavelength range from 500 Å to 5.5 μm with resolutions of $R = 500,000$ in the optical and near IR, $R = 100,000$ in the IR and $\Delta\lambda = 0.1\AA$ in the UV. The parameter space covers 2300 K $\leq T_{\rm eff} \leq$ 12000 K, 0.0 $\leq \log g \leq$ +6.0, -4.0 $\leq$ [Fe/H] $\leq$ +1.0, and 0.2 $\leq [\alpha/{\rm Fe}] \leq$ +1.2.

Solar spectra

In addition to synthetic spectra from model atmospheres, real data from high resolution spectra of the Sun are used in order to test the results coming from the models. The spectra are obtained from a photospheric region and a spot with the 1-meter Fourier Transform Spectrometer of the National Solar Observatory located at Kitt Peak (x. Dumusque, priv. comm.), and have a resolution of $R \sim 10^6$ covering from 390 nm to 665 nm. Figure 5.2 shows a comparison between the solar observed spectra and synthetic Phoenix spectra from Husser et al. (2013) for a Sun-like star, both for the quiet Sun and for a spot region. The temperature of the photospheric region was fixed to $T_{\rm eff}$ =5770 K for the synthetic spectrum, which correctly agrees with most of the features in the observed data. In the case of the spot data, $T_{\rm eff}$ was varied from 4500 to 5500 K, finding the best correlation for 5460 K (temperature contrast $\Delta T_{\rm spot}$=310 K) when considering all the available wavelength range, which is consistent with the measurements made by Eker

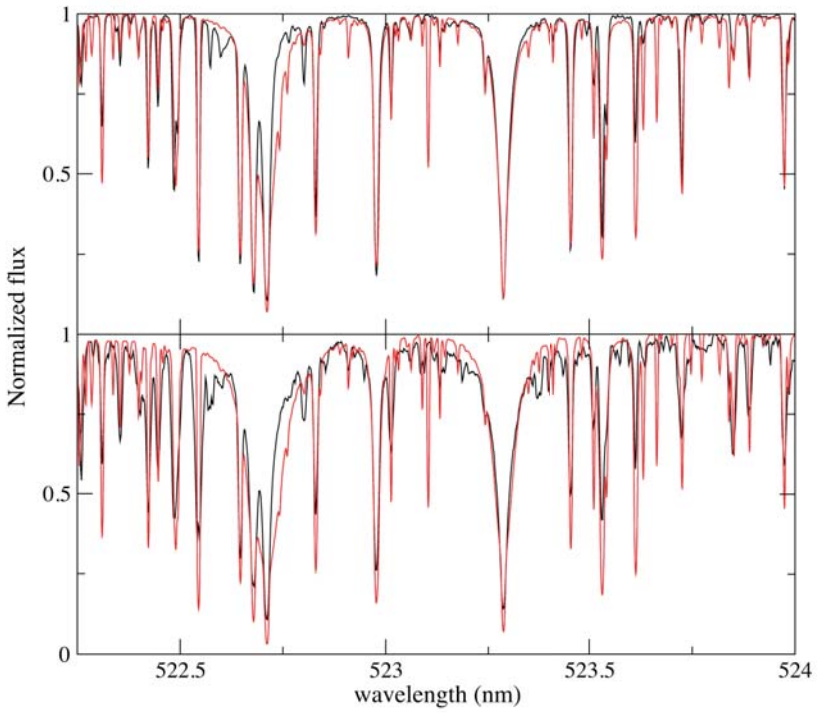

Figure 5.2: Top: Comparison between an observed high resolution spectrum for the solar photosphere from Fourier Transform Spectrometer (black) and Phoenix synthetic spectrum (red) from Husser et al. (2013) using $T_{\rm eff}$ =5770 K, $\log g = 4.5$ and solar abundances. Bottom: the same for the observed spectrum of a spot region (black), now compared to a Phoenix synthetic spectrum of $T_{\rm eff}$ =5460 K.

et al. (2003).

5.2.2 Data simulation

Model and stellar parameters

The stellar photosphere is divided into a grid of surface elements whose physical and geometric properties are described individually. The space resolution of the grid is an input parameter of the program, and $1^\circ \times 1^\circ$ size elements have been tested to be adequate to correctly reproduce most active region configurations and transiting planet effects up to $\sim 10^{-6}$ photometric precision. A complete list of the input parameters of the program `StarSim`, together with the typical considered ranges, is presented in Table 5.1.

The total number of active regions, as well as their surface and time distributions, are generated by the program following different statistics defined in the input parameters. The number of regions at a given time depends on a flat distribution between a specified minimum, $Nr_{\rm min}$, and a maximum, $Nr_{\rm max}$. The sizes of the spots follow a gaussian distribution, defined by a mean area $\bar{A}_{\rm Sn}$ and a standard deviation $\sigma(A_{\rm Sn})$, in units of the total stellar surface. Therefore,

the mean filling factor over time in the whole stellar surface is determined by the mean number of spots, $\bar{Nr} = (Nr_{\max} + Nr_{\min})/2$ and their mean area by:

$$\bar{FF} = \bar{Nr} \cdot \bar{A}_{\rm Sn} \tag{5.1}$$

Notice that this filling factor only varies due to active region evolution and is different from the projected filling factor, which also accounts for the geometric projection of spots due to stellar inclination and rotation modulation.

Each active region n is modelled as a circular spot of radius $R_{\rm Sn}$ surrounded by a facula region with a coronal shape, having an external radius $R_{\rm Fn} = \sqrt{Q+1} \cdot R_{\rm Sn}$ (see Fig.5.3), where Q is the ratio between the area of the surrounding faculae and the area of the spot, and it is assumed to be the same for all the active regions in the star. Our model does not distinguish between umbra and penumbra, but adopts a mean spot contrast at an intermediate temperature, as adopted by previous approaches (Chapman 1987; Unruh et al. 1999). The model of circular spots surrounded by a corona of faculae has also been adopted previously for spot modelling techniques and successfully reproduced spot maps for the Sun (Lanza et al. 2003) and for several low mass stars with high precision light curves. Solar observations have shown the presence of systematic changes in the contrast and size of faculae (Chapman 1987), with the value of Q decreasing for larger active regions that are more frequent around the maximum of activity (Foukal 1998). In our case, we choose a mean value around $Q \sim 8.0$ for the simulations of Sun-like stars data. In the case of young active dwarfs, several studies involving the modelling of high precision light curves conclude that lower values of Q or even the non existence of faculae provide the best description of the data for K and early M stars (Gondoin 2008; Lanza et al. 2010, 2011b).

The longitudes of the active regions in our simulations are equally distributed over the stellar surface, whereas the latitudes are distributed in two belts defined by gaussian functions centered at $\pm\bar{\theta}_{\rm belt}$. This configuration is well known for the Sun, together with a butterfly diagram evolution pattern, but also other long term variations and asymmetries have been observed (Pulkkinen et al. 1999). For other stars, latitudes of spots have been measured from observations of spot crossing events (Sanchis-Ojeda & Winn 2011). Also, the inclination of the stellar axis towards the observer is a parameter of our program and can vary from 0° to 90°.

Active region evolution is modelled with a linear increase of the spot sizes with time, followed by a constant size time interval and a final decay. The total typical lifetime of active regions, $\bar{L}_{\rm n}$, its standard deviation, $\sigma(L_{\rm n})$, and the growing/decaying rate, $a_{\rm rd}$, are also introduced as parameters in the simulation. Then, the duration of each active region is determined from a gaussian distribution with a mean $\bar{L}_{\rm n}$ and a standard deviation $\sigma(L_{\rm n})$. Spots are known to live for weeks on main sequence stars, and months in the case of locked binary systems (Hussain 2002; Strassmeier et al. 1994a,b). However, polar starspots have been observed to last for years (Olah & Pettersen 1991). Measurements of the decay rate of sunspots have shown that it follows a parabolic area decay law (Petrovay & van Driel-Gesztelyi 1997; Petrovay et al. 1999) although previous studies assumed both linear and non-linear laws (Martinez Pillet et al. 1993). Regarding other stars, Doppler imaging observations of isolated starspots over time are not yet available in high resolution. In the case of our simulations, a parabolic law is considered, both for the decay and for the emergence of the active regions, and the evolution rate is set to the solar values except for stars where the surface map has been modelled for a long enough time span to estimate spots lifetimes and observe variations in size.

Notice that `StarSim` does not model each active region as a group of small spots, but as a single circular spot. We assume that this approach, by considering the appropriate size and evolution of the active regions, generates mostly the same effects on the simulated photometric and spectroscopic data as using a more complicated groups-pattern configuration. In our simulations we adjust the number and size of active regions in order to be in agreement with the results from the literature that assume a two-temperature structure (Henry et al. 1995; Rodonò et al. 2000; Padmakar & Pandey 1999). Solanki & Unruh (2004) discuss the distribution of spot sizes for some Sun-like stars observed with the Doppler imaging technique. Although it is suggested that sizes could follow a lognormal distribution as on the Sun, we do not adopt such distribution because the smaller spots would not cause a significant effect on our simulations compared to large spots, especially for the most active stars where large spots dominate.

Spot temperatures have only been determined in a few cases, and the inhomogeneity of the results due to the diversity of techniques make this still an unconstrained parameter. Most of the current measurements made in main sequence stars come from Doppler imaging (Marsden et al. 2005; Strassmeier & Rice 1998) or multi-band light curve modelling (Petrov et al. 1994; O'Neal et al. 2004). Berdyugina (2005) showed that, on average, the spot temperature contrast $\Delta T_{\rm spot}$ has a dependence on the spectral type, being larger for hotter stars. However, there seems to be no correlation between spots temperatures and sizes (Bouvier & Bertout 1989; Strassmeier 1992) or activity cycles (Stix 2002; Albregtsen & Maltby 1981; Penn & MacDonald 2007) in the case of the Sun. In our model we assume the same $\Delta T_{\rm spot}$ for all the active regions, and the existence of a correlation between $\Delta T_{\rm spot}$ and the temperature of the photosphere, $T_{\rm eff}$.

As we said in Sect. 5.2.1, Phoenix models are used in order to reproduce the spectral signature of faculae in our approach. Faculae are known to be mainly a magnetic phenomenon affecting the intensity of the spectral lines, best reproduced by NLTE simulations (Carlsson & Stein 1992). The lack of high resolution models for faculae in the spectral range of our interest prevents us to include them in high resolution spectra simulations, restricting them to the simulations of broad band photometric jitters (see Sect. 5.2.2). A positive temperature contrast between the faculae and the photosphere, $\Delta T_{\rm fac} \simeq 30 - 50$ K is assumed, as reported by Badalyan & Prudkovskii (1973) from observations of the CO line in faculae and by Livshits & Polonskii (1968) from a more theoretical point of view. In Solanki (1993) we can find an extensive discussion and references on the weakening of lines in faculae and the needed $\Delta T_{\rm fac}$ to best reproduce the continuum brightness.

A transiting planet can also be introduced in the simulations for further investigation of activity effects on photometric and radial velocity observations during transits. The planet is modelled with a circular black disk and is described in the same way as a spot with zero flux, but assuming a circular projection on the stellar disk. The radius of the planet has no dependence on wavelength, so no planet atmosphere is considered in the current approach. The photometric signal for the primary transit is generated from the planet size, the ephemeris and the orbit orientation (inclination and spin-orbit angles), which are specified as input parameters. The semi axis of the orbit is computed from the orbital period, $P_{\rm planet}$, and the stellar mass, M_*, using the third Kepler law by assuming $M_* \gg m_{\rm planet}$. Eccentricity is considered to be zero for all cases in the current model.

Together with the physical parameters of the star-planet system, the spectral range for the output data, the time span of the simulations and cadence of the data series can be adjusted. The program `StarSim` generates the resulting time series spectra, the cross correlation function series from a specified reference spectrum, and also creates a light curve by convolving each

Table 5.1: Input parameters

Parameter	Typical values
Initial time of simulation (days)	-
Final time of simulation (days)	-
Data time cadence (minutes)	-
Working mode	Photometry / Radial vel.
Spectral range (nm)	500 - 50000 nm
Photometric filter	-
Grid resolution (°)	$1^\circ \times 1^\circ$
Radial velocity range of the cross correlation function, $\Delta v_{\rm CCF}$	2 - 10 km/s
Add photon noise	y/n
Stellar apparent magnitude K	-
Telescope area (m^2)	-
Detector efficiency	-
$T_{\rm eff}$ (K)	2600 - 12000 K
$\log g$	+3.5 - +5.0
[Fe/H]	-4.0 - +1.0
[α/Fe]	0.2 - +1.2
Spots temperature contrast, $\Delta T_{\rm spot}$ (K)	200 - 1500 K
Faculae temperature contrast, $\Delta T_{\rm fac}$ (K)	30 - 50 K
Facula-to-spot area ratio, Q	0.0 - 8.0
Rotation period, P_0 (days)	-
Differential rotation, $k_{\rm rot}$	-
Inclination angle, i_* (°)	0 - 90°
Minimum number of spots, Nr_{min}	-
Maximum number of spots Nr_{max}	-
Mean area of spots $\bar{A}_{\rm Sn}$	-
Standard deviation of the area of spots $\sigma(A_{\rm Sn})$	-
Mean lifetime of active regions, $\bar{L}_{\rm n}$ (days)	$10^1 - 10^3$
Standard deviation of lifetime of active regions $\sigma(L_{\rm n})$ (days)	-
Growing/decaying rate $a_{\rm rd}$	-
Mean latitude of active regions $\pm\bar{\theta}_{\rm belt}$ (°)	0 - 90°
Standard deviation of latitude of active regions $\sigma(\theta_{\rm belt})$ (°)	0 - 90°
Planet radius, $R_{\rm planet}/R_*$	-
Mid transit time, T_0 (days)	-
Orbital Period, $P_{\rm planet}$ (days)	-
Impact parameter, b	0 - 1
Spin-orbit angle, γ (°)	0 - 90°

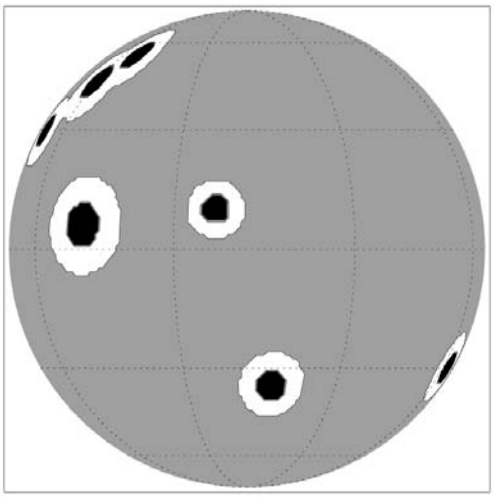

Figure 5.3: Projected map for an arbitrary distribution of active regions. The quiet photosphere is represented in grey, and each active region is modelled as a cold spot (black) and a hotter surrounding area to account for faculae (white).

generated spectrum with a filter passband specified from a database. If preferred, a filter with a rectangular transfer function can be defined and used in order to study the photometric signal at any desired wavelength range. Finally, the integration time, the telescope collecting area, the response of the detector and the target star magnitude are needed in order to apply photon noise statistics to the resulting fluxes.

Simulating photometric time series

To build the spectrum of the stellar spotted surface, three initial synthetic spectra generated from models with different temperatures are computed: for quiet photosphere, for spots and for faculae. The program reads the physical parameters for the three photospheric features of the modelled star and interpolates in $T_{\rm eff}$ within the corresponding model grids to generate the three synthetic spectra: $f_p(\lambda), f_s(\lambda)$ and $f_f(\lambda)$. The rest of the stellar parameters (i.e. $\log g$, metallicity, etc.) are not significantly variable over the stellar surface, and specifically for active regions. Therefore, a precise value is not critical for the purpose of our simulations, and the nearest values in the grid are considered instead of interpolating.

Also, Kurucz (ATLAS9) spectra are computed for the same parameters for the photosphere, spots and faculae, as these models provide information on the limb darkening profile function $I(\lambda,\mu)/I(\lambda,0)$. With our approach, a limb darkening factor for the stellar photosphere is computed separately for every surface element and λ by convolving the spectrum of the undarkened surface element ($f_p(\lambda)$ or $f_s(\lambda)$) with the corresponding limb darkening function, $I(\lambda,\mu)/I(\lambda,0)$ (see Eqs. 5.3,5.9,5.14). In the case of faculae, a different approach is considered, as it is known that these areas are brightened near the limb (Frazier & Stenflo 1978; Berger et al. 2007). A limb brightening law is considered in this case, as presented in Eq. 5.12.

The program produces a series of output observations considering the initial and final times

and the cadence of the time series specified in the input parameters. For each time step, the evolutionary stage (current size) and the projected position of each active region are computed. This last is obtained from the specified rotation period, P_0, and the differential rotation of the star, which is modelled as described by Beck (2000):

$$\Omega(\theta) = \Omega_0 + k_{\rm rot}(\Omega_{\odot \rm A} \cdot \cos^2\theta + \Omega_{\odot \rm B} \cdot \cos^4\theta), \tag{5.2}$$

where Ω_0 is the equatorial rate, $\Omega_{\odot \rm A} = 1.698^\circ$/day and $\Omega_{\odot \rm B} = 2.346^\circ$/day are the coefficients that describe the differential rotation for the Sun (Snodgrass & Ulrich 1990), $k_{\rm rot}$ is a factor that sets the differential rotation rate for the star and is specified in the input parameters (the value for a Sun-like star would be $k_{\rm rot}$=1), and θ denotes the colatitude.

In a first step, the spectrum for an immaculate photosphere is obtained from the contribution of all the surface elements, taking into account the geometry of the element, its projection towards the observer, the corresponding limb darkening profile and the radial velocity shift:

$$\begin{aligned} f_{im}(\lambda) &= \sum_k f_p(\lambda_k, \mu_k, a_k) = \\ &= \sum_k f_p(\lambda_k) \otimes \frac{I_p(\lambda_k, \mu_k)}{I_p(\lambda_k, 0)} \cdot a_k \cdot \mu_k \cdot \omega_k, \end{aligned} \tag{5.3}$$

where k is the surface element and μ_k is the cosine of its projection angle given by

$$\mu_k = \sin i_* \sin\theta_k \cos\phi_k + \cos i_* \cos\theta_k, \tag{5.4}$$

where θ_k and ϕ_k are the colatitude and longitude coordinates, respectively, and i denotes the stellar axis inclination.

The factor ω_k accounts for the visibility of the surface element and is given by

$$\omega_k = \begin{cases} 1 & \text{if } \mu_k \geq 0 \\ 0 & \text{if } \mu_k < 0, \end{cases} \tag{5.5}$$

and a_k is the area of the surface element, which can be computed from the spatial resolution of the grid ($\Delta\alpha$) by

$$a_k = 2 \cdot \Delta\alpha \cdot \sin(\frac{\Delta\alpha}{2}) \sin\theta_k. \tag{5.6}$$

Finally, λ_k are the wavelengths including the Doppler shift for the corresponding surface element,

$$\lambda_k = \lambda + \Delta\lambda_k, \tag{5.7}$$

with

$$\Delta\lambda_k \simeq -8.05 \cdot \lambda \cdot \frac{1}{c} \cdot R_{\rm star} \cdot \frac{2\pi}{P_0} \sin i_* \sin\theta_k \sin\phi_k. \tag{5.8}$$

These are computed from the equatorial rotation period given in the input parameters and the stellar radius calculated using its relation with $\log g$ and $T_{\rm eff}$ for main sequence stars.

The flux variations produced by the visible active regions are added to the contribution of the immaculate photosphere when computing the spectrum at each time step j. These are given by

$$\begin{aligned}
&\Delta f_j^{ar}(\lambda) = \\
&= \sum_k [(f_s(\lambda_k) \otimes J_s^{kj}(\lambda_k) - f_p(\lambda_k) \otimes J_p^{kj}(\lambda_k)) \cdot p_s^{kj} + \\
&+ (f_f(\lambda_k) \otimes J_f^{kj} - f_p(\lambda_k) \otimes J_p^{kj}(\lambda_k)) \cdot p_f^{kj}],
\end{aligned} \tag{5.9}$$

where the first term accounts for the flux deficit produced by the spots and the second is the overflux produced by faculae. The quantities $J_p^{kj}(\lambda_k)$, $J_s^{kj}(\lambda_k)$ and J_f^{kj} account for the geometric and the limb darkening/brightening factors for the surface element k at the time step j of the simulation, and are given by:

$$\begin{aligned}
J_p^{kj}(\lambda_k) &= \frac{I_p(\lambda_k, \mu_{kj})}{I_p(\lambda_k, 0)} \cdot a_k \cdot \mu_{kj} \cdot \omega_{kj} \\
J_s^{kj}(\lambda_k) &= \frac{I_s(\lambda_k, \mu_{kj})}{I_s(\lambda_k, 0)} \cdot a_k \cdot \mu_{kj} \cdot \omega_{kj} \\
J_f^{kj} &= c_{\rm f}(\mu_{kj}) \cdot a_k \cdot \mu_{kj} \cdot \omega_{kj}.
\end{aligned} \tag{5.10}$$

The factors p_s^{kj} and p_f^{kj} are the fractions of the surface element k covered by spot and faculae, respectively. These amounts are computed for every surface element considering their distance to the center of all the neighbour active regions at each observation j. There is also a time dependence of the projection of the surface elements, given by

$$\mu_{kj} = \sin i_* \sin\theta_k \cos[\phi_k + \Omega(\theta) \cdot (t_j - t_0)] + \cos i_* \cos\theta_k. \tag{5.11}$$

Finally, $c_f(\mu_{kj})$ accounts for the limb brightening of faculae, which is assumed to follow the same model used by Meunier et al. (2010a):

$$c_{\rm f}(\mu_{kj}) = \left(\frac{T_{\rm eff} + \Delta T_\mu(\mu_k)}{T_{\rm eff} + \Delta T_{\rm fac}} \right)^4, \tag{5.12}$$

where

$$\Delta T_\mu(\mu) = a_\mu + b_\mu \cdot \mu_k + c_\mu \cdot \mu_k^2. \tag{5.13}$$

The coefficients are $a_\mu = 250.9$, $b_\mu = -407.4$ and $c_\mu = 190.9$ (see Meunier et al. (2010a) for the details), so that $c_{\rm f}(\mu_{kj}) \sim 1$ at the center of the disk and ~ 1.16 near the limb for a Sun-like star with $\Delta T_{\rm fac} = 30$ K. This is in agreement with the parametrizations presented by Unruh et al. (1999). The observations show that the contribution of faculae dominate the irradiance in

the case of the Sun, where active regions are ∼1.2 times brighter at the limb than at the center of the stellar disk (Ortiz et al. 2002; Ball et al. 2011; Steinegger et al. 1996).

As explained in Sect. 5.2.2, a transiting planet can be included by modelling it as a dark circular spot with a constant radius over wavelength (no atmosphere) crossing the stellar disk. For each time step j, the planet position is obtained from the given ephemeris and the flux deficit is computed from the eclipsed surface elements of the star:

$$\Delta f_j^{tr}(\lambda) = -\sum_k f_p(\lambda_k) \otimes J_p^{kj}(\lambda_k) \cdot p_{tr}^{kj}, \tag{5.14}$$

where p_{tr}^{kj} is the fraction of the surface element k covered by the planet at time step j. In the case that an active region is partially occulted by the planet, the corresponding spot (p_s^{kj}) and facula (p_f^{kj}) fractions (see Eq. 5.9) in the occulted surface elements are computed within the planet covered fraction (p_{tr}^{kj}) instead.

Finally, the spectrum for the observation j is obtained by adding the contribution of the immaculate photosphere, the active regions and the transiting planet:

$$f_j(\lambda) = f^{im}(\lambda) + \Delta f_j^{ar}(\lambda) + \Delta f_j^{tr}(\lambda). \tag{5.15}$$

When working with the low resolution Phoenix spectra in order to produce photometric time series, the resulting spectra are convolved with the specified filter passband (see Fig.5.4) to obtain the total flux and compute the jitter produced by activity at the desired spectral range. The photometric jitter is evaluated by computing the rms of the flux over time for the whole photometric data series.

A comparison between two light curves obtained from Phoenix models and solar observed spectra (see Sect. 5.2.1) for the Johnson-V band is presented in Fig. 5.5. The simulation spans over four rotation periods of the star. Active regions were modelled as circular spots with no faculae ($Q = 0$), and a total of 13 spots were introduced, assuming $\Delta T_{\rm spot} = 310$ K for the Phoenix models, the mean area of the spots of $\bar{A}_{\rm Sn} = 2 \cdot 10^{-3}$ (in units of the stellar surface) and the spots lifetime of $\bar{L}_{\rm n} = 30$ days. The difference between both light curves is always near $\sim 10^{-4}$, with an rms of $6.5 \cdot 10^{-5}$ in relative flux units.

The position of the photocenter on the stellar disk is also computed for each time step j of the simulations. This is implemented for a further investigation of the astrometric jitter caused by the presence of active regions or transiting planets, as will be presented in a paper that is in preparation. The astrometric shifts depend on wavelength and are computed separately for the equatorial axis (X) and the spin projected axis of the star (Y) by:

$$\begin{aligned}\Delta X^j(\lambda) = \sum_k \{ & f_p(\lambda_k) \otimes J_p^{kj}(\lambda_k) \cdot x_{kj} + \\ & + [f_s(\lambda_k) \otimes J_s^{kj}(\lambda_k) - f_p(\lambda_k) \otimes J_p^{kj}(\lambda_k)] \cdot p_s^{kj} \cdot x_{kj} + \\ & + [f_f(\lambda_k) \otimes J_f^{kj} - f_p(\lambda_k) \otimes J_p^{kj}(\lambda_k)] \cdot p_f^{kj} \cdot x_{kj} + \\ & + f_p(\lambda_k) \otimes J_p^{kj}(\lambda_k) \cdot p_{tr}^{kj} \cdot x_{kj} \}\end{aligned} \tag{5.16}$$

and

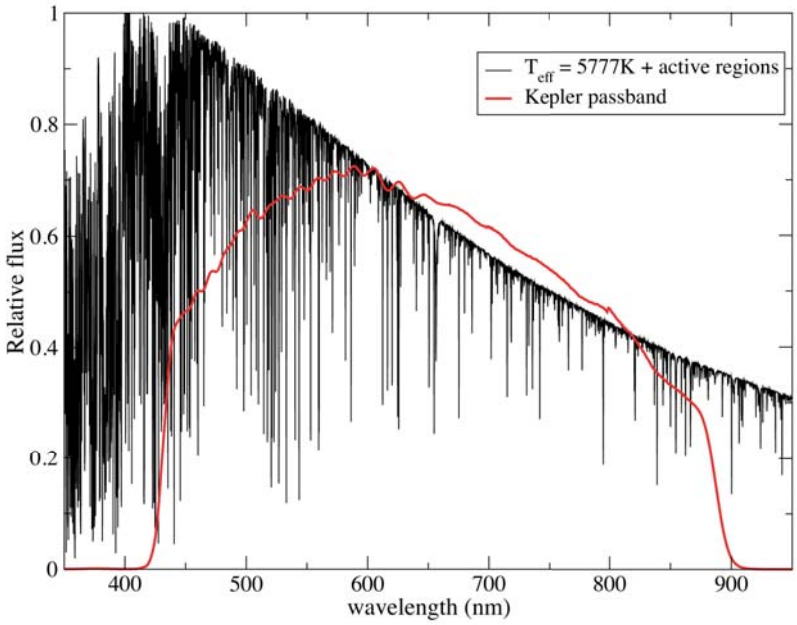

Figure 5.4: Normalized flux for a simulated spectrum of a Sun-like star with several active regions, generated from BT-Settl model spectra (black). In red, the transmission function of the Kepler filter.

$$\begin{aligned}\Delta Y^j(\lambda) = \sum_k \{ & f_p(\lambda_k) \otimes J_p^{kj}(\lambda_k) \cdot y_{kj} + \\ & + [f_s(\lambda_k) \otimes J_s^{kj}(\lambda_k) - f_p(\lambda_k) \otimes J_p^{kj}(\lambda_k)] \cdot p_s^{kj} \cdot y_{kj} + \\ & + [f_f(\lambda_k) \otimes J_f^{kj} - f_p(\lambda_k) \otimes J_p^{kj}(\lambda_k)] \cdot p_f^{kj} \cdot y_{kj} + \\ & + f_p(\lambda_k) \otimes J_p^{kj}(\lambda_k) \cdot p_{tr}^{kj} \cdot y_{kj} \}, \end{aligned} \tag{5.17}$$

where the quantities $J_p^{kj}(\lambda)$, $J_s^{kj}(\lambda)$ and $J_f^{kj}(\lambda)$ are given by Eq. 5.10 and x_{kj} and y_{kj} denote the position of the surface element k projected on the X and Y axes, respectively, at the time step j of the simulation. The rest of the variables are defined in Eqs. 5.3 to 5.14.

The first term in Eqs. 5.16 and 5.17 compute the position of the photocenter for an immaculate photosphere, whereas the second, third and fourth add the contribution of spots, faculae and planet to the astrometric shifts. As in Eq. 5.14, the corresponding flux contribution is computed within p_{tr}^{kj} and subtracted from p_s^{kj} or p_f^{kj} when the planet is occulting a spot or a facula, respectively, on the surface element k.

$\Delta X^j(\lambda)$ and $\Delta Y^j(\lambda)$ vectors are finally convolved with a given instrumental response function or a filter passband in order to produce astrometry jitter curves. A simple case is presented in Fig. 5.6 for a star with $T_{\rm eff} = 6000$ K and $\log g = 4.5$ observed at $i = 90°$ with only one active region consisting on a spot with a size of $A_{\rm Sn} = 7.5 \cdot 10^{-3}$ stellar surfaces and $\Delta T_{\rm spot} = 350$ K, and a surrounding area of faculae with $Q = 3.0$, located at the northern hemisphere of the star ($\theta = 80°$). The photometric signature can be seen in the top panel, and it is only dominated by

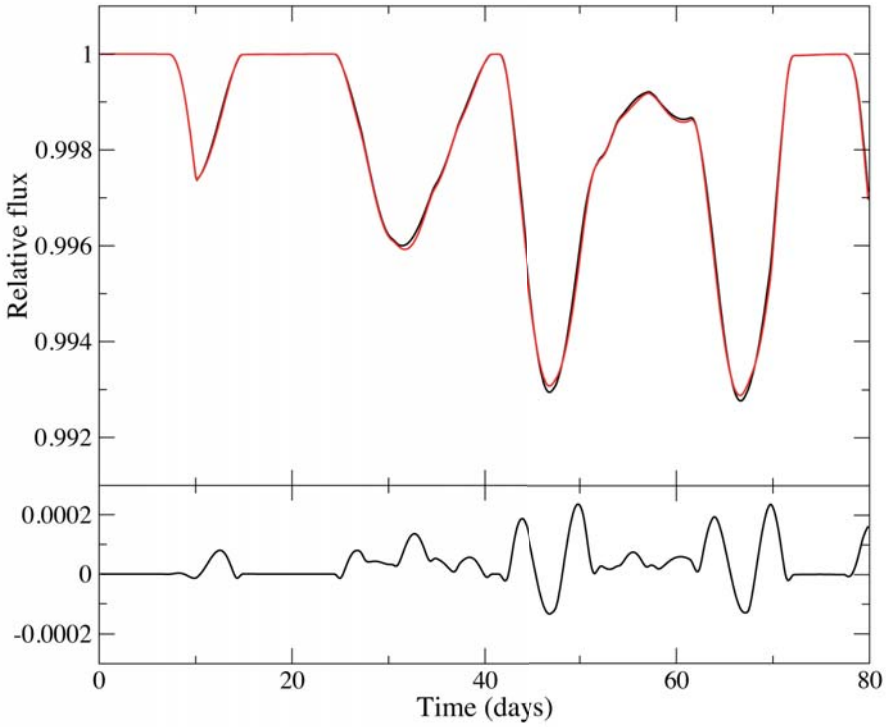

Figure 5.5: Top panel: A comparison between two light curves obtained for a star with $T_{\rm eff}$ = 5777 K and $\Delta T_{\rm spot}$ = 310 K from Phoenix BT-Settl models (red) and solar observed spectra (black), by introducing 13 active regions with a mean area of $\bar{A}_{\rm Sn} = 2 \cdot 10^{-3}$ (in units of the stellar surface) and a mean lifetime of $\bar{L}_{\rm n}$ =30 days. Bottom panel: The difference between both light curves.

faculae when the active region appears at the edges of the stellar disk (phases ~ 0.2 and ~ 0.6) as an effect of limb brightening of faculae, whereas the dark spot produces a descent of ~ 0.006 in relative flux units at the center of the stellar disk. The astrometric signature (middle panel) peaks at $\pm 0.01 R_*$ for the equatorial axis. This jitter would only affect astrometric measurements at the expected precision of the Gaia space mission (Lindegren et al. 2008; Eyer et al. 2013) for Sun-like stars located at 130 pc or closer. Further analysis and discussion on astrometric jitter simulations will be presented in a paper that is currently in preparation.

Simulating radial velocity data

A similar methodology as the one presented in Sect. 5.2.2 is implemented for the simulation of time series data in order to obtain radial velocity jitter measurements. A drawback of that approach is the large amount of data produced when working with high resolution spectra, which is solved as follows.

Three synthetic spectra ($f_p(\lambda), f_s(\lambda)$ and $f_f(\lambda)$) for the given wavelength range are computed for different temperatures corresponding to the quiet photosphere, spots and faculae, by interpolating from Husser et al. (2013) Phoenix library (see Sect. 5.2.1). The nearest values in the grid to the specified ones are considered for the rest of the parameters, as in Sect. 5.2.2. Then, individual cross correlation functions (thereafter CCFs) corresponding to the three features ($C_p(v), C_s(v)$ and $C_f(v)$) are computed, respectively, from the three spectra and a template mask consisting of a synthetic spectrum of a slow rotating inactive star of the same parameters. Working with the integration of CCFs instead of high resolution spectra makes the computation time much shorter.

The global CCF of the projected stellar surface is computed from the contribution of the individual surface elements. First, the signature of the immaculate photosphere is obtained by

$$C^{im}(v) = \sum_k C_p(v_k, \mu_k, a_k) = \sum_k C_p(v_k) \cdot H_p^k, \tag{5.18}$$

where the quantity H_p^k accounts for the intensity and geometric factors of the surface element k,

$$H_p^k = \sum_\lambda f_p(\lambda) \otimes \frac{I_p(\lambda, \mu_k)}{I_p(\lambda, 0)} \cdot a_k \cdot \mu_k \cdot \omega_k. \tag{5.19}$$

The sumatory covers the whole wavelength range specified for $f_p(\lambda)$.

The shifted velocities, v_k, are computed from the contribution of the Doppler shift and the effects of convection,

$$v_k = v + \Delta v_k^{\mathrm{DS}} + \Delta v_k^{\mathrm{C}}(C_l), \tag{5.20}$$

for $l = \{p, s, f\}$, where Δv_k^{DS} is the contribution from the Doppler shift for the surface element k (see Eq. 5.8) and $\Delta v_k^{\mathrm{C}}(C_i(v))$ is the effect of convective blueshift, which has a dependence on line depth and can be characterized by studying the line bisectors, which will typically show a distinctive C-shape due to granulation in the photosphere (Gray 1992).

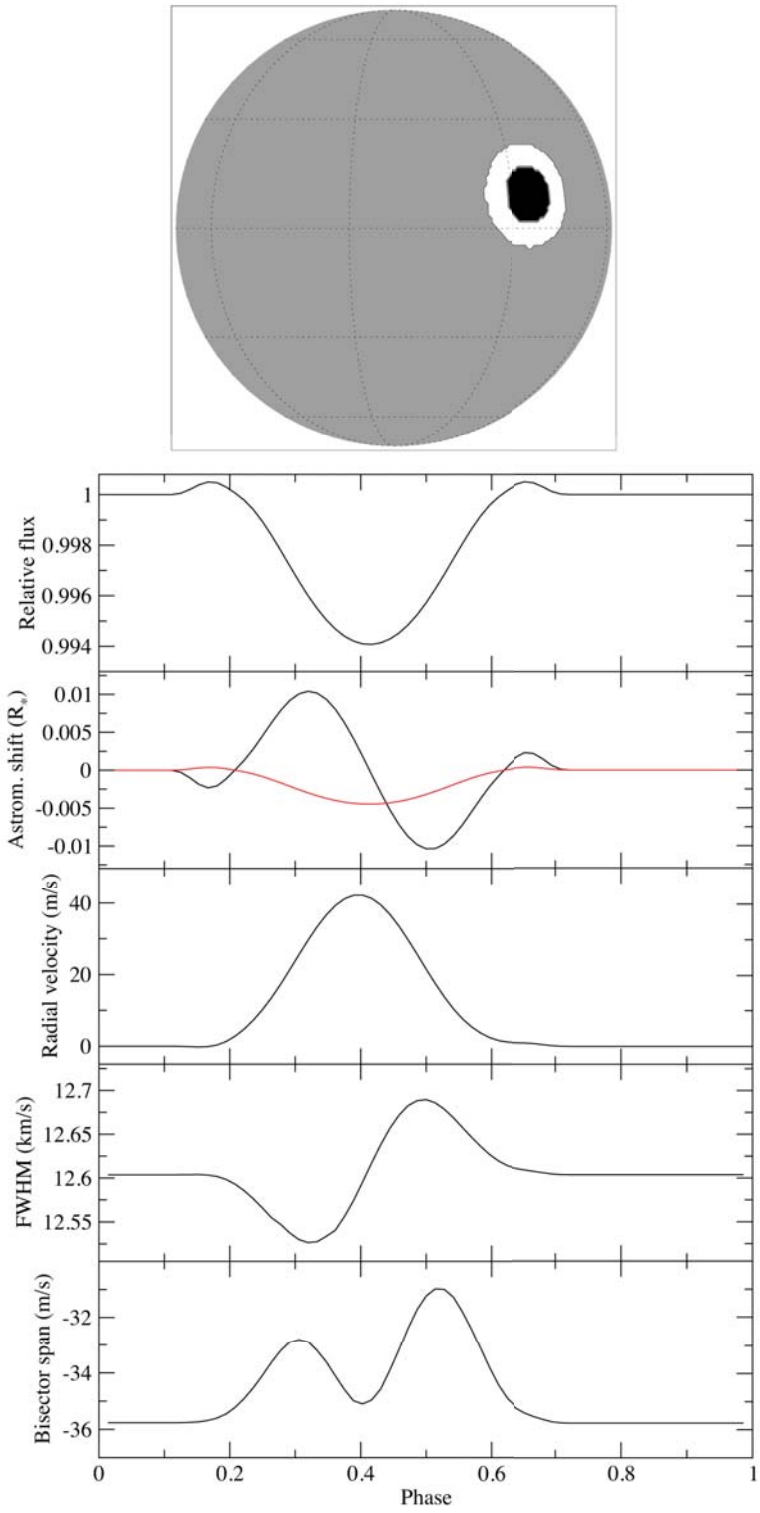

Figure 5.6: Example of a spot at $\theta = 80°$ with a size of $A_{\rm Sn} = 7.5 \cdot 10^{-3}$ stellar surfaces and $\Delta T_{\rm spot} = 350$ K and a surrounding area of faculae with $Q = 3.0$ on a Sun-like star. The rotation period is 25 days and the inclination is 90°, yielding $v \sin i = 2$ km s^{-1}. From top to bottom: stellar surface at phase=0.5, photometric light curve In Kepler band, astrometric jitters in equatorial (black) and polar (red) axes for the same band, radial velocity curve in the HARPS spectral range, FWHM of the cross correlation function and bisector span variations.

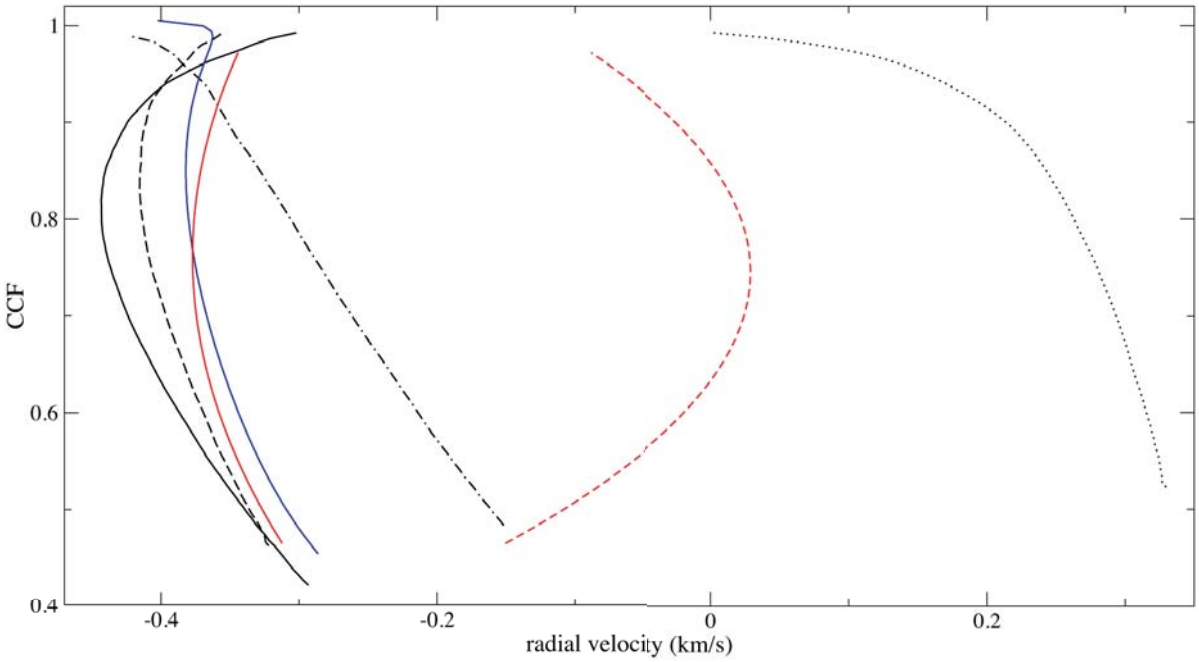

Figure 5.7: Line bisectors computed using the whole HARPS instrument range (∼380 - 670 nm) from CIFIST 3D model spectra at $\mu = 1.0$ (black solid line), $\mu = 0.79$ (black dashed line), $\mu = 0.41$ (black dashed dotted line) and $\mu = 0.09$ (black dotted line). The same for the solar observed spectra for a quiet Sun region (red solid line) and a spot (red dashed line), and the the bisector computed from the integrated CCF of a non-spotted photosphere of a Sun-like star (blue solid line).

Notice that the effects of convection are already included in the Phoenix spectra from Husser et al. (2013) (see Sect. 5.2.1) assuming a surface element in LTE observed at $\mu = 1$. In the case of quiet photosphere and faculae regions, the convection effects of the Phoenix spectra are modelled by fitting a low order polynomial function to the CCF computed with the whole spectral range, and then subtracted. Next, the convective blueshift (i.e., the line bisectors) are modelled with the same type of functions from CCFs computed from CIFIST 3D model spectra (Ludwig et al. 2009). These models are available (C. Allende, priv. comm.) for a Sun-like star and several projection angles ranging from the disk center to the stellar limb. We assumed solar values and we obtained the $\Delta v_k^{\rm C}(C_p)$, $\Delta v_k^{\rm C}(C_s)$ and $\Delta v_k^{\rm C}(C_f)$ for any projection angle μ_k from a lineal interpolation of the available models. In the case of the active regions (i.e., both spot and faculae zones), where convection is known to be blocked by strong magnetic fields (see Strassmeier 2009 and references therein), the solar high resolution observed spectra described in Sect. 5.2.1 are used in order to compute the shift of the line bisector with respect to the photosphere. This is then scaled with μ added to the amounts $\Delta v_k^{\rm C}(C_s)$ and $\Delta v_k^{\rm C}(C_f)$ in the surface elements where a contribution of spot or faculae is present. Figure 5.7 shows four of the bisectors computed using the whole HARPS instrument range (∼380 - 670 nm) from CIFIST 3D model spectra, the same for the solar observed spectra for a quiet Sun region and a spot, and the bisector computed from the integrated CCF of a non-spotted photosphere of a Sun-like star.

The vertical component of the convective velocity produces a maximum shift at the center

of the stellar disk, while the effect is barely seen near the limb where the projected velocity is zero. On the other hand, an apparent redshift of the spectral lines in comparison to the quiet photosphere is observed in spotted and facular areas as convective motions are blocked (Meunier et al. 2010b). Therefore, convection effects will introduce a maximum jitter in radial velocity measurements when a dark spot is crossing the center of the stellar disk.

The variations produced by active regions on the observed CCF at each time step j of the simulation are given by

$$\begin{aligned}
&\Delta C_j^{ar}(v) = \\
&= \sum_k \{[C_s(v_k) \cdot H_s^{kj} - C_p(v_k) \cdot H_p^{kj}] \cdot p_s^{kj} + \\
&+ [C_f(v_k) \cdot H_f^{kj} - C_p(v_k) \cdot H_p^{kj}] \cdot p_f^{kj}\},
\end{aligned} \tag{5.21}$$

where the quantities H_p^k, H_s^k and H_f^k are computed by

$$\begin{aligned}
H_p^{kj} &= \sum_\lambda f_p(\lambda) \otimes \frac{I_p(\lambda, \mu_{kj})}{I_p(\lambda, 0)} \cdot a_k \cdot \mu_{kj} \cdot \omega_{kj} \\
H_s^{kj} &= \sum_\lambda f_s(\lambda) \otimes \frac{I_s(\lambda, \mu_{kj})}{I_s(\lambda, 0)} \cdot a_k \cdot \mu_{kj} \cdot \omega_{kj} \\
H_f^{kj} &= \sum_\lambda f_f(\lambda) \cdot c_f(\mu_{kj}) \cdot a_k \cdot \mu_{kj} \cdot \omega_{kj}.
\end{aligned} \tag{5.22}$$

The first term in Eq. 5.21 computes the contribution of spots, while the second is the contribution for the regions with faculae.

The effect of a transiting planet is modelled as a circular dark spot (see Sect. 5.2.2). Therefore, the variations produced on the global CCF can be computed by

$$\Delta C_j^{tr}(v) = -\sum_k C_p(v_k) \cdot H_p^{kj} \cdot p_{tr}^{kj}, \tag{5.23}$$

As in Eqs. 5.14, 5.16 and 5.17, if the planet occults part of an active region, the corresponding fraction of the surface is computed within p_{tr}^{kj} instead of the occulted p_s^{kj} or p_f^{kj}.

Finally, the total CCF simulated for the observation j is obtained by adding the contribution of the active regions (Eq. 5.21) and the transiting planet (Eq. 5.23) to the signature of the unspotted photosphere (Eq. 5.18):

$$C_j(v) = C^{im}(v) + \Delta C_j^{ar}(v) + \Delta C_j^{tr}(v). \tag{5.24}$$

The function $C_j(v)$ is fitted with a gaussian function using a least squares algorithm in order to obtain an accurate measurement of the peak, which is associated to the radial velocity measurement for the time step j of the simulation. The fit is made for the data contained in a range $\Delta v_{\rm CCF}$, specified in the input parameters, around the maximum of $C_j(v)$. A value of 4 to 8 km s^{-1} for $\Delta v_{\rm CCF}$ has been tested to be optimal for the simulations of Sun-like stars.

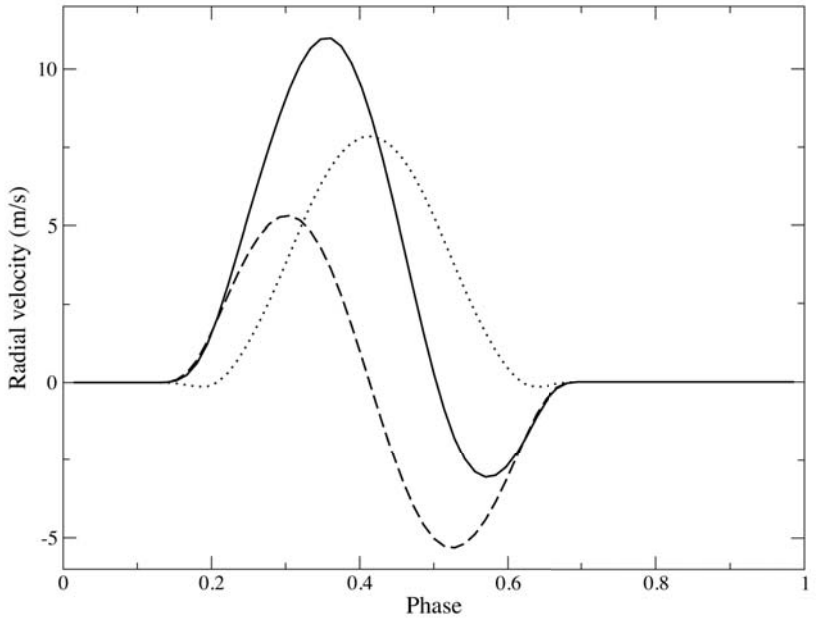

Figure 5.8: Radial velocity shifts produced by a single spot at $\theta = 65°$ with a size of $A_{\rm Sn} = 10^{-3}$ stellar surfaces and no faculae ($Q = 0$), on a Sun-like star. The result of simulating a rotating star ($P_{\rm rot} = 25$ days) with no convection is plotted with a dashed line. The simulation of a convective star with no Doppler shifts is plotted with a dotted line. Both effects are included in the results plotted with a solid line. All the HARPS instrument band is used to compute the radial velocities.

Further details will be presented in Herrero et al. (in prep.). The FWHM of the gaussian fit is also provided as an output of the simulations, as this is related to broadening mechanisms (Gray 1992). Finally, the bisector span is computed at each time step of the simulation from the difference between the mean of the top 40% and the mean of the bottom 40% of the bisector of the CCF in Eq. 5.24.

Figure 5.6 (bottom panel) shows the radial velocity signature produced by a single active region consisting on a spot and a surrounding facula region ($Q = 3.0$) on a Sun-like star with a rotation period $P_{\rm rot} = 25$ days ($v \sin i \simeq 2$ km s^{-1}). The HARPS instrument wavelength range (∼370 to 680 nm) was used for the computation of the CCF time series. Figure 5.8 shows the radial velocity signature of a single spot with no faculae ($Q = 0$) on a Sun-like star. The contribution of convective blueshift is plotted with a dotted line, whereas the effect of Doppler shift is plotted with a dashed line. Both effects are included in the results plotted with a solid line.

5.3 Characterizing activity jitter

5.3.1 The spectral signature of active regions

As presented in Sect .5.2, the photometric and spectroscopic variability of an active star can be modelled with cooler starspots and hotter faculae modulated by stellar rotation. The spectral signature of active regions is defined as the dependence of the flux variability or photometric jitter introduced by active regions with the equivalent wavelength of the observations. This can only be measured from time series spectroscopy or multi-band photometry of spotted stars and provides the key for the estimation temperatures and sizes of spots, which remain degenerated when observations in a single photometric band are available. Sing et al. (2011) provide a measurement of the temperature contrast of spots in HD 189733 by computing the wavelength dependence of the amplitude of the flux rise caused by a spot occultation observed during a planetary transit, yielding $\Delta T_{\rm spot} \geq 750$ K, which is consistent with a typical projected filling factor of 1 - 3% to be in agreement with the observed variability in the MOST photometry (Lanza et al. 2011a; Aigrain et al. 2012).

The methodology implemented in the program `StarSim`, as presented in Sect. 5.2.2, provides a tool to model the spectral signature of spots and faculae from multi-band observations of activity effects. We may adopt the flux rms as an adequate measurement of the variability in a given light curve. Simulations for a case test Sun-like star ($T_{\rm eff} = 5770$ K, $\log g = 4.5$ and solar abundances) with a rotation period of 25 days are performed in order to generate synthetic time series photometry for 12 different filters, ranging from the visible to the mid-infrared (Johnson UBVRI, 2MASS JHK and Spitzer IRAC bands). The time series photometry covers 3 complete rotation periods with a cadence of 1 day. The stellar surface is populated with a distribution of 3 to 8 active regions composed of spots of a mean size $\bar{A}_{\rm Sn} = 2 \cdot 10^{-3}$, in units of the total stellar surface. Two different scenarios are considered regarding the presence of faculae, assuming facular-to-spotted area ratios of $Q = 0.0$ and $Q = 8.0$ (see Sect. 5.2.2). The temperature contrasts are initially set to $\Delta T_{\rm spot} = 350$ K and $\Delta T_{\rm fac} = 30$ K. The active regions are located at a mean latitude of $\pm 40^{\circ}$ and evolve with a typical lifetime of 40 days.

The resulting spectral signatures of the active regions computed from ~ 300 to ~ 8000 nm and different configurations are presented in Fig. 5.9, together with a snapshot of the stellar surface map at the initial time of the simulations with $Q = 0.0$ (no faculae). The same active regions map is used for all the simulations. In a first step, a scenario with $Q = 0.0$ was considered and $\Delta T_{\rm spot} = 350$ K and $\bar{A}_{\rm Sn} = 2 \cdot 10^{-3}$ were assumed. The resulting spectral signature is plotted with a black line in the middle panel of Fig. 5.9. Then, spot areas were scaled to +50% and −50% and the corresponding $\Delta T_{\rm spot}$ which preserve the flux rms in the Johnson V band were found, thus obtaining $\Delta T_{\rm spot}^{+50\%} = 230$ K and $\Delta T_{\rm spot}^{-50\%} = 730$ K. The resulting spectral signatures for these two configurations of temperature contrasts and sizes of spots are also plotted in the middel panel of Fig. 5.9 with a red line and a blue line, respectively. Whereas the variability differs more than $2 \cdot 10^{-3}$ (relative flux units) in the ultraviolet, the signature of the spots is barely distinguishable for the three parameter configurations in the rest of the spectral range. The results change dramatically when surrounding faculae are included around the spots, as shown in the bottom panel of Fig. 5.9. We assume $Q = 8.0$, which is near the mean solar value (Chapman 1987; Lanza et al. 2003), and $\Delta T_{\rm fac} = 30$ K in all cases. Then, we recompute the spectral signature for the same three configurations previously described. The signature of active regions is flatter than in the cases of $Q = 0.0$, especially for the configurations of

$\Delta T_{\rm spot} = 350$ K (black line) and $\Delta T_{\rm spot} = 230$ K (red line), thus being the signature of faculae dominant, whereas the signature of the spots dominates when the temperature contrast is higher ($\Delta T_{\rm spot} = 730$ K, blue line).

5.3.2 Light curve scaling

The methodology implemented in the program `StarSim` and described in Sect. 5.2.2 allows us to cover any broad spectral range and generate time series. We have used the simulator including both the visible and the near-infrared ranges to perform several tests for infrared missions data-type optimization. We can accurately analyse and compare activity photometric signal amplitudes and patterns at different wavelengths and spectral resolutions.

We have considered a number of combinations of stellar photospheres and active region parameters (size and location of spots, temperature contrast) to improve the statistical view of the results. The process was performed for 11 cases of star-planet systems randomly selected from a set of 5 stellar models ($T_{\rm eff}$ = 6200 K, 5850 K, 5060 K, 4060 K, 3580 K) having four different possible active region maps and a rotation period of 15 days. The rotation period is not a relevant parameter in this case, as we are analyzing low resolution data and Doppler broadening is negligible. The spot temperature contrast was scaled with the effective temperature of the star according to Berdyugina (2005) and the planet parameters were fixed in all cases to $R_{\rm planet} = 0.05 R_{\rm star}$, $P_{\rm planet} = 2.54$ days, $b = 0.2$ (impact parameter), which correspond to a standard hot Neptune when a Sun-like host is considered, and provide a $\sim 0.25\%$ transit depth. The faculae temperature contrast and the facular-to-spotted area ratio (Q) were fixed in all cases to $\Delta T_{\rm fac} = +100$ K and $Q = 7.0$, respectively. Narrow bandpasses equivalent to a single spectral resolution element at $R = 300$ centered at 0.8 μm, 2.5 μm and 5.0 μm were used in order to generate light curves of the spotted rotating stars.

The approach we have investigated to correct near-infrared time series data for stellar activity is based on scaling the higher-amplitude optical light curve to the near-infrared wavelengths and carry out a direct subtraction. This procedure was defined so that it could resemble a practical procedure to use with visible and infrared simultaneous observations. The detailed steps are:

1. We first normalized the fluxes and calculated the standard deviation of the optical and near-infrared photometry, $\sigma(0.8\mu{\rm m})$, $\sigma(2.5\mu{\rm m})$ and $\sigma(5.0\mu{\rm m})$.
2. Ratios of these standard deviations (near-infrared to visible), defined as $K_{2.5} = \sigma(2.5\mu{\rm m})/\sigma(0.8\mu{\rm m})$ and $K_{5.0} = \sigma(5.0\mu{\rm m})/\sigma(0.8\mu{\rm m})$, were calculated.
3. The scaling factors $K_{2.5}$ and $K_{5.0}$ were applied to the optical light curve.
4. The final near-infrared light curve was obtained from the ratio of the generated time series to the scaled optical light curve.

Tests showed that the time modulation of the near-infrared light curves could be significantly removed or corrected following this approach. The sequence above was both applied to a light curve without exoplanet transits and to a light curve including transits.

We evaluated the possible performance of the method in removing activity signals by comparing the resulting corrected light curve with a light curve including transits and corresponding to a star with an immaculate photosphere (with no spots). This was carried out to check whether

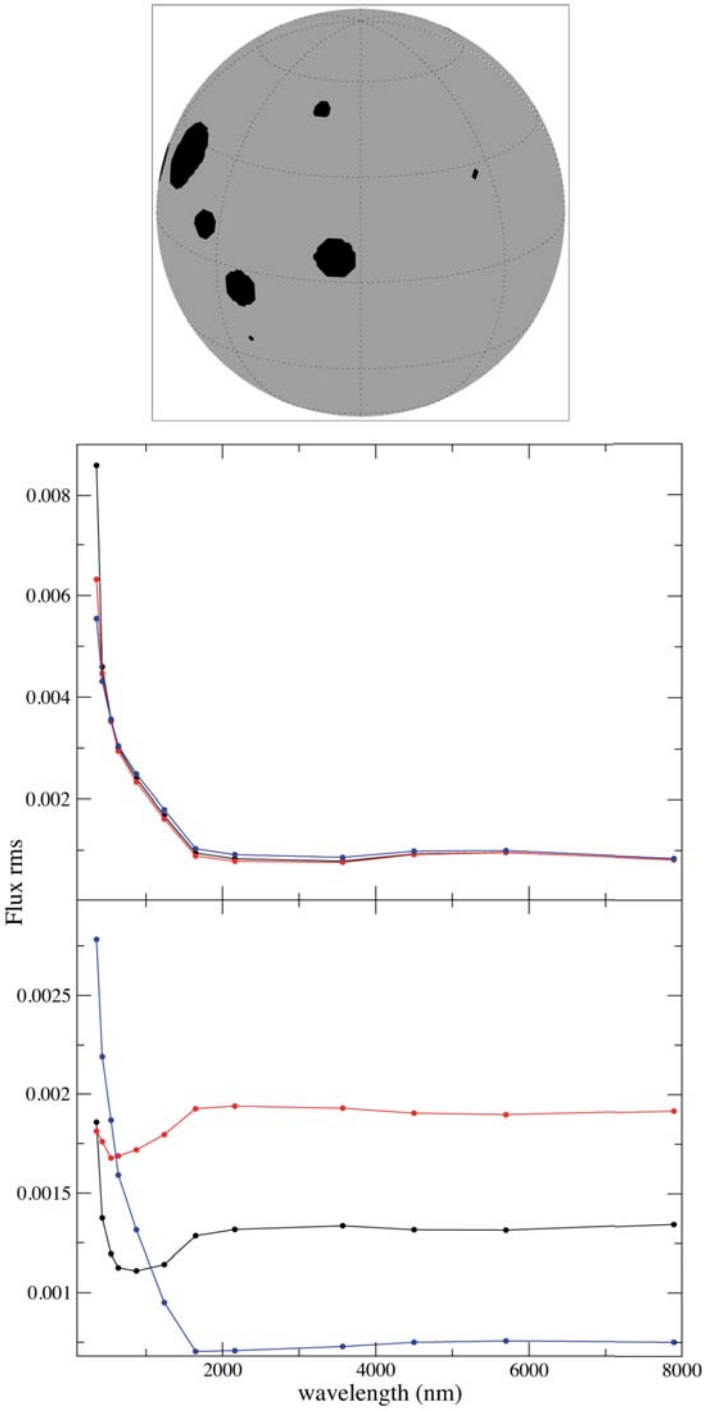

Figure 5.9: Top panel: the map of the initial distribution of active regions as used for the simulations in Sect. 5.3.1 in the case of $Q = 0.0$. Middle panel: the spectral signature (Flux rms vs. wavelength) for three different configurations of the active regions: $\Delta T_{\rm spot} = 350$ K and $\bar{A}_{\rm Sn} = 2 \cdot 10^{-3}$ (black line), $\Delta T_{\rm spot} = 350$ K and a 50% increase in the area of the spots (red line), and $\Delta T_{\rm spot} = 350$ K and a 50% decrease in the area of the spots (blue line). Bottom panel: the same as in the middle panel including faculae regions with $Q = 8.0$ and $\Delta T_{\rm fac} = 30$ K.

Table 5.2: Results for the simulations of 11 cases of star-planet systems randomly selected from a set of 5 stellar models and 4 different possible active region maps, and with a rotation period of 15 days. The planet parameters were fixed to $R_{\rm planet} = 0.05 R_{\rm star}$, $P_{\rm planet} = 2.54$ days, $b = 0.2$ (impact parameter). The faculae temperature contrast and the facular-to-spotted area ratio (Q) were fixed to $\Delta T_{\rm fac} = +100$ K and $Q = 7.0$, respectively. The first three columns indicate the temperature for the quiet photosphere, the spot contrast and the spot filling factor. The following three columns list the standard deviation of the (spotted) light curves at 0.8 μm, 2 μm and 5 μm. The two columns labelled $rms_{\rm T}$ show the standard deviation of the in- transit sections at 2.5 μm and 5.0μm after correcting for activity and transit effects. The final two columns give the standard deviation of the data analysed in the previous two columns but after correcting for outliers caused by spot crossing events.

$T_{\rm eff}$ (K)	$\Delta T_{\rm sp}$ (K)	Filling factor	rms (0.8μm)	rms (2.5μm)	rms (5.0μm)	$rms_{\rm T}$ (2.5μm)	$rms_{\rm T}$ (5.0μm)	$rms_{\rm T(corr)}$ (2.5μm)	$rms_{\rm T(corr)}$ (5.0μm)
5850	500	0.0050	2.33e-3	7.18e-4	7.42e-4	4.52e-5	4.58e-5	1.07e-5	1.12e-5
4060	400	0.0063	1.70e-3	1.32e-3	6.92e-4	5.70e-5	2.76e-5	1.24e-5	5.25e-6
5060	500	0.0089	1.85e-3	8.97e-4	6.43e-4	3.36e-5	2.63e-5	1.01e-5	9.13e-6
3850	400	0.0077	1.75e-3	9.62e-4	3.97e-4	4.83e-5	5.04e-5	3.55e-6	4.66e-6
5850	500	0.0063	1.70e-3	9.78e-4	7.46e-4	2.99e-5	2.26e-5	6.94e-6	7.20e-6
6200	550	0.0077	9.76e-4	3.85e-4	4.06e-4	1.08e-5	1.16e-5	2.68e-6	2.77e-6
4060	400	0.0050	3.38e-3	2.56e-3	1.30e-3	1.26e-4	6.17e-5	2.08e-6	1.02e-5
4060	400	0.0077	1.35e-3	1.06e-3	5.30e-4	3.25e-5	1.56e-5	6.38e-6	3.69e-6
5850	500	0.0077	9.43e-3	4.41e-4	4.95e-4	1.30e-5	1.37e-5	1.70e-6	1.76e-6
3850	400	0.0089	2.21e-3	1.13e-3	9.35e-4	5.16e-5	3.99e-5	1.17e-5	9.01e-6
5060	500	0.0482	1.55e-2	7.09e-3	5.25e-3	1.31e-4	1.02e-4	3.53e-5	2.77e-5

systematic effects inside the transits were left over when following the procedure. Indeed, depending on the distribution of starspots and the trajectory of the planet across the stellar disk, the depth of the transit could experience variations (which would mask or bias the measurement of the planetary atmosphere) both in the case of spot crossing events but also if only photosphere is occulted (e.g., Ballerini et al. 2012).

In our test we divided the resulting clean infrared light curves (i.e., corrected by scaling the 0.8 μm light curve as described above) by light curves generated for an immaculate star for the same stellar and planet parameters. Then, data intervals of $2 \cdot T14$ (i.e., twice the total duration of the transit) around the transit events were selected for analysis. The out-of-transit baselines at either side of the transit were used to fit a linear trend that was subsequently applied to the in-transit observations. This is analogous to the common procedure used to analyse and fit transit data. The standard deviations were computed for the in-transit sections of the complete data series (which includes 10 transits). The results of this set of simulations can be seen in Table 5.2 and Fig. 5.10. Table 5.2 shows the stellar parameters adopted and standard deviation caused by the spot modulation at 0.8 μm, 2.5 μm and 5.0 μm bandpasses. The last two columns list the standard deviation of the in-transit data at 2.5 μm and 5.0 μm after correcting for spot modulation using the procedure described above.

As can be seen in Table 5.2, most of the cases (10) that we have analysed thus far correspond to standard stars of GKM spectral types with filling factors of 0.5% to 0.9%. To define the context, our Sun ranges from filling factors of $\sim 0\%$ to $\sim 0.2\%$. So, the stellar parameters that we have simulated correspond to stars that are some 2-3 times more active than the active Sun.

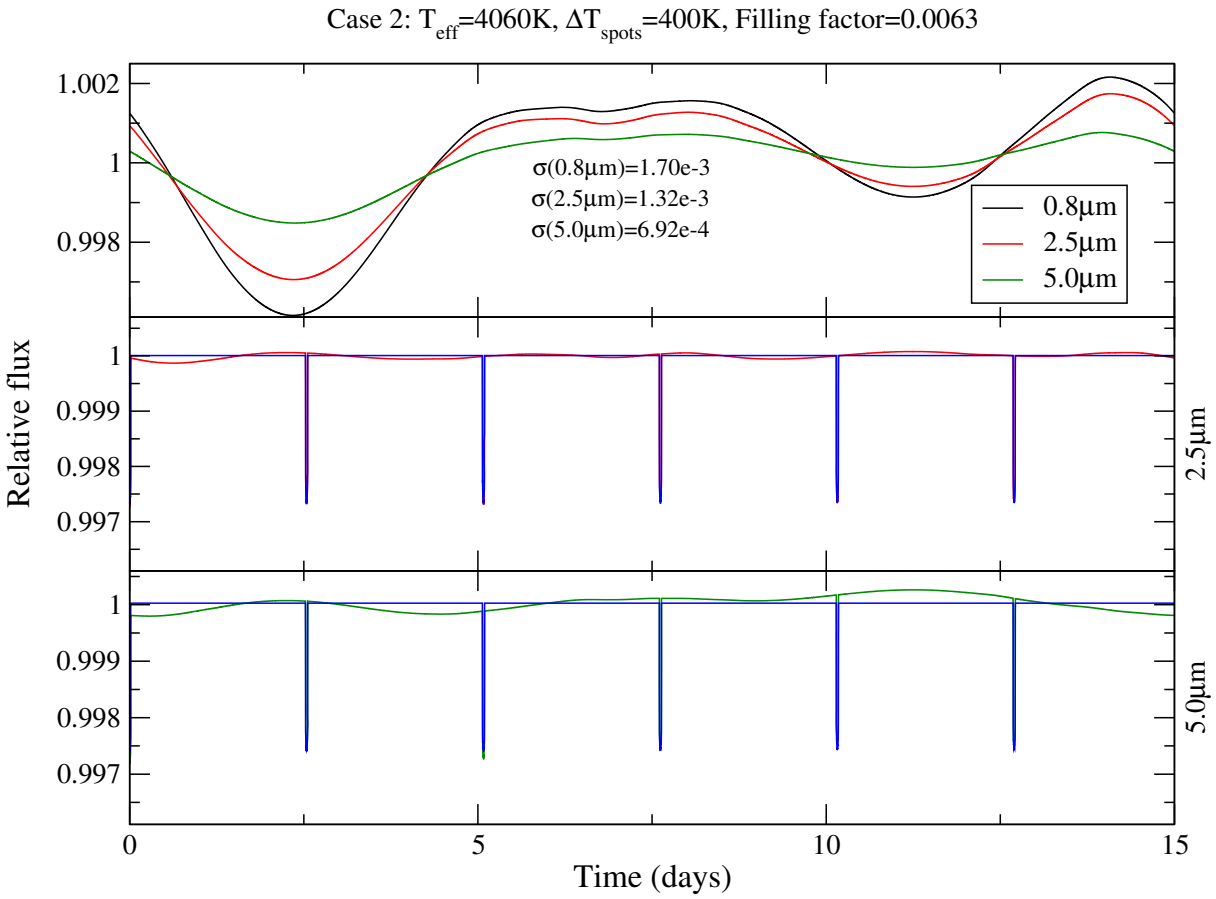

Figure 5.10: Top: Normalized light curves for three narrow passbands (R=300) centered at 0.8 μm (black), 2.5 μm (red) and 5.0μm (green) for one of the cases generated in the sample. The standard deviations of the data series, used in order to compute the scale factors, are also indicated. Bottom: 2.5 μm (red) and 5.0 μm (green) light curves for the same star including a transiting planet, and corrected from the activity signal by using the scaled 0.8 μm light curve. The light curves for an immaculate star are shown in blue.

According to the Kepler mission results (e.g., Basri et al. 2013), this would be representative of the 20% of the solar neighborhood population and thus indicate a statistical upper limit to what we can expect of the exoplanet host distribution. As can be seen from Table 5.2, in the first 10 cases the plain direct procedure that we have used here provides a correction to the transit data to better than 10^{-4} and often as good as a few parts in 10^{-5}. Note also that, if obvious photometric outliers corresponding to spot crossing events are cleaned, the results are further improved and in all cases the residual standard deviation is below $\sim 1.3 \cdot 10^{-5}$.

The last row of Table 5.2 corresponds to a rather active star with similar parameters to the exoplanet host HD 189733. The filling factor is around 5% and in this case the standard deviation of the 0.8 μm, 2.5 μm and 5.0 μm light curves is of the order of 5-10 times greater than in the previous 10 cases. However, the results show that the scaling procedure works quite efficiently in this case as well and the standard deviations of the corrected transit events is of $\sim 1 \cdot 10^{-4}$. The standard deviation is further reduced to $\sim 3 \cdot 10^{-5}$ when spot crossing outliers are cleaned.

The procedure explained here constitutes a direct methodology to correct transit data that may be the simplest approach to address stellar activity effects. Even in this case, our results show that it is possible to reach precisions better than 10^{-4} on transit data in the near IR for most of the stellar host population. If further care is taken and outliers caused by spot crossing events are cleaned, the precision reachable approaches 10^{-5} or better in most instances. This is even the case of a moderately active exoplanet host such as HD 189733. The tests that we present show that the final in-transit standard deviation is a factor 2 to $5{\cdot}10^2$ smaller than the original standard deviation of the light curve at 0.8 μm. This simple rule-of-thumb can be used to assess the maximum photometric activity tolerable to attain the precision requirements of any future IR instrument or mission with this direct scaling technique. More strongly active targets, are very likely to require a more sophisticated analysis methodology in order to reach precisions in the range 10^{-4} to 10^{-5}.

A shortcoming of this methodology is that it requires continuous or nearly-continuous spectrophotometry to model the out-of-transit variability and calculate the scaling factors. In the case of infrared space missions, this may occur for some transiting planets with a very large number of observations or may require of supporting ground-based observations to monitor the photometric variations. Given these restrictions we have explored another method to correct transit and eclipse data that does not require other observations than those of the events themselves.

5.3.3 Characterization and correction of transit depth variations

In view of the need of continuous spectrophotometry to apply the methodology in Sect. 5.3.2, we have investigated a direct method of correlating activity-induced variations in the visible with those in the infrared. The underlying hypothesis is that variations of the transit depth in the visible are solely caused by stellar activity effects and not influenced by the atmosphere of the transiting planet. The spectral signal of the planetary atmosphere in the visible is significantly weaker than in the infrared and time variations should be negligible, thus lending support to the working hypothesis. In this framework, by characterizing variations in the visible it should be possible to correct out activity-induced variations in the infrared.

To simulate the performance of the method we have considered a random selection for the same combinations of stellar photospheres, active region parameters and transiting planet pa-

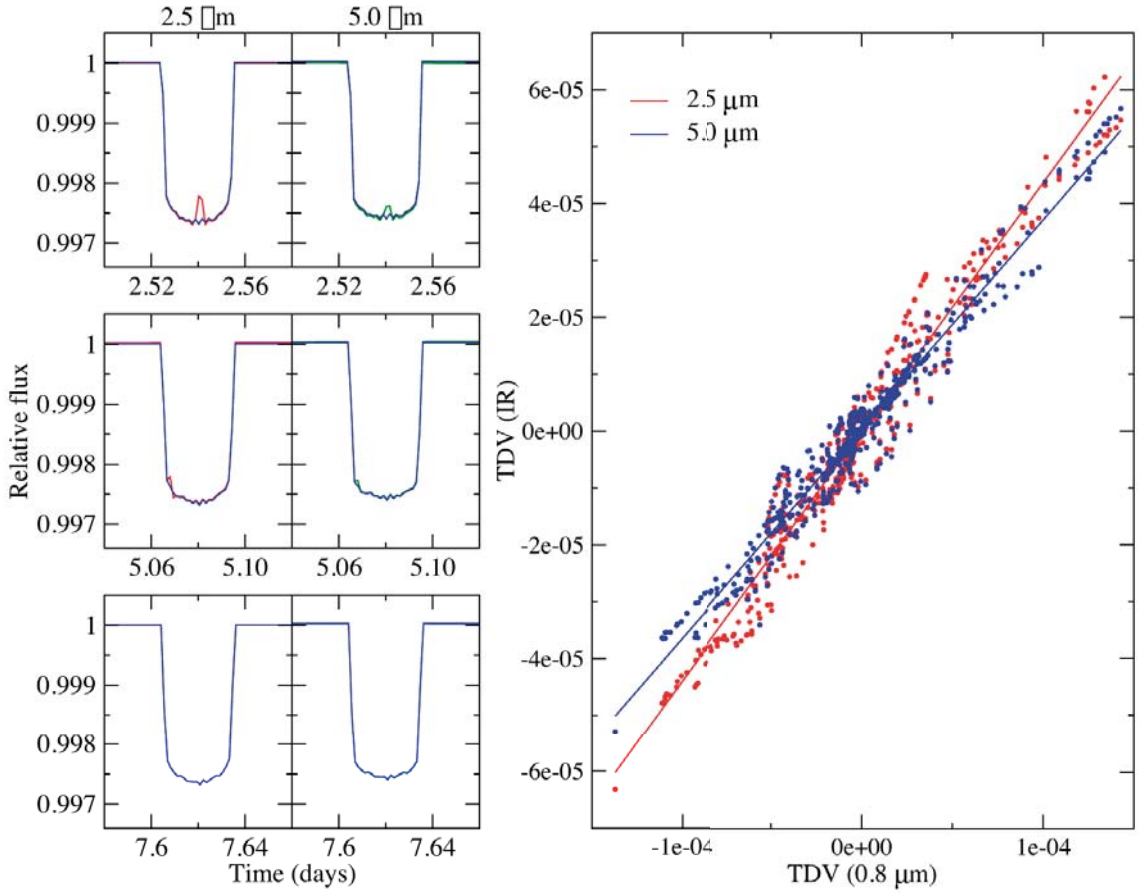

Figure 5.11: Left: Three of the transit light curves at 2.5 μm (red) and 5.0 μm (green) for one of the cases generated in the sample, compared with the transit light curve of an immaculate star (blue). Note the small systematic deviations and the more apparent spot crossing events. Right: Correlation of activity-induced transit depth variations (TDV) for all the studied cases and transit events in the visible (0.8 μm) and the IR (2.5 and 5.0 μm).

rameters as in Sect. 5.3.2. The list of cases with initial parameters and results is presented in Table 5.3. Note that we are now considering a wider range of filling factors than in the case of Sect. 5.3.2, so that the effects of both non-occulted spots and spot crossing events will be more easily studied than in the case of rather inactive stars on a short series of transit observations.

From the modelled light curve we have measured the transit depths, using common techniques, and calculated the variations of those depths with time. This was repeated for all the transit events (60 for each object) of all our simulated cases. The combined dataset of all transit depths was then analysed for correlations. We have found that there is a well-defined correlation between activity-induced transit depth variations in the visible (0.8 μm) and the infrared (2.5 and 5.0 μm). An illustration of the transit light curves generated by the simulator and the correlation between visible and infrared transit depth variations (thereafter TDVs) can be seen in Fig. 5.11, including linear regression fits.

The methodology for correcting infrared data for stellar activity effects using, for example, a

Table 5.3: Results for the simulations of the 10 cases randomly selected from the same parameter combinations as in Table 5.2, but considering a wider range of filling factors. The first three columns indicate the temperature for the quiet photosphere, the spot contrast and the spot filling factor. The following three columns list the rms of the in-transit sections at 0.8 μm, 2.5 μm, and 5.0 μm. The next two columns give the rms of the in-transit sections at 2.5 μm and 5.0 μm after correcting for activity effects using the procedure described in the text. The final two columns give the correction factor at 2.5 μm and 5.0μm.

$T_{\rm eff}$ (K)	$\Delta T_{\rm sp}$ (K)	Filling factor	$rms_{\rm T}$ (0.8μm)	$rms_{\rm T}$ (2.5μm)	$rms_{\rm T}$ (5.0μm)	$rms_{\rm T(corr)}$ (2.5μm)	$rms_{\rm T(corr)}$ (5.0μm)	Corr.fact (2.5μm)	Corr. fact (5.0μm)
5060	500	0.061	9.0e-3	3.9e-3	3.0e-3	1.7e-5	2.3e-5	2.3e-2	1.3e-2
5850	500	0.053	7.3e-3	2.9e-3	2.9e-3	4.0e-5	2.5e-5	7.3e-1	1.2e-2
6200	550	0.049	4.4e-3	1.7e-3	1.8e-3	5.3e-6	5.9e-5	3.2e-2	3.1e-2
3580	400	0.055	1.1e-2	6.2e-3	4.7e-3	3.8e-5	2.2e-5	1.6e-2	2.1e-2
4060	400	0.035	7.1e-3	5.3e-3	2.6e-3	4.4e-5	3.4e-5	1.2e-2	7.6e-2
5850	500	0.008	1.9e-4	1.4e-4	1.5e-4	8.9e-6	9.8e-5	1.6e-1	1.5e-1
5850	500	0.060	6.3e-3	2.6e-3	2.7e-3	3.2e-5	2.7e-5	8.1e-1	1.0e-2
3850	400	0.066	1.5e-2	8.3e-3	6.4e-3	3.0e-5	2.2e-5	2.8e-2	2.9e-2
5850	500	0.020	2.0e-3	9.2e-4	9.7e-4	1.9e-5	2.4e-5	4.8e-1	4.0e-1
5060	500	0.074	5.1e-3	2.2e-3	1.7e-3	1.4e-5	1.5e-5	1.6e-2	1.1e-2

series of measurements in the visible and an infrared band can be carried out using the following expression:

$$d_{IR}^{corr} = d_{IR} + a_0 + a1 \cdot (d_{VIS} - \langle d_{VIS} \rangle), \tag{5.25}$$

where d stands for the transit depth, and a_0 and a_1 are the coefficients of a linear fit that can be determined from simulations (shown in Fig. 5.11 as an example for our simulated cases). Actually, our tests show that a_0 takes negligible values and can be adopted as 0.

We tested the performance of the method by coming back to our simulated transit depth data. The linear regression takes values $a_1 = 0.438$ for the 2.5 μm data and $a_1 = 0.368$ for 5.0 μm. For each transit event, we used the general coefficients and the visible TDV to correct the infrared depth for stellar activity. Then, we analysed the resulting scatter in the depth variations of the combined events for each simulated case. The results can be seen in Table 5.3. The cases that we have analysed represent standard stars of GKM spectral types with filling factors of 1-7%, i.e., corresponding to stars that are ∼4-30 times more spotted than the active Sun. The case in row 1 has parameters similar to HD 189733. As can be seen from Table 5.3, we start with initial transit depth rms values that are generally around 10^{-3}. Correction using the procedure described decreases such rms by factors ranging from 20 to several hundreds. Thus, the resulting rms in the transit depth variations in the infrared shows that this procedure provides a correction of the transit data to a few times 10^{-5}. For more active stars (which will be a very small subsample, anyway) the correction may not reach this high performance, but the final TDV rms is very likely not to exceed 10^{-4}.

5.3.4 Astrometric jitter

The methodology implemented in the program `StarSim` and explained in Sect. 5.2 to simulate the photosphere of active rotating stars with surface integration techniques is also used in order to compute the position of the photocenter within the stellar disk (see Sect. 5.2.2 for a detailed description). The astrometric shifts $\Delta X^j(\lambda)$ and $\Delta Y^j(\lambda)$ are computed independently for each element of the wavelenth array (see Eqs. 5.16 and 5.17), so that the resulting observed shift can be computed by convolving these quantities with the passband of a specific filter or instrument:

$$\begin{aligned} \Delta X^j &= \int_{\lambda 1}^{\lambda 2} \Delta X^j(\lambda) \otimes h(\lambda)\,\mathrm{d}\lambda \\ \Delta Y^j &= \int_{\lambda 1}^{\lambda 2} \Delta Y^j(\lambda) \otimes h(\lambda)\,\mathrm{d}\lambda \end{aligned} \tag{5.26}$$

for the time step j of the simulation, being $h(\lambda)$ the flux transfer function of the instrument. We define the total astrometric shift in units of R_* by

$$\Delta A^j = \sqrt{(\Delta X^j)^2 + (\Delta Y^j)^2}. \tag{5.27}$$

Figure 5.12 illustrates the effect produced on the photocenter when a dark spot is appearing near the limb of the star, computed for the response function of the main detector of the Gaia space mission (Eyer et al. 2013). In the case of a Sun-like star with $i = 60°$ with a single spot of $\Delta T_{\rm spot} = 500$ K and a size $A_{\rm S} \simeq 5.5 \cdot 10^{-3}$ (maximum projected filling factor of $\sim 1.8\%$) located at $\theta = 65°$, the maximum astrometric shift is $\Delta A \simeq 0.018 R_*$ (see Fig. 5.12). While the maximum ΔY occurs at mid-transit of the spot, the maximum ΔX is found when the spot is located at $0.45 R_*$. This profile can significantly change depending on the spectral type of the star and the instrument configuration, as it is strongly dependent on the limb darkening effect. The maximum ΔA in the example above would be within the Gaia detection limits if the star was at a distance lower than ~ 240 pc. Therefore, astrometric jitter could be significant in the measurements of active stars in the solar neigborhood. However, a sample of Sun-like stars with realistic distributions of active regions must be studied considering both the effects of spots and faculae, as their possible effects on astrometric jitter might be cancelled or significantly reduced when the configuration is more homogeneous than in the case of a single dark spot.

The astrometric shift was also simulated in the case of a synthetic data series of a planetary transit event. The same Sun-like star synthesized for the simulation shown in Fig. 5.12 was considered with no active regions and a planet with $R_p/R_* = 0.16$ transiting with an impact parameter $b = 0.5$. The resulting astrometric shift curves computed for the Gaia passband are shown in Fig. 5.13. The maximum ΔA in this case is of $\sim 0.179 R_*$ and occurs when the planet is at a projected distance of $\sim 0.56 R_*$ from the center of the stellar disc. This peak is closer to the limb than in the case of a single spot for the same star and passband due to the fact that the projected area of the spots is reduced as they move towards the limb, whereas in the case of the planet it is a projected circle with a constant size.

A sample of Sun-like stars with a specific range of geometrical and physical properties and random distributions of active regions was studied in order to evaluate the effects of astrometric jitter and its correlation with the amplitude observed in the light curve. The Gaia instrumental passband was used and a sample of 10000 stars with temperatures ranging from 4200 to 6800 K,

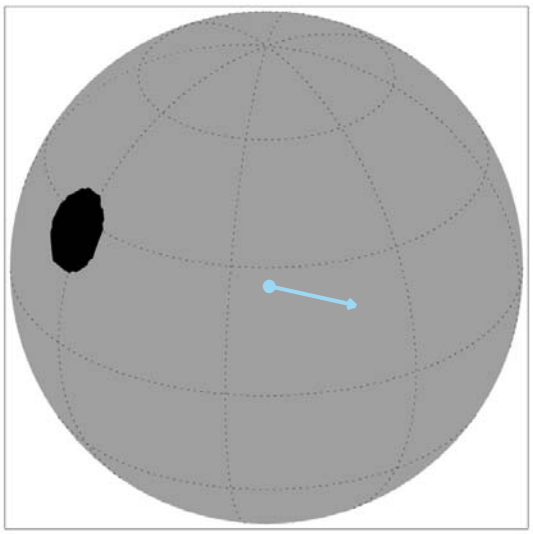

Figure 5.12: Astrometric shift of the photocenter produced by a single spot on the surface of a Sun-like star. The blue arrow indicates the direction, and its modulus has been enlarged by a factor of 20 to better illustrate the effect.

surface gravities corresponding to main sequence stars, and solar metallicities and abundances. The stellar axis inclination of each star was determined stochastically from a flat distribution in $\sin i$ (see Sect. 3.3.2), and the rotation period was generated from a gaussian distribution with $\bar{P_{\rm rot}} = 25$ days and $\sigma(P_{\rm rot}) = 10$ days. The number of active regions of the stochastically generated distributions was always between 5 and 15, considering a temperature contrast $\Delta T_{\rm fac} = 300 - 800$ K linearly scaled with $T_{\rm eff}$, a mean spot size $\bar{A}_{\rm Sn} = (1.9 \pm 0.3) \cdot 10^{-3}$ in units of the total stellar surface, and a lifetime of 90 ± 30 days. Faculae with a temperature contrast $\Delta T_{\rm fac} = 30$ K and a facular-to-spotted area ratio $Q = 8.0$ were considered for all the active regions in all the stars. No transiting planets were introduced in these simulations.

The results of the 10000 synthetic data series along 100 days with a cadence of 1 day are plotted in Fig. 5.14, showing the rms of the light curve ($\rm rms_{flux}$) vs. the rms of the astrometric shift ($\rm rms_A$). A strong correlation between both quantities is evident for all the simulated sample. However, the dispersion increases with activity (i.e., with the number of spots) due to the different distributions of the active regions in the stellar surfaces and also the different geometrical configurations of the stars (i.e., the inclinations of the stellar rotation axes). Notice that a given distribution of spots will produce a maximum $\rm rms_{flux}$ when the star has an inclination $i \simeq 90°$, as rotation modulation will produce a higher signal, while only flux variations due to evolution of active regions will be observable when the star is observed pole on. On the other hand, astrometric jitter is produced at similar amplitude scales for all geometric configurations. Therefore, a star with a specific axis inclination will be most likely found in a determined region of the diagram in Fig. 5.14. The stars with $i < 40°$ are plotted with blue dots, the ones with $40° < i < 70°$ are plotted with black dots, and $i > 70°$, thus showing the highest $\rm rms_{flux}$, are plotted with red dots.

Although the time span and cadence of the synthetic data series does not correspond to the real data monitoring strategy of the Gaia mission (see Eyer et al. 2013), the results presented in

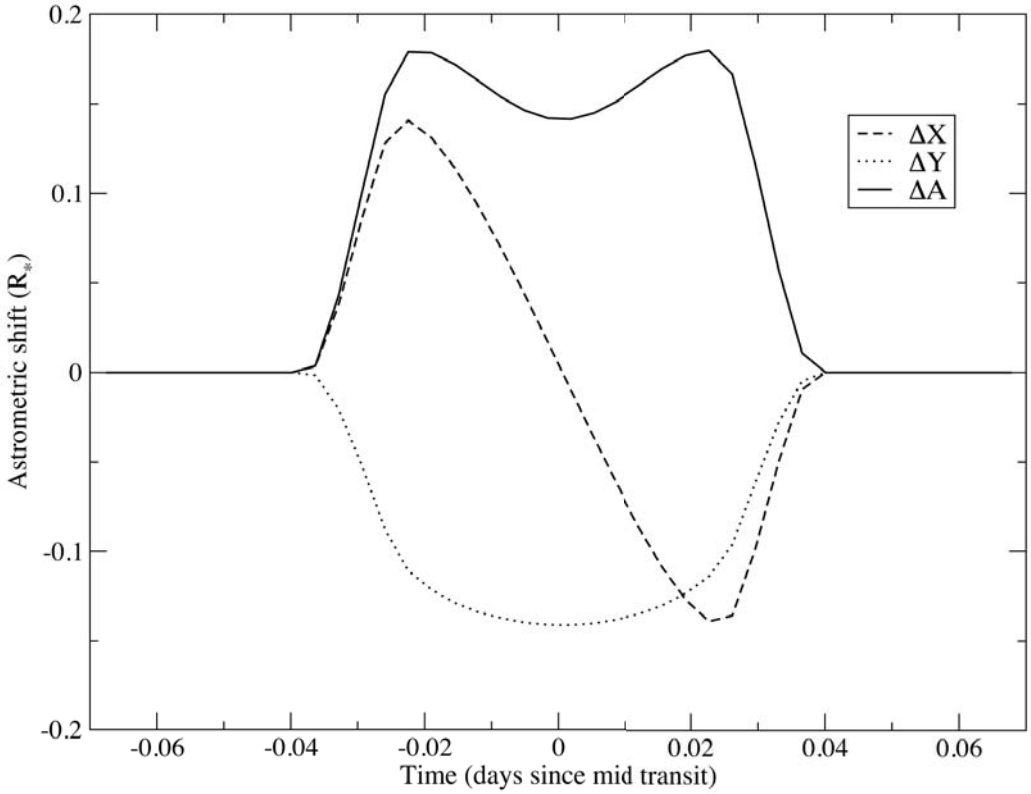

Figure 5.13: Astrometric shifts on the X and Y and the total ΔA produced during a transit of a hot Jupiter planet with $R_p/R_* = 0.16$ and an impact parameter $b = 0.5$ on the same star simulated in Fig. 5.12.

this work are intended to highlight the detectability and effects of activity jitter in astrometric measurements, as well as to evaluate strategies to put constraints on stellar inclinations. Notice that for all the cases in the sample shown in Fig. 5.14, the astrometric jitter is of a lower order than in the first example where a single spot was considered (see Fig. 5.12). An $\mathrm{rms_A}$ of $0.002R_*$, containing $\sim 33\%$ of the stars of the simulated sample, would be above the detection limit of the Gaia mission only for stars at distances lower than ~ 26.7 parsecs, thus for a low number of candidates. Therefore, the implementation of this methodology to put constraints on stellar inclinations would be currently limited to the most active stars in the solar neighborhood. A similar statistical methodology to constrain stellar inclinations from simulated samples, together with a discussion on the importance of axis inclination measurements in exoplanetary sciences, is presented in Chapter. 3. A further study on inclination constraints from astrometric and flux jitters and its application to Gaia observations will be carried out as future work.

5.4 Activity effects in HD 189733

5.4.1 System parameters and active regions

The exoplanet host HD 189733 is a bright (V = 7.67 mag) K0V-type star known to present significant rotation modulation in its light curve (Winn et al. 2007) with a period of ~ 11.9 days and to be relatively active from the measurement of the chromospheric activity indexes (Wright et al. 2004; Moutou et al. 2007). The existence of a hot Jupiter planet with a short period (2.2 days) was first reported by Bouchy et al. (2005b). Several studies have reported the presence of activity effects on the radial velocity measurements up to ~ 15 m s^{-1} (Lanza et al. 2011a; Bouchy et al. 2005b) and have obtained information about the stellar surface photosphere from the modelling of the flux variations (Croll et al. 2007; Lanza et al. 2011a). The parameters for the HD 189733 system, as used in all the simulations in this section, are presented in Table 5.4.

Miller-Ricci et al. (2008) studied the transit timing variations (TTVs) and the transit depth variations (TDVs) from 6 transit observations obtained by MOST, which monitored HD 189733 for 21 days during July - August 2006. No significant effects of spot crossing events were observed at any phase of the transits, but no further discussion on the possible effects of non-occulted spots is presented. When a transiting planet passes in front of a starspot, the depth of the transit is shallower in a portion of the transit due to the fact that the planet has crossed a dimmer region of the photosphere. In the case of low signal-to-noise observations that cannot resolve the event, this would affect the overall transit depth fit. Also, TTVs of ~ 1 minute would be induced if a spot crossing event occurred at the ingress or egress phases of the transit. See Barros et al. (2013) for an extensive discussion on the effects of a spot crossing event on transit measurements of a hot Jupiter planet. On the other hand, non-occulted spots present during the transit time introduce a wavelength dependent variation of the stellar flux (see Sect. 5.3.3 for further discussion on the chromatic effects of activity on TDVs). Thereafter, they can produce a bias in the transit depth measurement and modify the signature of the atmosphere of the planet as studied by transmission spectroscopy. Since a spot is modelled as a cooler region in the stellar surface, its signal will be higher in the blue, where the temperature dependence increases, than in the red.

Pont et al. (2007) describe some properties of the groups of starspots in HD 189733 from the observation of two spot crossing events. The features observed in the transit light curves show a wavelength dependence and can be explained by the presence of cool regions with

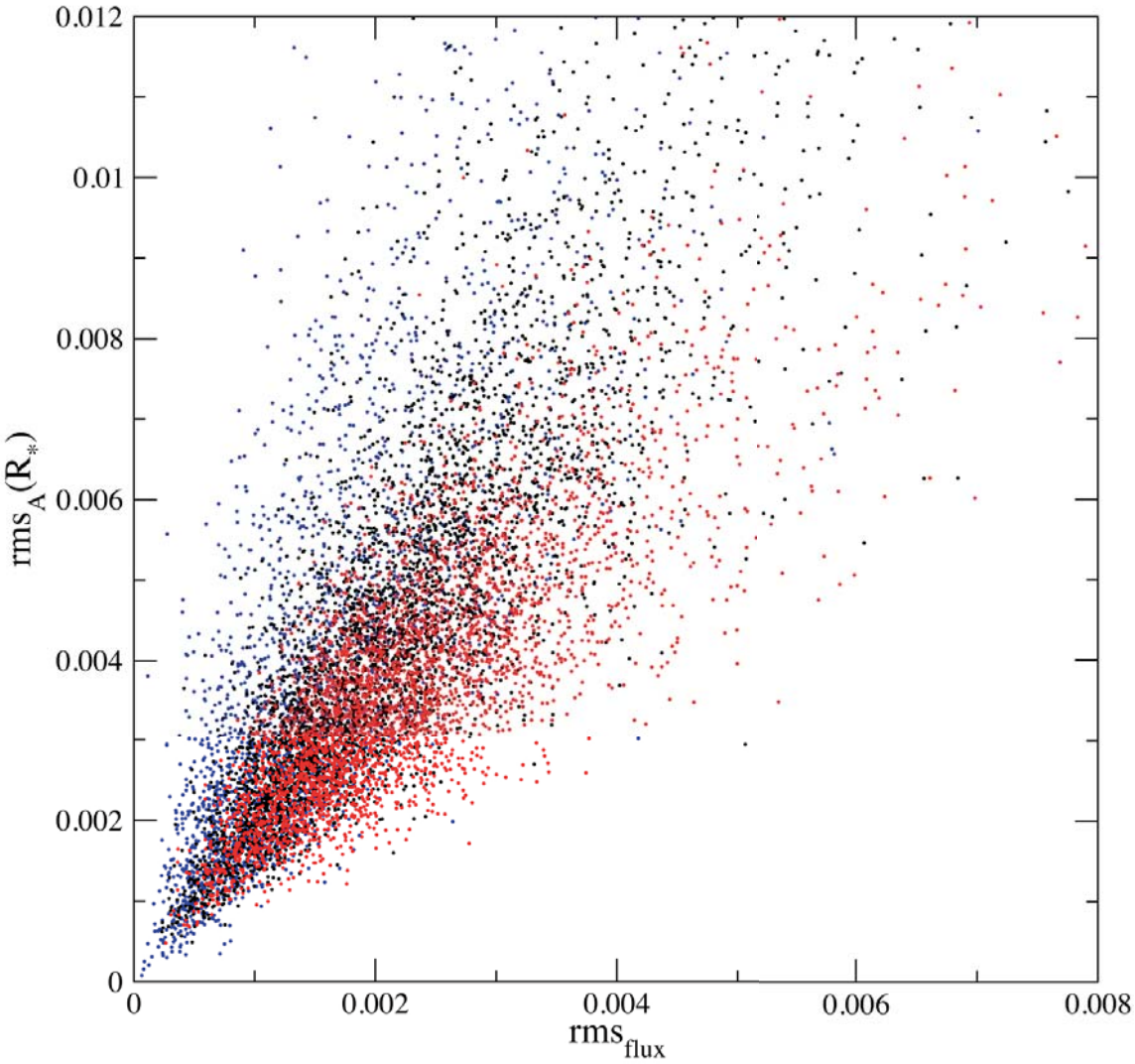

Figure 5.14: The rms of the astrometric jitter in the Gaia passband vs. the rms of the flux variations (in relative flux units) for a sample of 10000 stars. Stars with an axis inclination $i < 40°$ are plotted with blue dots, $40° < i < 70°$ are plotted with black dots, and $i > 70°$ are plotted with red dots.

Table 5.4: Parameters for the system HD 189733

Parameter	Value	Reference
$T_{\rm eff}$	5050±50 K	M06
$\log g$	4.53±0.14	M06
[Fe/H]	-0.03±0.04	M06
$\Delta T_{\rm spot}$	∼560 K	L11
Q	0.0	L11
P_0	10.7 days	H14
i_*	$85.5^\circ \pm 0.1^\circ$	T09
$A_{\rm Sn}$	$5 \cdot 10^{-4} - 3 \cdot 10^{-3}$	L11
$P_{\rm planet}$	2.2185733±0.0000014 days	MR08
$R_{\rm planet}/R_*$	0.1572±0.0004	P07
b	0.671±0.008	P07
γ	1.4±1.1°	W06

References: M06 (Melo et al. 2006); MR08 (Miller-Ricci et al. 2008); P07 (Pont et al. 2007); L11 (Lanza et al. 2011a); H08 (Henry & Winn 2008); T09 (Triaud et al. 2009); W06 (Winn et al. 2006), H14 (this work).

$\Delta T_{\rm spot}$ ∼1000 K and a size of ∼ 12000 km to ∼ 80000 km, which correspond to $A_{\rm Sn}$ of $\sim 2 \cdot 10^{-5}$ to $\sim 6 \cdot 10^{-3}$ in units of the total stellar surface.

Lanza et al. (2011a) obtain a more detailed map of the active regions distribution by modelling MOST photometry and radial velocity measurements from SOPHIE obtained for the same time span. Their approach is based on reconstructing maximum entropy map with regularization (see Sect. 4.4.2 in this work for further details on the methodology). This allows to model the longitudinal evolution of active regions over time, but the information on the latitudes is cancelled particularly when the inclination of the rotation axis along the line of sight is close to 90°, as is the case. So the method tends to assume that the spots are located near the stellar equator, hence adopting the minimum possible size for the spots to model the observed variations. The results show that the data can be explained by the presence of 2 to 4 active regions up to $4 \cdot 10^{-4}$ precision in relative flux units for the photometry, and a few m s^{-1} for the radial velocity measurements. The individual spots cover 0.2 to 0.5% of the stellar disc and their lifetimes are comparable or longer than the duration of MOST observations (i.e., ∼ 30 days), while the rise and decay occur in 2-5 days. In this case, the spot contrast is computed assuming a spot effective temperature of 4490 K (i.e., $\Delta T_{\rm spot} = 560$ K). A different spot contrast will imply a change in the absolute spot coverage to explain the same photometric signature (Pont et al. 2007), and despite not having a significant effect in a single band photometric time series as long as consistent values are adopted, it would affect the spectral signature of the spots, as discussed later (see Sect. 5.4.2). Fares et al. (2010) measured the equatorial and polar rotation periods obtaining 11.94 ± 0.16 days and 16.53 ± 2.43 days, respectively, thus giving a relative amplitude of $\Delta\Omega/\Omega = 0.39 \pm 0.18$, which is very similar to the Sun (so we assume $k_{\rm rot} = 1$). Then, the migration rates of spots measured by Lanza et al. (2011a) indicate that most of the spots are located at latitudes ranging from 40° to 80°.

In this work we use the use the distribution of active regions as defined from the information and surface map given by Lanza et al. (2011a) as an initial approximation and then use the program `StarSim` in order to manually fit the parameters of a set of 13 spots that best reproduce

the MOST photometry, as will be presented in Sect. 5.4.2, and to derive the resulting radial velocity variations (see Sect. 5.4.3). The adopted stellar and planet parameters are presented in Table 5.4. The presented synthetic data series will allow us to characterize the chromatic effects of activity on HD 189733b transit observations and optimize the design of future observation strategies.

5.4.2 Activity effects in transit photometry

Synthetic light curves for HD 189733 were generated using the methodology implemented in the program `StarSim` and presented in Sect. 5.2.2 for a set of twelve different photometric passbands ranging from the blue-visible to the mid-infrared (Johnson UBVRI, 2MASS HJK and Spitzer IRAC filters) covering the whole time span of the simultaneous MOST/SOPHIE observations (i.e., 14 transits of the exoplanet HD 189733b), from HJD 2454298.55874 to 2454329.05818. The light curve in the MOST photometric passband was also computed and a map of 13 active regions with the properties described in Sect. 5.4.1 was considered in order to model the MOST data. Whereas longitudes and sizes of the spots were iteratively varied to minimize the χ^2 of the residuals, a uniform distribution of latitudes in the northern hemisphere was considered. Photon shot noise was also introduced assuming that the data were obtained with a 1 m telescope and a 0.7 quantum efficiency detector. However, the effect is negligible due to the brightness of HD 189733 and the use of broad band filters. The resulting light curve has a maximum amplitude of ~ 0.012 mag in the MOST passband. The light curve fit to the MOST photometry and examples of one of the near-infrared and mid-infrared bands are presented in Fig. 5.15, together with the residuals between the MOST photometric model and the observations. The residuals of the fit show an rms of $4.72 \cdot 10^{-4}$ in relative flux units. In comparison, an rms of $4.86 \cdot 10^{-4}$ is obtained with the maximum entropy model by Lanza et al. (2011b). The slight improvement may be due to the fact that the methodology presented in Sect. 5.2.2, based on the integration of stellar models, reproduces better the resulting flux contributions from the photosphere and the spots.

The residuals in Fig. 5.15 show some oscillations with a typical timescale of $\sim 1-2$ days. Lanza et al. (2011b) suggest that these could be due to spot size variations of the order of $\sim 0.2-0.3$ percent of the stellar disc, that are not correctly reproduced by a model without evolution of spots. Although our model can reproduce the rise and decay of spots (see Sect. 5.2.2), not enough information on the rise and decay rates of the active regions in HD189733 is available to include this effect in our simulations. Also, very small spots with lifetimes shorter than the rotation period were not included in our model, as they do not produce significant flux modulation at the largest timescales represented in the data. These could also be responsible for the oscillations in the residuals.

The effect of the spots is characterized by a dependence of the amplitude of the light curve on the passband (see Sect. 5.3.1). This spectral signature of the activity jitter is shown in Fig. 5.16 by plotting the rms of the out-of-transit data series vs. the equivalent wavelength of the passband. The effect is strongly dependent on wavelength up to $\lambda \sim 1500$ nm, and almost constant onwards. Observations of the chromatic dependence of jitter, i.e. simultaneous time series photometry in different filters, would help to solve solve the degeneracy between the spot filling factor $\bar{F}F$ and the temperature contrast $\Delta T_{\rm spot}$.

For each passband, data intervals of $2 \cdot T14$ (i.e., twice the total duration of the transit) around the transit events were selected for analysis. The out-of-transit baselines at either side

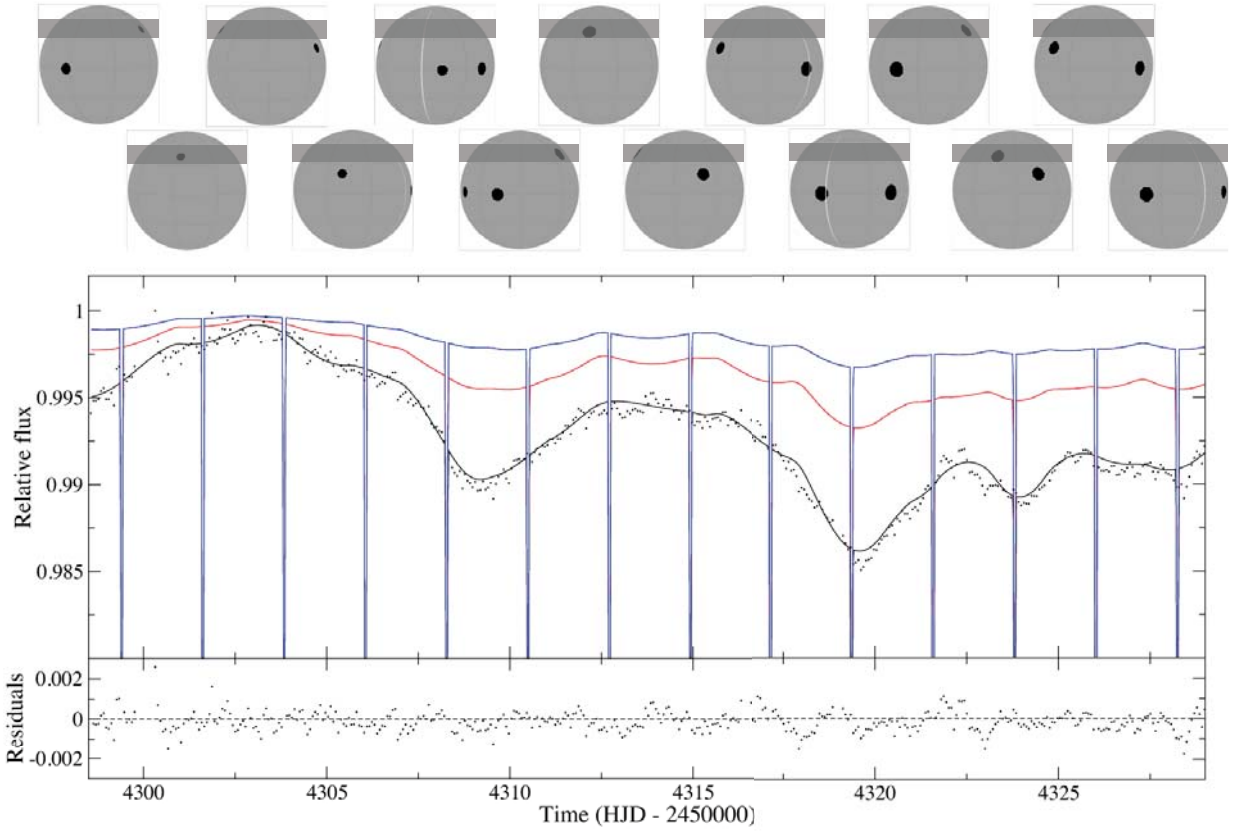

Figure 5.15: Synthetic light curves generated for HD 189733 with the methodology described in Sect. 5.2.2 assuming the parameters and active regions distribution described in Sect. 5.4.1 for the MOST (black line), 2 MASS J (red line) and IRAC 2 (blue line) passbands. The flux is in relative units with respect to the maximum along the light curve and shows the 14 analysed transit events. Observed data from the MOST 2007 campaign is plotted with black dots. The projected maps of the stellar surface at the mid-transit times are plotted in the upper part, including a dark grey band that indicates the region of the star occulted by the planet.

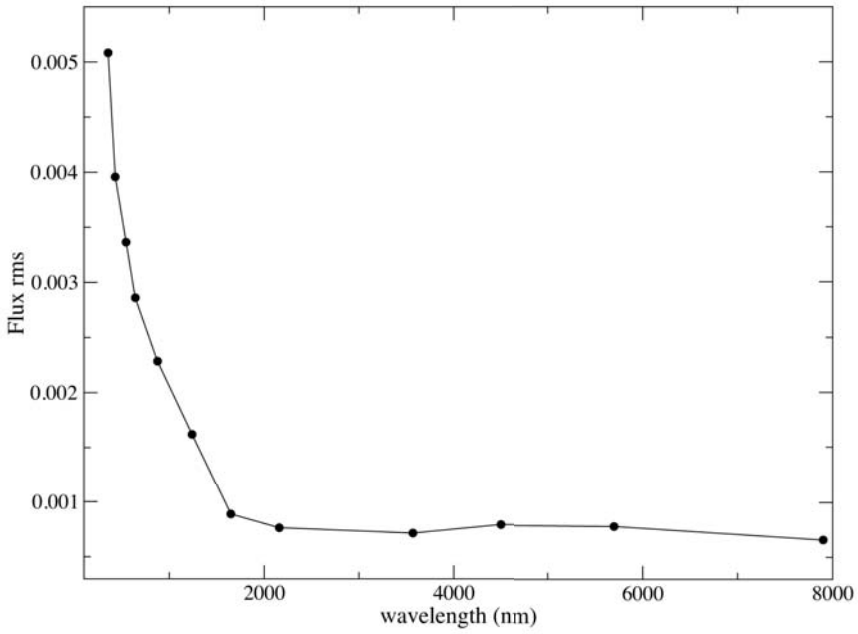

Figure 5.16: The rms of the out-of-transit relative flux computed for the synthetic light curves with 12 different filters (Johnson UBVRI, 2MASS JHK and four IRAC) vs. the equivalent wavelength of the filters.

of the transit were used in order to fit a parabolic trend that was subsequently subtracted from the in-transit observations. Then, a Mandel & Agol (2002) model was fitted to each individual transit using `JKTEBOP` code in order to measure the transit depth and the mid transit time. In a first step, precise quadratic limb darkening coefficients were obtained for each passband by fitting a model to a transit light curve generated for an unperturbed photosphere (without spots). With these limb darkening coefficients, the whole series of transits was analysed by fitting the planet radius and the time zero of ephemeris. The rest of the parameters were fixed to the ones presented in Table 5.4.

A number of spot crossing events have been detected in HD 189733b transit observations (Miller-Ricci et al. 2008; Sing et al. 2011; Pont et al. 2013). The observed occurrence of these events combined with the assumption that the planet is crossing a typical zone of the stellar surface in terms of spot coverage, leads to a $1-2\%$ of projected spots filling factor (Sing et al. 2011), which is in agreement with the results by Lanza et al. (2011a) and the spots map used in this work. In the case of our synthetic data, as the active regions map is poorly constrained due to the low signal-to-noise ratio of the MOST observations (see Lanza et al. 2011a), and especially the latitudes of spots are degenerated, we do not expect all the events from the MOST data to be accurately reproduced. On the other hand, the 14 synthetic transit observations contain a variety of spot distributions, both occulted and non-occulted by the planet, and allowed us to study and quantify the chromatic effects of activity in HD 189733b transit observations. The photometry of the transit occurring at HJD$\sim$2454321.575 is shown in Fig.5.17, also displaying a map of the stellar surface, which shows the position of the spots and the area occulted by the planet. The bottom panel shows the flux residuals after subtracting the out-of-transit trend and

the model of an unperturbed transit. One prominent feature corresponding to a spot crossing event appears after the mid transit. The second feature is a non-occulted spot, which produces an increase on the overall transit depth (see Sect.5.4.1). So both active areas introduce some effect in the transit measurement parameters, especially in the transit depth and the mid transit time.

The results for the analysis of the series of synthetic transit data are displayed in Fig.5.18, showing the chromatic dependence of the planet radius determination for each transit event. Some of the transits are affected by spot crossing events and are plotted in red. All transits present some effect of non-occulted spots. All the measurements for R_p/R_* are normalized by the values obtained for the transit light curve simulated on an unperturbed photosphere.

Occultations of spots have remarkable effects in the visible wavelengths, but their signal is much lower in the near and mid-infrared, so that simultaneous observations in the visible may be essential in most cases in order to detect their presence. The most typical approach is to remove the part of the data affected by spot crossing events before performing transit measurements. Pont et al. (2013) use the entire data for the infrared wavelengths, where the features are negligible, and estimate the uncertainties from the light curve variability. However, by assuming that the effects of occultations are averaged, a significant bias is introduced in the planet radius measurement ($\Delta\left(R_p/R_*\right) \sim -0.001$) with respect to the unperturbed transit measurement for the Spitzer IRAC filters. This is shown by the red dots in the upper panel of Fig. 5.18, which are systematically below $R_{\rm planet}/R_* = 0.1572$ for the infrared.

On the other hand, spots not occulted by the planet introduce a regular behavior from the ultraviolet to the mid-infrared wavelengths. As the presence of spots in the stellar surface changes the overall transit depth measurement, and the duration of the transit is much lower than the stellar rotation period (i.e. the typical changes in the projected filling factor), there are no significant differences on the measured times of mid-transit. However, the spectral signature of the spots clearly dominates the effects introduced on the transit depth, as seen in the top panel of Fig. 5.18. The results for one of the passbands in the visible, the near-infrared and the mid-infrared are also presented in Table 5.5 together with the spot filling factor at the mid-transit times. For all transit simulated observations, the effect produced by spots is much stronger in the blue than in the mid-infrared, thus reproducing the shape of the spectral signature of the spots (see Fig. 5.16). However, notice that the shift on the transit depth measurement introduced by non-occulted spots is also scaled with the current filling factor, ranging from $\Delta\left(R_p/R_*\right) \sim 0.0001$ for a nearly unspotted surface (corresponding to the 3rd transit, at HJD$\sim$2454301.8 in Fig. 5.15) to ~ 0.0012 for the 10th transit in the series, occurring near HJD$\sim$2454319.5, when the surface presents a spot filling factor of 2.45%. Figure 5.19 displays the measured R_p/R_* vs. the projected filling factor of spots at the mid transit times for all the filters used in this analysis, showing a linear dependence in all cases. Again, a strong effect is observed especially in the visible bands, where the observed variations in the filling factor during the analysed transit series produce up to $\Delta\left(R_p/R_*\right) \sim 0.001$ variations. This is an important information to account for when correcting the transit depths for activity, as there is a significant variability on the filling factor over time in the case of HD 189733. Notice that the spot filling factors affecting our simulations (shown in Table 5.5) assume that the star is unperturbed at the moment of the flux maximum in the MOST light curve (Lanza et al. 2011a). Although the evolution of the spots map we used accurately reproduces the variations, a zero point in the filling factor of spots could be present. However, the statistics of spot crossing events during HST observations and the characteristics of the transmission spectrum in the visible (Sing et al. 2011), indicate that the projected spots

Table 5.5: Activity effects in transit depth measurements of HD 189733b. Transit events affected by spot crossing events are indicated with a $*$ symbol.

Transit	Projected spots filling factor (%)	R_p/R_* Johnson U	R_p/R_* 2MASS J	R_p/R_* IRAC 4
1*	0.85	0.1581 ± 0.0002	0.15754 ± 0.00003	0.15728 ± 0.00001
2*	0.38	0.152 ± 0.001	0.1562 ± 0.0001	0.15691 ± 0.00004
3	0.34	0.15718 ± 0.00002	0.157251 ± 0.000008	0.157225 ± 0.000006
4	0.68	0.15745 ± 0.00002	0.157317 ± 0.000008	0.157247 ± 0.000006
5	1.46	0.15790 ± 0.00002	0.157478 ± 0.000007	0.157313 ± 0.000005
6*	1.75	0.1599 ± 0.0005	0.15810 ± 0.00008	0.15737 ± 0.00002
7*	0.99	0.146 ± 0.003	0.1550 ± 0.0003	0.1564 ± 0.0001
8	1.03	0.15760 ± 0.00003	0.157387 ± 0.000008	0.15728 ± 0.000006
9	1.59	0.15782 ± 0.00002	0.157495 ± 0.000007	0.157327 ± 0.000005
10	2.45	0.15843 ± 0.00002	0.157697 ± 0.000008	0.157410 ± 0.000006
11*	1.93	0.1641 ± 0.0006	0.1584 ± 0.0001	0.15737 ± 0.00004
12*	1.97	0.149 ± 0.003	0.1554 ± 0.0003	0.15660 ± 0.00009
13	1.72	0.15783 ± 0.00002	0.157526 ± 0.000007	0.157334 ± 0.000006
14	1.76	0.15798 ± 0.00002	0.157523 ± 0.000007	0.157333 ± 0.000006

filling factor is not much higher than 1-2 %.

5.4.3 Activity-induced radial velocity variations

In order to simulate and analyze the effects of the radial velocity variations produced by activity, we adopted the distribution of active regions derived with `StarSim` from the MOST photometry and the map by Lanza et al. (2011a) as described in Sect. 5.4.1. The signal of the planet was removed and we considered the stellar parameters from Table 5.4. The time span of the simulations covers around three stellar rotation periods from HJD$\sim$2454298, and is simultaneous to the radial velocity measurements obtained for HD 189733 with the high resolution spectrograph SOPHIE (Boisse et al. 2009). The cross-correlation for the computation of radial velocities (see Sect. 5.2.2) in our simulations was performed using a HARPS mask template for a K5 type star (Lovis et al. private communication). This consists on a selection of delta-peak lines, whose height corresponds to the line equivalent width. The resulting radial velocity measurements for the whole time span of the observations is shown in Fig. 5.20, adopting a time cadence of 10 minutes, compared to the radial velocity residuals from SOPHIE observations. The rms of the synthetic radial velocity curve is $\mathrm{rms_{RV}} = 5.953$ m s^{-1}. This is significantly lower than the ~ 9.9 m s^{-1} found in the measurements by Boisse et al. (2009) and than the model fit developed by Lanza et al. (2011a) for the same time span. Also, Winn et al. (2006) measure 12 m s^{-1} and Bouchy et al. (2005b) obtain 15 m s^{-1}. The residuals between our model and the observations show an rms of 9.862 m s^{-1} and a reduced χ^2 of 2.938. If we exclude the 4 datapoints between HJD$\sim$2454306 and $\sim$2454310 (indicated with dotted lines in Fig. 5.20), then the rms is 5.325 m s^{-1}. Therefore, our model obtains slightly better results than Lanza et al. (2011a) (rms=5.55 m s^{-1}) and Aigrain et al. (2012) (rms=6.6 m s^{-1}). However, some fast fluctuations are still present in the residuals, especially in the area between dotted lines in Fig. 5.20. These could be due to some effects not accounted for in our simulations, as the presence of faculae or

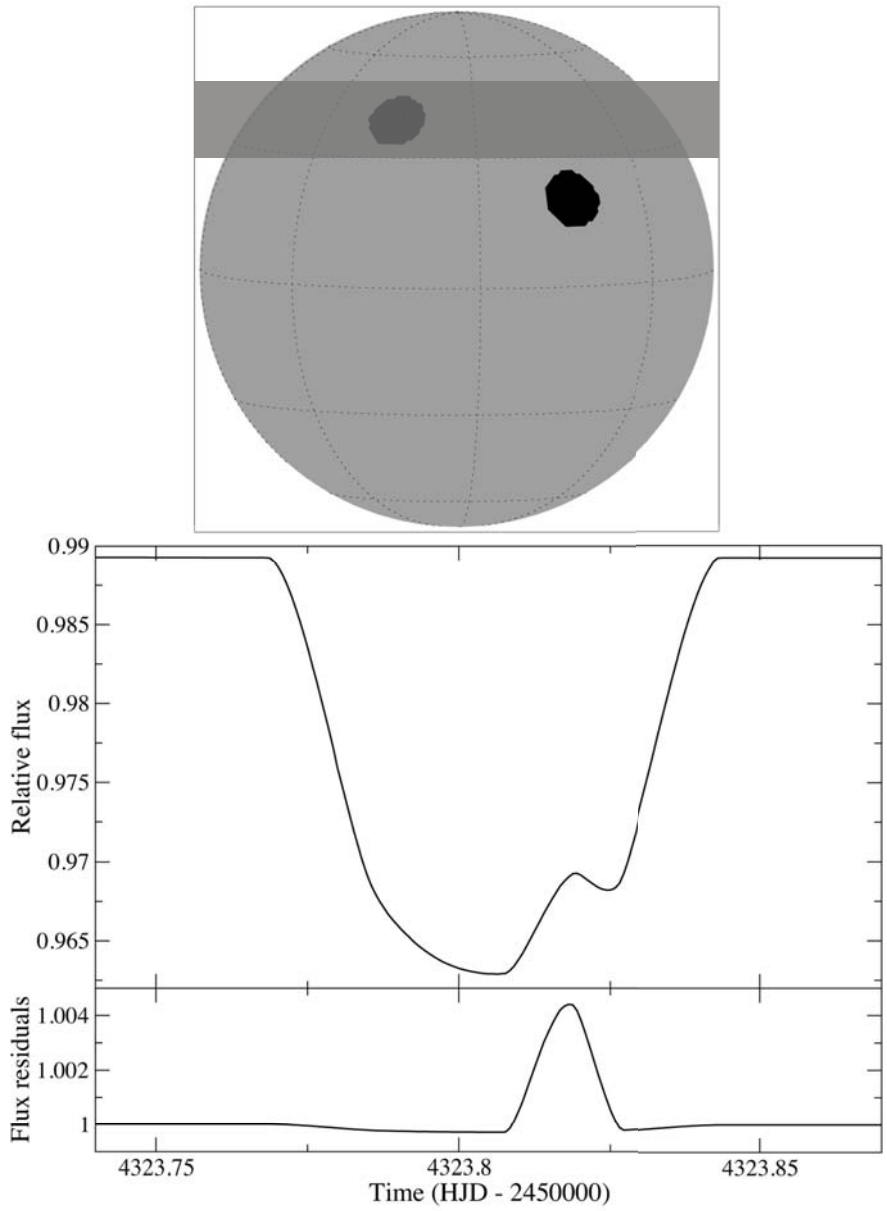

Figure 5.17: A detailed map of the stellar surface during the eleventh transit event of the generated data series, including the band occulted by the planet in dark grey. The corresponding Johnson V filter light curve in relative flux units, showing two spot crossing events, and the flux residuals resulting from the out-of-transit trend and the unperturbed transit model subtractions.

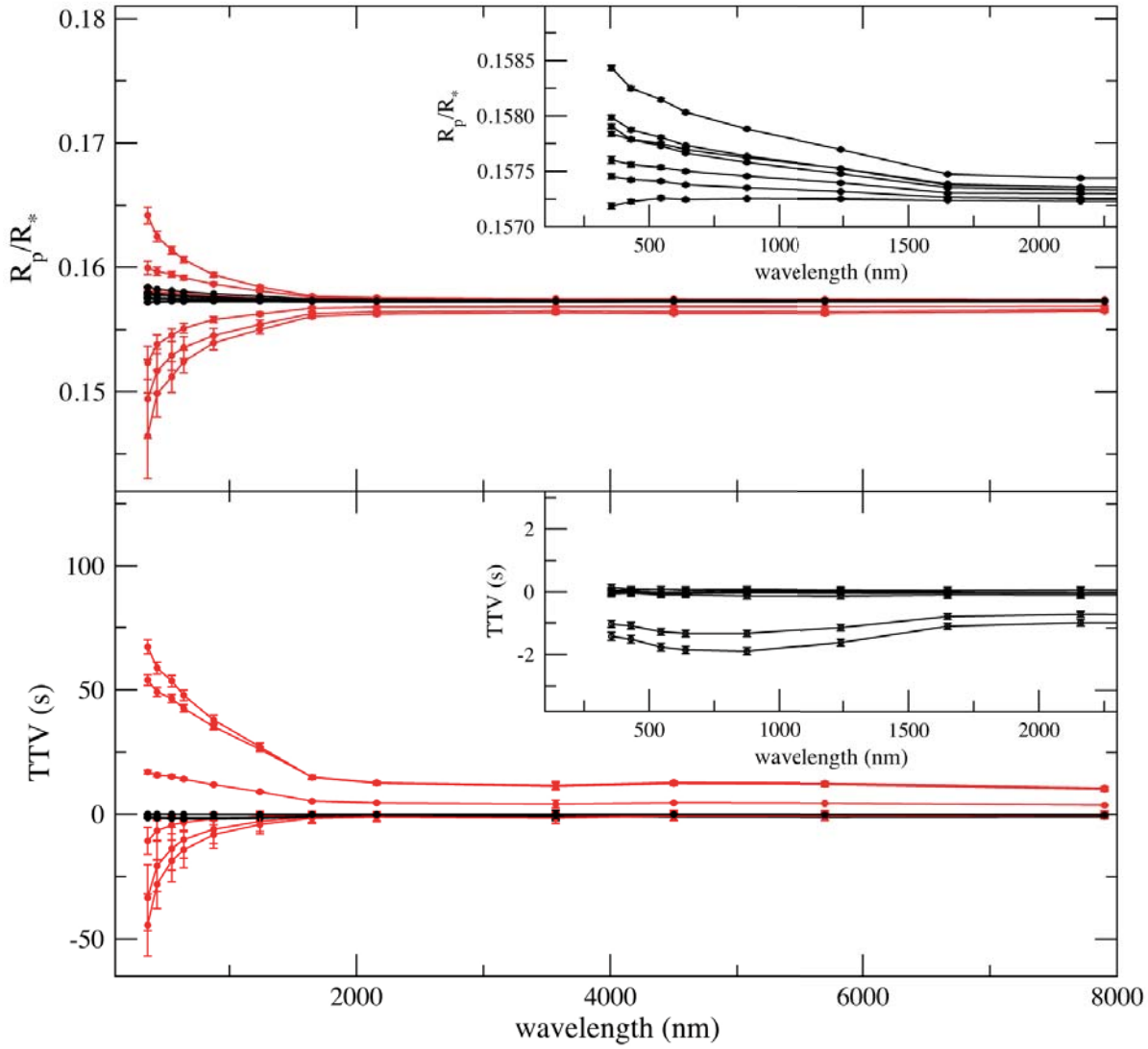

Figure 5.18: Upper panel: variations on the transit depth R_p/R_* vs. the central wavelength of 12 different filters produced by several configurations of spots on the 17 synthetic transits of HD 189733b in the simulated light curves, relative to the transit depth in an unperturbed transit.Transit observations affected by spot crossing events are plotted in red. The upper right panel is a zoom in showing only the observations affected by non-occulted spots. Bottom panel: the same for the transit time variations. The two transits with non-occulted spots showing TTVs of $\sim 1-2$ s correspond to the 3rd and 8th transit, were actually a small spot is occulted very close to the limb (see Fig. 5.15).

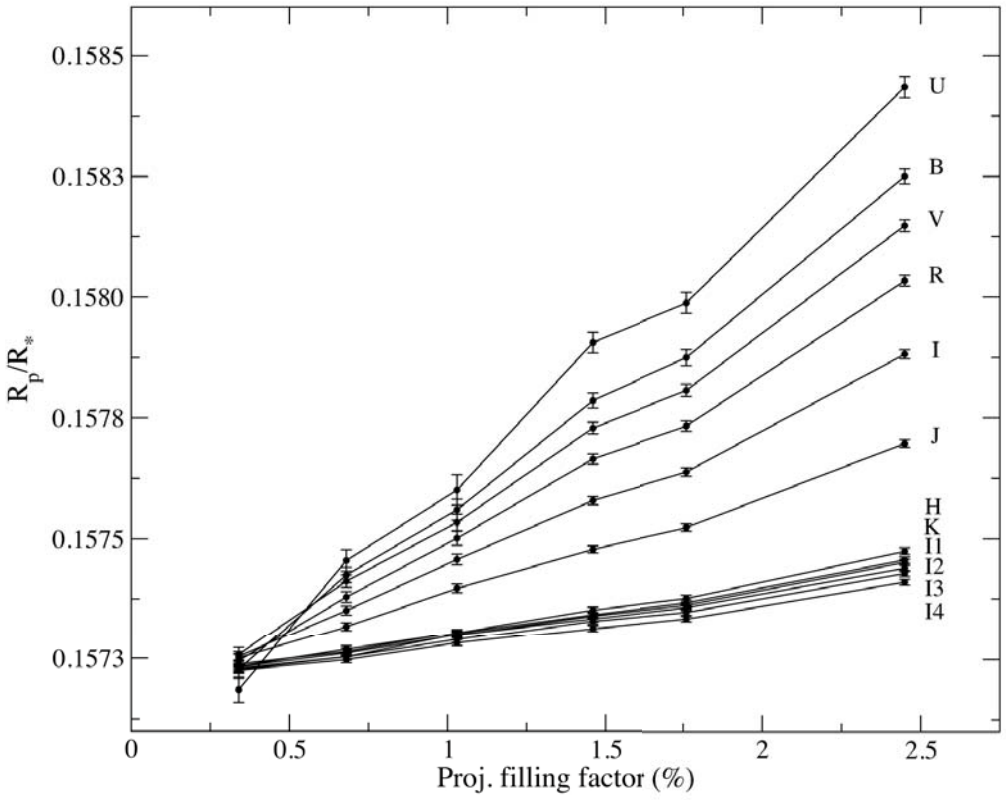

Figure 5.19: Variations on the transit depth R_p/R_* vs. the projected filling factor of spots at mid transit for the each of the 12 different filters used in our analysis (indicated with labels). The transits affected by spot crossing events have been removed.

rapidly evolving groups of spots, and also to possible instrumental systematics of SOPHIE.

Similar synthetic time series of radial velocity data were generated introducing constraints on the spectral range for the calculation of the CCFs. As the spectral signature of the active regions in our model is stronger in the blue than in the red part of the visible spectrum, significant differences are expected for the resulting radial velocity signal. Specific wavelength ranges may contain groups of lines with a different sensitivity on small temperature changes and magnetic field, and therefore a careful selection of the most suitable ranges for the computation of the CCF may be performed. For this simple test we obtain radial velocity curves computed from the lines in a range 370 - 450 nm and in 550 - 680 nm, and the results are plotted in Fig. 5.20. For the selection of the blue range, the resulting rms of the radial velocity curve is 7.789 m s^{-1}, whereas in the red it is 4.897 m s^{-1}. A more detailed strategy for the selection of spectral lines that minimize the radial velocity signal induced by active regions, is left as future work (see Sect. 6.2).

In order to study the effects of activity on planet parameter measurements from spectroscopy, 1000 synthetic radial velocity curves were computed from the simulated data series displayed in Fig. 5.20 using the full HARPS range, each one containing a random selection of 30 measurements distributed along the night times and with a minimum separation of 2 hours. Each of these radial velocity measurement series is equivalent to the sampling in the data presented by Boisse et al. (2009) and simulates a typical follow-up campaign for planet characterization (Bouchy & Queloz 2007) as the ones performed with the SOPHIE at OHP, HARPS at ESO and the HIRES at Keck spectrographs. The offset of the mean radial velocity and the rms of the jitter were computed for each data series. Histograms showing the distributions of these two quantities for the 1000 series are displayed in Fig. 5.21. A gaussian fit to the distribution of mean radial velocities provides a standard deviation $\sigma_{\mathrm{meanRV}} = 1.118$ m s^{-1}. This is a good estimation for the uncertainty introduced by activity on the mean radial velocity of the system when a low number of measurements is available. The distribution of the rms in the 1000 generated runs (lower panel in Fig. 5.21) is centered at $\mathrm{rms_{RV}}$ and has a standard deviation of 0.570 $\mathrm{ms^{-1}}$. On the other hand, a lower number of measurements in the data series broadens the probability distribution. A set of synthetic light curves containing 15 measurements were also computed, and the distribution of $\mathrm{rms_{RV}}$ was fitted with a gaussian with a standard deviation of 1.325 m s^{-1}. This prevents us to interpret the variation observed in the rms of the radial velocity residuals from Winn et al. (2006) and Bouchy et al. (2005b) results (both obtained from < 20 radial velocity measurements) as a significant variability in the activity level.

Orbital elements from Boisse et al. (2009) were used in order to produce a theoretical radial velocity curve with the program SBOP (Etzel 1985). This was added to the 1000 synthetic data series with the previously modelled activity signal, and SBOP was applied to determine the spectroscopic solution for the radial velocity semi-amplitude K, while fixing the rest of the parameters. The distribution of the results for the 1000 tests is presented in Fig. 5.22. The peak of the resulting distribution is $K = 200.179$ m s^{-1}, which is in very close agreement with the initial value of 200.56 ± 0.88 m s^{-1} (Boisse et al. 2009), thus indicating that no significant biases are introduced by activity effects in the determination of the planetary mass. The standard deviation of the distribution is 1.974 m s^{-1}. Therefore, activity effects prevent to determine the planetary mass up to a precision lower than $\sim 0.011 M_{\mathrm{Jup}}$ when only 30 measurements are available.

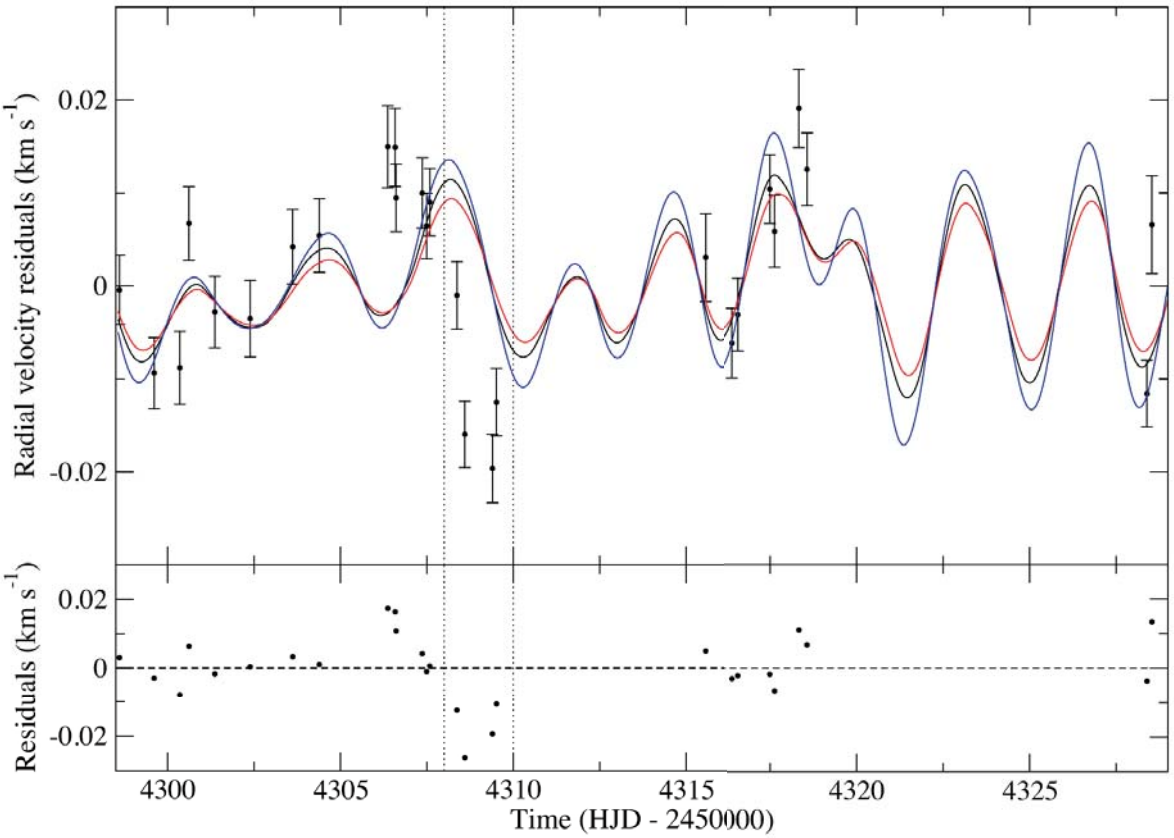

Figure 5.20: Upper panel: Synthetic radial velocity curve generated for HD 189733 computed using the whole range of the HARPS instrument (black line), the blue range (370 - 450 nm, blue line) and the red range (550 - 680 nm, red line), with the methodology described in Sect. 5.2.2 assuming the parameters and active regions distribution described in Sect. 5.4.1 and with the signal from the planet orbital motion removed. The observations from SOPHIE after subtraction of the planet orbit signal are plotted with black dots. The vertical dotted lines indicate the time interval with steep variations that cannot be explained with our model. Lower pannel: Residuals between the model computed with the whole HARPS range and the SOPHIE observations.

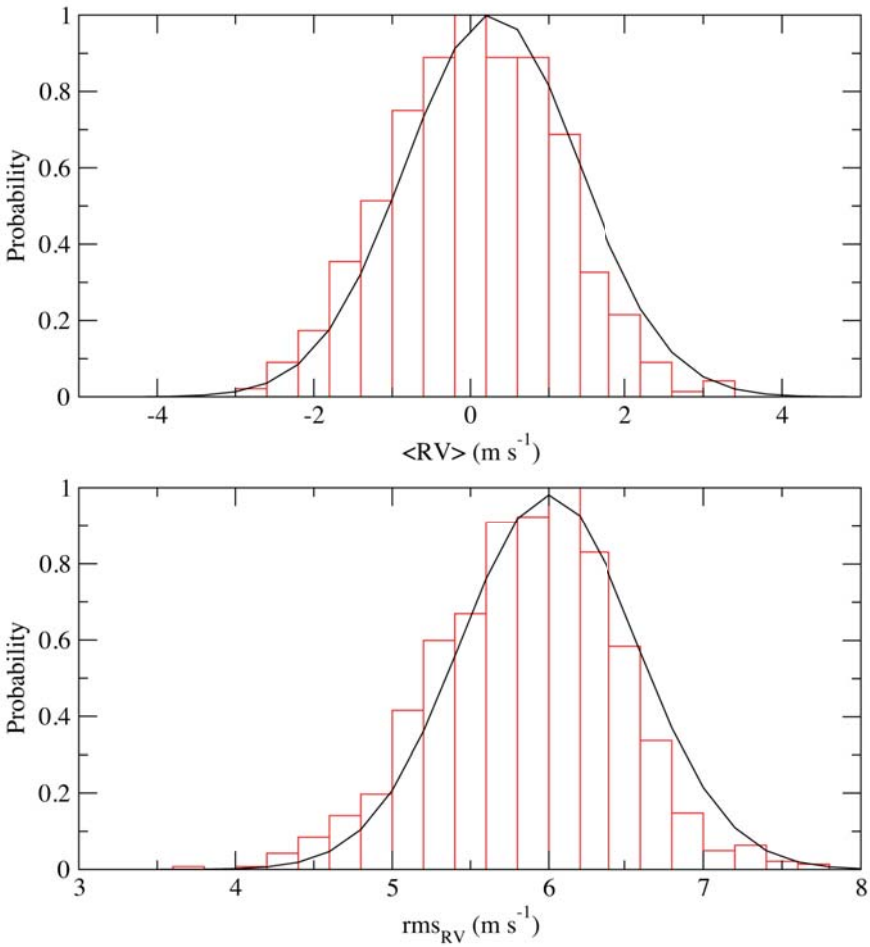

Figure 5.21: Upper panel: probability distribution for the mean radial velocity including the effects of a distribution of active regions in HD 189733, derived from a sample of 1000 synthetic radial velocity curves with 30 data points each. The best fit gaussian function, with a standard deviation $\sigma_{\rm meanRV} = 1.118$ m s^{-1}, is plotted with a black line. Bottom panel: the same for the rms of the radial velocity in the data series. A best fit gaussian function is plotted with a black line, having a standard deviation of 0.570 m s^{-1}.

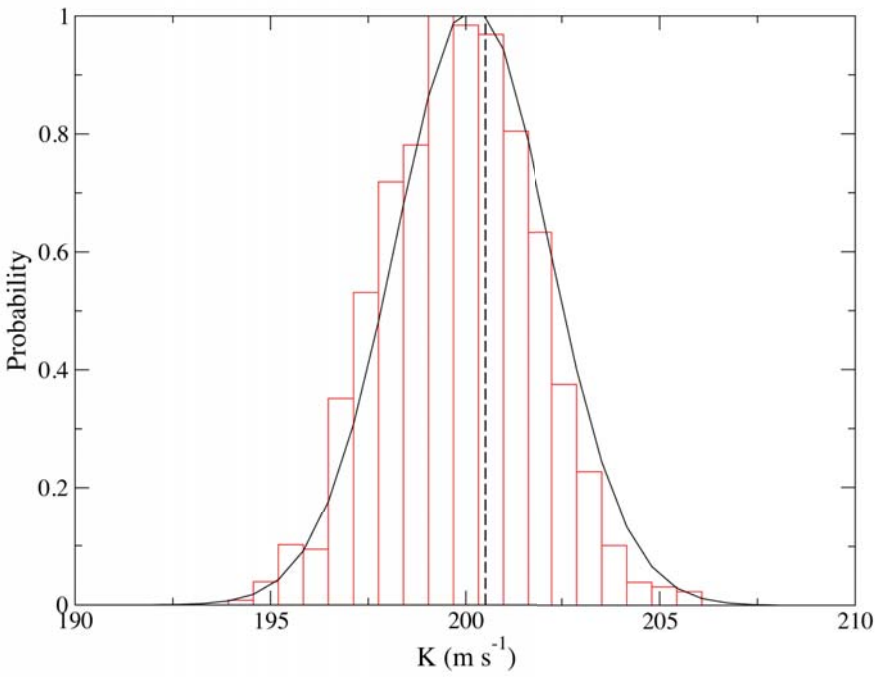

Figure 5.22: Probability distribution for the radial velocity semi-amplitude K determined using SBOP for a set of 1000 curves including simulated activity effects. The best gaussian fit of the distribution, with a standard deviation of 1.974 m s^{-1}, is plotted with a solid line. The value of K introduced in the theoretical orbit is indicated with a dashed line.

5.5 Discussion and conclusions

A methodology to simulate the photosphere of a rotating spotted star was presented. This is implemented in the program `StarSim`, which allows us to generate synthetic photometric and spectroscopic time series data from a set of given parameters and a library of atmosphere stellar models. The main purposes of this methodology are the characterization of the effects produced by activity and time series observations, especially multi-band studies of exoplanetary transits, and the design of strategies for the minimization of activity effects, both when searching and when characterizing exoplanets. A faster version of the program is currently being developed and will be available in the near future. This will have a limited number of free parameters and some optimized routines in order to be able to model photometric and spectroscopic observations to obtain detailed stellar surface maps and also fit transit observations including activity effects. Regarding the current implementation, several aspects should be taken into account in order to discuss the credibility of the results and their interpretation.

First, we assumed LTE stellar models for the emission of the quiet photosphere and also for the spots and facula regions. This is a limitation imposed by the availability of stellar model libraries with high resolution spectra. The synthetic spectrum shown in Fig. 5.2 correctly fits the observed spectrum of a spot and provides a temperature contrast in agreement with most of the values in the literature (see Sect 5.2.1). However, certain lines are not reproduced, which suggests that the spot spectrum is different from a cooler stellar photosphere. In the case of faculae, no high resolution observed spectra are currently available, and the most recent non-LTE models for the Sun are the ones presented by Fontenla et al. (2009). The differences in the spectrum of active regions mainly affect the existence of certain lines, but have no significant effect on the flux when considering a broad range of the spectrum. Therefore, the currently used models are suitable for the characterization of activity effects in the observations for most of the photometric instrumentation. Some more considerations on the influence of the models for the different photospheric features will be exposed in a future paper addressing strategies for the correction of radial velocity measurements in active stars.

Second, the maps of active regions currently used in our simulations are limited to a model of circular spots with a surrounding coronal facula, instead of a more complex structure with groups of small spots. Our approach is very similar to the one adopted by Lanza et al. (2003) and subsequent papers that use this type of spot maps in order to model the surface of a number of active stars (see Sect. 4.2). In that case, the regularization of the maximum entropy algorithm provides a smooth distribution of active regions instead of a more irregular surface map populated with a lot of small spots. Although our model also allows for an unlimited number of spots of a small size to be included in the stellar surface, more simple distributions have proved to adequately reproduce photometric signature in active stars.

An example of the capabilities of the methodology for the characterization of activity effects is presented for the case of a Sun-like star with a typical distribution of active regions (see Sect. 5.3.1). The spectral signature (flux rms vs. wavelength) of the active regions is studied in visible and infrared passbands for several configurations of the parameters of the stellar surface. Different configurations of the temperature contrast ($\Delta T_{\rm spots}$) and the typical area of the spots ($\bar{A}_{\rm Sn}$) are found to show a very similar signature when no faculae are introduced. In the presence of faculae ($Q = 8.0$, $\Delta T_{\rm fac} = 30$ K), the wavelength dependence is inverted in the red and near-infrared wavelengths when the temperature contrast of the spots is < 300 K, thus being the contribution of faculae dominant. In all cases, the dependence is strong in the visible and near-

infrared, while no signature is observed in the mid-infrared. Real observations of the spectral signature for active stars in visible and near-infrared filters may provide new estimations of the facular-to-spotted area ratio (Q) and the parameters of the spots.

Some methodologies are presented in order to correct for activity effects on exoplanet transit observations when multiband photometric data are available. We proved that activity effects introduced in transit measurements can be removed up to 10^{-4} photometric precision if the scaled data in the visible band are subtracted to the infrared band data (see Sect. 5.3.2). About $\sim 3 \cdot 10^{-5}$ precisions are achieved if spot crossing events are independently removed. However, as continuous monitoring of all targets is not available from most observation campaigns, a second approach to correct for activity jitter is presented considering only a series of transit observations. A correlation of transit depth variations between visible and infrared bands is found. Thus, our methodology directly provides the coefficients to correct transit depth measurements from the effects of non-occulted spots when simultaneous multiband observations are available. The results in Sect. 5.3.3 show that up to 10^{-5} photometric precision can be achieved when correcting transit depth variations even in significantly active stars (2-10 times more than the active Sun).

The program `StarSim` was also used for the characterization of activity effects in exoplanetary observations of HD 189733b in Sect. 5.4, as a large number of photometric and spectroscopic data is available and several studies have already addressed the present activity jitter in the observations of this hot Jupiter planet. By considering the active regions map derived by Lanza et al. (2011a) from the MOST 2007 campaign observations, a more simple surface map was obtained that improves the light curve fit. Then, the photometric data series containing 14 transits was analysed to characterize the effects of both occulted and non-occulted spots on the mid-transit time and planet radius measurements.

The results show that data affected by spot crossing events should be removed or corrected regardless of the wavelength, as even in the mid-infrared they can introduce up to $\sim 1.2\%$ of error in the transit depth and almost 30 second differences in the mid-transit time. Therefore, the results from Pont et al. (2013) could be biased in the range of infrared wavelengths, considering the high occurrence of spot occultations. For passbands in the visible range, where the spectral signature of the spots can be ~ 5 times higher (see Fig. 5.16) our results are similar to the ones presented by Barros et al. (2013) for the case of WASP-10b.

Regarding spots not occulted by the planet, the surface map modelled from the MOST data shows that very different scenarios can be found during transit events, with spot filling factors ranging from $\sim 0.3\%$ to $\sim 2.5\%$, when considering a spots temperature contrast of 560 K. Whereas in the first case the transit depth measurement remains unperturbed up to the 10^{-4} precission in R_p/R_* for any filter passband, a strong effect is introduced when the star is highly spotted. Moreover, the difference is wavelength dependent, being ~ 0.0012 in the blue, and only ~ 0.0005 in the mid-infrared. Figures 5.18 and 5.19, together with Table 5.5 display the wavelength dependence of the transit measurements for the different spot coverages found during the simulated transit events. Therefore, up to 10^{-3} errors can be introduced in R_p/R_* measurements for 300 - 500 nm wavelengths if a constant spot filling factor is assumed for the non-occulted spots correction (Sing et al. 2011; Pont et al. 2013) instead of considering the appropriate spots map. Time series photometry simultaneous to the transits observation campaign would be needed in order to be able to reproduce the evolution of the filling factor of spots and adequately scale the correction for each transit event.

The derived map of spots of HD 189733 was used in order to obtain synthetic radial velocity measurements reproducing the spectroscopic observations from SOPHIE, which are simultaneous

to the modelled MOST photometry. Our model is in better agreement with the observations that the previous results by Lanza et al. (2011a) and Aigrain et al. (2012) and explain most of the variations seen in the radial velocity measurements, which probably have underestimated uncertainties. A set of 1000 synthetic time series spectroscopic observations containing a fixed number of measurements were generated for the same time span, allowing us to study the uncertainties introduced by activity effects on transit measurements when a limited number of data are available.

We conclude that the approach exposed in this paper to generate synthetic time series data accurately accounts for all the physical processes significantly affecting spectroscopic and photometric variations produced by activity, which currently represents the main obstacle for exoplanet characterization and searches. In fact, our approach can help to model and correct for the effects of activity jitter on photometric and radial velocity observations of extrasolar planets, especially if the system parameters are known and the surface map of the stellar host has been previously modelled. Our simulations allowed to study the effects of the amount of faculae as well as of the spots temperature contrast and sizes of spots on multi-band simultaneous photometry. The methodology is currently being implemented in a more efficient way in order to be able to model multi-band photometric and spectroscopic radial velocity data simultaneously, thus obtaining detailed maps for the characterization of stellar photospheres. Several applications of the methodology to real observations and to the design optimized strategies for the search and characterization of exoplanets will be presented in a series of papers in the near future.

Chapter 6

Conclusions

6.1 Summary and results

The main goal of this work was to present several methodologies to understand, simulate and model the effects of stellar activity on low mass stars in order to improve the capabilities of exoplanet searches and characterization experiments. The activity jitter that appears in photometric and spectroscopic observations is mainly produced by the different rotational and convective signature of active regions. Also, activity measurements and their correlation with stellar parameters can be used in order to understand stellar properties and produce statistical selections of targets of interest. In the following, we summarize the main results and conclusions from each part of this thesis work.

We have presented the case of WASP-33, a δ Scuti variable hosting a hot Jupiter (see Chapter 2, also Herrero et al. 2011). A close collaboration of our group with several amateur observatories lead to the discovery of the photometric variability in this star, and the follow-up campaign was carried out with the Joan Oró telescope at the Montsec Astronomical Observatory. Despite being related to δ Scuti oscillations, and hence not directly connected to activity effects, the case is presented because of the interest of the observational and theoretical techniques on the rest of the work, and also for the implicit value and interest of the finding, as WASP-33 becomes the first known planet host with δ Scuti pulsations. A frequency search was performed with several data weighing criteria, revealing a main periodicity of about 68 minutes with a semi-amplitude of 1 mmag. This comes out to be commensurable with the planet orbital period at a factor of 26, thus suggesting some kind of star-planet interactions. This result aroused the interest of the exoplanet community on this object for the valuable information on stellar pulsations and their possible relations with the presence of a massive planet in a close-in orbit (Smith et al. 2011; Kovács et al. 2013). Our group has also recently participated on a further study of the periodicities observed in the oscillations of WASP-33 (von Essen et al. 2014), involving multiband observations with a longer time baseline than in the work by Herrero et al. (2011).

We have designed and proposed a methodology to increase the efficiency of targeted exoplanet searches with the transit technique when chromospheric activity and $v \sin i$ measurements are available (see Chapter 3, also Herrero et al. 2012). We showed that these observables allow to put constraints on the rotation axis inclination of the stars. Also, we assumed that close-in planets presumably orbit near the plane of the stellar equator. The lack of a large database of $\log(R'_{HK})$

and $v \sin i$ measurements arose the need to perform simulations of stellar parameters using the known activity - rotation relations, allowing us to study the statistical distribution of stars with different inclinations in the activity - $v \sin i$ diagram. We designed a relatively simple statistics that can be performed for any object with $(B-V)$, $\log(R'_{HK})$ and $v \sin i$ measurements, thus providing its probability to have an inclination i larger than a threshold value, and allowing us to select the most interesting targets. We proved that a preselection of about 10% of the initial samples can be made achieving a mean efficiency (quantified by the number of stars with $i > 80°$) that is 2 to 3 times higher than with any preselection. Assuming the existence of spin-orbit aligned planets around all stars, this would mean that an exoplanet transit search with a success rate ∼3 times higher can be performed. We also presented a sample of preselected targets of interest by applying this methodology on the ∼1200 stars with currently available data.

Activity effects are manifested on the stellar photosphere in the form of spots and faculae, which produce photometric and radial velocity variations in time series data as a result of the different spectral signature of active regions. This can be used in order to map the surface of stars and study the distribution and evolution of active regions, as well as their connection with the structure of magnetic fields. We presented a spot modelling analysis of the Kepler target LHS 6343 A (see Sect. 4.4, also Herrero et al. 2013), an M4V star with a brown dwarf companion eclipsing the primary every 12.71 days. A first methodology is based on a regularized maximum entropy spot model (see Lanza et al. 2003 and subsequent papers for a detailed description), which provides the best fit for the longitudinal distribution of active regions. The regularization of the entropy function ensures that a smooth spatial and temporal map of spots is derived, instead of an irregular distribution with a high number of very small spots. Several methodologies and ways to optimize the algorithms implemented in the spot modelling technique presented by Lanza et al. (2003) were explored. The model also includes the effects of faculae as brighter zones around the spots. In the case of LHS 6343 A, the first seven quarters (∼508 days) of Kepler photometry were studied. The photometry of the eclipses was analysed with common techniques in order to compute a new best fit to the mean profile, thus revealing the presence of several spot crossing events and confirming the system parameters previously found by Johnson et al. (2011). The out-of-eclipse photometry of LHS 6343 A showed a modulation that persists all over the available observations, with an amplitude of $\sim 2 \cdot 10^{-4}$ in relative flux units, with the same periodicity as the orbital motion of the brown dwarf, and with photometric minimums systematically preceding the eclipses by a phase lag of $\sim 100°$. Our maps showed that active regions tend to appear near the same longitude leading the substellar point, and with a mean rotation rate $P_{\rm rot} = 13.14 \pm 0.02$ days, implying that the system is quasi-synchronized. The persistence of this possible active longitude for more than 500 days provides evidence that the brown dwarf companion could be affecting the photospheric activity of the primary. A possible explanation, which is discussed in Sect. 4.4.5, is a magnetic interaction between the coronal field of the M dwarf and the brown dwarf, thus producing a modulation of the stellar dynamo.

Further study of the LHS 6343 system revealed that Doppler-beaming effect could be significant at the Kepler photometric precision (see Sect. 4.5, also Herrero et al. 2014a). The data were fitted using a Bayesian approach implemented through a Monte Carlo Markov chain method. We conclude that the light modulation is dominated by the Doppler-beaming effect, which leads to system parameter results that are consistent with those derived from spectroscopic measurements by Johnson et al. (2011). A Lomb Scargle period search on the residuals showed a significant periodicity of 42.5 ± 3.2 days, probably associated with the rotational modulation of

the primary component.

Chapter 5 presents a surface integration modelling of stellar surface with activity effects, which is more sophisticated that the current modelling techniques. The methodology is intended to simulate time series photometric and spectroscopic observations of active rotating low mass stars, which can provide information to understand the effects of activity jitter at different timescales and wavelengths. The approach was implemented in the program `StarSim`, that allows to obtain synthetic time series data from a set of parameters and a library of stellar atmosphere models. The availability of a database of high resolution Phoenix models for low mass stars (Husser et al. 2013) allows us to perform both photometric and spectroscopic measurements on the light contribution of the simulated stellar photospheres. This provides flux, astrometric, and radial velocity variations as produced by any defined or stochastically generated distribution of active regions formed by spots and faculae.

The spectral signature (flux variation vs. wavelength) of the active regions in visible and infrared passbands was studied, by using the program `StarSim`, for several sets of stellar parameters and properties of the spots in order to derive a method to estimate temperature and sizes of spots, as well as the contribution of faculae through the parameter Q (see Sect. 5.3.1). We conclude that the effects of active regions are strong in the visible and near-infrared, while no signature is observed in the mid-infrared up the 10^{-4} photometric precision. The contribution of faculae dominates the spectral signature of active regions when representing a solar analog ($Q = 8.0$, $\Delta T_{\rm fac} = 30$ K). Simultaneous photometric observations up to the $10^{-3} - 10^{-4}$ precision in visible and near-infrared filters would be needed in order to obtain estimations on the properties of active regions.

Also, we used the synthetic photometry generated with `StarSim` in order to design a strategy to remove activity effects from transit measurements made in the infrared, where several instruments and characterization missions will be focussed in the near future. In a first approach, this is done by directly scaling the data in the visible, that are then subtracted to the infrared data. This method is presented and discussed in detail in Sect.5.3.2, concluding that up to $\sim 3 \cdot 10^{-5}$ precisions can be achieved for the in-transit photometry after correcting for activity and rejecting spot crossing events. If spectroscopic monitoring is only available during transit events, as is the case for most measurement experiments, a second methodology is proposed based on the correlation of transit depth variations between visible and infrared bands (see Sect.5.3.3). Our simulations directly provide the coefficients to correct transit depth measurements from the effects of non-occulted spots when simultaneous multiband observations are available. In this case, up to 10^{-5} precisions can be achieved in the transit photometry even for significantly active stars.

Astrometric jitters produced by activity are also studied from synthetic data obtained with the program `StarSim`. A sample of Sun-like stars with different distributions of active regions is studied (see Sect.5.3.4) in order to evaluate the detectability of astrometric shifts produced by the presence of spots and faculae on the stellar disk, as well as to find possible correlations with photometric jitters. These correlations are dependent on the stellar parameters and, in particular, on the stellar axis inclination, thus providing a possible methodology to constrain it when simultaneous time series data of both observables are available. A comprehensive analysis of the effects of activity on astrometric measurements as the ones performed by the Gaia space mission, as well as possible strategies to remove them, is left for future work.

Finally, `StarSim` is used to analyze the activity effects on transit measurements of the hot Jupiter planet orbiting the active star HD 189733. Simultaneous photometric data from the

MOST space mission and radial velocity measurements from SOPHIE are available for a ~ 30 day time baseline. Synthetic multi-band photometry and radial velocity time series are obtained by adopting the known system parameters and stellar surface map derived by manually fitting the parameters of the spots. The effects of spot crossing events and non-occulted spots are studied for a set of simulated transits. The results show that the effects of occulted spots are still significant in the mid-infrared, while non-occulted spots can introduce variations in R_p/R_* measurements with a signature and amplitude which are very similar to the signal of an atmosphere dominated by dust when the star is relatively active. Radial velocity jitter limits the measurement of the semiamplitude K to an error of ~ 1.9 m s^{-1} when only ~ 30 measurements are obtained.

Therefore, all the results presented in this work show that activity effects introduce jitters on astrometric, photometric and spectroscopic data that may significantly affect exoplanet searches and characterization. However, we conclude that the understanding of the signature produced by stellar activity through modelling and simulating methodologies can provide a better knowledge on stellar properties, as well as strategies to improve the capabilities of exoplanet observation campaigns on low mass stars.

6.2 Future prospects

Further work is needed to confirm some of the results presented, as well as to expand the exploitation capabilities of the methodologies for modelling and simulating activity effects.

- The spot modelling routines implemented in Sect. 4.2 include a number of parameters that must be currently tuned manually for each analysed star in order to find the best fit and guarantee that a consistent solution is obtained. Some of these tasks could be converted into semi-automatic procedures in order to be able to study samples of stars and obtain representative information on the typical filling factor of spots, the lifetime of active regions or the differential rotation, as well as their possible relations with stellar type and age. This work should be done in close collaboration with the group of A. F. Lanza.

- The large amount of Kepler data provides a unique opportunity to study the different effects related to stellar variability in low mass stars, from granulation (i.e., minutes or hours) to activity cycles (i.e., years). This information is collected in the frequency spectrum, and its study is especially interesting for the coolest stars, near the fully convection boundary, where the connection of activity with other stellar processes is still not clear. We already cross-matched the Kepler catalog with the M dwarf catalog from Lépine & Gaidos (2011), resulting on a sample of ~ 700 targets, and produced Lomb Scargle periodograms including all the frequencies of interest. These show a great diversity of phenomena that should be interpreted in terms of stellar rotation, evolution of active regions, and probably activity cycles. The next implementations of the program `StarSim` will be intended to help on these tasks.

- A faster version of the program `StarSim` is currently being developed and will be available in the near future. This will have a limited number of free parameters and some optimized routines in order to be able to simultaneously model photometric and spectroscopic observations to obtain detailed stellar surface maps and also fit transit observations including activity effects.

- A more comprehensive study on the activity effects produced on photometric and spectroscopic observations of active exoplanet hosts, such as HD 189733, will be carried out in the near future. This should be based on simultaneous photometric and radial velocity measurements, as an accurate map of the stellar surface is needed in order to correctly reproduce the amount of effect introduced in transit measurements and radial velocity data. In this way, a version of `StarSim` with the capability to simultaneously model photometric and spectroscopic observations for any instrumental band, that is currently under development, would provide very valuable information for the study of these targets.

- The HARPS-N (3.5 m TNG, La Palma) and HARPS-S (ESO La Silla 3.5 m telescope) spectrographs are currently producing the most accurate radial velocity measurements. The reduction pipeline uses mask reference spectra to obtain the radial velocity measurements from the cross correlation with the observed spectra (see Sect. 5.2.2). An optimization of the HARPS masks, composed by lists of selected lines, is essential. This would basically consist on the removal of the lines that are more sensitive to activity jitter (i.e., temperature and magnetic field variations) when computing the CCF, thus significantly reducing activity effects from the radial velocity measurements. The program `StarSim`, together with Monte Carlo methods, is currently being used to obtain optimized lists of lines that significantly reduce activity jitter. These capabilities to remove spectroscopic jitter will be further studied and presented in the near future.

- The presence of spots and faculae in the surface of Sun-like stars was proven to produce astrometric shifts that could be significant at the precision level of the Gaia space mission measurements (see Sect. 5.3.4). Further study of the effects of activity jitter on astrometric measurements, including a wider range of spectral types and activity scenarios, and taking into account the observing strategy of the Gaia space mission, will be carried out in the near future.

Bibliography

Abreu, J. A., Beer, J., Ferriz-Mas, A., McCracken, K. G., & Steinhilber, F. 2012, Astronomy and Astrophysics, 548, A88

Affer, L., Micela, G., Favata, F., & Flaccomio, E. 2012, MNRAS, 424, 11

Aigrain, S., Pont, F., & Zucker, S. 2012, MNRAS, 419, 3147

Albregtsen, F. & Maltby, P. 1981, Solar Physics, 71, 269

Allard, F., Homeier, D., & Freytag, B. 2011, in Astronomical Society of the Pacific Conference Series, Vol. 448, 16th Cambridge Workshop on Cool Stars, Stellar Systems, and the Sun, ed. C. Johns-Krull, M. K. Browning, & A. A. West, 91

Allard, F., Homeier, D., Freytag, B., et al. 2013, Memorie della Societa Astronomica Italiana Supplementi, 24, 128

Amado, P. J. & Zboril, M. 2002, Astronomy and Astrophysics, 381, 517

Audard, M., Güdel, M., Drake, J. J., & Kashyap, V. L. 2000, The Astrophysical Journal, 541, 396

Auvergne, M., Bodin, P., Boisnard, L., et al. 2009, Astronomy and Astrophysics, 506, 411

Badalyan, O. G. & Prudkovskii, A. G. 1973, Soviet Astronomy, 17, 356

Bakos, G. Á., Howard, A. W., Noyes, R. W., et al. 2009a, The Astrophysical Journal, 707, 446

Bakos, G. Á., Pál, A., Torres, G., et al. 2009b, The Astrophysical Journal, 696, 1950

Bakos, G. Á., Torres, G., Pál, A., et al. 2010, The Astrophysical Journal, 710, 1724

Ball, W. T., Unruh, Y. C., Krivova, N. A., Solanki, S., & Harder, J. W. 2011, Astronomy and Astrophysics, 530, A71

Ballerini, P., Micela, G., Lanza, A. F., & Pagano, I. 2012, Astronomy and Astrophysics, 539, A140

Baraffe, I., Chabrier, G., Allard, F., & Hauschildt, P. H. 1998, Astronomy and Astrophysics, 337, 403

Barnes, J. R., Jeffers, S. V., & Jones, H. R. A. 2011, MNRAS, 412, 1599

Barnes, J. W. 2009, The Astrophysical Journal, 705, 683

Barnes, S. A. 2003, The Astrophysical Journal, 586, 464

Barnes, S. A. 2007, The Astrophysical Journal, 669, 1167

Barros, S. C. C., Boué, G., Gibson, N. P., et al. 2013, MNRAS, 430, 3032

Basri, G., Walkowicz, L. M., & Reiners, A. 2013, The Astrophysical Journal, 769, 37

Bazot, M., Vauclair, S., Bouchy, F., & Santos, N. C. 2005, Astronomy and Astrophysics, 440, 615

Beatty, T. G. & Seager, S. 2010, The Astrophysical Journal, 712, 1433

Beck, J. G. 2000, Solar Physics, 191, 47

Berdyugina, S. V. 2005, Living Reviews in Solar Physics, 2, 8

Berger, E. 2006, The Astrophysical Journal, 648, 629

Berger, T. E., Rouppe van der Voort, L., & Löfdahl, M. 2007, The Astrophysical Journal, 661, 1272

Bloemen, S., Marsh, T. R., Østensen, R. H., et al. 2011, MNRAS, 410, 1787

Boisse, I., Moutou, C., Vidal-Madjar, A., et al. 2009, Astronomy and Astrophysics, 495, 959

Bonomo, A. S. & Lanza, A. F. 2008, Astronomy and Astrophysics, 482, 341

Borucki, W. J., Koch, D., Basri, G., et al. 2010a, Science, 327, 977

Borucki, W. J., Koch, D. G., Basri, G., et al. 2011a, The Astrophysical Journal, 728, 117

Borucki, W. J., Koch, D. G., Basri, G., et al. 2011b, The Astrophysical Journal, 736, 19

Borucki, W. J., Koch, D. G., Brown, T. M., et al. 2010b, The Astrophysical Journal, Letters, 713, L126

Bouchy, F., Bazot, M., Santos, N. C., Vauclair, S., & Sosnowska, D. 2005a, Astronomy and Astrophysics, 440, 609

Bouchy, F. & Queloz, D. 2007, in Astronomical Society of the Pacific Conference Series, Vol. 366, Transiting Extrapolar Planets Workshop, ed. C. Afonso, D. Weldrake, & T. Henning, 193

Bouchy, F., Queloz, D., Deleuil, M., et al. 2008, Astronomy and Astrophysics, 482, L25

Bouchy, F., Udry, S., Mayor, M., et al. 2005b, Astronomy and Astrophysics, 444, L15

Bouvier, J. & Bertout, C. 1989, Astronomy and Astrophysics, 211, 99

Brandenburg, A., Sokoloff, D., & Subramanian, K. 2012, Space Science Reviews, 169, 123

Breger, M., Lenz, P., Antoci, V., et al. 2005, Astronomy and Astrophysics, 435, 955

Breton, R. P., Rappaport, S. A., van Kerkwijk, M. H., & Carter, J. A. 2012, The Astrophysical Journal, 748, 115

Bruntt, H., Deleuil, M., Fridlund, M., et al. 2010, Astronomy and Astrophysics, 519, A51

Bryan, R. K. & Skilling, J. 1980, MNRAS, 191, 69

Budding, E. 1977, Astrophysical Journal Supplement Series, 48, 207

Burke, C. J., McCullough, P. R., Valenti, J. A., et al. 2007, The Astrophysical Journal, 671, 2115

Burrows, A., Hubeny, I., & Sudarsky, D. 2005, The Astrophysical Journal, Letters, 625, L135

Burrows, A., Sudarsky, D., & Hubeny, I. 2006, The Astrophysical Journal, 650, 1140

Caffau, E., Ludwig, H.-G., Steffen, M., Freytag, B., & Bonifacio, P. 2011, Solar Physics, 268, 255

Canto Martins, B. L., Das Chagas, M. L., Alves, S., et al. 2011, Astronomy and Astrophysics, 530, A73

Carlsson, M. & Stein, R. F. 1992, The Astrophysical Journal, Letters, 397, L59

Carter, J. A., Rappaport, S., & Fabrycky, D. 2011, The Astrophysical Journal, 728, 139

Carter, J. A. & Winn, J. N. 2009, The Astrophysical Journal, 704, 51

Cassan, A., Kubas, D., Beaulieu, J.-P., et al. 2012, Nature, 481, 167

Catala, C., Donati, J.-F., Shkolnik, E., Bohlender, D., & Alecian, E. 2007, MNRAS, 374, L42

Chabrier, G. & Baraffe, I. 1997, Astronomy and Astrophysics, 327, 1039

Chapman, G. A. 1987, Annual Review of Astronomy and Astrophysics, 25, 633

Charbonneau, D., Brown, T. M., Latham, D. W., & Mayor, M. 2000, The Astrophysical Journal, Letters, 529, L45

Charbonneau, D., Brown, T. M., Noyes, R. W., & Gilliland, R. L. 2002, The Astrophysical Journal, 568, 377

Charbonneau, D., Irwin, J., Nutzman, P., & Falco, E. E. 2008, in Bulletin of the American Astronomical Society, Vol. 40, American Astronomical Society Meeting Abstracts #212, 242

Christensen-Dalsgaard, J., Kjeldsen, H., Brown, T. M., et al. 2010, The Astrophysical Journal, Letters, 713, L164

Christian, D. J., Pollacco, D. L., Skillen, I., et al. 2006, MNRAS, 372, 1117

Ciardi, D. R., von Braun, K., Bryden, G., et al. 2011, The Astronomical Journal, 141, 108

Claret, A. & Bloemen, S. 2011, Astronomy and Astrophysics, 529, A75

Cohen, O., Drake, J. J., Kashyap, V. L., et al. 2009, The Astrophysical Journal, Letters, 704, L85

Cohen, O., Drake, J. J., Kashyap, V. L., Sokolov, I. V., & Gombosi, T. I. 2010, The Astrophysical Journal, Letters, 723, L64

Collier Cameron, A., Guenther, E., Smalley, B., et al. 2010, MNRAS, 407, 507

Colomé, J., Ribas, I., Fernández, D., et al. 2008, in Society of Photo-Optical Instrumentation Engineers (SPIE) Conference Series, Vol. 7019, Society of Photo-Optical Instrumentation Engineers (SPIE) Conference Series

Croll, B. 2006, Publications of the Astronomical Society of the Pacific, 118, 1351

Croll, B., Matthews, J. M., Rowe, J. F., et al. 2007, The Astrophysical Journal, 671, 2129

Croll, B., Walker, G. A. H., Kuschnig, R., et al. 2006, The Astrophysical Journal, 648, 607

Cuntz, M., Saar, S. H., & Musielak, Z. E. 2000, The Astrophysical Journal, Letters, 533, L151

Cuntz, M. & Shkolnik, E. 2002, Astronomische Nachrichten, 323, 387

de Medeiros, J. R. & Mayor, M. 1999, Astronomy & Astrophysics, Supplement, 139, 433

Deleuil, M., Deeg, H. J., Alonso, R., et al. 2008, Astronomy and Astrophysics, 491, 889

Delfosse, X., Forveille, T., Perrier, C., & Mayor, M. 1998, Astronomy and Astrophysics, 331, 581

Deutsch, A. J. 1958, in IAU Symposium, Vol. 6, Electromagnetic Phenomena in Cosmical Physics, ed. B. Lehnert, 209

Donahue, R. A., Saar, S. H., & Baliunas, S. L. 1996, The Astrophysical Journal, 466, 384

Donati, J.-F., Moutou, C., Farès, R., et al. 2008, MNRAS, 385, 1179

Dorren, J. D. 1987, The Astrophysical Journal, 320, 756

Dumusque, X., Santos, N. C., Udry, S., Lovis, C., & Bonfils, X. 2011a, Astronomy and Astrophysics, 527, A82

Dumusque, X., Udry, S., Lovis, C., Santos, N. C., & Monteiro, M. J. P. F. G. 2011b, Astronomy and Astrophysics, 525, A140

Duncan, D. K., Vaughan, A. H., Wilson, O. C., et al. 1991, The Astrophysical Journal, Supplement, 76, 383

Dunham, E. W., Borucki, W. J., Koch, D. G., et al. 2010, The Astrophysical Journal, Letters, 713, L136

Durney, B. R., De Young, D. S., & Roxburgh, I. W. 1993, Solar Physics, 145, 207

Eker, Z., Brandt, P. N., Hanslmeier, A., Otruba, W., & Wehrli, C. 2003, Astronomy and Astrophysics, 404, 1107

Engle, S. G. & Guinan, E. F. 2011, in Astronomical Society of the Pacific Conference Series, Vol. 451, Astronomical Society of the Pacific Conference Series, ed. S. Qain, K. Leung, L. Zhu, & S. Kwok, 285

Etzel, P. B. 1985, SBOP - Spectroscopic Binary Orbit Program, Program's Manual.

Eyer, L., Holl, B., Pourbaix, D., et al. 2013, Central European Astrophysical Bulletin, 37, 115

Fares, R., Donati, J.-F., Moutou, C., et al. 2010, MNRAS, 406, 409

Feigelson, E. D., Gaffney, III, J. A., Garmire, G., Hillenbrand, L. A., & Townsley, L. 2003, The Astrophysical Journal, 584, 911

Fontenla, J. M., Curdt, W., Haberreiter, M., Harder, J., & Tian, H. 2009, The Astrophysical Journal, 707, 482

Fontenla, J. M., Harder, J., Livingston, W., Snow, M., & Woods, T. 2011, Journal of Geophysical Research (Atmospheres), 116, 20108

Ford, E. B. 2006, The Astrophysical Journal, 642, 505

Fortney, J. J., Marley, M. S., & Barnes, J. W. 2007, The Astrophysical Journal, 659, 1661

Foukal, P. 1998, The Astrophysical Journal, 500, 958

Frasca, A., Fröhlich, H.-E., Bonanno, A., et al. 2011, Astronomy and Astrophysics, 532, A81

Frazier, E. N. & Stenflo, J. O. 1978, Astronomy and Astrophysics, 70, 789

Fressin, F., Torres, G., Charbonneau, D., et al. 2013, The Astrophysical Journal, 766, 81

Fröhlich, H.-E., Frasca, A., Catanzaro, G., et al. 2012, Astronomy and Astrophysics, 543, A146

Gazak, J. Z., Johnson, J. A., Tonry, J., et al. 2012, Advances in Astronomy, 2012

Gillon, M., Smalley, B., Hebb, L., et al. 2009, Astronomy and Astrophysics, 496, 259

Gilman, P. A. 1980, in Lecture Notes in Physics, Berlin Springer Verlag, Vol. 114, IAU Colloq. 51: Stellar Turbulence, ed. D. F. Gray & J. L. Linsky, 19–37

Gizis, J. E., Monet, D. G., Reid, I. N., et al. 2000, The Astronomical Journal, 120, 1085

Głębocki, R. & Gnaciński, P. 2003, in The Future of Cool-Star Astrophysics: 12th Cambridge Workshop on Cool Stars, Stellar Systems, and the Sun, ed. A. Brown, G. M. Harper, & T. R. Ayres, Vol. 12, 823–827

Gondoin, P. 2008, Astronomy and Astrophysics, 478, 883

Gonzalez, G., Carlson, M. K., & Tobin, R. W. 2010, MNRAS, 403, 1368

Gray, D. F. 1982, The Astrophysical Journal, 258, 201

Gray, D. F. 1992, The observation and analysis of stellar photospheres.

Gray, R. O., Corbally, C. J., Garrison, R. F., et al. 2006, The Astronomical Journal, 132, 161

Grillmair, C. J., Burrows, A., Charbonneau, D., et al. 2008, Nature, 456, 767

Handler, G., Balona, L. A., Shobbrook, R. R., et al. 2002, MNRAS, 333, 262

Handler, G. & Shobbrook, R. R. 2002, MNRAS, 333, 251

Hartman, J. D., Bakos, G. Á., Torres, G., et al. 2009, The Astrophysical Journal, 706, 785

Hebb, L., Collier-Cameron, A., Triaud, A. H. M. J., et al. 2010, The Astrophysical Journal, 708, 224

Hempelmann, A., Schmitt, J. H. M. M., Schultz, M., Ruediger, G., & Stepien, K. 1995, Astronomy and Astrophysics, 294, 515

Henry, G. W., Eaton, J. A., Hamer, J., & Hall, D. S. 1995, The Astrophysical Journal, Supplement, 97, 513

Henry, G. W., Marcy, G. W., Butler, R. P., & Vogt, S. S. 2000, The Astrophysical Journal, Letters, 529, L41

Henry, G. W. & Winn, J. N. 2008, The Astronomical Journal, 135, 68

Henry, T. J., Soderblom, D. R., Donahue, R. A., & Baliunas, S. L. 1996, The Astronomical Journal, 111, 439

Herrero, E., Lanza, A. F., Ribas, I., et al. 2014a, Astronomy and Astrophysics, 563, A104

Herrero, E., Lanza, A. F., Ribas, I., Jordi, C., & Morales, J. C. 2013, Astronomy and Astrophysics, 553, A66

Herrero, E., Morales, J. C., Ribas, I., & Naves, R. 2011, Astronomy and Astrophysics, 526, L10

Herrero, E., Ribas, I., & Jordi, C. 2014b, Experimental Astronomy, in press

Herrero, E., Ribas, I., Jordi, C., Guinan, E. F., & Engle, S. G. 2012, Astronomy and Astrophysics, 537, A147

Huber, K. F., Czesla, S., Wolter, U., & Schmitt, J. H. M. M. 2010, Astronomy and Astrophysics, 514, A39

Husnoo, N., Pont, F., Mazeh, T., et al. 2012, MNRAS, 422, 3151

Hussain, G. A. J. 2002, Astronomische Nachrichten, 323, 349

Husser, T.-O., Wende-von Berg, S., Dreizler, S., et al. 2013, Astronomy and Astrophysics, 553, A6

Irwin, J., Berta, Z. K., Burke, C. J., et al. 2011, The Astrophysical Journal, 727, 56

Irwin, J., Charbonneau, D., Nutzman, P., et al. 2008, The Astrophysical Journal, 681, 636

Jenkins, J. M., Caldwell, D. A., Chandrasekaran, H., et al. 2010a, The Astrophysical Journal, Letters, 713, L87

Jenkins, J. M., Caldwell, D. A., Chandrasekaran, H., et al. 2010b, The Astrophysical Journal, Letters, 713, L120

Jenkins, J. S., Murgas, F., Rojo, P., et al. 2011, Astronomy and Astrophysics, 531, A8

Johnson, J. A., Apps, K., Gazak, J. Z., et al. 2011, The Astrophysical Journal, 730, 79

Joy, A. H. & Abt, H. A. 1974, The Astrophysical Journal, Supplement, 28, 1

Kaltenegger, L., Eiroa, C., Ribas, I., et al. 2010, Astrobiology, 10, 103

Kasting, J. F. 2010, in Astronomical Society of the Pacific Conference Series, Vol. 430, Pathways Towards Habitable Planets, ed. V. Coudé du Foresto, D. M. Gelino, & I. Ribas, 3

Kővári, Z., Oláh, K., Bartus, J., Strassmeier, K. G., & Granzer, T. 2006, Astrophysical Journal Supplement Series, 304, 55

Kharchenko, N. V. & Roeser, S. 2009, VizieR Online Data Catalog, 1280, 0

Kim, Y.-C. & Demarque, P. 1996, The Astrophysical Journal, 457, 340

Kipping, D. M. 2010, MNRAS, 408, 1758

Kipping, D. M. 2012, MNRAS, 427, 2487

Kiraga, M. & Stepien, K. 2007, Acta Astronomica, 57, 149

Kitchatinov, L. L. & Rüdiger, G. 1999, Astronomy and Astrophysics, 344, 911

Knutson, H. A., Charbonneau, D., Noyes, R. W., Brown, T. M., & Gilliland, R. L. 2007, The Astrophysical Journal, 655, 564

Knutson, H. A., Howard, A. W., & Isaacson, H. 2010, The Astrophysical Journal, 720, 1569

Koch, D. G., Borucki, W. J., Basri, G., et al. 2010, The Astrophysical Journal, Letters, 713, L79

Kopparapu, R. K. 2013, The Astrophysical Journal, Letters, 767, L8

Kopparapu, R. K., Ramirez, R., Kasting, J. F., et al. 2013, The Astrophysical Journal, 765, 131

Kovács, G., Bakos, G. Á., Hartman, J. D., et al. 2010, The Astrophysical Journal, 724, 866

Kovács, G., Kovács, T., Hartman, J. D., et al. 2013, Astronomy and Astrophysics, 553, A44

Kowalski, A. F., Hawley, S. L., Hilton, E. J., et al. 2009, The Astronomical Journal, 138, 633

Kraft, R. P. 1967, The Astrophysical Journal, 150, 551

Lagrange, A.-M., Desort, M., & Meunier, N. 2010, Astronomy and Astrophysics, 512, A38

Lammer, H., Lichtenegger, H. I. M., Kulikov, Y. N., et al. 2007, Astrobiology, 7, 185

Lane, C., Hallinan, G., Zavala, R. T., et al. 2007, The Astrophysical Journal, Letters, 668, L163

Lanza, A. F. 2008, Astronomy and Astrophysics, 487, 1163

Lanza, A. F. 2009, Astronomy and Astrophysics, 505, 339

Lanza, A. F. 2011, Astrophysical Journal Supplement Series, 336, 303

Lanza, A. F. 2012, Astronomy and Astrophysics, 544, A23

Lanza, A. F., Aigrain, S., Messina, S., et al. 2009a, Astronomy and Astrophysics, 506, 255

Lanza, A. F., Boisse, I., Bouchy, F., Bonomo, A. S., & Moutou, C. 2011a, Astronomy and Astrophysics, 533, A44

Lanza, A. F., Bonomo, A. S., Moutou, C., et al. 2010, Astronomy and Astrophysics, 520, A53

Lanza, A. F., Bonomo, A. S., Pagano, I., et al. 2011b, Astronomy and Astrophysics, 525, A14

Lanza, A. F., Bonomo, A. S., & Rodonò, M. 2007, Astronomy and Astrophysics, 464, 741

Lanza, A. F., Catalano, S., Cutispoto, G., Pagano, I., & Rodono, M. 1998, Astronomy and Astrophysics, 332, 541

Lanza, A. F., Pagano, I., Leto, G., et al. 2009b, Astronomy and Astrophysics, 493, 193

Lanza, A. F., Rodonò, M., & Pagano, I. 2004, Astronomy and Astrophysics, 425, 707

Lanza, A. F., Rodonò, M., Pagano, I., Barge, P., & Llebaria, A. 2003, Astronomy and Astrophysics, 403, 1135

Leconte, J., Chabrier, G., Baraffe, I., & Levrard, B. 2010, Astronomy and Astrophysics, 516, A64

Léger, A., Rouan, D., Schneider, J., et al. 2009, Astronomy and Astrophysics, 506, 287

Lenz, P. & Breger, M. 2005, Communications in Asteroseismology, 146, 53

Lépine, S. & Gaidos, E. 2011, The Astronomical Journal, 142, 138

Lindegren, L., Babusiaux, C., Bailer-Jones, C., et al. 2008, in IAU Symposium, Vol. 248, IAU Symposium, ed. W. J. Jin, I. Platais, & M. A. C. Perryman, 217–223

Lissauer, J. J., Fabrycky, D. C., Ford, E. B., et al. 2011a, Nature, 470, 53

Lissauer, J. J., Ragozzine, D., Fabrycky, D. C., et al. 2011b, The Astrophysical Journal, Supplement, 197, 8

Livshits, M. A. & Polonskii, V. V. 1968, Soviet Astronomy, 11, 965

Loeb, A. & Gaudi, B. S. 2003, The Astrophysical Journal, Letters, 588, L117

López-Morales, M. 2011, in Highlights of Spanish Astrophysics VI, ed. M. R. Zapatero Osorio, J. Gorgas, J. Maíz Apellániz, J. R. Pardo, & A. Gil de Paz, 60–72

López-Santiago, J., Montes, D., Gálvez-Ortiz, M. C., et al. 2010, Astronomy and Astrophysics, 514, A97

Ludwig, H.-G., Caffau, E., Steffen, M., et al. 2009, Mem. Societa Astronomica Italiana, 80, 711

Ludwig, H.-G., Freytag, B., & Steffen, M. 1999, Astronomy and Astrophysics, 346, 111

Mallik, S. V. 1998, Astronomy and Astrophysics, 338, 623

Mamajek, E. E. & Hillenbrand, L. A. 2008, The Astrophysical Journal, 687, 1264

Mandel, K. & Agol, E. 2002, The Astrophysical Journal, Letters, 580, L171

Marcy, G., Butler, R. P., Fischer, D., et al. 2005, Progress of Theoretical Physics Supplement, 158, 24

Marigo, P., Girardi, L., Bressan, A., et al. 2008, Astronomy and Astrophysics, 482, 883

Marsden, S. C., Waite, I. A., Carter, B. D., & Donati, J.-F. 2005, MNRAS, 359, 711

Martinez Pillet, V., Moreno-Insertis, F., & Vazquez, M. 1993, Astronomy and Astrophysics, 274, 521

Maxted, P. F. L., Marsh, T. R., & North, R. C. 2000, MNRAS, 317, L41

Mayor, M., Bonfils, X., Forveille, T., et al. 2009, Astronomy and Astrophysics, 507, 487

Mayor, M. & Queloz, D. 1995, Nature, 378, 355

McCullough, P. R., Stys, J. E., Valenti, J. A., et al. 2006, The Astrophysical Journal, 648, 1228

McIvor, T., Jardine, M., & Holzwarth, V. 2006, MNRAS, 367, L1

McLaughlin, D. B. 1924, The Astrophysical Journal, 60, 22

Melo, C., Santos, N. C., Pont, F., et al. 2006, Astronomy and Astrophysics, 460, 251

Messina, S. & Guinan, E. F. 2003, in The Future of Cool-Star Astrophysics: 12th Cambridge Workshop on Cool Stars, Stellar Systems, and the Sun, ed. A. Brown, G. M. Harper, & T. R. Ayres, Vol. 12, 941–945

Meunier, N., Desort, M., & Lagrange, A.-M. 2010a, Astronomy and Astrophysics, 512, A39

Meunier, N., Lagrange, A.-M., & Desort, M. 2010b, Astronomy and Astrophysics, 519, A66

Miller, G. E. & Scalo, J. M. 1979, The Astrophysical Journal, Supplement, 41, 513

Miller-Ricci, E., Rowe, J. F., Sasselov, D., et al. 2008, The Astrophysical Journal, 682, 593

Mohanty, S. & Basri, G. 2003, The Astrophysical Journal, 583, 451

Montesinos, B., Thomas, J. H., Ventura, P., & Mazzitelli, I. 2001, MNRAS, 326, 877

Morris, S. L. 1985, The Astrophysical Journal, 295, 143

Mosser, B., Baudin, F., Lanza, A. F., et al. 2009, Astronomy and Astrophysics, 506, 245

Moulds, V. E., Watson, C. A., Bonfils, X., Littlefair, S. P., & Simpson, E. K. 2013, MNRAS, 430, 1709

Moutou, C., Donati, J.-F., Savalle, R., et al. 2007, Astronomy and Astrophysics, 473, 651

Murphy, S. J. 2012, MNRAS, 422, 665

Murray, C. D. & Dermott, S. F. 1999, Solar system dynamics

Narita, N., Enya, K., Sato, B., et al. 2007, Publications of the Astronomical Society of Japan, 59, 763

Nielsen, M. B., Gizon, L., Schunker, H., & Karoff, C. 2013, Astronomy and Astrophysics, 557, L10

Noyes, R. W., Hartmann, L. W., Baliunas, S. L., Duncan, D. K., & Vaughan, A. H. 1984, The Astrophysical Journal, 279, 763

Olah, K. & Pettersen, B. R. 1991, Astronomy and Astrophysics, 242, 443

O'Neal, D., Neff, J. E., Saar, S. H., & Cuntz, M. 2004, The Astronomical Journal, 128, 1802

Ortiz, A., Solanki, S. K., Domingo, V., Fligge, M., & Sanahuja, B. 2002, Astronomy and Astrophysics, 388, 1036

Padmakar & Pandey, S. K. 1999, Astronomy & Astrophysics, Supplement, 138, 203

Palla, F. & Baraffe, I. 2005, Astronomy and Astrophysics, 432, L57

Penn, M. J. & MacDonald, R. K. D. 2007, The Astrophysical Journal, Letters, 662, L123

Perryman, M. 2011, The Exoplanet Handbook

Perryman, M. A. C. 2002, Astrophysical Journal Supplement Series, 280, 1

Petrov, P. P., Shcherbakov, V. A., Berdyugina, S. V., et al. 1994, Astronomy & Astrophysics, Supplement, 107, 9

Petrovay, K., Martínez Pillet, V., & van Driel-Gesztelyi, L. 1999, Solar Physics, 188, 315

Petrovay, K. & van Driel-Gesztelyi, L. 1997, Solar Physics, 176, 249

Pfahl, E., Arras, P., & Paxton, B. 2008, The Astrophysical Journal, 679, 783

Pietrinferni, A., Cassisi, S., Salaris, M., & Castelli, F. 2004, The Astrophysical Journal, 612, 168

Pizzolato, N., Maggio, A., Micela, G., Sciortino, S., & Ventura, P. 2003, Astronomy and Astrophysics, 397, 147

Pont, F., Gilliland, R. L., Moutou, C., et al. 2007, Astronomy and Astrophysics, 476, 1347

Pont, F., Sing, D. K., Gibson, N. P., et al. 2013, MNRAS, 432, 2917

Pont, F., Zucker, S., & Queloz, D. 2006, MNRAS, 373, 231

Popper, D. M. & Etzel, P. B. 1981, The Astronomical Journal, 86, 102

Press, W. H. & Rybicki, G. B. 1989, The Astrophysical Journal, 338, 277

Press, W. H., Teukolsky, S. A., Vetterling, W. T., & Flannery, B. P. 1992, Numerical recipes in FORTRAN. The art of scientific computing

Press, W. H., Teukolsky, S. A., Vetterling, W. T., & Flannery, B. P. 2002, Numerical recipes in C++ : the art of scientific computing

Preusse, S., Kopp, A., Büchner, J., & Motschmann, U. 2006, Astronomy and Astrophysics, 460, 317

Pulkkinen, P. J., Brooke, J., Pelt, J., & Tuominen, I. 1999, Astronomy and Astrophysics, 341, L43

Rasio, F. A. & Ford, E. B. 1996, Science, 274, 954

Reiners, A. & Basri, G. 2007, The Astrophysical Journal, 656, 1121

Reiners, A. & Basri, G. 2009, Astronomy and Astrophysics, 496, 787

Reiners, A., Basri, G., & Browning, M. 2009, The Astrophysical Journal, 692, 538

Reiners, A., Joshi, N., & Goldman, B. 2012, The Astronomical Journal, 143, 93

Ribárik, G., Oláh, K., & Strassmeier, K. G. 2003, Astronomische Nachrichten, 324, 202

Rice, J. B., Wehlau, W. H., & Khokhlova, V. L. 1989, Astronomy and Astrophysics, 208, 179

Rodonò, M., Messina, S., Lanza, A. F., Cutispoto, G., & Teriaca, L. 2000, Astronomy and Astrophysics, 358, 624

Rossiter, R. A. 1924, The Astrophysical Journal, 60, 15

Rüdiger, G., Schultz, M., & Elstner, D. 2011, Astronomy and Astrophysics, 530, A55

Rybicki, G. B. & Lightman, A. P. 1979, Astronomy Quarterly, 3, 199

Sabha, N., Witzel, G., Eckart, A., et al. 2010, Astronomy and Astrophysics, 512, A2

Sajina, A., Scott, D., Dennefeld, M., et al. 2006, MNRAS, 369, 939

Sanchis-Ojeda, R., Fabrycky, D. C., Winn, J. N., et al. 2012, Nature, 487, 449

Sanchis-Ojeda, R. & Winn, J. N. 2011, The Astrophysical Journal, 743, 61

Sanchis-Ojeda, R., Winn, J. N., Holman, M. J., et al. 2011, The Astrophysical Journal, 733, 127

Sato, B., Fischer, D. A., Henry, G. W., et al. 2005, The Astrophysical Journal, 633, 465

Schlaufman, K. C. 2010, The Astrophysical Journal, 719, 602

Schuh, S. 2010, Astronomische Nachrichten, 331, 489

Seager, S. & Mallén-Ornelas, G. 2003, The Astrophysical Journal, 585, 1038

Shakura, N. I. & Postnov, K. A. 1987, Astronomy and Astrophysics, 183, L21

Shkolnik, E., Bohlender, D. A., Walker, G. A. H., & Collier Cameron, A. 2008, The Astrophysical Journal, 676, 628

Shkolnik, E., Walker, G. A. H., Bohlender, D. A., Gu, P.-G., & Kürster, M. 2005, The Astrophysical Journal, 622, 1075

Silva-Valio, A. & Lanza, A. F. 2011, Astronomy and Astrophysics, 529, A36

Silva-Valio, A., Lanza, A. F., Alonso, R., & Barge, P. 2010, Astronomy and Astrophysics, 510, A25

Silvotti, R., Schuh, S., Janulis, R., et al. 2007, Nature, 449, 189

Sing, D. K., Pont, F., Aigrain, S., et al. 2011, MNRAS, 416, 1443

Skumanich, A. 1972, The Astrophysical Journal, 171, 565

Smith, A. M. S., Anderson, D. R., Skillen, I., Collier Cameron, A., & Smalley, B. 2011, MNRAS, 416, 2096

Snellen, I. A. G., de Mooij, E. J. W., & Burrows, A. 2010, Astronomy and Astrophysics, 513, A76

Snodgrass, H. B. & Ulrich, R. K. 1990, The Astrophysical Journal, 351, 309

Soderblom, D. R. 1985, Publications of the Astronomical Society of the Pacific, 97, 57

Solanki, S. K. 1993, Space Science Reviews, 63, 1

Solanki, S. K. & Unruh, Y. C. 2004, MNRAS, 348, 307

Southworth, J., Maxted, P. F. L., & Smalley, B. 2004a, MNRAS, 351, 1277

Southworth, J., Zucker, S., Maxted, P. F. L., & Smalley, B. 2004b, MNRAS, 355, 986

Sozzetti, A., Torres, G., Charbonneau, D., et al. 2009, The Astrophysical Journal, 691, 1145

Steinegger, M., Brandt, P. N., & Haupt, H. F. 1996, Astronomy and Astrophysics, 310, 635

Stellingwerf, R. F. 1978, The Astrophysical Journal, 224, 953

Stix, M. 2002, Astronomische Nachrichten, 323, 178

Strassmeier, K. G. 1992, in Astronomical Society of the Pacific Conference Series, Vol. 34, Robotic Telescopes in the 1990s, ed. A. V. Filippenko, 39–52

Strassmeier, K. G. 2002, Astronomische Nachrichten, 323, 309

Strassmeier, K. G. 2009, Astronomy and Astrophysics Reviews, 17, 251

Strassmeier, K. G., Hall, D. S., & Henry, G. W. 1994a, Astronomy and Astrophysics, 282, 535

Strassmeier, K. G. & Rice, J. B. 1998, in Astronomical Society of the Pacific Conference Series, Vol. 154, Cool Stars, Stellar Systems, and the Sun, ed. R. A. Donahue & J. A. Bookbinder, 2048

Strassmeier, K. G., Welty, A. D., & Rice, J. B. 1994b, Astronomy and Astrophysics, 285, L17

Swain, M., Deroo, P., Tinetti, G., et al. 2013, Icarus, 225, 432

Swain, M. R., Tinetti, G., Vasisht, G., et al. 2009, The Astrophysical Journal, 704, 1616

Swain, M. R., Vasisht, G., & Tinetti, G. 2008, Nature, 452, 329

Tinetti, G., Deroo, P., Swain, M. R., et al. 2010, The Astrophysical Journal, Letters, 712, L139

Tinetti, G., Vidal-Madjar, A., Liang, M.-C., et al. 2007, Nature, 448, 169

Toma, E. 1972, Astronomy and Astrophysics, 19, 76

Torres, G., Bakos, G. Á., Kovács, G., et al. 2007, The Astrophysical Journal, Letters, 666, L121

Triaud, A. H. M. J., Collier Cameron, A., Queloz, D., et al. 2010, Astronomy and Astrophysics, 524, A25

Triaud, A. H. M. J., Queloz, D., Bouchy, F., et al. 2009, Astronomy and Astrophysics, 506, 377

Unruh, Y. C., Solanki, S. K., & Fligge, M. 1999, Astronomy and Astrophysics, 345, 635

van Kerkwijk, M. H., Rappaport, S. A., Breton, R. P., et al. 2010, The Astrophysical Journal, 715, 51

van Leeuwen, F., ed. 2007, Astrophysics and Space Science Library, Vol. 350, Hipparcos, the New Reduction of the Raw Data

Verde, L., Peiris, H. V., Spergel, D. N., et al. 2003, The Astrophysical Journal, Supplement, 148, 195

Vitense, E. 1953, Zeitschrift fuer Astrophysik, 32, 135

Vogt, S. S., Penrod, G. D., & Hatzes, A. P. 1987, The Astrophysical Journal, 321, 496

von Essen, C., Czesla, S., Wolter, U., et al. 2014, Astronomy and Astrophysics, 561, A48

Walker, G., Matthews, J., Kuschnig, R., et al. 2003, Publications of the Astronomical Society of the Pacific, 115, 1023

Walker, G. A. H., Croll, B., Kuschnig, R., et al. 2007, The Astrophysical Journal, 659, 1611

Walker, G. A. H., Croll, B., Matthews, J. M., et al. 2008, Astronomy and Astrophysics, 482, 691

Walkowicz, L. M., Basri, G., & Valenti, J. A. 2013, The Astrophysical Journal, Supplement, 205, 17

Walkowicz, L. M., Johns-Krull, C. M., & Hawley, S. L. 2008, The Astrophysical Journal, 677, 593

Welsh, B. Y., Wheatley, J. M., Seibert, M., et al. 2007, The Astrophysical Journal, Supplement, 173, 673

West, A. A. & Basri, G. 2009, The Astrophysical Journal, 693, 1283

West, A. A., Hawley, S. L., Bochanski, J. J., et al. 2008, The Astronomical Journal, 135, 785

West, A. A., Hawley, S. L., Walkowicz, L. M., et al. 2004, The Astronomical Journal, 128, 426

Willems, B. & Claret, A. 2005, in Astronomical Society of the Pacific Conference Series, Vol. 333, Tidal Evolution and Oscillations in Binary Stars, ed. A. Claret, A. Giménez, & J.-P. Zahn, 52

Winn, J. N. 2011, Exoplanet Transits and Occultations, ed. S. Seager, 55–77

Winn, J. N., Holman, M. J., Henry, G. W., et al. 2007, The Astronomical Journal, 133, 1828

Winn, J. N., Johnson, J. A., Marcy, G. W., et al. 2006, The Astrophysical Journal, Letters, 653, L69

Wright, J. T. 2005, Publications of the Astronomical Society of the Pacific, 117, 657

Wright, J. T. & Howard, A. W. 2009, The Astrophysical Journal, Supplement, 182, 205

Wright, J. T., Marcy, G. W., Butler, R. P., & Vogt, S. S. 2004, The Astrophysical Journal, Supplement, 152, 261

Wu, Y. & Murray, N. 2003, The Astrophysical Journal, 589, 605

Zucker, S., Mazeh, T., & Alexander, T. 2007, The Astrophysical Journal, 670, 1326

Appendix A

Influence of the model parameters on the spot maps of LHS 6343 A

A.1 Time resolution ($\Delta t_{\rm f}$) and amount of regularization (β)

In Sect. 4.4.3 we discussed the method applied to determining the maximum time interval $\Delta t_{\rm f}$ that our model can accurately fit when considering a fixed distribution of three active regions (Lanza et al. 2003). This corresponds to the time resolution of our model, since we assume that active regions do not evolve on timescales shorter than $\Delta t_{\rm f}$. The total interval T was divided to $N_{\rm f}$ segments so that $\Delta t_{\rm f} = T/N_{\rm f}$. The optimal $N_{\rm f}$ was found to be 58 from the best fit of the three-spot model, as measured from the χ^2 statistics.

Three cases corresponding to different lengths of the time interval $\Delta t_{\rm f}$ are presented in Fig. A.1, where the ratio $\chi^2/\chi^2_{\rm min}$ is plotted vs. Q, the facular-to-spotted area ratio; χ^2 is the chi square of the composite best fit to the total time series; and $\chi^2_{\rm min}$ is the minimum χ^2 obtained for $N_f = 58$ and $Q = 8.0$. The corresponding spot model is discussed in the text. Here we explore the case with $N_{\rm f} = 50$ and perform an ME analysis with the corresponding time interval, i.e., $\Delta t_{\rm f} = 10.1719$ days, to investigate the effect of a different $\Delta t_{\rm f}$ on our results. The same approach as described in Sect. 4.4.4 was considered, and regularized ME models were iteratively adjusted until $\beta = 2$. The isocontour map of the distribution of the spot filling factor vs. time and longitude is presented in Fig. A.2. It is remarkably similar to the one presented in Fig. 4.8 and the phased activity enhancement around $\sim 350^\circ$ is still visible, although the migration of the starspots and their changes on short timescales are less evident. Therefore, a longer time interval limits the possibility of accurately measuring spots' migration and estimate their lifetimes.

In a second test, we chose the same time interval as in Sect. 4.4.4, i.e., $N_{\rm f} = 58$, to explore the effects of a different amount of regularization on the ME spot maps. In Fig. A.3, we present a spot map obtained with a lower regularization ($\beta = 1$). At that point, the large starspots appearing in Fig. 4.8 are resolved into several smaller spots. This fine structure changes vs. the time without any clear regularity, as expected for an artefact due to overfitting the noise present in the data.

Finally, we plot the distribution of the filling factor obtained with $\beta = 3$ in Fig. A.4. The effects of the overegularization described in Sect. 4.4.4 can be seen as a tendency for the appear-

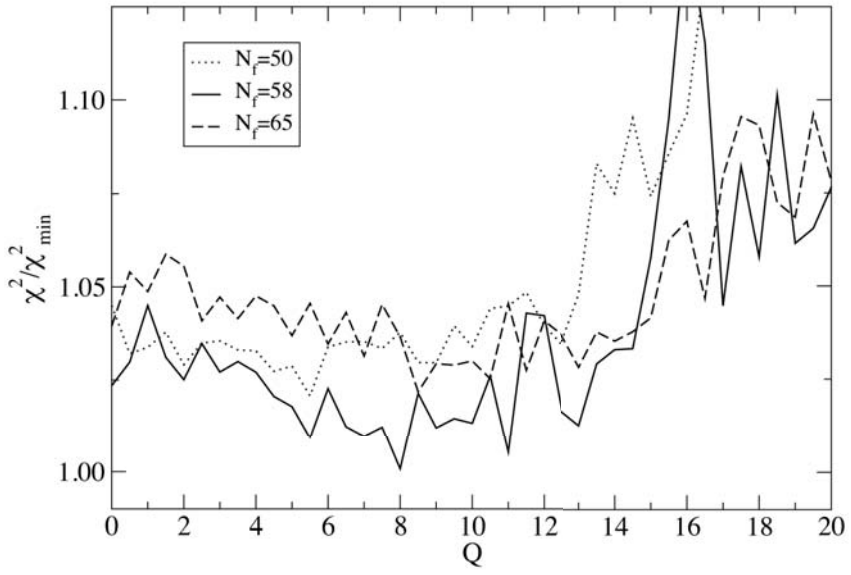

Figure A.1: The ratio of the χ^2 of the three-spot model fit to the minimum value for $N_f = 58$ ($\chi^2_{\rm min}$) vs. the parameter Q, i.e., the ratio of the facular area to the cool spot area in active regions. Solution series for three different values of the time interval $\Delta t_{\rm f} = T/N_f$ are shown.

ance of larger and smoother spot groups that include previously resolved starspots. Three main groups separated by approximately 120° in longitude generally appear, showing the same backwards migration as with $\beta = 2$, the optimal value adopted for the regularization. The residuals of the composite best fit to the light curve (not shown) show larger systematic deviations than in the cases with $\beta = 1$ or $\beta = 2$, again a sign of overegularization.

A.2 Inclination of the stellar spin axis

The inclination of the stellar spin is assumed to be equal to that of the orbit of the BD companion in our analysis, i.e. $i = 89.°60$. An isotropic orientation of the stellar spin axis has its mode at $i = 90°$ (Herrero et al. 2012), so it is reasonable to choose a value close to this, given that there is no a priori information to constrain the parameter.

The tidal timescale for the alignment of the stellar spin and the orbital angular momentum are comparable, in the case of LHS 6343 A, to the synchronization timescale that is estimated to be ≈ 7.5 Gyr. Given a probable age of the system between 1 and 5 Gyr, we cannot be sure that the obliquity has been damped by tides, unless we assume that most of the damping occurred during the pre-main-sequence phase when the tidal interaction was stronger due to a larger $R_{\rm A}$ (cf. Sect. 4.4.5). Therefore, we adopt a prudential approach and explore different cases in which the system is out of spin-orbit alignment.

We adopt the same parameters as in Sect. 4.4.4 and compute a regularized ME best fit of

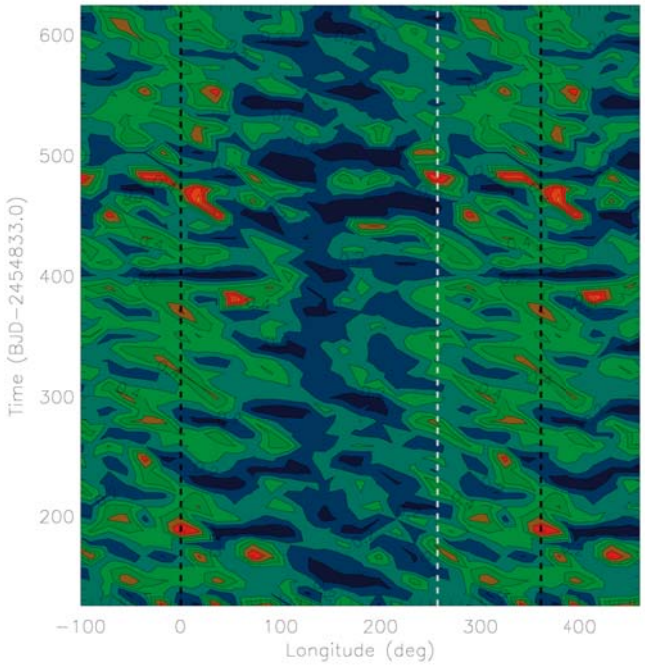

Figure A.2: As in Fig. 4.8, but adopting a longer time interval $\Delta t_{\rm f} = 10.1719$ days.

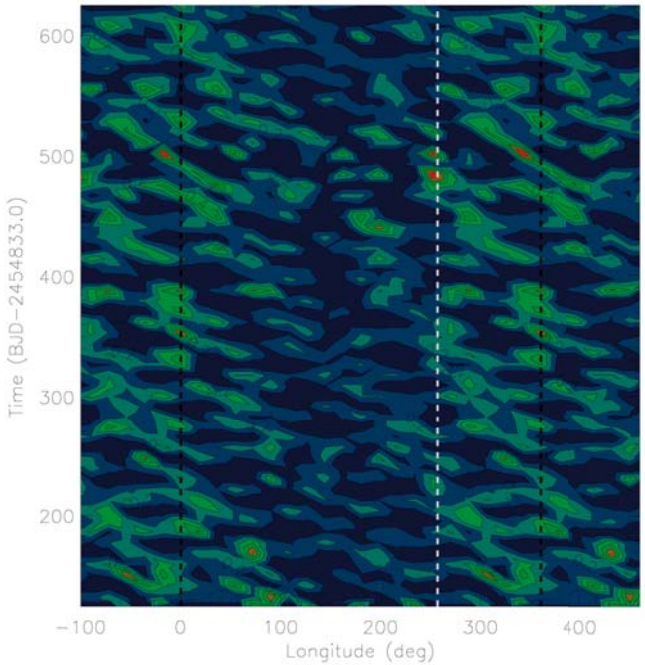

Figure A.3: As in Fig. 4.8, but performing an ME regularization with $\beta = 1$.

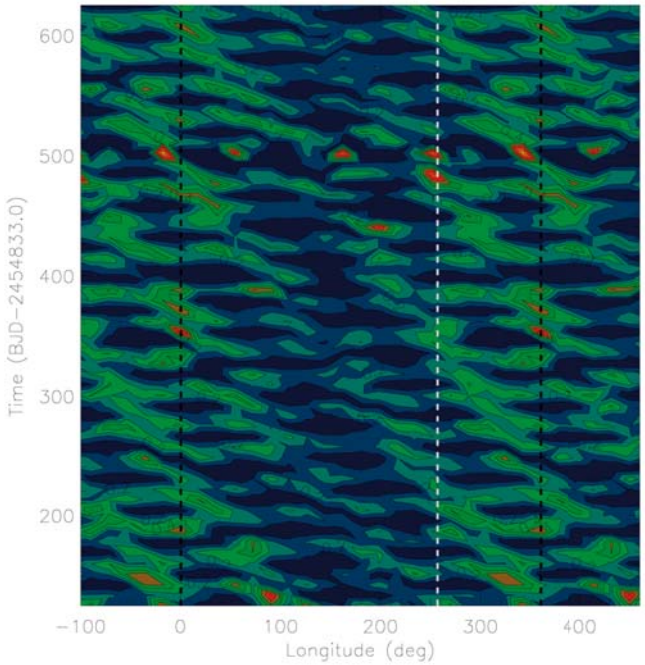

Figure A.4: As in Fig. 4.8, but performing an ME regularization with $\beta = 3$.

the light curve with $\beta = 2$, fixing the stellar inclination to $i = 60°$ and $i = 45°$. The resulting spot maps are plotted in Figs. A.5 and A.6, respectively. We may expect that the latitudinal distribution of the spots are remarkably different, especially for $i = 45°$. On the other hand, the plotted distributions of the filling factor vs. longitude and time are similar to what is computed with $i = 89.°60$. Also the evolution and migration of the active regions are similar to that case. Only some details appear to be critically dependent on the adopted inclination.

The results of the tests described in this Appendix confirms that by averaging the ME spot maps over latitude, we can effectively remove most of the degeneracy present in the light curve inversion process.

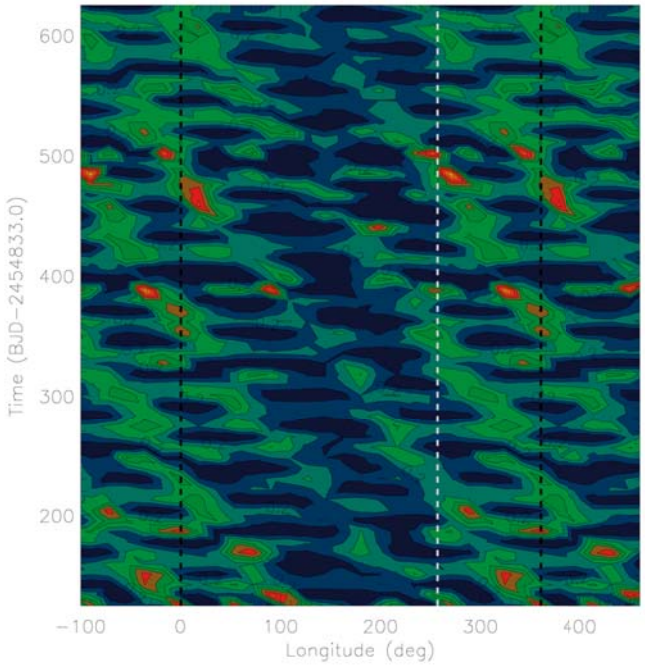

Figure A.5: As in Fig. 4.8, but adopting a stellar inclination of $i = 60°$.

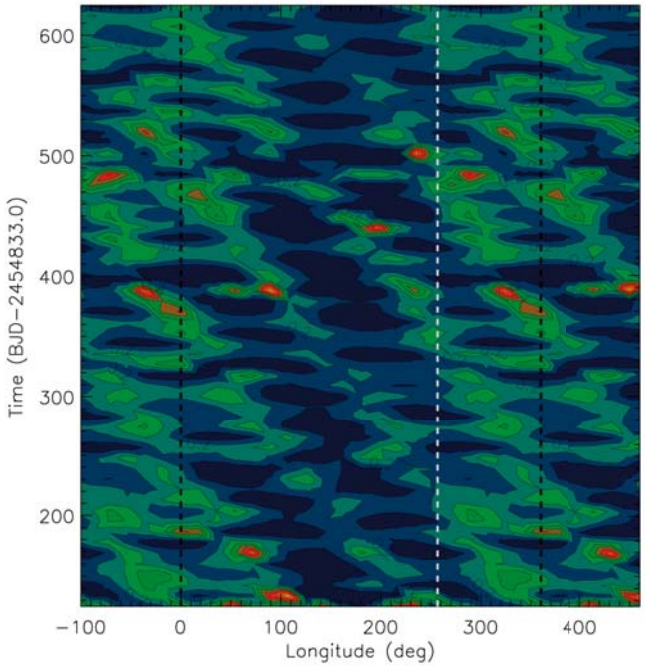

Figure A.6: As in Fig. 4.8, but adopting a stellar inclination of $i = 45°$.